Quantum information in time-frequency continuous variables

Nicolas Fabre

Université de Paris

Ecole doctorale [Physique en Ile de France, ED 564]

Laboratoire Matériaux et Phénomènes Quantiques

Quantum information in time-frequency continuous variables

Par Nicolas Fabre

Thèse de doctorat de **Physique**

Dirigée par Perola Milman
Et par Arne Keller

Présentée et soutenue publiquement le 02/11/2020

Devant un jury composé de :

Professeur	Olivier Pfister (Univ. Virginia): Président du jury
Professeur associé	Lorenzo Maccone (Univ. Pavia): Rapporteur
Maitre de conf.	Valentina Parigi (Univ. Sorbonne): Examinatrice
Professeur	Marco Liscidini (Univ. Pavia): Examinateur
Dir. de recherche	Perola Milman (Univ. Paris): Directrice de thèse
Professeur	Arne Keller (Univ. Paris): Co-directeur de thèse
Professeure	Sara Ducci (Univ. Paris): Invitée

Titre : Information Quantique en variables continues temps-fréquence

Résumé : Cette thèse aborde l'encodage de degrés de liberté continus temps-fréquence de photon uniques. Les similitudes mathématiques avec les quadratures du champ électromagnétique amène à généraliser des protocoles exprimées dans ces variables dans notre encodage. On introduit un nouveau type de qubit robuste contre des erreurs du type déplacement dans l'espace des phases temps-fréquence. Un nouvel espace des phases doublement cylindriques est étudié et est une représentation particulièrement adaptée pour des états ayant une symétrie de translation. On étudie également comment construire une distribution de phase fonctionnelle permettant de décrire un état quantique possédant des degrés de libertés continus spectraux et en quadrature.

Mots clefs : Photons uniques, Optique quantique, Information quantique, Variables continus, Circuits intégrés, Espace des phases, Variables modulaires

Title : Quantum information in time-frequency continuous variables.

Abstract : This thesis tackles the time-frequency continuous variables degree of freedom encoding of single photons and examine the formal mathematical analogy with the quadrature continuous variables of the electromagnetic field. We define a new type of qubit which is robust against time-frequency displacement errors. We define a new double-cylinder phase space which is particularly adapted for states which have a translational symmetry. We also study how to build a functional phase space distribution which allows to describe a quantum state with spectral and quadrature continuous variables degrees of freedom.

Keywords : Single photons, Quantum optics, Quantum information, Continuous variables, Integrated waveguide circuit, Phase space, Modular variables.

Abstract

La seconde révolution quantique est liée au développement d'applications de la mécanique quantique où la logique quantique joue un rôle important et direct. Ces nouvelles technologies s'étendent de la métrologie, à la simulation quantique de systèmes complexes, jusqu'aux communications quantiques plus sécurisées en passant par le calcul quantique.

Utiliser les propriétés de superposition cohérente et l'intrication de qubits peut permettre à une machine quantique de résoudre des problèmes exponentiellement plus rapide que des algorithmes déterministes ou probabilistes classiques. L'engouement récent pour le calcul quantique repose sur une plateforme bien particulière, celle des puces supraconductrices. Cela est du à la première demonstration de la suprématie quantique par l'ordinateur quantique Sycamore de Google possédant 53 qubits. Toutefois, les tâches résolubles par cette machine sont encore bien limitées. Celle réalisée et publiée en 2019 consiste à trouver des agencements dans des nombres aléatoires produits par les qubits de la machine eux-mêmes. Cette tâche a été résolue en 3 minutes par Sycamore et prendrait 10 000 ans avec un super calculateur classique. Il faut noter, pour les sceptiques, que malgré le refroidissement nécessaire pour avoir des matériaux dans l'état supraconducteur et donc l'augmentation de la facture d'électricité, la résolution de ces tâches en un temps record est également moins gourmande en énergie. Bien d'autres compagnies ont démontré comment résoudre certaines tâches difficiles pour des ordinateurs classiques avec des machines quantiques du même style. IBM propose à n'importe quel utilisateur d'effectuer des calculs quantiques sur le cloud sur un arsenal de près de 20 machines, a également développé en 2019 une machine à 53 qubits. Leur expertise porte essentiellement sur la simulation quantique de molécules. La compagnie IonQ propose quant à elle un ordinateur quantique reposant sur la plateforme d' atomes d'Ytterbium ionisés piégés. Cette plateforme est à ce jour celle dont l'erreur par opération quantique effectuée est la moindre. La scalabilité de ces deux plateformes, pour des raisons différentes, est très limitée. Il n'est pas possible de désigner un candidat idéal pour le moment. Un état quantique ne peut pas être stocké indéfiniment et est par nature fragile aux interactions avec l'environnement: aucune des machines citées n'est encore pourvue de code correcteur d'erreurs.

Les photons uniques ont été désigné comme les candidats naturels pour les communications quantiques. Un argument est d'ordre technologique: il est plus facile de

développer une plateforme par rapport à une autre lorsque celle-ci est déjà robuste. Cela ne signifie pas que des qubits définis à partir de photons uniques ne pourront jamais être utilisés pour effectuer du calcul quantique, au contraire des qubits supraconducteurs. Mais la technologie reste à être développée, celle des circuits optiques intégrés.

Les photons uniques sont des porteurs d'information et ils ont l'avantage d'interagir peu avec l'environnement ce qui garantit d'une bonne cohérence. Ils sont facilement mesurables et peuvent être produits à la demande. Néanmoins, ils sont difficiles à intriquer par des opérations déterministes et sont perdus facilement ce qui les rendent moins aptes pour des tâches de calculs. Des preuves expérimentales d'un avantage quantique, qui est loin d'être trivial à définir, dans des protocoles de calculs quantiques et de communication quantique en encodant de l'information sous forme discrète dans des photons uniques ont été démontrés. L'information est encodée dans des degrés de liberté de photons uniques. On peut nommer la polarisation, le temps d'arrivée d'un photon unique ou leur fréquence. La démonstration de protocole de QKD (quantum key distribution) en utilisant des qubits en polarisation par des communications satellites-sol par des chercheurs d'universités chinoises a été une impressionnante preuve de l'utilité de cette plateforme.

Une autre manière d'encoder l'information en optique quantique consiste à utiliser les variables continues des quadratures du champ électromagnétique. L'exemple à ce jour le plus démonstratif sont les peignes de fréquence qui sont des états comprimés multimodes. La promesse de la production de ces états grâce à des circuits intégrés est portée par la compagnie Xanadu. Cette start-up propose depuis septembre 2020, comme IBM, d'utiliser un ordinateur quantique photonique accessible depuis le cloud. La motivation principale est pour le moment le calcul quantique. Cette approche est également pertinente lorsque les systèmes à simuler sont naturellement exprimés à l'aide de variables continues, comme en théorie quantique des champs par exemple.

Ce manuscrit de thèse aborde l'encodage de l'information quantique en utilisant les degrés de liberté continus temps-fréquence de photons uniques. Cet encodage partage des similitudes mathématiques avec les variables continues quadrature position-impulsion d'un champ électromagnétique monomode. Ces variables sont sensibles au nombre de photons mais leur interprétation et utilisation dans des protocoles quantiques sont physiquement très différentes.

Cette étude est motivée par les réalisations expérimentales de sources de photons uniques avec des circuits intégrés fonctionnant en température ambiante au sein de notre laboratoire Matériaux et Phénomènes Quantiques, dans l'équipe QITE dirigée

par Sara Ducci. Deux structures de guide d'onde semi-conductrice en AlGaAs ont été élaborées et caractérisées produisant des paires de photons se propageant dans le même sens ou dans des sens opposés, par un processus de génération d'émission spontanée (SPDC) de type-II. Les corrélations en fréquence de ces paires de photons peuvent être contrôlées soit avant leur génération dans le cas du dispositif dit contrapropageant, soit après leur génération dans les deux types de guide d'onde avec les éléments d'optiques habituels. Les circuits intégrés possèdent plusieurs avantages par rapport à l'optique dite de volume, on peut citer leur petite taille, leur stabilité et la scalabilité. L'objectif étant de miniaturiser les composants afin construire des machines plus complexes et de taille réduite pour des systèmes embarqués dans des satellites par exemple. Ces dispositifs intégrés ont la particularité d'être pourvus d'un grand indice de réfraction et sont placés en air libre. Les paires de photons avant de sortir du cristal font plusieurs allers-retours au sein de celui-ci. L'état produit est appelé un micro-peigne quantique, "micro" pour l'aspect photon unique et "peigne" pour l'aspect granuleux du spectre joint en fréquence de la paire de photon. Il est alors envisagé d'utiliser ces systèmes à haute dimensionnalité pour définir des qubits robustes contre des erreurs de type déplacement temps et fréquence, analogues aux états Gottesman, Kitaev et Preskill (GKP). Une erreur de ce type est habituellement décrite en électromagnétisme par l'étalement temporel d'un paquet d'onde dù à des effets dispersifs. L'intrication en fréquence de ces états résultant de leur génération par SPDC se prête facilement à la correction d'erreur.

On commence par un rappel du formalisme de la mécanique quantique, la description d'un état quantique par une fonction d'onde ou plus généralement par une matrice densité ainsi que les postulats de la mécanique quantique. L'encodage de l'information quantique dans des systèmes de dimension finie et infinie est abordé, ainsi que la correction d'erreur dans chaque cas. On introduit la notion d'espace des phases, qui permet de représenter un système quantique par une quasi-distribution de probabilité et celle-ci est en correspondance biunivoque avec la matrice densité. Cette distribution est notamment très utilisée pour décrire des systèmes quantiques avec des variables continues et a l'avantage contrairement à la matrice densité, d'être accessible expérimentalement. La notion de calcul universel quantique est alors introduite. Un ensemble universel quantique est un ensemble de portes qui contient à la fois des portes efficacement simulables en temps polynomial par une ordinateur classique et une porte qui ne l'est pas. Cet ensemble fini d'opérations permet d'approximer n'importe quel porte quantique.

Une majeure partie de la thèse est consacrée à l'étude de variables continues temps-fréquence de photons uniques. On apporte alors les différents outils pour convaincre le lecteur de l'aspect novateur de cet encodage dont l'aspect quantique est

retenu par le photon unique. L'aspect continu de ses degrés de liberté permet de définir des qubits plus robustes et de réutiliser dans notre contexte les nombreux protocoles utilisant les variables continues des quadratures position et impulsion du champ électromagnétique par analogie mathématique. Une description rigoureuse de l'espace des phases temps-fréquence à l'échelle du photon individuel est introduite, montrant le caractère quantique de la distribution de Wigner dite chronocyclique de cet espace, de par la non-commutativité d'opérateurs déplacements temps-fréquence qui a pour origine la restriction de notre formalisme dans le sous-espace du photon unique. On explicite ensuite les opérateurs temps et fréquence dans le cadre de notre formalisme et ceux-ci ne sont pas triviaux à définir. En effet, les valeurs propres de l'opérateur ne peuvent pas correspondre au temps propre de photons de par sa nature relativiste. Ce qui est effectivement mesuré est le temps d'arrivée à un détecteur. Celui-ci "click" à condition que le photon soit présent. L'introduction de ces opérateurs permet également de faciliter les analogies entre les deux types de variables continues. Notamment les opérateurs du set universel des variables continues temps-fréquence d'un photon individuel sont directement ceux des variables quadratures du champ électromagnétique. Ce set a déjà été introduit pour les variables transversales position et impulsion de photon unique, mais il est écrit dans cette thèse de manière plus transparente dans l'espace du photon unique. Comme première application de ces analogies mathématiques, on met en évidence qu'un protocole montrant l'existence de discorde quantique, une classe de corrélations quantiques, peut être démontré dans notre encodage en s'inspirant de protocoles déjà existants sur des photons uniques en polarisation et sur des états Gaussien.

Les spectres joints de la paire de photons produite par les deux circuits intégrés sont ensuite décrits mathématiquement. L'intrication en fréquence est attestée par le critère de Simon, généralisé dans le cas de nos variables continues, puis est ensuite quantifié à l'aide d'une décomposition de Schmidt du spectre joint de la paire de photons. On démontre à l'aide de cette décomposition l'augmentation de l'intrication en fréquence de la paire de photons, et qu'elle est influencée par la présence de la cavité optique. L'interféromètre de Hong, Ou et Mandel (HOM) est exploité pour apporter des informations sur la discernabilité des particules pénétrant dans ce dispositif, sur leur nature bosonique ou fermionique, sur les propriétés de symétries du spectre de paires de photons et permet également de faire une tomographie partielle de l'état. L'influence de la résolution temporelle des photodétecteurs utilisée lors de cette expérience est aussi abordée.

Basé encore sur l'analogie avec les variables continues traditionnelles, on introduit une zoologie complète d'état quantiques temps-fréquence. Les états dit chats temps-fréquence sont une superposition linéaire d'états d'un photon unique dans deux

modes en fréquence (ou en temps). On montre qu'ils peuvent être produits par une post-selection en fréquence avec un interféromètre de HOM. La signature de la superposition linéaire en fréquence est obtenue par mesure des coincidences à l'aide de ce même interféromètre. L'analogie de l'expérience d'HOM avec l'expérience des trous de Young avec des états à deux photons est également abordée. On démontre ensuite que des états GKP temps-fréquence peuvent être produit par un processus SPDC d'un cristal non linéaire placé dans une cavité optique et dont la correction d'erreur est dans cet encodage un protocole simple à réaliser. On s'intéresse également à la manipulation du spectre en fréquence de la paire de photons avec les dispositifs intégrés construit en laboratoire, menant à de l'intrication à haute dimensionnalité et à la simulation des statistiques fermioniques avec des photons. Les portes d'un set universel possible utilisant les degrés de liberté temps et fréquence de photons uniques sont finalement proposées expérimentalement.

On s'attarde ensuite à combiner les degrés de liberté continues en fréquence et celui des quadratures du champ. Une distribution de probabilité fonctionnelle est alors construite, dont les variables continues sont une fonction de l'amplitude spectrale et une autre sensible aux nombres de photons. Celle-ci a été introduite en physique des hautes énergies, mais est conceptualisée dans le cadre de l'optique quantique. Les états usuels de l'optique quantique généralisés dans cet espace multimode sont donnés, ainsi que leur distribution de Wigner fonctionnelle associées. Cette distribution permet par un jeu de limite de retrouver les distributions de Wigner bien connues, celle dont le mode est fixé et le nombre de photons pouvant varier, et le cas contraire appelé la fonction de Wigner chronocyclique. Cette distribution a déjà montré ces preuves pour quantifier l'intrication en haute dimensionnalité de champs produit par SPDC. D'autres perspectives en simulation quantique sont également abordées.

La thèse est clôturée par un dernier chapitre portant sur une nouvelle représentation mathématique des états grilles, ou état GKP. Ceux-ci possèdent en effet une symétrie de translation et se décrivent naturellement grâce aux variables modulaires. En discrétisant une variable continue réelle et sa variable conjuguée réelle, on définit les variables modulaires comme les variables bornées dont le spectre est entre deux pics du réseau. Ces variables modulaires ont des variables conjuguées entières de type moment angulaire. Un système quantique décrit par des variables continues peut alors être défini par deux paires de coordonnées du type moment angulaire-phase. On construit alors un espace des phases doublement cylindrique, et donc une distribution de Wigner possédant quatre variables - deux à valeurs entières et deux à valeurs bornées. Les états GKP ont un aspect type chat de Schrödinger dans cet espace. La correction d'erreur d'état GKP est visualisée dans cet espace des phases,

et on propose des moyens de faire la reconstruction tomographique de la distribution de Wigner en variables modulaires. Cette étude rentre dans le cadre général de trouver un espace des phases adapté aux symétries de l'état quantique considéré.

Ainsi plusieurs distributions de probabilité adaptées pour différents systèmes exhibant des variables continues sont définies. La première, bien connue, est celle dont les variables sont les quadratures du champ électromagnétique qui sont sensibles au nombre de photons du champ, appelée couramment la distribution de Wigner. La deuxième bien connue également mais peu utilisée et mal comprise, a comme variable les degrés de liberté continus d'une particule individuelle. Cette distribution est appelée la distribution de Wigner chronocyclique. La distribution qui combine ces deux types de variables continues et qui mène à une distribution de probabilité fonctionnelle est appelé la distribution de Wigner fonctionnelle. Ces trois espaces de phases sont symplectiques et ont une géométrie plane infinie, rectangulaire, puisque les variables sous-jacentes sont réelles. Le dernier espace des phases décrit est constitué de deux cylindres, et permet également de représenter des systèmes possédant des variables continues. Mais cet espace est plus adapté pour ceux qui exhibent une symétrie de translation.

Acknowledgements

Je voudrais commencer par remercier ma directrice de thèse Perola Milman et sa manière désarçonnante de dégager de la physique pure, très oraculaire. Cela a heureusement terni sur moi, et je n'ai même plus besoin de respirer du soufre maintenant. Je voudrais ensuite remercier mon co-directeur Arne Keller pour son calme (!) et sa volonté pédagogique. Un grand merci à Sara Ducci, Florent Baboux et Maria Amanti pour leur patience. Ecouter un théoricien déblatérer n'est jamais évident. Et un grand merci à tous les cinq pour leur grande patience sur mes compétences anglistiques. Une pensée pour Thomas Coudreau.

Je voudrais aussi remercier Olivier Pfister pour m'avoir accueilli pendant deux mois à l'université de Virginie. Les échanges avec ce groupe experimental (que sur papier) ont été particulièrement enrichissant. Et, j'ai presque réussi à apprendre à parler anglais. Thanks to Rajveer Neera, Miller Eaton, Carlos Gonzalez-Arciniegas, Catherine Zhu, Chun Hung Chang, for discussions on continuous variables, quantum meiosis and all these moments of conviviality. Also, I thank the black bears which came especially for me. I would also like to thank the condensed matter team, with Mathias Wampler and Israel Kirsch and the particle's physicists team, Simonetta Luiti and Brandon Kriesten.

I would like to thank Filippus Stefanus Roux for this early collaboration during my thesis. We manage to produce something in a short amount of time, with only one visio-call, followed by many discussions.

Il y a ensuite les gens qui vous supporte au jour le jour. C'est aussi une charge de travail, pour eux en tout cas. D'abord Louis Garbe, qui arrive à m'apprendre trop de choses, même sur ma propre région. Il y a Gaël Massé qui devrait changer d'affiliation politique, et Simone Felicetti, le socle indestructible. Félicien Appas, le bicrave parisien devenu gréviste. Saverio Francesconi qui s'est coupé les cheveux mais a fait une rechute. Théo Henner, qu'il faut apprendre à nourrir autre chose que des compotes sucrées. Jérémie Schumann, pour son sens de la convivialité accrue et pour trouver des vrais cadeaux de thèse. Arnault Raymond pour son sens de la propreté. Thanks also to Giorgio Maltese for many discussions, which brought me closer to experiments, but not too much. Merci aussi à Andreas Ketterer, Jonathan

Belhassen et Aurianne Minecci. Une pensée pour Guillaume Mastio, le mystique informaticien.

Un dernier paragraphe pour mes parents, qui m'ont donné la rage du travail. Mais pas autant que les gens pensent. Il vaut mieux être efficace que de regarder des vidéos de chatons pendant les horaires de travail. On n'oublie que l'on ne vit qu'une fois.

A la mielleuse question demandée il y a si longtemps par un enseignant inapte: "Alors sans rancunes? ≫. J'y réponds maintenant: ≪ Seul le purin te mérite ≫.

Contents

Chapter I

Introduction

This thesis brings a new way for encoding quantum information by using continuous variables time-frequency degrees of freedom of single-photons. This quantum information carrier has the advantage of having a low coupling to the environment which guarantees a good optical coherence. Single-photons are easily measurable and can be produced on-demand. Nevertheless, they are hard to entangle by deterministic operations and are lost easily.

This study is motivated by the experimental fabrication of integrated single-photon sources working at room temperature, in our laboratory. Two AlGaAs waveguide semiconductor devices have been built and produce photon pairs by a spontaneous parametric down conversion (SPDC) process. The frequency correlation of the photon pairs can be controlled, before or after their generation. Integrated circuits possess many advantages: their small size, stability and scalability of manufacturing. The aim is to miniaturize optical devices for building complex machines, as a quantum computer, or for embarked systems in satellites. The particularity of the studied devices is that they have a high refractive index, and are hence natural Fabry-Perot cavities. The joint spectral distribution of the photon pair has a comb structure. We then consider to use this high dimensional system, constituted by the frequency mode of the cavity, for defining robust qubits in time-frequency continuous variables of single-photon, called time-frequency GKP states. This idea is inspired directly from the Gottesman, Kitaev and Preskill (GKP) states which are qubit states encoded into an oscillator.

In Chap. II, we start by reminding the quantum mechanics formalism, the description of a quantum state by a wave function, and more generally by a density matrix followed by the postulates of quantum mechanics. In photonics, encoding quantum information can be done by using the finite dimensional Hilbert space of degree of freedom of single-photons or by using the quadrature position-momentum variables of an electromagnetic field. We then explain how to correct possible errors in these encodings. We also introduce the notion of phase-space distribution which is an equivalent representation of a quantum state. Such distribution can be measured experimentally. We then introduce the universal set of gates, which is the minimum number of quantum gates which allows to perform any unitary operation and we precise what are the quantum operations which can not be efficiently simulated in polynomial time with a

classical computer.

In Chap. III, we tackle another type of continuous variables, which are the time-frequency degrees of freedom of single photons. After the introduction on how qubits or qudits single-photon states can be used to perform quantum computation (QC), we then extend this result for infinite dimensional modes of single-photons. This type of continuous variables is very different from the "traditional" ones, since we are restricted here to the single-photon subspace. Indeed, the degrees of freedom of single photons, polarization, or in this thesis time and frequency, are manipulated as the ones of a classical field. But this fact does not prevent of the existence of quantum correlation between single-photons, and of the existence of a non-commutative algebra in the single photon subspace of time-frequency operators or displacement operators.

In Chap. IV, we provide the mathematical description of the frequency spectrum of photon pairs produced by two integrated non-linear waveguides conceived in the QITE team of the MPQ (Matériaux et Phénomènes Quantiques) laboratory. The frequency entanglement is then assessed by the generalization of the Simon's criterion in the time-frequency continuous variables encoding, and it is quantified using a Schmidt decomposition. Finally, we introduce the Hong, Ou and Mandel interferometer which allows to measure a signature of the manipulation of the photon pairs.

Based on the analogy with the quadrature position-momentum variables, we introduce a zoology of time-frequency continuous variables quantum states in Chap. V. The time-frequency cat state is a linear superposition of single photons in two frequencies or times. We show that they can be produced with a Hong, Ou and Mandel interferometer by spectral post-selection. We then demonstrate that the time-frequency GKP state can be produced by SPDC in a non-linear crystal placed in an optical cavity. The error in that encoding is the increase of the temporal width of the wave packet owing to a second-order dispersive effect. The error correction of these states is in this encoding a simple and implementable protocol. We introduce the universal set of gates in the time-frequency continuous variable of single-photons and we propose experimental ways to implement the gates composing this set.

In Chap. VI, we provide the description of a quantum field which has both quadrature position and spectral continuous variables. It leads to another type of continuous variables, actually a function, which manage to combine both these continuous variables. The chapter brings a new phase space distribution, called the functional Wigner distribution, which has as continuous variables functions. Such distribution was introduced in high energy physics, but it is here contextualized in a quantum optics framework. This functional distribution allows to recover well-known Wigner distributions. We can for instance obtain the one whose the mode of the quantum state is fixed and where the quadrature position-momentum variables can vary: it is the "traditional" Wigner distribution. Alternatively, we can obtain the chronocyclic Wigner distribution, where the number of photons is fixed and the spectral distribution can vary. The

Wigner functional distribution has already shown its utility for quantifying the high dimensional entanglement of signal and idler fields produced by SPDC. Other perspectives in quantum simulation and quantum computation are also mentioned.

The last chapter VII provides an alternative mathematical representation of GKP states. These states have translational symmetry and can be described naturally with modular variables. By discretizing a continuous variable and its conjugated one, we can define such modular variables as bounded variables whose spectra lie between two peaks of the position (resp. momentum) lattices. A quantum system describes by continuous variables can then be defined by two pairs of angular momentum-phase variables. We then built a phase space composed of two cylinders. The distribution into that phase space is called the modular Wigner distribution and has four variables, two integers and two bounded. These variables correspond to two angular momentum and two modular variables. Using this formalism, we develop the noise model which allows for building GKP states in this new representation. The GKP error correction, using the Steane error correction procedure, is visualized in this double-cylinder phase space and we propose two ways for performing the tomographical reconstruction of the modular variable Wigner distribution. This study enters in the general framework to find an adapted phase space for the symmetries of the considered quantum state.

Chapter II

Encoding information in discrete and continuous variables

In this chapter, after a brief reminder of the quantum mechanics formalism from [Le Bellac, 2013], we introduce how to perform quantum computation in discrete and continuous variables of physical quantum systems and provide a Hilbert space description along with a phase space one. We also explain how error correction is processed in quantum mechanics.

II.1 Description of a quantum state

II.1.1 The wave function in quantum mechanics

A physical system in quantum mechanics (QM) is described by a wave function $|\psi\rangle$, a vector of complex numbers and belongs to a finite or infinite dimensional Hilbert space $\mathcal{H}$. The dual vector is noted $\langle\psi| \in \mathcal{H}^\dagger$ which is a linear functional *i.e* a linear map from the vector space to the complex numbers. The scalar product of two ket $|\psi\rangle$, $|\phi\rangle$ noted $\langle\psi|\phi\rangle$ is a complex number. A vector can be decomposed into an orthonormal basis $(|k\rangle)_{1\leq k\leq n}$ (discrete one for example) of a Hilbert space of dimension n:

$$|\psi\rangle = \sum_{k=1}^{n} \psi_k |k\rangle , \tag{II.1}$$

where the coefficients of the basis $\psi_k = \langle k|\psi\rangle$ are the amplitude of probability of state $|k\rangle$. Then, $p_k = |\psi_k|^2$ represents the probability of state $|k\rangle$. Taking another quantum state $|\chi\rangle = \sum_{k=1}^{n} \chi_k |k\rangle$, the scalar product of two physical states is defined as the overlap:

$$\langle\chi|\psi\rangle = \sum_{k=1}^{n} \chi_k^* \psi_k. \tag{II.2}$$

The norm is defined as $||\psi||^2 = |\langle\psi|\psi\rangle|^2 = \sum_{k=1}^{n} |\psi_k|^2$. For two orthogonal states, $\langle\chi|\psi\rangle = 0$ and the overlap is then zero. We now give two examples of infinite-dimensional Hilbert space.

• $l^{(2)} = \{(c_i) \in \mathbb{C}^\infty / ||\psi||^2 = \sum_{k=1}^{\infty} |\psi_k|^2 < \infty\}$.

• The space of square normalizable function: $L^{(2)}(\mathbb{R}) = \{\psi(x) \in \mathbb{C} / ||\psi||^2 = \int |\psi(x)|^2 dx < \infty.\}$.

In quantum mechanics, a physical state is a unit vector so that all probabilities p_k add to one. For instance, for a state belonging to a finite-dimensional Hilbert space, the state is in fact square normalizable to one: $i.e\ \sum_{k=1}^{n} |\psi_k|^2 = 1$, as it is for a valid probability distribution $|\psi_k|^2$. The wave function describes a non-relativistic massive particle, as well as relativistic massless ones such as single photons (see Chap. III). The wave function $|\psi\rangle$ contains all the information relative to the particle, such as position, polarization, frequency, or any possible degree of freedom.

We are interested to know the evolution after a time t, considered as a parameter. The dynamics obey the Schrödinger equation:

$$i\hbar \frac{d}{dt} |\psi(t)\rangle = \hat{H}(t) |\psi(t)\rangle , \tag{II.3}$$

where $\hbar \approx 1.054 \cdot 10^{-34}$ J.s is the Planck's constant and $\hat{H}(t)$ is a self-adjoint operator known as the Hamiltonian, and we will assume in the following that it does not depend on time $\hat{H}(t) \equiv \hat{H}$. The Hamiltonian contains information on the dynamics of the wave function and is associated with the total energy of the system. Its mathematical expression depends on the nature of the particle, bosonic or fermionic, the characteristic of the particle such as its mass, spin, etc. It also contains terms that describe the possible interaction of the considered particle with another system. Given an initial condition $|\psi(t_0)\rangle$, at time $t > t_0$, or $t < t_0$ because the dynamics is reversible, the solution of the Schrödinger equation, which is a first-order differential equation in time, is given by:

$$|\psi(t)\rangle = \exp(-i(t - t_0)\hat{H})) |\psi(t_0)\rangle . \tag{II.4}$$

The description of quantum mechanics is probabilistic in nature because a quantum system is described by the amplitude of probability namely the wave function. Nevertheless the dynamics is purely deterministic. The operator $\hat{U}(t, t_0) = \exp(-i(t - t_0)\hat{H}))$ is unitary since we have: $\hat{U}^\dagger(t, t_0)\hat{U}(t, t_0) = \mathbb{I}$, which guarantees that the norm of the wavefunction stays equal to one after its evolution.

Description of a measurement A physical quantity A in QM is described by a Hermitian operator $\hat{A}$, called an observable, acting on the Hilbert space of the system. We assume that its eigenvalues are discrete and not degenerate $\hat{A} |k\rangle = a_k |k\rangle$, such as the spectral decomposition of $\hat{A}$ is: $\hat{A} = \sum_k a_k |k\rangle \langle k|$. Then, the measurement of a physical quantity associated with an observable $\hat{A}$, conditioned that the state is $|\psi\rangle$, gives random outcomes corresponding to the eigenvalues a_k of $\hat{A}$ with the corresponding probability given by the Born's rule:

$$p_k = |\langle k|\psi\rangle|^2. \tag{II.5}$$

Because the system is updated in that case to the eigenstate $|k\rangle$ of $\hat{A}$, we talk about the collapse of the wavefunction. If the measurement is ideal, namely the state is not destroyed, then the state is projected, or collapses, on the state $|k\rangle$:

$$|\psi'\rangle = \frac{\hat{P}_k |\psi\rangle}{\sqrt{\langle\psi| \hat{P}_k |\psi\rangle}}, \tag{II.6}$$

where $\hat{P}_k$ is the projector on state $|k\rangle$ and can be written as $\hat{P}_k = |k\rangle\langle k|$. The denominator ensures that the state after the measurement $|\psi'\rangle$ is still normalizable to one. We will see that the measurement can be described more generally than with projectors (see Sec. II.1.2).

If many experiments are conducted with the same initial state $|\psi\rangle$, the expected value of the observable A can be obtained through:

$$\langle\hat{A}\rangle = \sum_k p_k a_k = \langle\psi|\,\hat{A}\,|\psi\rangle\,. \tag{II.7}$$

Example: polarization of single photons In quantum mechanics, the polarization of single photons is treated as the eigenvalues of an angular momentum operator observable, which can take two values corresponding to its two helicities. The polarization state of a single photon is then described by a two-dimensional Hilbert space. A horizontal (resp. vertical) linear polarization state is described by a vector $|x\rangle = (1,0)^\intercal$ or $|y\rangle = (0,1)^\intercal$. In general, such state can be in a linear superposition of the two orthogonal polarizations:

$$|\psi_{\alpha,\phi}\rangle = \cos(\alpha)\,|x\rangle + e^{i\phi}\sin(\alpha)\,|y\rangle\,, \tag{II.8}$$

where α direction is the angle between the polarization state and the x axis. The state is said to be circularly polarized with left and right helicities if $\alpha = 1/\sqrt{2}$ and $\phi = \pm\pi/2$. Such unitary vector $|\psi_{\alpha,\phi}\rangle$ is called a Jones vector and is also employed for describing the polarization of classical fields. But in this last case, the coefficients of the basis do not correspond to amplitudes of probability for finding the state with x or y direction.

A polarizer can be used to manipulate the polarization state of a single photon. Its action is described by the operator: $\hat{P}_\theta = |\theta\rangle\langle\theta|$, with $|\theta\rangle = \cos(\theta)\,|x\rangle + \sin(\theta)\,|y\rangle$, where θ defined the optical axis of the polarizer and can be further written in the matrix form in the basis $\{|x\rangle\,, |y\rangle\}$:

$$\hat{P}_\theta = \begin{pmatrix} \cos^2(\theta) & \cos(\theta)\sin(\theta) \\ \cos(\theta)\sin(\theta) & \sin^2(\theta) \end{pmatrix} \tag{II.9}$$

After the polarizer, a quantum state of single photon $|\psi\rangle$ state collapses on the state $|\psi_\theta\rangle$, by using the measurement postulate Eq. (II.6):

$$|\psi_\theta\rangle = \frac{\langle\theta|\psi\rangle}{|\langle\theta|\psi\rangle|}\,|\theta\rangle\,. \tag{II.10}$$

Its new polarization state is in the direction of the optical axis of the polarizer. For instance, a linear polarized state along the x-axis described by the wave vector $|\psi\rangle = |x\rangle$ collapses on the state $|\psi_\theta\rangle$ after the polarizer:

$$|\psi_\theta\rangle = \cos(\theta)\,|x\rangle + \sin(\theta)\,|y\rangle\,. \tag{II.11}$$

The probability to find the state polarized along the x direction is $P_x(\theta) = |\langle x|\psi_\theta\rangle|^2 = \cos^2(\theta)$ while the probability to find the state polarized along the y direction is $P_y(\theta) = |\langle y|\psi_\theta\rangle|^2 =$

$\sin^2(\theta)$.

We want now to describe an unpolarized single photon which is linearly polarized at 50% along the x direction and linearly polarized at 50% along the y direction with no phase relation between the two components. The experiment says that whatever the orientation of the polarizer, the intensity output is reduced from 50%. We point out that there is no wave function that can describe such state. A more general mathematical object is hence introduced to describe such a quantum system and is now provided.

II.1.2 Mixed state

In general, a quantum system can be in a statistical ensemble of different state vectors which do not have any phase relationship. Such state is called a mixed state and corresponds to a convex sum of pure states:

$$\hat{\rho} = \sum_i p_i \left|\psi_i\right\rangle \left\langle\psi_i\right| . \tag{II.12}$$

It can be seen as the probability ignorance over a pure state: with probability p_i the superposition is $|\psi_i\rangle$. The p_i coefficients represent a probability distribution as they verify $p_i \geq 0$ and $\sum_i p_i = 1$ which is a consequence of the normalization of the density matrix $\mathrm{Tr}(\hat{\rho}) = 1$. Note that the $\{|\psi_i\rangle\}$ are not necessarily orthogonal. When $p_1 = 1$, the state can be written as $\hat{\rho} = |\psi\rangle \langle\psi|$ and corresponds to a pure state, a state of maximal knowledge. In any other case, the state is said to be mixed.

The density matrix can be explicitly expanded, for instance, on an orthonormal basis $(|i\rangle)_{1\leq i\leq n}$,

$$\hat{\rho} = \sum_{i,j}^{n} \rho_{i,j} \left|i\right\rangle \left\langle j\right| . \tag{II.13}$$

The diagonal coefficients $\rho_{ii} = \langle i|\,\hat{\rho}\,|i\rangle$ are positive and called the population terms: they represent probability distribution to be in the state i. In contrast, the non-diagonal elements $\langle i|\,\hat{\rho}\,|j\rangle$ (with $i \neq j$) are in general complex and are called the coherences. The purity of the state can be quantified by $P = \mathrm{Tr}(\hat{\rho}^2)$ which is equal to one if the state is pure and lower than one for a mixed state. For a totally mixed state defined as $\hat{\rho} = \mathbb{I}/n$, the purity is $P = 1/n$.

For instance, an unpolarized light can be described by the density matrix $\hat{\rho} = \frac{1}{2}(|x\rangle \langle x| + |y\rangle \langle y|) = \mathbb{I}/2$ and is called a maximally mixed state because it is an incoherent sum with equal weight of polarization x and y. We cannot find $|\psi\rangle$ such as $\hat{\rho} = |\psi\rangle \langle\psi|$. A polarized single photon at 45 degrees can be written as: $\hat{\rho} = \frac{1}{2}(|x\rangle \langle x| + |x\rangle \langle y| + |y\rangle \langle x| + |y\rangle \langle y|)$: there is in that case not only population terms, but also interferences terms: $|x\rangle \langle y|$ and $|y\rangle \langle x|$. Then, an equal mixture of $|x\rangle$ and $|y\rangle$ is different from a superposition of $\frac{1}{\sqrt{2}}(|x\rangle + |y\rangle)$.

The expectation value of an observable $\hat{A}$ in a state represented by the density matrix $\hat{\rho}$ is given by $\langle \hat{A} \rangle_\rho = \mathrm{Tr}(\hat{\rho}\hat{A})$ and is a generalization of Eq. (II.7).

The evolution of the density matrix is given by the von-Neumann equation:

$$i\hbar \frac{\partial \hat{\rho}}{\partial t} = [\hat{H}, \hat{\rho}], \tag{II.14}$$

which can be shown using the Schrödinger equation (see Eq. (II.3)). The density matrix at time t, knowing its initial state $\hat{\rho}(t_0)$ can be explicitly written as: $\hat{\rho}(t) = \hat{U}^\dagger(t)\hat{\rho}(t_0)\hat{U}(t)$.

Measurement on a density matrix The measurement postulate can be generalized for systems described by a density matrix. The density matrix after a measurement described by the operator $\hat{\Pi}_k$ collapses on the state:

$$\hat{\rho}' = \frac{\hat{\Pi}_k^\dagger \hat{\rho} \hat{\Pi}_k}{\sqrt{\mathrm{Tr}(\hat{\Pi}_k^\dagger \hat{\rho} \hat{\Pi}_k)}}, \tag{II.15}$$

with probability $P_k = \mathrm{Tr}(\hat{\Pi}_k \hat{\rho} \hat{\Pi}_k)$. $\hat{\Pi}_k$ can be a projector as before, but the more general object for describing a measurement is a positive operator value measurement (POVM). A POVM is a set of operators which verify the properties: $\sum_k \hat{\Pi}_k \hat{\Pi}_k^\dagger = \mathbb{I}$ and $\hat{\Pi}_k \geq 0$. The projector $\hat{\Pi}_k = |k\rangle \langle k|$, as described before, is a particular case of a POVM. This set of operators describes an imperfect measurement. Knowing the POVM of a detection scheme is equally important to the knowledge of a density matrix.

We now give some examples. In any measurement basis, a maximally mixed state $\hat{\rho} = \mathbb{I}/n$ gives the same result $1/n$. The action of a polarizer oriented along the direction θ, described by the projector $\hat{\Pi}_\theta = |\theta\rangle \langle \theta|$ of an unpolarized light gives the pure state $|\theta\rangle \langle \theta|$.

Composite quantum systems We consider two quantum systems described by their Hilbert spaces $\mathcal{H}_1$ and $\mathcal{H}_2$ of dimension n_1 and n_2. The Hilbert space of the global system, called a composite system, is the tensorial product of the two individual Hilbert space: $\mathcal{H} = \mathcal{H}_1 \bigotimes \mathcal{H}_2$. We can express a multipartite density matrix as the tensor product of individual ones, which can be written in the matrix form:

$$\hat{\rho}_{12} = \sum_{i,j,k,l} \rho_{i,j,k,l} \, |i,j\rangle \langle k,l| \, . \tag{II.16}$$

The state is said to be separable if the full density matrix is a convex sum of product state:

$$\hat{\rho} = \sum_k p_k \hat{\rho}_1^k \otimes \hat{\rho}_2^k, \tag{II.17}$$

where $\hat{\rho}_{1,2}$ are density matrices on the Hilbert spaces $\mathcal{H}_{1,2}$. If the bipartite state is not separable, then the state is said to be entangled. The separable mixed bipartite state given by Eq. (II.17) cannot be efficiently simulated by choosing two classical fields with probability p_k.

Such interpretation gives rise to the conclusion that under local measurement and classical communication, there is no quantumness about this state. It is in fact wrong, as the separability alone does not imply the absence of quantum correlation (see also Sec. III.5.1). Indeed, classical communication can give rise to quantum correlation but not to entanglement [Giorda and Paris, 2010]. Hence, mixed separable states, depending on the form of the probability distribution p_k can be separated into states that can exhibit classical or quantum correlation.

If one of the subsystems is not known, let say the second, the subsystem is said to be discarded. The mathematical description of such operation is described by the partial trace of $\hat{\rho}_{12}$ over 2:

$$\hat{\rho}_1 = \mathrm{Tr}_2(\hat{\rho}_{12}). \tag{II.18}$$

The resulting state is a mixed one since it cannot be written as a pure state $\hat{\rho}_1 \neq |\psi\rangle\langle\psi|$. Nevertheless, if the state is pure $\hat{\rho}_{12}$ and separable, the resulting state after the partial trace $\hat{\rho}_1$ remains pure. In such an operation, information is lost because the resulting state $\hat{\rho}_1$ is mixed which is not desired for instance to produce single photons (see Sec. IV.4.3). For instance, such operation is performed if one discards the information in one arm of the interferometer, which is relevant for performing a displacement operation (see Sec. II.4.6). In the other direction, $\hat{\rho}_1 \to \hat{\rho}_{12}$ is called a purification protocol. It means that any mixed state can be viewed as an entangled pure state in a larger Hilbert space. Additional formalism on entanglement will be given in Chap. III.5.1.

II.2 Encoding information in discrete variables

II.2.1 Classical bit and error correction

A bit represents a binary variable which can take the value 0 or 1. The low and high values of voltage of an electric signal is one instance on how a bit can be produced. The goal of classical computation is to perform operations on multiple bits, a string of length n $\{0,1\}^n$ to achieve complex calculations. We aim to find the minimum set of logical operations in order to achieve any type of operations. We define a universal gate as a set of gates that can evaluate any Boolean functions. It is preferred, in general, to use a universal set of gates which is composed of only one gate, because it reduces the number of logical gates needed for a given calculation. The reason is also economic.

Nevertheless, by defining a universal set of gates, it does not confer the code, namely a bit string, a protection against noise which consists of bit-flip operations. These undesired operations which happen during the propagation of the signal into a wire, deteriorate the initial string $\{0,1\}^n$ that one wants to transmit. Also, logical operations are not perfect and introduce errors during a given computation. The final output data, a sequence of n-bits is not readable. How can we correct the errors?

Classical repetition code The sender wants to transmit one bit at a time in a noisy channel, where bit-flip operations happen with probability p. How to decrease the error probability? The idea is to repeat one bit to be transmitted three times and the receiver decodes the information by taking the bits which occur the most. The most simple protocol is the classical repetition code: if the sender wants to transmit 0, it is encoded by three bits 000. Then, if one error occurs, which flip the second bit: 010. The receiver then reads 010 and assumes that only one bit-flip has occurred and thus understands that the message is 000 because the bit zero is more present in that string. The new probability of error is the sum that no flip has occurred and one bit-flip happens and shrinks as $P = (1-p)^3 + 3p(1-p)^2 = 1 - (3p^2 - 2p^3)$. There exist more powerful codes to correct errors which consist in adding other bits and to optimize the strategy of the receiver to extract the data and is not going to be developed.

II.2.2 Quantum bit

The quantum bit is the unit of information in quantum mechanics and is described by a normalized wave function belonging to a two-dimensional Hilbert space. In contrast to his bit's counterpart, it can be written as a complex superposition of the two orthogonal vectors which spans the Hilbert space:

$$|\psi\rangle = \cos(\frac{\theta}{2})\,|0\rangle + \sin(\frac{\theta}{2})e^{i\phi}\,|1\rangle\,, \tag{II.19}$$

where the two parameters $\theta \in [0, \pi[$ and $\phi \in [0, 2\pi[$ are the colatitude and the longitude. Hence, the qubit state is represented in a sphere, called the Bloch sphere represented in Fig. II.1. The $|0\rangle$ (resp. $|1\rangle$) logical state lies on the north (resp. south) pole, whereas linear superpositions with equal weight but with different phases are along the equatorial axis.

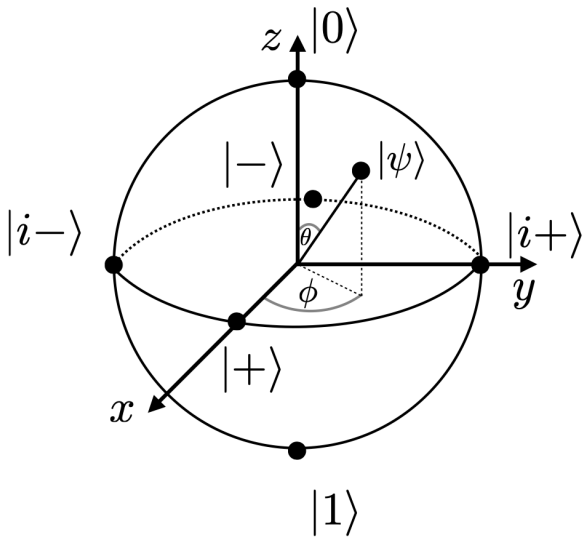

Figure II.1: The surface of the Bloch sphere is occupied by pure state while the interior by mixed state. The $|0\rangle$ and $|1\rangle$ occupied the north and the south pole, while linear combination of these logical states are in the equatorial axis $|\pm\rangle = 1/\sqrt{2}(|0\rangle \pm |1\rangle)$ and $|i\pm\rangle = 1/\sqrt{2}(|0\rangle \pm i\,|1\rangle)$.

Single qubit operations on a qubit state consist of rotations on the sphere. Going from the north to the south pole (or inversely) corresponds to a NOT gate called $\hat{\sigma}_x = \hat{X}$ gate, whereas a π rotation along the equatorial axis is called a PHASE gate called $\hat{\sigma}_z = \hat{Z}$ gate. These two gates with a third one called the $\sigma_y = \hat{Y}$ form a basis of the Lie algebra $su(2)$ defined by:

$$\hat{\sigma}_x = |0\rangle\langle 1| + |1\rangle\langle 0| \tag{II.20}$$

$$\hat{\sigma}_y = i|1\rangle\langle 0| - i|0\rangle\langle 1| \tag{II.21}$$

$$\hat{\sigma}_z = |0\rangle\langle 0| - |1\rangle\langle 1|. \tag{II.22}$$

The Pauli matrices verify the commutation and anti-commutation equation:

$$[\hat{\sigma}_i, \hat{\sigma}_j] = 2i\epsilon_{ijk}\hat{\sigma}_k, \ \{\hat{\sigma}_i, \hat{\sigma}_j\} = 2\delta_{ij}\mathbb{I}, \tag{II.23}$$

where ϵ_{ijk} is the Levi-Civita symbol, which is equal to one if i, j, k is an even permutation of $1, 2, 3$ and -1 for odd permutations. The Pauli matrices and the identity form a basis for 2×2 Hermitian matrices, a general density matrix can be written as:

$$\hat{\rho} = \frac{1}{2}(\mathbb{I} + \vec{n} \cdot \vec{\hat{\sigma}}). \tag{II.24}$$

The pure states are unit vectors and hence lie on the surface of the Bloch sphere. The mixed states verify $\mathrm{Tr}(\hat{\rho^2}) \leq 1$ which means that $||\vec{n}|| \leq 1$. Hence, they are vectors inside the sphere and the maximally mixed state $\hat{\rho} = \mathbb{I}/2$ is of radius zero and is located at the origin of the sphere.

The operators $i\sigma_j$ are the infinitesimal generators of the Lie group $SU(2)$, the group of unitary two dimensional matrix with determinant 1, which can be written as follows

$$\hat{R}_n(\psi) = \exp(-\frac{i\psi(\vec{n} \cdot \vec{\hat{\sigma}})}{2}), \tag{II.25}$$

where ψ is the rotation angle along the unit vector $\vec{n} = (n_x, n_y, n_z)$. This unitary operation $\hat{R}_n(\psi)$ allows to define two important one qubit gates for quantum computation. The Hadamard gate is a single qubit gate consisting of two rotations, one of angle π along the the x axis followed by a $\pi/2$ along the z axis:

$$\hat{H} = e^{i\pi/2}[\cos(\pi/2)\mathbb{I} + \frac{i}{\sqrt{2}}\sin(\pi/2)(\hat{\sigma}_x + \hat{\sigma}_y)] \tag{II.26}$$

$$= \frac{1}{\sqrt{2}}\begin{pmatrix} 1 & 1 \\ 1 & -1 \end{pmatrix} \tag{II.27}$$

It transforms the logical state $|0/1\rangle$ into their superposition $\hat{H}|0,1\rangle = \frac{1}{\sqrt{2}}(|0\rangle \pm |1\rangle)$. The $\pi/8$-rotation gate can be expressed as:

$$\hat{T} = \begin{pmatrix} e^{-i\pi/8} & 0 \\ 0 & e^{i\pi/8} \end{pmatrix} \tag{II.28}$$

We now proceed to the description of the measurement of the $\hat{\sigma}_z$ observable in the computational basis $\{|0\rangle, |1\rangle\}$. The probability to measure the state $|0\rangle, |1\rangle$, the state being in the state $\cos(\frac{\theta}{2})|0\rangle + \sin(\frac{\theta}{2})e^{i\phi}|1\rangle$ is given by $\cos^2(\frac{\theta}{2})$ and $\sin^2(\frac{\theta}{2})$. It is also a single-qubit operation.

One qubit is not enough for practical quantum computing, since measurement alters or destroys the state. In addition, the power of quantum computation resides on the exponential size of the Hilbert space of the composite system of n-qubits 2^n. We hence want to generalize the conditional operation in the quantum case, which is operated through entanglement in quantum mechanics. The composite Hilbert space of multiple qubits is $H = \bigotimes_{i=1}^{n} H_i$ and again is dimension 2^n. We consider two important quantum gates which act on two qubits labelled 1 and 2, the controlled-NOT ($\hat{C}_X$) and the controlled-PHASE ($\hat{C}_Z$) gates which are given by:

$$\hat{C}_X = \begin{pmatrix} 1 & 0 & 0 & 0 \\ 0 & 1 & 0 & 0 \\ 0 & 0 & 0 & 1 \\ 0 & 0 & 1 & 0 \end{pmatrix}, \; \hat{C}_Z = \begin{pmatrix} 1 & 0 & 0 & 0 \\ 0 & 1 & 0 & 0 \\ 0 & 0 & 1 & 0 \\ 0 & 0 & 0 & -1 \end{pmatrix}. \tag{II.29}$$

These gates perform a controlled operation depending on the state of the first qubit: the qubit 2 is flipped only if the controlled qubit 1 is in the $|1\rangle$ state. Indeed, we have: $\hat{C}_X |00\rangle = |00\rangle, \hat{C}_X |01\rangle = |01\rangle, \hat{C}_X |10\rangle = |11\rangle, \hat{C}_X |11\rangle = |10\rangle$.

All the mentioned gates, single or two qubits operations, are all unitaries and describe perfect gates without losses. Finally, we define the Pauli group P_n as the tensorial product of the gates I, $\hat{X}$, $\hat{Y}$, $\hat{Z}$ which act on n qubits with an overall phase ± 1 and $\pm i$. Any element of P_n squares to $\pm\mathbb{I}$ and any $\hat{P}, \hat{Q} \in P_n$ commute or anti commute.

Quantum circuit is a model of quantum computation in which computation is an ordered sequence of gates and measurements which can give data to control further operations. In Fig. II.2, we show how the operations are represented. A given operation is realized by a quantum circuit represented by a black box. Successive operations are performed from the left to the right, directed by a quantum wire represented by a black line. Classical operations are indicated by two black lines, the obtained measurement result can be used for further quantum operations II.2(f). The operations are not always unitaries, for instance the erasure gate consists of a trace operation or a partial trace operation (see Sec. II.1.2). Finally, to achieve any quantum operation, the set of employed gates must be universal as explained below (see Sec. II.2.4).

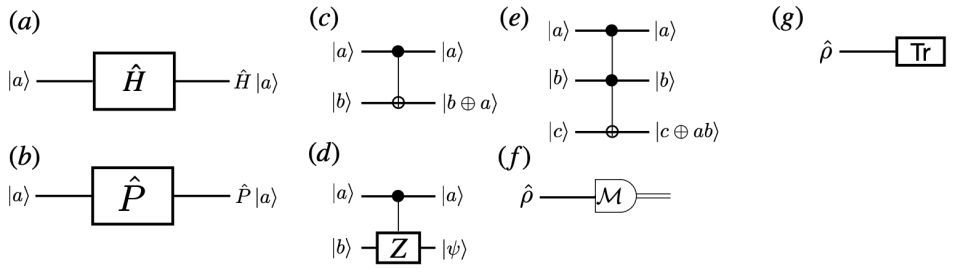

Figure II.2: Quantum circuit (a) Hadamard gate. (b) Phase gate $\hat{P}$ which can be for instance the $\pi/8$ gate (see Eq. (II.28)). (c) $\hat{C}_X$ gate (d) $\hat{C}_Z$ (e) Toffoli gate (f) Measurement. The double line means that after the measurement, the obtained result can be classically transmitted afterwards to control another qubit. (g) Erasure gate consists of a partial trace on a subsystem or a full trace.

II.2.3 Remark on the polarization of single photon and classical field

One example of a qubit state is the two orthogonal polarizations of single photons and not of classical electromagnetic fields. Let us clarify the difference between a quantum field - a single photon here - and a classical field. For a single photon in a coherent superposition of two orthogonal polarization, if one proceeds to a polarization measurement, at each run of the experiment, there are only two possible outcomes that can happen randomly at a given time t. We talk about the collapse of the wave function when the measurement is proceeded. Conversely, for a classical field, at a given time t we measure the intensity of the electromagnetic wave in one direction, and not probability. In that context, there are no random outcomes. The intensity measurement of a stochastic classical field is similar to the click distribution of a single-photon. Nevertheless, the measurement makes collapse of a quantum state, but it does not affect a classical stochastic field.

The Jones vector formalism describes the polarization of a classical field can be mapped into the probability amplitude of a qubit polarization state of a single photon. In other words, the Jones vector formalism permits to describe both classical fields and single photons. Every transformation on Jones vectors also applies to quantum field operators. In addition, the fact that the operations which are applied on single photons are unitaries is the consequence of the energy conservation.

A quantum field presents some features of a particle, in addition to a wave aspect. The first two experiments which have lead to the idea that the electromagnetic field is composed of wave packet interpreted as photons, whose energy is given by $E = \hbar\omega$, $\hbar$ being the Planck's constant are the photo-electric effect and the black-body radiation, in the beginning of the 20th century. It is the first step to quantize the field. The relation $E = \hbar\omega$, $\hbar$ does not make any sense for a classical field since such a field does not have a countable number of photons. The correspondence principle states that the density energy of "many" N photons and the density energy of a classical fields $|E_0|^2\epsilon_0$ must coincide in a box of volume V: $N\hbar\omega/V = |E_0|^2\epsilon_0$ in the large number of photons limit. We have noted E_0 the amplitude of the electric field and ϵ_0 the permittivity of the vacuum. The spin angular momentum of a classical field is given by $L_z = \epsilon_0/\omega(|E_{0L}|^2 - |E_{0R}|^2)$ where $\left|E_{0L/R}\right|^2$ is the total intensity of the field of helicities L and R. By writing $|E_{0L,R}|^2 = |E_0|P_{L,R}$ where $P_{L,R} \in [0,1]$ and by using the correspondence principle, the spin angular momentum of a classical field can be written as $L_z = N\hbar/V(P_R - P_L)$. Then, the spin angular momentum of a single photon will have a similar expression $l_z = \hbar(P_R - P_L)$. $P_{R/L}$ is now interpreted as the probability of having to measure a single photon polarized with a R (resp. L) helicity. In addition, in contrast to a classical field, a single photon has a quantized $\pm\hbar$ angular momentum corresponding to the two helicities, as well as its energy $E = \hbar\omega$ as mentioned before.

II.2.4 Universal quantum computation

Solovay-Kitaev theorem Given a unitary matrix of $SU(2)$ dimensional Hilbert space, what set of gates has to be chosen to approximate such unitary matrix? This answer is given by the Solovay-Kitaev theorem [Dawson and Nielsen, 2005]. In its simple formulation, the theorem states that if single-qubit gates generate a dense subset of $SU(2)$, then any desired gate can be approximated by a finite short sequence of such gates from this generating subset. In other words, the numbers of gates required to approximate a given operation scales well with respect to the accuracy ϵ as it required poly$(\log(1/\epsilon))$ gates. This theorem constrains the repertoire of unitary gates, but to define explicitly the set has still to be done. It allows us to define quantum computation classes: since we pass from an infinite number of gates to a finite number N of gates to perform a computation. This same number N is used as a measure of complexity. Namely, a given task is classified depending on the calculation time required to perform it and enters in one computation class.

Gottesman-Knill theorem, limitation of quantum computation By consequence of the last theorem, the unitary matrix of size 4^n can be approximated by concatenating single-qubits and one two-qubit gate. But can we choose any of them? It is answered by the Gottesman-Knill theorem [Gottesman, 1998], which limits the power of quantum computation (QC). It says that a certain class of quantum circuit, called stabilizer circuit, can be efficiently simulated on a classical computer in polynomial time. The stabilizer circuit is composed of gates belonging to the normalizer of the Pauli group, called the Clifford group. The theorem formally states that a given quantum computation composed of three steps:
(1) Preparation of the qubits state in the computational basis (Pauli eigenstates).
(2) Quantum gates from Clifford group.
(3) Measurement in the computational basis
can be efficiently simulated by a classical computer. The gates $(\hat{H}, \text{CNOT})$ belong to the Clifford group and hence can generate a high degree of entanglement but they are not enough to achieve a quantum advantage.

A universal set of gates in QC is composed of both Clifford and Non-Clifford gates, as the Toffoli or the $\pi/8$ gates. Non-Clifford gates cannot be efficiently simulated by a classical computer, and can be seen as a consequence of the large intrinsic size of the Hilbert space 2^n. Some examples of universal set of gates for quantum computation are the CNOT, Hadamard and $\pi/8$ gate or the Toffoli, Hadamard and $\pi/4$ gate. Other possible sets are also possible. All these operations are the building blocks of discrete variable quantum algorithms.

Magic state distillation Achieving universal quantum computation and circumventing the Gottesman-Knill theorem is possible with magic state distillation [Bravyi and Kitaev, 2005, Knill, 2005, Zhou et al., 2000]. The principle is to take multiple noisy quantum states (*i.e* mixed

states) and create a smaller number of less noisy (more pure) quantum states. It is called a purification scheme. It was shown that magic state distillation combined with Clifford gates are universal for quantum computation.

The noise is inherent to the propagation of a quantum carrier, and the description of such errors and how to correct them is now investigated.

II.2.5 Quantum error correction

The need for error correction with quantum resources is more crucial than with classical ones. For instance, with a superconducting qubit, once qubit state is prepared in an excited state $|1\rangle$. The longitudinal relaxation time T_1 from which the state relaxes in the groundstate $|0\rangle$ is $54\mu s$ for the 5-qubit IBM machine [IBM, 2019]. For a classical machine, a bit prepared in a high value of voltage state can stay into that state indefinitely. Furthermore, a quantum machine is also characterized by the transversal relaxation time T_2 from which a phase-flip event can happen and is equal to 74.3μs for the same IBM machine. This type of error does not have an equivalent in classical information. Hence, once a quantum state is prepared, it must live long enough, by being store into a quantum memory (see Ref. [Heshami et al., 2016]) so that several operations can be performed and then the state can be read by measurement.

Errors are unavoidable and one idea to tackle them would be to generalize the classical repetition code in quantum information. Quantum and classical error correction differs in two main aspects. The non-cloning theorem [Park, 1970, Wootters and Zurek, 1982] states that it is impossible to create an identical copy of an arbitrary quantum state using a unitary transform $|\psi\rangle \rightarrow |\psi\rangle \otimes |\psi\rangle$. The strategy of copying an arbitrary quantum state multiple times to protect it is not possible, by using the classical repetition code. Another difference is that the measurement process in QM makes collapse the wavefunction into a superposition in the measurement basis. A different strategy needs to be formulated for correcting errors occurring in a quantum state.

First, we recap all the possible errors which can happen during a quantum computation. Imperfect gates or interaction of the qubits with their environment are two main sources of errors. The errors are of the following types:

• Bit-flip gate $\hat{X}$, analog to the bit flip error in classical encoding. The phase error gate $\hat{Z}$ which does not have any classical analog. We suppose again than one error happens with a probability of p (as in Sec. II.2.1).

• Continuous errors rotation around a given axis of the Bloch sphere (see Fig. II.1).

• The interaction of qubits with the environment can transform a pure state into a mixed state. This type of error and how to correct it will not be discussed.

II.2.5.1 Correction of one bit error

The repetition code cannot be directly translated to the quantum realm since it would require cloning qubits. Nevertheless, the idea to protect the quantum information is the same as with classical code: one physical qubit is encoded into many qubits. This introduction is based on the Refs. [Gottesman, 1998].

Correction of one bit-flip error: three qubit bit flip code. The state $|\psi\rangle = \alpha|0\rangle + \beta|1\rangle$ is protected by entangling it with two ancilla qubits such as:

$$\alpha|0\rangle + \beta|1\rangle \rightarrow \alpha|000\rangle + \beta|111\rangle\,. \tag{II.30}$$

The preparation of this entangled state, called the three qubit bit flip code, is represented in a quantum circuit in Fig. II.4(a). Note that it is not a separable state corresponding to the formal generalization of the classical repetition code, which could be cast as the tensorial product of three identical state $(\alpha|0\rangle+\beta|1\rangle)^{\otimes 3} \neq \alpha|000\rangle+\beta|111\rangle$. It is called the three qubits bit-flip code because it is designed to protect the state $\alpha|0\rangle+\beta|1\rangle$ against one bit-flip error. The three qubits state is sent in a quantum channel, which flips only one qubit. We assume that for instance it is the second qubit which is flipped, an operation represented by a $\hat{\sigma}_x$ Pauli matrix. The state is then: $\alpha|000\rangle + \beta|111\rangle \rightarrow \alpha|010\rangle + \beta|101\rangle$. The goal of the receiver is to recover the state $\alpha|0\rangle + \beta|1\rangle$ but it does not know if errors have happened during the transmission. The errors can be identified using two other qubits, initialized in the $|0\rangle$ state. They are entangled with the qubits of the sender, with CNOT operations represented in Fig. II.4. The resulting state is given by:

$$(\alpha|000\rangle + \beta|111\rangle)|00\rangle \rightarrow (\alpha|010\rangle + \beta|101\rangle)|10\rangle \tag{II.31}$$

If one qubit error happens in one of the other qubit, where all the cases are recapped in Fig, II.3 then the receiver measures different syndromes and knows what operations he has to perform to correct the state. When we measure the syndrome, the superposition $\alpha|0\rangle + \beta|1\rangle$ does not collapse. The full quantum circuit for detecting errors and correcting them is represented in Fig. II.3. Finally, once the full state is corrected, the two other qubits which were used to protect the quantum state of interest $|\psi\rangle = \alpha|0\rangle+\beta|1\rangle$ are unentangled $\alpha|000\rangle+\beta|111\rangle \rightarrow (\alpha|0\rangle+\beta|1\rangle)|00\rangle$ in a decoding operation.

Correction of one phase flip error: three qubit phase flip code The given code confers protection against one bit-flip error but is unprotected against one phase-flip error represented by the $\sigma_z = \hat{Z}$ Pauli matrix. The three qubit bit-flip code is not adapted for correcting phase flip. Indeed, if each phase flip occurs on a three qubit code with probability $p < 1/2$ the probability that one or three phase flip is: $3p(1-p)^2 + p^3 > p$ and it is then worse than without the two additional ancilla.

In order to protect against one phase-flip error, instead of taking the eigenvectors of $\hat{Z}$, we take the eigenvectors of $\hat{X}$, which is done by performing three Hadamard gates on the initial

State	Syndrome	Correction gate	Probability of the event
$(\alpha\|000\rangle + \beta\|111\rangle)\|00\rangle$	00	$\mathbb{I}$	$(1-p)^3$
$(\alpha\|100\rangle + \beta\|011\rangle)\|11\rangle$	11	X_3	$p(1-p)^2$
$(\alpha\|010\rangle + \beta\|101\rangle)\|10\rangle$	10	X_2	$p(1-p)^2$
$(\alpha\|001\rangle + \beta\|110\rangle)\|01\rangle$	01	X_1	$p(1-p)^2$
$(\alpha\|110\rangle + \beta\|001\rangle)\|01\rangle$	01	X_1	$p^2(1-p)$
$(\alpha\|101\rangle + \beta\|010\rangle)\|10\rangle$	10	X_2	$p^2(1-p)$
$(\alpha\|011\rangle + \beta\|100\rangle)\|11\rangle$	11	X_3	$p^2(1-p)$
$(\alpha\|111\rangle + \beta\|000\rangle)\|00\rangle$	00	$\mathbb{I}$	p^3

Figure II.3: Three qubit bit-flip code entangled with two syndrome qubits, which catch the error which occurred in one of the first three qubits. Depending on the value of the syndrome, corrections gates must be performed to return to the original state.

entangled state $\alpha|000\rangle + \beta|111\rangle$ which gives: $\alpha|+++\rangle + \beta|---\rangle$, which defines the three qubit phase-flip code. Then the same protocol as before is repeated and allows us to correct one phase flip error. Nevertheless, the three qubit phase-flip code is not adapted to correct against bit-flip.

Shor 9-qubit code In order to protect against both phase and bit flips, the solution was proposed by Peter Shor [Shor, 1995] and consists to concatenate the three qubits bit and phase flip code. The quantum state to transmit $\alpha|0\rangle + \beta|1\rangle$ and thus to protect is encoded into nine physical qubits as:

$$\alpha\frac{(|000\rangle + |111\rangle)(|000\rangle + |111\rangle)(|000\rangle + |111\rangle)}{2\sqrt{2}} + \beta\frac{(|000\rangle - |111\rangle)(|000\rangle - |111\rangle)(|000\rangle - |111\rangle)}{2\sqrt{2}}. \tag{II.32}$$

Without detailing the full protocol, the next step consists of detecting and correcting errors by adding ancilla qubits and proceed to syndrome measurement, which permits to identify errors and take actions to correct then.

We also note that this code can actually correct arbitrary continuous error as $\begin{pmatrix} e^{-i\theta} & 0 \\ 0 & e^{i\theta} \end{pmatrix}$. It is a consequence of the theorem that a QECC that correct $\hat{I}, \hat{X}, \hat{Y}, \hat{Z}$, as the Shor 9-qubit code, can also correct any arbitrary qubits error. This result is important because it implied that we do not need an infinite number of qubits for correcting this type of error.

There are other types of code which outperform the Shor 9-qubit code. The idea behind any correction code is to add ancilla qubits which undergo the errors to protect the quantum state of interest. Then, after reading the measurement result, the aim is to find an efficient strategy to take subsequent actions to correct the errors. All correcting codes have a common mathematical description which is now provided.

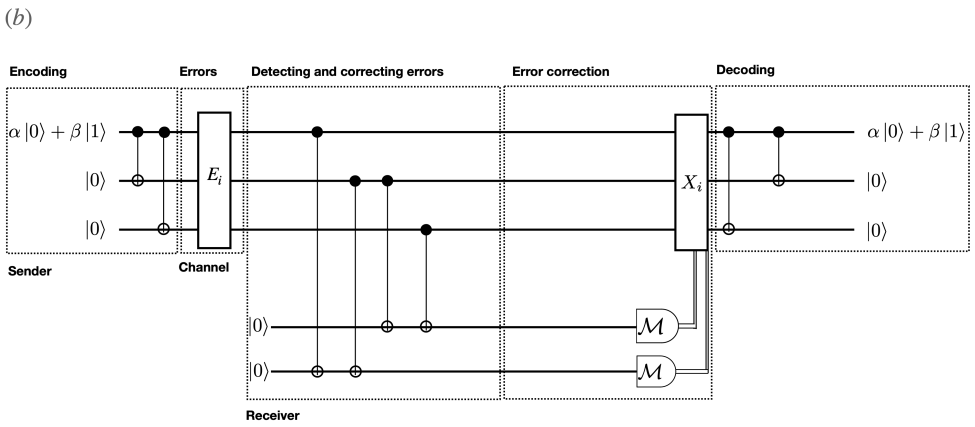

Figure II.4: Three qubit bit-flip code error correction with measurement. The protocol starts with the encoding, where the qubit to send $\alpha|0\rangle+\beta|1\rangle$ is encoded with two other qubits ancilla. The total state is entangled (see Eq. (II.30)). Then, the state crosses a channel where one bit-flip can occur. The receiver first detects the errors by entangling two other ancillas, called the syndrome qubits and by measuring it, which have as consequence not to destroy the state to send. Then, once the errors are known, a correction step is undergone. Finally, the last step is the decoding, in order to recover the state of interest $\alpha|0\rangle+\beta|1\rangle$.

II.2.5.2 Stabilizer codes

A certain class of quantum codes known as stabilizer codes is widely studied and permits to identify and correct errors. Without giving the full formalism, we give the principal ideas and results. A $[[n,k]]$ stabilizer code is a k qubit state which encodes a n physical qubit. The stabilizer operator $\hat{S}$ is defined as the operator which has as eigenstate the stabilizer code with the $+1$ eigenvalue: $\hat{S}|\psi\rangle=+1|\psi\rangle$. By considering qubit systems, the structure of the stabilizers are the tensorial product of Pauli gates. The stabilizer operators belong to a subgroup of the abelian Pauli group noted S.

Examples • The stabilizer operators of the EPR state $|\psi\rangle=\frac{1}{\sqrt{2}}(|00\rangle+|11\rangle)$ are the product of Pauli matrices: $\hat{X}_1\hat{X}_2$ and $\hat{Z}_1\hat{Z}_2$ and belong to a subset of the Pauli group P_2.
• The stabilizer operators of the 3-qubit bit-flip code $[[1,3]]$ $|000\rangle+|111\rangle$ are $\hat{Z}_1\hat{Z}_2$ and $\hat{Z}_2\hat{Z}_3$.
• The stabilizer operators of the 3-qubit phase-flip code $[[1,3]]$ $|+++\rangle+|---\rangle$ are $\hat{X}_1\hat{X}_2$ and $\hat{X}_2\hat{X}_3$.
• The stabilizer operators of the 9-qubit Shor code [[9,1,3]] are $\hat{Z}_1\hat{Z}_2$, $\hat{Z}_2\hat{Z}_3$, $\hat{Z}_4\hat{Z}_5$, $\hat{Z}_5\hat{Z}_6$, $\hat{Z}_7\hat{Z}_8$, $\hat{Z}_8\hat{Z}_9$.

Errors denoted by the operator $\hat{E}$ also belong to the Pauli group. Single qubit errors can be written under the general form: $\hat{E}=a_0\mathbb{I}+a_1\hat{X}+a_2\hat{Z}+a_3\hat{X}\hat{Z}$. The measurement of the stabilizer allows us to identify errors. If the stabilizer commute with the errors $[\hat{S},\hat{E}]=0$ the erroneous state $\hat{E}|\psi\rangle$ is moved into the $+1$ eigenspace of the stabilizer $\hat{S}\hat{E}|\psi\rangle=+\hat{E}|\psi\rangle$. If they anti-commute $\{\hat{S},\hat{E}\}=0$, the erroneous state $\hat{E}|\psi\rangle$ is moved into the -1 eigenspace of the stabilizer $\hat{S}\hat{E}|\psi\rangle=-\hat{E}|\psi\rangle$. The syndrome measurement consists of measuring the eigenvalues

of the stabilizers, it gives information on the nature of the error and allow taking measures to measure them. All the detectable errors are the ones that anti-commute with at least one stabilizer. A "bad" error occurs when $\hat{E}\left|\psi\right\rangle \neq \left|\psi\right\rangle$ which means that the syndrome is outside the quantum code subspace.

Example For the 3-qubit bit-flip code if $\hat{X}_1$ or $\hat{X}_2$ errors occurs, then the stabilizer operator is $\hat{Z}_1\hat{Z}_2 = (\left|00\right\rangle\left\langle 00\right| + \left|11\right\rangle\left\langle 11\right|) - (\left|01\right\rangle\left\langle 01\right| + \left|10\right\rangle\left\langle 10\right|)$ and consist to two projective measurements. If the qubit 1 and 2 are the same (resp. orthogonal), then the measurement will give the ± 1 value, and hence the flip-error can be detected.

Knill and Laflamme have formulated a set of conditions [Bacon, 2006, Bergmann and Van Loock, 2016, Knill and Laflamme, 1997] which precise when it is possible to detect and correct such errors. We assume that we have a stabilizer subspace for a code $\left|\psi_i\right\rangle$ generated by $(S_i)_{1\leq i\leq d}$ and we note $\hat{P}$ a Pauli operator which anticommutes with one of these generators S_i. P will be written as a product of errors $\hat{E}_i^\dagger\hat{E}_j$. Then we have the condition: $\left\langle\psi_k\right|\hat{E}_i^\dagger\hat{E}_j\left|\psi_l\right\rangle = 0$. In the other case where $\hat{E}_i^\dagger\hat{E}_j \in S$, we obtain a similar condition: $\left\langle\psi_k\right|\hat{E}_i^\dagger\hat{E}_j\left|\psi_l\right\rangle = \delta_{kl}$. The two cases are special case of the quantum error correcting criteria which is:

$$\left\langle\psi_k\right|\hat{E}_i^\dagger\hat{E}_j\left|\psi_l\right\rangle = C_{ij}\delta_{kl}. \tag{II.33}$$

If C_{ij} contains only diagonal elements, then the code is not distorted by the errors. The Kronecker delta enforces that the code, called non-degenerate code, and their erroneous version are orthogonal (namely $\left\langle\psi_k\hat{E}_i\middle|\hat{E}_j\psi_l\right\rangle = 0$).

The quantum error correcting criteria can be rewritten in an alternative (more modern) way [Kribs et al., 2006, Poulin, 2005]. We define the triplet (R, E, C), where the error E and the recovery R are operations acting on the quantum code C subspace of a Hilbert space H. E is a superoperator, a channel which can be written in terms of the $\hat{E}_i$ operations belonging to S: $E(\hat{\rho}) = \sum_i \hat{E}_i\hat{\rho}\hat{E}_i^\dagger$. When such R exists, the system is correctable for the error E, which mathematically means:

$$(R \circ E)(\hat{\rho}) = \hat{\rho}\ \forall\hat{\rho} = \hat{P}_C\hat{\rho}\hat{P}_C \tag{II.34}$$

where $\hat{P}_C$ is the projection of the Hilbert space H onto the quantum code C. The Eq. (II.34) can be reformulated in terms of the $\hat{E}_i$ as:

$$P_C\hat{E}_i^\dagger\hat{E}_jP_C = \lambda_{ij}P_C\ \forall i,j \tag{II.35}$$

for a given matrix of coefficients λ_{ij}. This condition is also sufficient for the error E to be corrected.

Finally, we define the weight of an operator as the number of qubits on which it acts. For instance, the weight of the stabilizer $\hat{Z}_1\hat{Z}_2$ of the three-qubit bit-flip code is two. The distance d of a code $[[n, k]]$ is defined as the smallest weight of a nontrivial Pauli operator which acts on

the code space to itself, but such operator is not the identity. It is shown that a code of distance d can correct errors of at least $(d-1)/2$ qubits. The theory of quantum error correction gives a condition verifies by the sets of integer $[[n, k, d]]$ to encode many qubits and to correct as many errors as possible, and give hence some constraints when one designs a stabilizer code.

II.2.5.3 Fault tolerance

A fault-tolerant code aims to compute in the codespace of a stabilizer code, subsequently followed by multiple error correction stages. The principle for designing a fault-tolerant protocol is that when an error occurs at a single location, a faulty gate or an error which is occurred on the qubit state, it must not affect the other qubits which are entangled with him. In other words, if the execution of the quantum circuit interactions through entanglement leads to the copy of errors, the computation will fail [Paler and Devitt, 2015]. When one designs a code and a quantum circuit for executing a certain task, the question resides on how to prepare and measure qubits fault-tolerantly. The errors are unavoidable, but the aim of quantum computation is to manage to create both Clifford and non-Clifford operations despite the presence of errors, in a fault-tolerant way.

The quantum threshold theorem quantifies how to correct errors faster than they are created (see for instance [Aharonov and Ben-Or, 1999]). The theorem states that it exists a threshold error rate p_t such that if an error rate per gate and time step fulfills the condition $p < p_t$, then it exists a fault-tolerant protocol for arbitrary long of length T with an arbitrary low logical error rate. In other words, the theorem gives a threshold from which thanks to a fault-tolerant encoding, a quantum computer suppresses the logical error rate to low levels.

A solution is to encode one logical qubit into many physical qubits. The simplest fault-tolerant code are the Steane code and the Bacon-Shor code composed of 7 and 9 physical qubits respectively. In general, a surface code is considered, which is represented by a graph of various geometries, where each node corresponds to a qubit. The surface code with a square geometry has a high noise threshold $p_c \approx 0.6 - 1\%$. One logical qubit is composed of d^2 physical qubits in addition to $d^2 - 1$ ancilla qubit for the stabilizer measurement for a code of distance d [Campbell et al., 2017].

The other ingredient is to use transversal gates when it is possible. It consists of interacting the errors which have occurred on the k-th qubit with an ancilla belonging to another block of the code. Nevertheless, transversal gates cannot implement universal fault-tolerant gates, which is a simple way of citing the Eastin-Knill theorem [Eastin and Knill, 2009]. To tackle this obstacle, the methods are to use magic state distillation (see Sec. II.2.4), teleportation of continuous variable gates (see Sec. II.4) among others.

II.3 Discrete variable system in a d-dimensional Hilbert space

In the last section, we have explained how to define a qubit which is one unit of information in a quantum carrier, a single photon. We now provide the description of a quantum state with a higher dimensional space of degree of freedom.

II.3.1 Quantum dits

The motivation of encoding information in states which belong to a larger dimensional Hilbert space is that such a state can store more information. For instance, the use of a larger space allows the improvement of channel capacity, *i.e* the amount of information that is reliably transmitted over a communication channel, and permits also an increasing of the information security [Cerf et al., 2002, Sheridan and Scarani, 2010]. This encoding allows for sending more than one bit of information per photon. Nevertheless, only a linear scaling of the Hilbert space is possible with an increasing number of modes [Imany et al., 2019] and hence does not allow for an exponential scaling which is required for fault-tolerant quantum computing.

A general qudit state is a state of a d-dimensional Hilbert space and can be expressed in the computation basis $\{|j\rangle, j = 1, ..., d\}$ by:

$$|\psi\rangle = \sum_{j=1}^{d} \alpha_j |j\rangle , \tag{II.36}$$

where α_j are complex numbers verifying the normalization condition $\sum_{j=1}^{d} |\alpha_j|^2 = 1$. The canonical conjugate basis $\left|\tilde{j}\right\rangle$ is related to the computational basis by a discrete Fourier transform: $\left|\tilde{j}\right\rangle = \frac{1}{\sqrt{d}} \sum_{j=1}^{d} e^{\frac{2i\pi j\tilde{j}}{d}} |j\rangle$. The single-qudits gates are the Heisenberg-Weyl gates, which act on the computational basis as shift and phase operations:

$$\hat{X}_d |j\rangle = |j + 1(\mathrm{mod}d)\rangle , \tag{II.37}$$

$$\hat{Z}_d |j\rangle = e^{2i\pi j/d} |j\rangle . \tag{II.38}$$

The modulo operation has been abbreviated by "mod". They are unitaries operators which can be explicitly written in an exponential representation:

$$\hat{X}_d = e^{-2i\pi \hat{P}/d}, \tag{II.39}$$

$$\hat{Z}_d = e^{2i\pi \hat{X}/d}, \tag{II.40}$$

where $\hat{X}$ and $\hat{P}$ are discrete position and momentum operators. The generalized Pauli operators are given by:

$$(\hat{X}_d)^a (\hat{Z}_d)^b, a, b \in 1, 2, ...d, \tag{II.41}$$

and act on the computational basis as: $(\hat{X}_d)^a |j\rangle = |j + a(\mathrm{mod}d)\rangle$ and $(\hat{Z}_d)^b |j\rangle = e^{2i\pi jb/d} |j\rangle$. $\hat{X}_d$ and $\hat{Z}_d$ generate the non-commutative generalized Pauli group under matrix multiplication, verifying:

$$\hat{Z}_d \hat{X}_d = \exp(2i\pi/d) \hat{X}_d \hat{Z}_d. \tag{II.42}$$

The operators $\hat{X}_d$ and $\hat{Z}_d$ also satisfy the cyclic property: $(\hat{X}_d)^d = (\hat{Z}_d)^d = \mathbb{I}$. These operators are important for quantum error correction involving qudits, in the same spirit as in Sec. II.2.5. In analogy with the Hadamard gate, we define the Fourier transform gate:

$$\hat{F} = \sum_{j,k=1}^{n} \omega^{jk} |j\rangle \langle k| \tag{II.43}$$

where $\omega = e^{2i\pi/d}$. For quantum computation, the controlled NOT qudit gate is required and is defined by

$$\hat{C}_X = \sum_{j,k=1}^{d} |j\rangle \langle j| \otimes |k+j\rangle \langle k| . \tag{II.44}$$

Such a gate can be experimentally realized thanks to a four-wave mixing process (see Ref. [Bartlett et al., 2002a] for an implementation using the orbital angular momentum of single photons). Finally, the qudits gate set:

$$\{\hat{X}_d, \hat{Z}_d, \hat{C}_X\} \tag{II.45}$$

is universal for quantum computation [Luo and Wang, 2014, Sawicki and Karnas, 2017]. We also mention that error correction protocol with qudits was proposed in [Looi et al., 2008].

II.3.2 Phase space description

In this section, we describe the phase space formulation of a qudit system [Asadian et al., 2016, Miquel et al., 2002, Proctor et al., 2015] and can be seen as a generalization of the qubit phase space [Wootters, 2004].

Displacement operators, Discrete Wigner distribution The unitaries corresponding to discrete phase displacement for a d-level system are defined by:

$$\hat{D}(l,m) = \hat{Z}^l \hat{X}^m e^{-i\pi lm/d}, \tag{II.46}$$

where $l, m \in [|1, d|]$. They satisfy the orthogonality relation:

$$\mathrm{Tr}(\hat{D}(l,m)\hat{D}^\dagger(l',m')) = d \times \delta_{l,l'}\delta_{m,m'}. \tag{II.47}$$

The discrete displacement operators obey to the Weyl relation:

$$\hat{D}(l,m)\hat{D}(l',m') = e^{i\phi_d}\hat{D}(l+l', m+m'), \tag{II.48}$$

where ϕ_d called the cocycle is: $\phi_d = \pi/d(lm' - l'm)$. One consequence of this relation, is that the accumulated phase to join two points of coordinate (l,m) and (l',m') depends on the chosen path. It corresponds to a simple example of the Berry's phase. Any operator, as the density matrix $\hat{\rho}$, can be decomposed into the discrete displacement operators basis:

$$\hat{\rho} = \frac{1}{d}\sum_{l,m=1}^{d} \mathrm{Tr}(\hat{\rho}\hat{D}(l,m))\hat{D}^\dagger(l,m), \tag{II.49}$$

where $\mathrm{Tr}(\hat{\rho}\hat{D}(l,m))$ are the coefficients decomposition into that basis. Many attempts have been done for building distribution on a discrete phase space. One way is to double the size of phase space. This procedure starts by performing the symplectic Fourier transform of the discrete displacement operator which leads to the phase point operator [Miquel et al., 2002]:

$$\begin{aligned}\hat{A}(l,m) =& \frac{1}{(2d)^2}\sum_{l',m'=1}^{2d-1}\hat{D}(l,m)\exp(-2i\pi(lm'-l'm)/2d)\\ =& \frac{1}{2d}\hat{X}^l\hat{\Pi}\hat{Z}^{-m}e^{i\pi lm/d},\end{aligned} \tag{II.50}$$

where $\hat{\Pi}$ is the parity operator which acts on an element of the computational basis: $\hat{\Pi}\,|l\rangle = |-l(\mathrm{mod}d)\rangle$. Further properties of such point operators are given in [Miquel et al., 2002]. Finally, the discrete Wigner distribution is given by the average value of the point operator

$$W_{\hat{\rho}}(l,m) = \mathrm{Tr}(\hat{A}(l,m)\hat{\rho}). \tag{II.51}$$

Since the point operator $\hat{A}(l,m)$ is Hermitian, the Wigner distribution is real. This distribution allows computing inner products between states and gives the two correct marginal distributions, *i.e* the diagonal elements of the density matrix in the computational basis and respectively its canonical conjugate one.

The phase space defined here by these operators is a torus owing to the cyclic property (see Eq. (II.37)), with discrete points, a toroidal lattice $\mathbb{Z}(d)\times\mathbb{Z}(d)$ of $2d\times 2d$ points, this doubling is necessary in order to have the desired properties for the Wigner distribution, namely the correct marginals. In addition, this distribution obeys to the Stratonovich-rules, which corresponds to the set of conditions for building a valid distribution in a given phase space (see Sec. VII.1). Visualizing quantum protocols in such discrete phase space, such as the Grover's algorithm, was done in [Miquel et al., 2002].

Continuous limit The continuous limit can be taken first by defining the rescaled position and momentum operators $\hat{x} = \hat{X}\sqrt{2\pi/d}$ and $\hat{p} = \hat{P}\sqrt{2\pi/d}$ and by taking the limit $d\to\infty$. The Heisenberg commutation relation $[\hat{x},\hat{p}] = i\mathbb{I}$ is found as well as the position and momentum displacement operators (see later Eq. II.83). In that limit, the torus phase space becomes rectangular and is going to be investigated in the next section.

II.4 Infinite dimensional Hilbert space: Continuous variables

II.4.1 Bosonic system

The transition to infinite dimensional Hilbert space can be made by taking the limit $d\to\infty$. The analog to a qudit state is now an infinitely localized state which is the continuous eigenspectra of the position operators $\hat{q}$ and momentum $\hat{p}$:

$$\hat{x}\,|x\rangle = x\,|x\rangle\,,\ \hat{p}\,|p\rangle = p\,|p\rangle\,. \tag{II.52}$$

The position and momentum states $|x\rangle, |p\rangle$ are related by a Fourier transform:

$$|x\rangle = \frac{1}{\sqrt{2\pi\hbar}} \int_{\mathbb{R}} e^{-ixp/\hbar} |p\rangle \, dp. \tag{II.53}$$

The position and momentum basis fulfill the completeness relation,

$$\int_{\mathbb{R}} dx \, |x\rangle \langle x| = \int_{\mathbb{R}} dp \, |p\rangle \langle p| = \mathbb{I} \tag{II.54}$$

and are orthogonal:

$$\langle x|x'\rangle = \delta(x - x'), \ \langle p|p'\rangle = \delta(p - p'). \tag{II.55}$$

They do not represent physical states, since they correspond to infinitely squeezed states in position or momentum and are not square normalizable [Braunstein and Van Loock, 2005]. They are nonetheless useful for building physical states, namely with a finite width in position or momentum, which is described by the wave function:

$$|\psi\rangle = \int_{\mathbb{R}} dx \psi(x) |x\rangle = \int_{\mathbb{R}} dp \tilde{\psi}(p) |p\rangle, \tag{II.56}$$

where $\psi(x), \tilde{\psi}(p) \in \mathbb{C}$ are Fourier transform of each other. $|\psi(x)|^2$ (resp. $|\psi(p)|^2$) represents the position probability distribution to find the probability at position x (resp. at momentum p) and is normalized to unity: $\int dx |\psi(x)|^2 = \int dp \left|\tilde{\psi}(p)\right|^2 = 1$.

The fractional Fourier transform $\hat{F}_\alpha$ of the position state $|x\rangle$ is:

$$\hat{F}_\alpha |x\rangle = |q_\alpha\rangle = c_\alpha e^{-i\pi \text{cotan}(\alpha) p^2} \int_{\mathbb{R}} e^{-i\pi/2 \text{cotan}(\alpha) x^2 - 2i\pi xp/\sin(\alpha)} |x\rangle \, dx, \tag{II.57}$$

which is a continuous rotation of angle α of state $|x\rangle$. In particular, for a $\pi/2$ rotation angle, the state is the momentum state $\left|q_{\pi/2}\right\rangle = |p\rangle$, which means that $\hat{F}_{\pi/2} = \hat{F}$ is the Fourier transform. This transform can be written in terms of the amplitude of the wave function:

$$F_\alpha \psi(q) = c_\alpha e^{-i\pi \text{cotan}(\alpha) p^2} \int_{\mathbb{R}} e^{-i\frac{\pi}{2} \text{cotan}(\alpha) x^2 - \frac{2i\pi xp}{\sin(\alpha)}} \psi(x) dx. \tag{II.58}$$

II.4.2 First example of continuous variables: Quadratures of the Electromagnetic field

We demonstrate that continuous variables arise from the quadrature and phase-amplitude of quantized electromagnetic fields. The description of a quantized electromagnetic field is motivated by the understanding of the black-body experiment, among many others. The quadrature "position" and "momentum" CVs change their interpretation compared to the classical field case: they become the eigenvalues of non-commuting operators.

The quantization procedure starts from the classical solution of the Maxwell's equation in the vacuum:

$$\vec{\nabla} \cdot \vec{E} = 0 \ , \ \vec{\nabla} \times \vec{E} = -\frac{\partial \vec{B}}{\partial t}, \tag{II.59}$$

$$\vec{\nabla} \cdot \vec{B} = 0 \ , \ \vec{\nabla} \times \vec{B} = \frac{1}{c^2} \frac{\partial \vec{E}}{\partial t}, \tag{II.60}$$

which are a sum of plane waves:

$$\vec{E}(\vec{r},t) = \sum_l (\vec{\epsilon_l} E_l(t) e^{i\vec{k_l}\cdot\vec{r}} + \vec{\epsilon_l^*} E_l^*(t) e^{-i\vec{k_l}\cdot\vec{r}}), \tag{II.61}$$

$$\vec{B}(\vec{r},t) = \sum_l (\frac{\vec{k_l}\times\vec{\epsilon_l}}{\omega_l} E_l(t) e^{i\vec{k_l}\cdot\vec{r}} + \frac{\vec{k_l}\times\vec{\epsilon_l^*}}{\omega_l} E_l^*(t) e^{-i\vec{k_l}\cdot\vec{r}}), \tag{II.62}$$

where $c \approx 299\ 792\ 458$ m/s is the speed of light. Each mode l is characterized by its polarisation $\vec{\epsilon_l}$, the direction of the electric field, which is perpendicular to the wave vector $\vec{k_l}$. The temporal evolution of the amplitude of the electric field is given by $E_l(t) = E_l(0)e^{-i\omega_l t}$ in the vacuum. According to the dispersion relation in the vacuum, we have $\omega_l = c\left|\vec{k_l}\right|$. We can now ask what are these modes and how they are used for the quantization procedure.

To answer this, we introduce a fictitious volume of integration $V = L^3$ with periodic boundary condition. In that case, the wave vector of a given mode l can be written as: $\vec{k} = \frac{2\pi}{L}(n_{lx}\vec{u}_x + n_{ly}\vec{u}_y + n_{lz}\vec{u}_z)$, where $(n_{lx}, n_{ly}, n_{lz}) \in \mathbb{Z}^3$. The total field energy H of the electromagnetic field is finite and is given by:

$$H = \int_V (\frac{\epsilon_0}{2}E^2 + \frac{1}{2\mu_0}B^2)dV. \tag{II.63}$$

After replacing the electric and magnetic fields by their expressions (see Eq. (II.61)) and performing the integration over the quantization volume V, the total energy can be written as:

$$H = 2\epsilon_0 L^3 \sum_l |E_l(t)|^2. \tag{II.64}$$

It means that the total energy is the sum of each mode and the modes are then decoupled. It permits the canonical quantization. The electric field is decomposed as $E_l(t) = iE_l\alpha_l(t)$ where we have chosen for the expression of the amplitude of a field $E_l = \sqrt{\hbar\omega_l/2\epsilon_0 L^3}$. We have to keep in mind that the next step is a quantization procedure, and the energy is quantized at the single photon level (see Sec. II.2.3). The energy scale $\hbar\omega_l$ is hence introduced owing to the correspondence principle. $\alpha_l(t)$ is decomposed into a real and imaginary part:

$$\alpha_l(t) = \frac{1}{2\hbar}(X_l(t) + iP_l(t)). \tag{II.65}$$

In a given mode, X and P corresponds to the real and imaginary part of the potential vector $\vec{A}$ defined by $\vec{E} = -\partial\vec{A}/\partial t$ in the Coulomb gauge [Haroche et al., 2006]. The energy of the given mode l can be expressed as:

$$H_l = \hbar\omega_l|\alpha_l|^2 = \frac{\omega_l}{2}(X_l^2 + P_l^2). \tag{II.66}$$

We recognize the energy of a one dimensional classical harmonic oscillator, where the first (resp. second) term is the potential (resp. kinetic) energy. Indeed, the Hamiltonian of a particle of mass m in a harmonic potential is:

$$H = \frac{p^2}{2m} + \frac{1}{2}m\omega^2 x^2, \tag{II.67}$$

where ω is the angular frequency of the harmonic oscillator. The correspondence between the electromagnetic field and the harmonic oscillator is fulfilled by adding the dynamics, which are the Hamilton equations:

$$\frac{dX_l}{dt} = \omega_l P_l \tag{II.68}$$

$$\frac{dP_l}{dt} = -\omega_l X_l. \tag{II.69}$$

We can then proceed to canonical quantization which consists of putting a "hat" above the position and momentum variables, more specifically $X_l \to \hat{X}_l$, or equivalently $\alpha_l \to \hat{a}_l$. The quantized electromagnetic field is hence described by the quadrature operators $\hat{X}$ and $\hat{P}$, whose eigenvalues are the position and momentum quadrature variables. This approach turned out to be valid, because the mathematical consequence of "putting hat" on quadrature position-momentum variables, namely to quantize them, leads to experimental verified results. They obey to the commutation relation $[\hat{X}_n, \hat{P}_m] = i\hbar\delta_{n,m}$, and can be expressed as:

$$\hat{X}_l = \sqrt{\frac{\hbar}{2\omega_l}}(\hat{a}_l + \hat{a}_l^\dagger), \tag{II.70}$$

$$\hat{P}_l = -i\sqrt{\frac{\hbar\omega}{2}}(\hat{a}_l - \hat{a}_l^\dagger), \tag{II.71}$$

where ω_l is the frequency of the mode l of the field. $\hat{a}_l$ and $\hat{a}_l^\dagger$ are the annihilation and creation operators (implicitly at the frequency ω_l) which obeys to the commutation relation $[\hat{a}_j, \hat{a}_k^\dagger] = \delta_{j,k}\mathbb{I}$. In a given mode, the quadrature operators $\hat{X}$ and $\hat{P}$ admit real eigenvalues noted x and p, called the position and momentum quadratures and are one example of continuous variables in quantum optics. Finally, the Hamiltonian of the quantized radiation with no external source is given by:

$$\hat{H} = \sum_l \frac{\omega_l}{2}(\hat{X}_l^2 + \hat{P}_l^2) = \sum_l \hbar\omega_l(\hat{a}_l^\dagger\hat{a}_l + \frac{1}{2}). \tag{II.72}$$

It is a set of independent quantum harmonic oscillators. After the quantization procedure, the electric and magnetic quantized field can be written as:

$$\hat{E}(\vec{r}, t) = i\sum_k \frac{\hbar\omega_k}{2\epsilon_0 V}\vec{\epsilon_k}[\hat{a}_k e^{-i\omega_k t + i\vec{k}\cdot\vec{r}} - \hat{a}_k^\dagger e^{i\omega_k t - i\vec{k}\cdot\vec{r}}], \tag{II.73}$$

$$\hat{B}(\vec{r}, t) = i\sum_k \frac{\hbar\omega_k}{2\epsilon_0 V\omega_k}(\vec{k_k} \times \vec{\epsilon_k})[\hat{a}_k e^{-i\omega_k t + i\vec{k}\cdot\vec{r}} - \hat{a}_k^\dagger e^{i\omega_k t - i\vec{k}\cdot\vec{r}}]. \tag{II.74}$$

We are now restricted to a monomode field. In such case, the Hamiltonian can be written as:

$$\hat{H} = \hbar\omega(\hat{a}^\dagger\hat{a} + \frac{1}{2}) \tag{II.75}$$

The spectrum of the number operator $\hat{N} = \hat{a}^\dagger\hat{a}$ is the set of positive or zero integers and their eigenstates $|n\rangle$ called the Fock states:

$$\hat{N}\,|n\rangle = n\,|n\rangle\,. \tag{II.76}$$

The integer n corresponds to the number of excitations of the electromagnetic field associated to the number of photons. The ladders operators act on the Fock states as:

$$\hat{a}\,|n\rangle = \sqrt{n}\,|n-1\rangle\,, \tag{II.77}$$

$$\hat{a}^\dagger\,|n\rangle = \sqrt{n+1}\,|n+1\rangle\,, \tag{II.78}$$

which allows to find an expression for the Fock state in terms of the creation operator:

$$|n\rangle = \frac{(\hat{a}^\dagger)^n}{\sqrt{n!}}\,|0\rangle \tag{II.79}$$

where $|0\rangle$ is the vacuum state and corresponds to the absence of excitation of the electromagnetic field. The Fock states form a complete $\sum_{n\in\mathbb{N}} |n\rangle\langle n| = \mathbb{I}$ and an orthogonal basis $\langle n|m\rangle = \delta_{n,m}$. The eigenstates of the Hamiltonian $\hat{H}\,|n\rangle = E_n\,|n\rangle$ are the quantized energy:

$$E_n = \hbar\omega(n+\frac{1}{2}). \tag{II.80}$$

The ground state is the vacuum state $|0\rangle$ of energy $\hbar\omega/2$. It means that each photon carries one quantum of energy $\hbar\omega$. The position amplitude wavefunction of the Fock state is:

$$\psi_n(x) = \langle n|x\rangle = \frac{1}{\pi^{1/4}}\frac{1}{\sqrt{2^n n!}}e^{-x^2/2}H_n(x), \tag{II.81}$$

where H_n are the Hermite polynomials defined by the relation: $e^{-x^2/2}H_n(x) = (x-\frac{d}{dx})^n e^{-x^2/2}$.

In the multimode case, a general Fock state can be written as:

$$|n_1, n_2, ..., n_N\rangle = \frac{1}{\sqrt{n_1!}}...\frac{1}{\sqrt{n_N!}}(\hat{a}^\dagger)^{n_1}...(\hat{a}^\dagger)^{n_N}\,|0\rangle \tag{II.82}$$

which describes a state with n_1 photons which occupy the first mode,n_2 photons which occupy the second mode, etc. N denotes the number of modes of the photonic field.

We can note that a finite quantization volume has been chosen. The quantization procedure can also be done with an infinite volume, but instead of having a sum in the quantized electromagnetic field expression (see Eq. (II.73)), we have an integral. To reach this limit, one cans at the end of the calculation perform $V \to \infty$.

Other examples of continuous variables appearing in quantum optics will be given in Chap. III which are the time-frequency degrees of freedom of single photons and in Chap. VI for a description of a multiphoton field with time-frequency degree of freedom.

II.4.3 Rectangular Phase space

A continuous variables quantum system described by a density matrix can be equivalently done with a phase space distribution which has as variables the quadrature position and momentum variables. The introduction of the phase space formalism is the same as in Sec. II.3.2, where the infinite limit $d \to \infty$ is now considered. We will see that there are three possible distributions which can be built with the proposed approach. One distribution is actually preferred

in quantum optics, called the Wigner distribution $W_{\hat{\rho}}(x,p)$, because its associated marginals correspond to the diagonal elements of the density matrix in the position and momentum basis, as it is for a classical phase space distribution. But the Wigner distribution is not necessarily positive and hence corresponds to a quasi-distribution probability. Other motivations can be specified for describing a quantum state with its associated phase space distribution. The first reason is for tomographical purposes of a quantum state. We will present two methods, among others, for measuring the Wigner distribution which is in one to one correspondence with the density matrix. The second reason is that a phase space approach makes clearer the classical limit, as it is briefly demonstrated in the following.

Displacement operators The infinite limit $d \to \infty$ of the discrete displacement operators Eq. (II.46) gives the phase space displacement operators defined by

$$\hat{D}_s(x,p) = e^{ip\hat{x}} e^{-ix\hat{p}} e^{-i(s-1)xp/2}, \tag{II.83}$$

$$\hat{D}_s(\alpha) = e^{\alpha\hat{a}^\dagger} e^{-\alpha^*\hat{a}} e^{-s|\alpha|^2/2}, \tag{II.84}$$

where we have noted $\alpha = x+ip$ and $s \in [-1,1[$. The average value of an operator decomposed as a power series of a polynomial product of creation and annihilation ladders operators, the index s translates different ordering of the ladders operators. In the normal (resp. anti-normal) ordering, the creation operators are placed to the left (resp. right) of the annihilation one. The symmetric ordering produces expression with a symmetrized product of operators. An immediate example is the displacement operator, which can be cast after a power series expansion of the exponential as [Cahill and Glauber, 1969]:

$$\hat{D}_s(\alpha) = \sum_{n,m} \frac{\alpha^n}{n!} \frac{(-\alpha)^{*m}}{m!} \{(\hat{a}^\dagger)^n, \hat{a}^m\}_s. \tag{II.85}$$

When $s=-1$, it corresponds to the normal ordering: $\{(\hat{a}^\dagger)^n, \hat{a}^m\}_{-1} = (\hat{a}^\dagger)^n \hat{a}^m$, when $s=1$ is the anti-normal ordering $\{(\hat{a}^\dagger)^n, \hat{a}^m\}_1 = \hat{a}^m (\hat{a}^\dagger)^n$. The displacement operators are unitaries: $\hat{D}_s(\alpha)\hat{D}_s^\dagger(\alpha) = \mathbb{I}$ and obeys to the Weyl's algebra: $\hat{D}_s(\alpha)\hat{D}_s(\beta) = e^{\alpha\beta^* - \alpha^*\beta}\hat{D}_s(\alpha+\beta)$. The position and momentum displacement operators act on a position state $|x'\rangle$ as $\hat{D}_s(x,p)\,|x'\rangle = e^{-isxp/2} e^{ix'p}\,|x+x'\rangle$. The displacement operators form an orthonormal basis, since we have:

$$\mathrm{Tr}(\hat{D}_s(x,p)\hat{D}_s^\dagger(x',p')) = \delta(x-x')\delta(p-p'). \tag{II.86}$$

The characteristic function is defined as the average value of the displacement operator:

$$\chi_{\hat{\rho}}^s(x,p) = \langle \hat{D}_s(x,p) \rangle = \mathrm{Tr}(\hat{\rho}\hat{D}_s(x,p)). \tag{II.87}$$

We note the identity $\chi_{\hat{\rho}}^s(0,0)$=1, and we have $\left|\chi_{\hat{\rho}}^s(x,p)\right| \leq 1$. The violation of this last inequality for the normal characteristic distribution $\chi_{\hat{\rho}}^1$ is a necessary and sufficient condition for non-classicality [Ryl et al., 2017]. In other words, the inequality is only valid for classical statistics

according to the Bochner's theorem. The Eq. (II.87) can be inverted to express the density matrix in the displacement operators basis:

$$\hat{\rho} = \iint dxdp\hat{D}^{\dagger}(x,p)\chi^{s}_{\hat{\rho}}(x,p). \tag{II.88}$$

Methods to measure the symmetric characteristic distribution $\chi^{0}_{\hat{\rho}}$, which fully characterize the state, can be done with an indirect measurement, (see Ref. [Flühmann and Home, 2020] for a recent experimental demonstration in a trapped ions circuit).

Wigner distribution The Fourier transform of the symmetric ($s = 0$) characteristic distribution leads to the Wigner distribution,

$$W_{\hat{\rho}}(x,p) = \frac{1}{\pi}\int_{\mathbb{R}} dx' e^{2ix'p} \left\langle x - x' \right| \hat{\rho} \left| x + x' \right\rangle \tag{II.89}$$

$$= \frac{1}{\pi}\int_{\mathbb{R}} dp' e^{2ip'x} \left\langle p - p' \right| \hat{\rho} \left| p + p' \right\rangle, \tag{II.90}$$

which is normalized to one, real but generally non-positive. The inverse relation allows expressing the diagonal element of the density matrix:

$$\langle x_1| \hat{\rho} |x_2\rangle = \int_{\mathbb{R}} W_{\hat{\rho}}(\frac{x_1 + x_2}{2}, p)e^{ip(x_1 - x_2)}dp, \tag{II.91}$$

and the state can be estimated by a finite number of measurement.

We now enumerate a number of properties of the Wigner distribution. The marginals of the Wigner distribution are:

$$P(p) = \int_{\mathbb{R}} W_{\hat{\rho}}(x,p)dx = \langle p| \hat{\rho} |p\rangle, \tag{II.92}$$

$$P(x) = \int_{\mathbb{R}} W_{\hat{\rho}}(x,p)dp = \langle x| \hat{\rho} |x\rangle, \tag{II.93}$$

and correspond to what is usually refers to the *correct* marginals, which means that we obtain the diagonal elements of the density matrix in the position and momentum basis. The inner product of two density matrix operators, if one of them at least is pure, is given by the overlap formula:

$$\mathrm{Tr}(\hat{\rho}_1\hat{\rho}_2) = \pi \iint dxdpW_{\hat{\rho}_1}(x,p)W_{\hat{\rho}_2}(x,p), \tag{II.94}$$

and corresponds to the idea of a transition probability. In addition, the Wigner distribution can be written as the average value of the displaced parity operator $\hat{\Pi}(x,p) = \hat{D}^{\dagger}(x,p)\hat{\Pi}\hat{D}(x,p)$:

$$W_{\hat{\rho}}(x,p) = \mathrm{Tr}(\hat{\rho}\hat{D}^{\dagger}(x,p)\hat{\Pi}\hat{D}(x,p)) \tag{II.95}$$

and was proven in [Royer, 1977]. $\hat{\Pi}$ is the parity operator, *i.e* the reflection operator which can be written in the position or momentum basis $\hat{\Pi} = \int_{\mathbb{R}} dx \left|x\right\rangle \left\langle -x\right| = \int_{\mathbb{R}} dp \left|p\right\rangle \left\langle -p\right|$, and can be considered as a π-rotation in the rectangular phase plane. $\hat{\Pi}$ is also called the photon number parity observable since it can be cast as:

$$\hat{\Pi} = e^{i\pi\hat{a}^{\dagger}\hat{a}}. \tag{II.96}$$

The even and odd Fock states are the eigenvectors of the parity operator with associated eigenvalues ± 1. The displaced parity operator $\hat{\Pi}(x,p)$ is also called the point operator, or the Stratonovich-Weyl quantizer is an element for building general distribution in phase space (see Chap. VII). Its hermiticity assures that the Wigner distribution is a real distribution and ensures that the Wigner distribution can be measured directly. We will present in Sec. II.4.6, two experimental techniques for measuring such distribution.

Thanks to the displacement operator expressed with the variables α (see Eq. (II.84)), the Wigner distribution can be written as:

$$W_{\hat{\rho}}(\alpha) = \frac{1}{\pi^2} \iint d\mathrm{Re}(\lambda) d\mathrm{Im}(\lambda) \chi^0_{\hat{\rho}}(\lambda) e^{\alpha\lambda^* - \alpha^*\lambda}, \tag{II.97}$$

but cannot be cast as Eq. (II.89).

Extension of the Wigner distribution to the multimode case We extend the definition of the Wigner distribution when the quantum electromagnetic field is composed of n modes:

$$W(x_1,p_1,...,x_n,p_n) = \frac{1}{\pi^n} \int dx'_1..dx'_n e^{2i(x'_1p_1+...+x'_np_n)} \langle x_1 - x'_1| \otimes ... \otimes \langle x_n - x'_n| \hat{\rho} |x_1 + x'_1\rangle \otimes ... \otimes |x_n + x'_n\rangle . \tag{II.98}$$

The multimode Wigner distribution is a valuable tool in the context of frequency comb created by an optical parametric oscillator (see Chap. IV) or a synchronously pumped optical parametric oscillator (SPOPO) [Roslund et al., 2014]. Each mode corresponds to a frequency peak of the comb. Such distribution can be measured by multiplexed homodyne detection. In Chap. VI, we will generalize this distribution for fields with a multimode continuous spectrum.

General Gaussian state Gaussian states are by definition states whose Wigner distributions, or characteristic distributions, in rectangular phase space are Gaussian [Braunstein and Van Loock, 2005], and are entirely characterized by their first two moments. They play a fundamental role in CVs quantum information since they can be easily produced experimentally, as coherent states and squeezed states. A pure Gaussian state has always a positive Wigner distribution according to the Hudson's theorem [Hudson, 1974], and the negativity of the Wigner distribution in the rectangular phase plane is a witness of quantumness feature. Quantum states which exhibit negative Wigner distribution are a valuable resource for quantum computing (see Sec. II.4.5), quantum metrology [Giovannetti et al., 2011] and lead to violation of the Bell's inequality using homodyne measurement [Wenger et al., 2003].

The multimode Wigner distribution of a Gaussian state can be written as:

$$W_{\hat{\rho}}(v) = \frac{\exp(-\frac{1}{2}(v-\overline{v})^T V^{-1}(v-\overline{v}))}{(2\pi)^N \sqrt{\det(V)}}, \tag{II.99}$$

where the vector v contains the quadrature position and momentum variables of all modes $v = (x_1,p_1,...,x_n,p_n)$, the first moment of the distribution is contained in the vector $\overline{v} = (\langle\hat{x}_1\rangle, \langle\hat{p}_1\rangle, ..., \langle\hat{x}_n\rangle, \langle\hat{p}_n\rangle)$. The second moment of the distribution, the covariance matrix is:

$$V_{ij} = \frac{1}{2}\langle\{\Delta\hat{x}_i, \Delta\hat{x}_j\}\rangle, \tag{II.100}$$

where $\Delta\hat{x}_i = \hat{x}_i - \langle\hat{x}_i\rangle$ and $\{,\}$ is the anti-commutator. We are far from being exhaustive in this formalism, in order to avoid being redundant with the formalism given in Sec. III.3.3, where a different type of continuous variables are introduced.

Classical limit In the following, we investigate how phase space distribution allows for a general procedure for quantization of functions of the position and momentum variables, called the Weyl quantization. We also explain the obtention of the classical limit. (x, p) in classical phase space are c-number but in a quantum phase space, these variables are the eigenvalues of non-commuting operators. Another quantization procedure was introduced and is completely equivalent to the canonical quantization.

The Weyl correspondence associates a quantum operator $\hat{A}$ to a classical-like function $A(q, p)$:

$$\hat{A} = \frac{1}{\pi\hbar}\iint dpdq \int dq' e^{-2ipq'/\hbar} A(p,q) \left|q - q'\right\rangle \left\langle q + q'\right| . \tag{II.101}$$

The inverse transform, called the Wigner transform, allows to express the classical-like function thanks to the matrix elements of A:

$$A(p,q) = \int dq' e^{-2ipq'/\hbar} \left\langle q + q'\right| \hat{A} \left|q - q'\right\rangle . \tag{II.102}$$

In the case where $\hat{A} = \hat{\rho}$, the corresponding classical-like function is the Wigner distribution. The classical function $A_{\mathrm{cl}}(q, p)$ corresponding to the operator $\hat{A}$ is obtained by taking the classical limit $\hbar \to 0$:

$$A_{\mathrm{cl}}(q,p) = \lim_{\hbar\to 0} A(p,q). \tag{II.103}$$

An illustration of this limit is the Wigner distribution of the ground state of the quantum harmonic oscillator, the vacuum state which is a Gaussian distribution centered at the phase space origin. In the classical limit [Curtright and Zachos, 2012], we have:

$$\lim_{\hbar\to 0}(\exp(-\frac{x^2+p^2}{\hbar^2})) = \delta(x)\delta(p) = W_{\mathrm{cl}}(x,p). \tag{II.104}$$

$W_{\mathrm{cl}}(x, p)$ consists, for such state, of one peak (point) in position and momentum variables and cannot correspond to the distribution of a quantum state, which is a consequence of the Heisenberg's inequality. Another way to see that the Wigner distribution cannot be highly localized in both canonical conjugate variables in the quantum case is because the distribution is bounded by:

$$-\frac{1}{\pi\hbar} \leq W(x,p) \leq \frac{1}{\pi\hbar} \tag{II.105}$$

and by adding the fact that the Wigner distribution is normalized.

Both classical and quantum phase space are symplectic, but the quantum one differs from the deformation parameter $\hbar$ which gives a non-commutative pair of functions on the phase space. This deformation can be mathematically operated through the product of observables

$\hat{A}\hat{B}$ which is realized directly with their associated phase space distribution $A(p,q)$ and $B(p,q)$ thanks to the star product defined as:

$$A * B(p,q) = A(p,q)\exp(\frac{i\hbar}{2}\sum_{j=1}^{N}(\overleftarrow{\partial_{x_j}}\overrightarrow{\partial_{p_j}} - \overleftarrow{\partial_{p_j}}\overrightarrow{\partial_{x_j}}))B(p,q). \tag{II.106}$$

The oriented arrows indicate where the partial derivatives are performed, on the function on their left or on their right. Hence, instead of formulated quantum optics in terms of operators acting on Hilbert space, one can use their associated phase space distribution.

There is an additional difference between quantum phase space distribution and its associated classical one, despite their close mathematical ressemblance. The equation of motion of the Wigner distribution is:

$$\frac{\partial W}{\partial t}(p,q,t) = \frac{2}{\hbar}\sin(\frac{\hbar}{2}(\partial_q\partial_p - \partial_p\partial_q))H(p,q)W(p,q,t). \tag{II.107}$$

We point out that the right handed term is a power series of $\hbar$. The term $\sin(\frac{\hbar}{2}(\partial_q\partial_p - \partial_p\partial_q))$ is reminiscent of the deformation quantization procedure. While the classical $W_{\rm cl}(q,p)$ and quantum distribution have the same mathematical structure (see Eq. (II.102) by replacing $\langle q+q'|\,\hat{A}\,|q-q'\rangle$ by $A(q-q')A(q+q')$ where A is some function), they differ by their equation of motion. The first term of the expansion in $\hbar$ is the classical term, the only term which survives to the classical limit $\hbar \to 0$. In that limit, we retrieve indeed the Liouville equation which describes the temporal evolution of the density probability $W_{\rm cl}(q,p)$.

Relation between different probability distributions In general, the Fourier transform of characteristic functions index by s leads to different phase space distribution. For $s=-1,0,1$, we obtain the Husimi distribution $Q_{\hat{\rho}}(x,p)$, the Wigner distribution and the P-distribution $P_{\hat{\rho}}(x,p)$ respectively. The three distributions are related by a convolutional product, which is a modified Weierstrass transform. For instance, the Husimi distribution is the convolution product $\circledast$ of the Wigner distribution and the Gaussian state centered at the origin of phase space $G(x,p) = \frac{2}{\hbar}\exp(-(p^2+q^2))$:

$$Q_{\hat{\rho}}(x,p) = W_{\hat{\rho}} \circledast G(x,p). \tag{II.108}$$

The Husimi distribution, also called the Berezin function, is a smeared version of the Wigner distribution, so that it becomes a positive distribution. In addition, in the classical limit, the two distributions are equals to the Dirac distribution. In Chap. VI (see Fig. VI.2), we will give all the relations between the distribution with another set of continuous variables.

II.4.4 Zoology of continuous variable states

In this section, we present a variety of continuous variables states and their associated representation in phase space. We will always assume that the field is monomode of frequency ω so that the position state can be written as $|x\rangle = |x\rangle_\omega$.

Fock states The Wigner distribution of the Fock state $|n\rangle$ is:

$$W_{|n\rangle\langle n|}(x,p) = \frac{(-1)^n}{\pi} e^{-(x^2+p^2)} L_n(2(x^2+p^2)), \tag{II.109}$$

where L_n denotes the n-th order Laguerre polynomial:

$$L_n(x) = \frac{e^x}{n!}\frac{d^n}{dx^n}(e^{-x}x^n). \tag{II.110}$$

All Fock states are rotationally invariant in the rectangular phase space. $|n=0\rangle$ is the vacuum state, namely it describes the absence of excitation of the electromagnetic field, and is a Gaussian state centered at the origin of phase space. We represent in Fig. II.5 (c) the Wigner distribution of the Fock state $n=1$, a non-Gaussian state, which is negative at the origin and is necessary for enhancing quantum computing. Such state exhibits sub-Poissonian statistics defined by $\Delta n^2 < \langle n\rangle$, which cannot be obtained with classical fields.

The state $|n=1\rangle$ is a non-Gaussian carrier of various modes, such as the polarization or its orbital angular momentum. The Fock states are considered in the monochromatic frequency mode ω, or at least with a frequency distribution centered at this same frequency and it is assumed that all the modes have the same Wigner distribution. The multimode generalization of these states will be investigated in Chap. VI. The one photon and the vacuum state in a given mode are two orthogonal states which allows defining a qubit in an approach of quantum computation called hybrid quantum computation (see Ref. [Sychev et al., 2018, Van Loock et al., 2008]).

Coherent state The coherent state is a specific state of the monomode multi-photon field [R and Bosture, 1985], its wave function in the position basis can be written as:

$$|x_0,p_0\rangle = \int_{\mathbb{R}} dx e^{-(x-x_0)^2/2\sigma^2} e^{ixp_0} |x\rangle . \tag{II.111}$$

The coherent state $|x_0,p_0\rangle$ also noted $|\alpha\rangle$ with $\mathrm{Re}(\alpha)=x_0$ and $\mathrm{Im}(\alpha)=p_0$ is the eigenvector of the annihilation operator $\hat{a}$ with the corresponding complex eigenvalue α. $|\alpha|^2$ is the average value of the photon number $\langle \hat{a}^\dagger \hat{a}\rangle$ of the monomode multi-photon field. The coherent state can be written in the Fock basis:

$$|\alpha\rangle = e^{-|\alpha|^2/2} \sum_{n\in\mathbb{N}} \frac{\alpha^n}{\sqrt{n!}} |n\rangle . \tag{II.112}$$

It consists of the displaced vacuum state since $|\alpha\rangle = \hat{D}(\alpha)|0\rangle$. The probability of detecting n photons on a photodetector is given by the Poisson's law:

$$P_n(\alpha) = |\langle\alpha|n\rangle|^2 = e^{-|\alpha|^2}\frac{|\alpha|^{2n}}{n!}. \tag{II.113}$$

The photon statistics is a Poissonian distribution of parameter $|\alpha|^2$ meaning that $\Delta n^2 = \langle n\rangle$ and can be described by a semi-classical theory where the light source is modeled by an atom described by quantum mechanics and the emitted field by a classical theory. It also means that all photo-detection events are independent, namely there is no time or frequency correlation

between photon detection events on a single detector. The associated Wigner distribution in the rectangular phase space is a Gaussian centered at the phase space point (x_0, p_0):

$$W_{|x_0,p_0\rangle\langle x_0,p_0|}(x,p) = \exp(-\frac{(x-x_0)^2}{2\sigma^2})\exp(-\frac{(p-p_0)^2}{2\sigma^2}). \tag{II.114}$$

The free evolution trajectory in the quadrature position-momentum phase space of a coherent state is a circle, as the classical harmonic oscillator. In addition, the dynamics of the coherent state in the classical limit is the classical trajectory of a harmonic oscillator [Curtright and Zachos, 2012]:

$$\lim_{\hbar\to 0}\frac{1}{\pi\hbar}\exp(-[(x-\cos(t)-p_0\sin(t))^2+(p-p_0\cos(t)+x_0\sin(t))^2]/\hbar^2) \\ = \delta(x-x_0\cos(t)-p_0\sin(t))\delta(p-p_0\cos(t)+x_0\sin(t)). \tag{II.115}$$

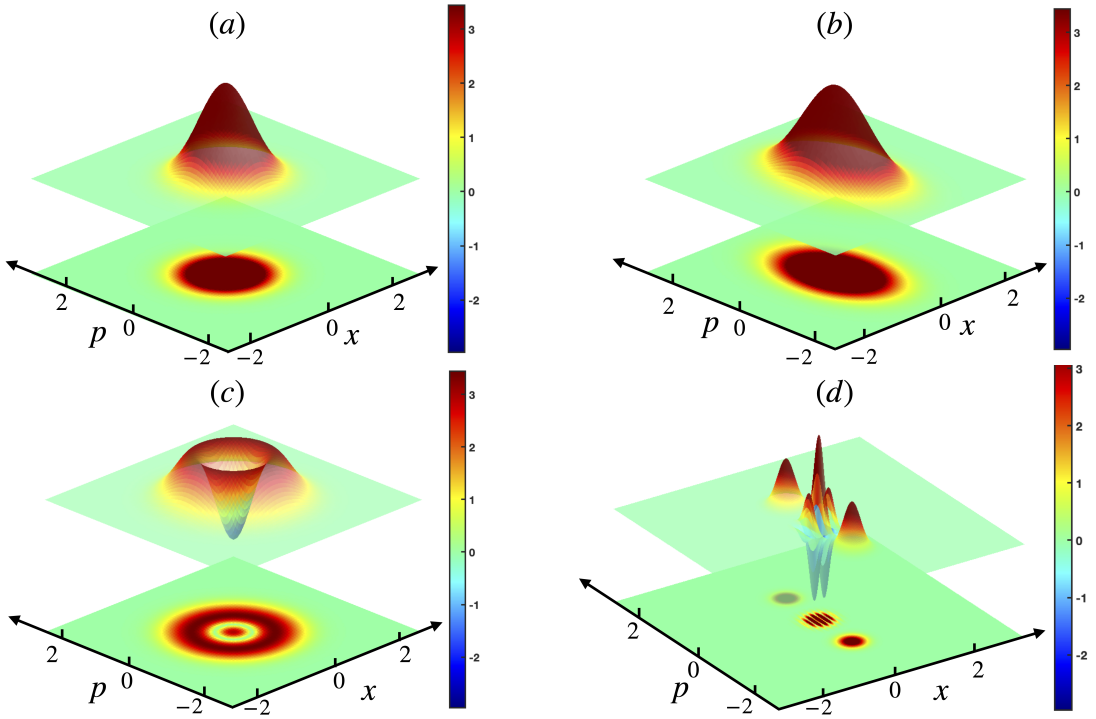

Figure II.5: Wigner distribution of different continuous variable states. (a) Vacuum state: it is a Gaussian state centered around the origin of phase space, whose widths along two orthogonal directions are equal. (b) Vacuum Squeezed state: it is also a Gaussian state centered at the origin of phase space but the widths along the p and x quadrature are not the same: if one is squeezed in a given amount the other quadrature is elongated in the same amount. (c) Fock state $n = 1$: it is a non-Gaussian state, which exhibits a characteristic negative peak at the origin (d) Even cat state: it is a non-Gaussian state composed an interference pattern perpendicular to the axis of two coherent states.

The variances of the quadrature of the coherent state are $\Delta\hat{X} = 1/\sqrt{2}$, $\Delta\hat{P} = 1/\sqrt{2}$ and their product is then equal to $\Delta\hat{X}\Delta\hat{P} = 1/2$. It is the equality case of the Heisenberg's inequality which is verified only for Gaussian states, as the coherent states.

Squeezed state Squeezed states are Gaussian states whose one of the quadratures has been squeezed, let us say that we have $\Delta\hat{X} < 1/\sqrt{2}$. The product of the variances still saturates the Heisenberg's inequality, $\Delta\hat{X}\Delta\hat{P} = 1/2$, because the state is still Gaussian, but in the conjugated quadrature, the fluctuation increases $\Delta\hat{P} > 1/\sqrt{2}$. Single-mode squeezing is described by the operator:

$$\hat{S}(\xi) = \exp((\xi\hat{a}^2 - \xi^*\hat{a}^\dagger)/2), \tag{II.116}$$

where $\xi = re^{i\phi}$: r is the squeezing parameter and ϕ is the angle of the quadrature which has been squeezed. Two important squeezed states are the vacuum squeezed state $|\xi\rangle = \hat{S}(\xi)\,|0\rangle$:

$$|\xi\rangle = \frac{1}{\sqrt{\cosh(\mathrm{r})}} \sum_{n=0}^{\infty} \frac{\sqrt{(2n!)}}{2^n n!} (-\tanh(\mathrm{r}))^n \,|2n\rangle\,. \tag{II.117}$$

and the coherent squeezed state $|\xi, \alpha\rangle = \hat{S}(\xi)\hat{D}(\alpha)\,|0\rangle$ which is the displaced squeezed vacuum state. Squeezed states of light are states which cannot be described with a classical radiation. Indeed, such a state exhibits sub-Poissonian statistics defined by $\Delta n^2 < \langle n\rangle$, and for having such statistics, one needs to quantize the electromagnetic field. The Wigner distribution of the squeezed vacuum state is:

$$W_{|\xi\rangle\langle\xi|}(x,p) = \exp(-\frac{x^2}{2e^{2r}})\exp(-\frac{p^2}{2e^{-2r}}) \tag{II.118}$$

and is represented in Fig. II.5(b). It is a Gaussian function centered at the origin with two different widths along the x and p-direction. The angle of squeezing has been set to zero $\phi = 0$, such as the state is squeezed along the x-quadrature. The variances of the squeezed state are given by:

$$\Delta\hat{X}^2 = \frac{1}{4}e^r, \tag{II.119}$$

$$\Delta\hat{P}^2 = \frac{1}{4}e^{-r}. \tag{II.120}$$

The squeezing parameter s is defined as the ratio of the variance of the squeezed state and the variance of the vacuum state: $s = \Delta x^2/\Delta x_0^2 = e^{-2r}$. Experimentally, its logarithm is generally used $s_{\mathrm{DB}} = 10\log(s)$. In Fig. II.5(b), the squeezing of the state is $s \approx 7$ dB.

Squeezed states are capable of overcoming the standard quantum limit and are hence directly useful in quantum metrology, for instance see Ref. [Toscano et al., 2006].

Cat state The even (resp. odd) cat state consists of the coherent superposition of two coherent states:

$$|\mathrm{cat}_\pm\rangle = \frac{1}{N_\pm(\alpha)}(|\alpha\rangle \pm |-\alpha\rangle), \tag{II.121}$$

the normalization factor being equals to $N_\pm(\alpha) = 2(1 \pm e^{-2|\alpha|^2})$. They are useful for defining a qubit in CVs (see Sec. II.5.1). These states capture the famous experiment of Erwin

Schrödinger. Using the expression of the coherent state in the position basis Eq. (II.112), the Wigner distribution associated of the cat state $|\text{cat}_\pm\rangle = \frac{1}{N_\pm(x_0,p_0)}(|0,p_0\rangle + |0,-p_0\rangle)$ is:

$$W_{|\text{cat}_\pm\rangle\langle\text{cat}_\pm|}(x,p) = \frac{1}{N_\pm(x_0,p_0)}[e^{-\frac{(x-x_0)^2}{2\sigma^2}}e^{-\frac{(p-p_0)^2}{2\sigma^2}} + e^{-\frac{(x-x_0)^2}{2\sigma^2}}e^{-\frac{(p+p_0)^2}{2\sigma^2}} \pm 2e^{-\frac{x^2}{2\sigma^2}}e^{-\frac{p^2}{2\sigma^2}}\cos(\frac{2p_0x}{\hbar})]. \tag{II.122}$$

The Wigner distribution of the cat state is composed of two Gaussian functions corresponding to the two coherent states $|0,\pm p_0\rangle$ and an interference term perpendicular to the axis of the two distinguishable states. The Wigner distribution of the even cat state is represented in Fig. II.5 (d), with the parameter $x_0 = 0$.

II.4.5 Universal quantum computation in continuous variables

In this section, we will see that any arbitrary quantum gate can be created using Hamiltonians which are polynomial in the quadrature operators. Owing to the Heisenberg algebra, the required set of gates for building a universal set is constrained as we will see.

Clifford group We first define the analogs of the Pauli and Clifford groups for CVs. The equivalent of the Pauli group in CVs is the Heisenberg-Weyl one, which consist of displacement operators described by:

$$\hat{X}(q) = e^{iq\hat{p}}\ ,\ \hat{Z}(p) = e^{-ip\hat{q}}, \tag{II.123}$$

where $q,p \in \mathbb{R}$. These operators acts on position and momentum state as:

$$\hat{X}(q)\,|p\rangle = e^{iqp}\,|p\rangle\,,\ \hat{X}(q)\,|q'\rangle = |q'+q\rangle\,, \tag{II.124}$$

$$\hat{Z}(p)\,|p'\rangle = |p'-p\rangle\,,\ \hat{Z}(p)\,|q\rangle = e^{ipq}\,|q\rangle\,. \tag{II.125}$$

The Fourier transform is the CV analog of the Hadamard gate (see Eq. (II.26)) defined as:

$$\hat{F} = e^{i\frac{\pi}{2}(\hat{q}^2+\hat{p}^2)} \tag{II.126}$$

and can be thought as a $\pi/2$ rotation in the rectangular phase space, since it acts on the quadrature operators as:

$$\hat{F}^\dagger\hat{q}\hat{F} = -\hat{p}\ ,\ \hat{F}^\dagger\hat{p}\hat{F} = \hat{q}. \tag{II.127}$$

We also point out that $\hat{F}^2 = \hat{\Pi}$ (see Eq. (II.96)) confirming that the parity operator is a π-rotation in the rectangular phase plane. Two-mode gates can be considered, as the CV controlled-Z (resp. X) $\hat{C}_Z$ and $\hat{C}_X$:

$$\hat{C}_Z = \exp(i\hat{q}_1\otimes\hat{q}_2),\ \hat{C}_X = \exp(i\hat{q}_1\otimes\hat{p}_2), \tag{II.128}$$

where 1 and 2 label two modes. It acts on position and momentum states as:

$$\hat{C}_Z\,|q\rangle_1\,|p\rangle_2 = |q\rangle_1\,|p+q\rangle_2\,,\ \hat{C}_Z\,|p\rangle_1\,|q\rangle_2 = |q+p\rangle_1\,|q\rangle_2\,, \tag{II.129}$$

which is a position displacement on the mode 2 of a value controlled by the state 1 (and reciprocally). Such a gate can be realized, up to a local transformation, by sending the two modes into a balanced beam-splitter. The phase gate $\hat{P}(\eta)$ is the shear operator defined by:

$$\hat{P}(\eta) = \exp(\frac{i\eta\hat{q}^2}{2}). \tag{II.130}$$

One example of set which generates the Heisenberg-Weyl group is $\{\hat{C}_X, \hat{F}, \hat{P}(\eta), \hat{X}(q); \eta, q \in \mathbb{R}\}$ [Bartlett et al., 2002b].

Extension of the Gottesman-Kitaev theorem for continuous variables states Gaussian gates cannot implement any desired unitary operation on n-harmonic oscillators, and can be understood by the fact that it is an extension of the Clifford group for CVs. From this mathematical fact, the Gottesman-Kitaev theorem has been extended for CVs and reads: QC involving only Gaussian states and Gaussian operations, elements of the Clifford group, can be efficiently simulated with a classical computer [Bartlett et al., 2002b, Lloyd and Braunstein, 1999].

We can sketch the mathematical proof behind this. All Gaussian gates are generated by the product of unitary gates $\hat{U} = \exp(if(\hat{X}, \hat{P}))$, $f(\hat{X}, \hat{P})$ being quadratic in the position and momentum operators. The product of Gaussians state cannot lead to polynomial of higher order than two of quadrature position and momentum operators, which can be mathematically justified by using the Baker-Hausdorff formula $\exp(\hat{A} + \hat{B}) = \exp(\hat{A})\exp(\hat{B})\exp(-\frac{1}{2}[\hat{A}, \hat{B}])$ and the commutation equation $[\hat{X}^{n_1}, \hat{P}^{n_2}] = g(\hat{X}, \hat{P})$ where g is a polynomial function of $\hat{X}$ and $\hat{P}$ of order less than two when $n_{1,2} \leq 2$.

A function $f(\hat{X}, \hat{P})$ which is polynomial of order three in position or momentum operators, is required for universal quantum computation. They are called non-Gaussian gates: one example is the cubic phase gate:

$$\hat{C}(\gamma) = e^{i\gamma\hat{x}^3}, \tag{II.131}$$

where $\gamma \in \mathbb{R}$. The deterministically experimental realization of such gates is difficult, because it needs strong nonlinear materials. One approach for implementing a cubic phase gate is based on a repeat until success operations [Marshall et al., 2015]. Another promising approach for the deterministic generation of a cubic or fourth order phase gate is by repeating non-commutative Rabi interaction between a harmonic oscillator and a single qubit ancillary system [Park et al., 2018]. To conclude, one universal set of quantum computing is $\{\hat{C}_X, \hat{F}, \hat{P}(\eta), \hat{X}(q), \hat{C}(\gamma); \eta, q, \gamma \in \mathbb{R}\}$

Nevertheless, the theorem does not say that Gaussian states and gates are useless. They constitute a building block for CVs quantum computation, as they are needed for the elaboration of cubic phase gates [Gottesman et al., 2001, Marshall et al., 2015, Yanagimoto et al., 2020] or as an input of continuous variable algorithm such as Gaussian Boson sampling [Björklund et al., 2019, Hamilton et al., 2017]. Also, for cryptographic protocols, the entanglement gate, or

more precisely non-locality, is a resource for achieving a quantum advantage.

Faced with the difficulty to implement a cubic or fourth phase gate, another non-Gaussian gate has been proposed to achieve universal quantum computation. This gate corresponds to a photon-number measurement resolving detection and is detailed in the next section. One should note that any non-Gaussian gate cannot be used to build a universal set of gates.

II.4.6 Balanced homodyne and PNR detection

We detail in this section two common measurements in quantum optics, the homodyne detection and the photon-number measurement resolving detection.

Balanced Homodyne detection The most common measurement in quantum optics is the homodyne detection which corresponds to a Gaussian measurement, which means that it yields a Gaussian distributed outcome when applied to Gaussian states. The measurement results are the marginal of the Wigner distribution. It works as follows.

The state to be measured $\hat{\rho}$ is combined into a balanced beam-splitter with a local oscillator, a coherent state with a large photon number and a well defined phase. The output spatial modes after the beam-splitter can be written as:

$$\hat{a}^\dagger_{1,2} = \frac{1}{\sqrt{2}}(\hat{a}^\dagger_{in} \pm \hat{a}^\dagger_{\mathrm{LO}}), \tag{II.132}$$

where $\hat{a}^\dagger_{in}$ and $\hat{a}^\dagger_{\mathrm{LO}}$ are creation operators in the spatial mode of the state of interest and the local oscillator respectively. The local oscillator is approximated by a classical field of amplitude α with phase θ, so that $\hat{a}^\dagger_{\mathrm{LO}} = \alpha_{\mathrm{LO}}$. The two outputs modes are sent to detectors which measure the photocurrent:

$$\langle \hat{I}_{1,2} \rangle = \frac{1}{2}\langle (\hat{a}^\dagger_{in} \pm \alpha^*_{LO})(\hat{a}_{in} \pm \alpha_{LO}) \rangle = \frac{1}{2}\langle (\hat{a}^\dagger_{in}\hat{a}_{in} + |\alpha_{LO}|^2 \pm \hat{a}^\dagger_{in}\alpha_{LO} \pm \hat{a}_{in}\alpha^*_{LO}) \rangle. \tag{II.133}$$

Then the two photocurrents are subtracted:

$$\langle \hat{I}_1 - \hat{I}_2 \rangle = |\alpha_{LO}| \langle \hat{a}^\dagger_{in} e^{i\phi_{LO}} + \hat{a}_{in} e^{-i\phi_{LO}} \rangle = |\alpha_{LO}| \langle \hat{x}(\phi) \rangle, \tag{II.134}$$

where the average value is taken with respect to the initial state $\hat{\rho}$. Repeating the measurement, we obtain the probability distribution $p(x, \phi_{LO})$ with mean value $\langle \hat{x}(\phi_{LO}) \rangle$. The question which arises is what relates this probability distribution to the state to be measured. We point out that the characteristic function is the Fourier transform of the probability distribution:

$$\begin{aligned} p(x, \phi_{LO}) &= \int dz e^{-izx} \langle e^{iz\hat{x}(\phi_{LO})} \rangle \\ &= \int dz e^{-izx} \langle \hat{D}(ize^{-i\phi_{LO}}) \rangle. \end{aligned} \tag{II.135}$$

After integration, we obtain:

$$p(x, \phi_{LO}) = \int dp W(x\cos(\phi_{LO}) + p\sin(\phi_{LO}), -x\sin(\phi_{LO}) + p\cos(\phi_{LO})), \tag{II.136}$$

which corresponds to the marginals of the Wigner distribution. The Wigner distribution is then reconstructed from the set of all marginals thanks to the inverse Radon's transform:

$$W_{\hat{\rho}}(x,p) = \int_{\mathbb{R}} \int_0^{\pi} \int_{\mathbb{R}} p(q,\phi)|\xi|\exp(i\xi(x\cos(\phi) + p\sin(\theta) - x))dxd\phi d\xi. \tag{II.137}$$

This technique is computationally intensive but is widely used in quantum optics. In the next section, we present another experimental technique for the tomographic reconstruction of a quantum state.

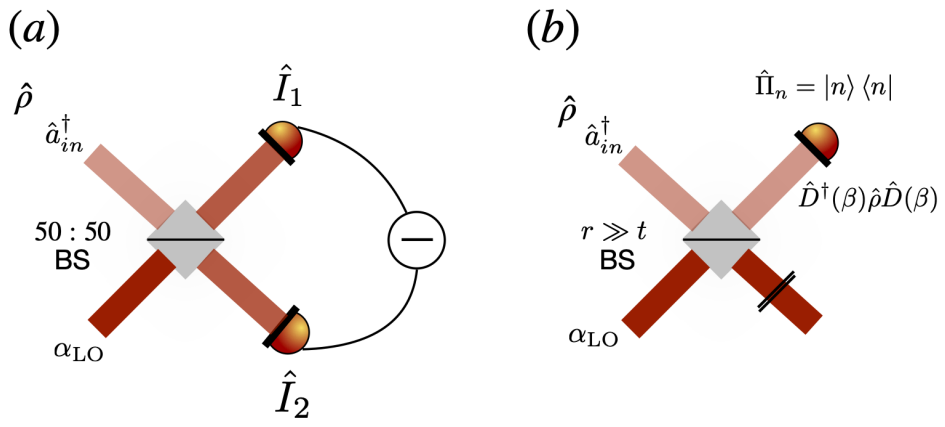

Figure II.6: (a) Balanced Homodyne measurement. (b) Quantum state tomography using PNR detectors. First a displacement on the state $\hat{\rho}$ is implemented by a beam-splitter a local oscillator of amplitude α and phase ϕ and by discarding the spatial mode labeled by two black lines in the figure. A PNR detector is placed in the other spatial port and can count photons, modeled by the projector $\hat{\Pi}_n = |n\rangle\langle n|$.

Displaced photon number measurement Photon number resolving (PNR) measurement is a non-Gaussian operation: the measurement of an input Gaussian state yields a non-Gaussian probability distribution. It relies on using detectors which are sensitive to the number of photons. Such measurement can be used to perform the tomographical reconstruction of the Wigner distribution. The protocol works as follows. The input state is a tensor product of the state to reconstruct $\hat{\rho}$ and a coherent state $|\alpha\rangle\langle\alpha|$, a local oscillator. They are combined into an unbalanced ($r \gg t$) beam-splitter. The transmitted spatial mode of the state $\hat{\rho}$ is discarded, which mathematically means that a partial trace on the density matrix of the state is performed [Paris, 1996]:

$$\hat{\rho}(\beta) = \hat{D}(\beta)\hat{\rho}\hat{D}^{\dagger}(\beta), \tag{II.138}$$

where $\beta = t\alpha$. The PNR detector measures a given state $\hat{\rho}(\beta)$ in the Fock's basis, described by the projector $\hat{\Pi} = |n\rangle\langle n|$ and gives access to the probability distribution $p_n(\beta) = \langle n|\,\hat{\rho}(\beta)\,|n\rangle$. From the Royer's formula Eq. (II.95), the average value of the parity operator is given by the Wigner distribution evaluated at the origin of phase space $W_{\hat{\rho}}(0) = \sum_n (-1)^n p_n(0)$, point obtained when the amplitude of the coherent state is set to zero. Varying the amplitude of the local oscillator α permits measuring all the Wigner distribution, point by point.

PNR detectors are transistor edge sensors consisting of tungsten chips cooled at 100 mK, such that the material is superconducting. When one photon is detected, the tungsten absorbs it and the resistivity of the material increases and is detected by a superconducting quantum interference device (SQUID). Using the photon absorption of the material allows for resolving until five photons (see for instance Ref. [Nehra et al., 2019b]), when the resistivity as a function of the temperature is linear. When this characteristic is not linear anymore, another technique was recently developed in the Andrew White team at Queensland University (not published yet) and permits to resolve until 15 photons. The technique relies on the measurement of the relaxation time from the normal phase (reached when one a photon is absorbed) to the superconducting one.

The measurement is limited by two main factors. The first is photon losses which can be significant for this type of device up to 40%, generally modeled by a balanced beam-splitter placed before the detector. It can be overcome by using a slightly modified optical scheme using semi-definite programming and compensating for losses (see Ref.[Nehra et al., 2019a]). The other limitation is related to the number of the Fock basis elements which is required for the reconstruction of the Wigner distribution. For quantum state whose decomposition in the Fock's basis does not need a large number of these states, as the single photon state $n = 1$, a detector which allows 5 photons to be resolved, is enough to measure the negativity of its associated Wigner distribution [Nehra et al., 2019b]. For larger Wigner distributions which require a larger number of Fock basis for their description, the technique based on the measurement of the relaxation time will be more reliable.

II.4.7 Discrete and continuous variables cluster state quantum computation

So far, we have developed the circuit model of universal QC, where a given operation is performed by a successive number of gates and measurements on a given quantum state. Another model of quantum computation which is equivalent to the circuit model is a measurement-based quantum computing or one-way QC. It was first introduced using quantum systems with DV and then extended with CVs.

In the cluster model of QC, or measurement-based quantum computation (MBQC) (see Ref. [Gottesman and Chuang, 1999] for the preliminary work which lead to this idea), a large entangled state is initially prepared and unitary operations are performed indirectly through measurement and by feed-forwarding the outcomes to the remaining states [Raussendorf et al., 2003, Ukai et al., 2011]. These successive operations allow unitary gates to be teleported through the cluster. The universality is achieved by adjusting the measurement basis, namely to measure out of the X and Z axis. The discrete variable cluster quantum computing (DVCQC) has been demonstrated with polarization qubits. The large qubit entangled state is modeled by a graph, where each node is occupied by one qubit and the edges correspond to CNOT gates. One qubit

measurement and the choice of the measurement basis have as effects to modify the connectivity of the graph of the remaining nodes and with additional phase gates. The advantages of DVCQC rely on the fact that high fidelity operations can be performed, but the generation of single photons are generally probabilistic (or near-deterministic with quantum dots see Ref. [Senellart et al., 2017]) and the preparation of a large entangled state is an experimental difficult task. The entangling gate requires non-linearity or probabilistic scheme [Knill et al., 2001]. The limitation in the DVCQC model does not come from the fact that the Hilbert space is finite-dimensional but it comes from single photons are difficult to manage. Nevertheless, using matter-light interaction, we should note that other strategy to deterministically generate cluster states have been developed (see Ref. [Schwartz et al., 2016] for one example).

The order of the different steps of a given computation using the continuous variables cluster quantum computing model (CVCQC) is the same. The principle is to start from an initial highly entangled state, or cluster state, composed of entangled qumode. Such states can be represented by a graph [Van Loock, 2007], where each node corresponds to a squeezed state and each line corresponds to an entanglement gate (see Fig. II.7). The cluster state is then a large entangled Gaussian state. Then, Gaussian measurements are performed, *i.e* homodyne measurements which allow to realize any Gaussian operation. The result is used to feed-forward unitaries on the remaining nodes. Once the successive measurements are performed, the quantum information flows through the cluster. Universal computation is achieved for instance with a rectangular lattice since homodyne detection in this geometry can perform any Gaussian operation, and by adding non-Gaussian operations. But other geometry of cluster states is also possible for achieving universal quantum computation. A graph of a given geometry which is not useful for QC could be relevant for quantum communication protocols for instance. The possibility of scalability using this model of quantum computation has been demonstrated by the experimental realization of multimode CV cluster states [Asavanant et al., 2019, Larsen et al., 2019] of a quantum frequency comb. The limitations in this encoding are that the fidelity of the operations is lower compared to the DVCQC. The non-Gaussian gates are required for achieving universality but are hard to produce experimentally. It can be done by using PNR measurement for instance, but an effective representation is needed to represent the effect of non-Gaussian operation into a graph state, since the cluster states are Gaussian states.

We now give two examples of continuous variables cluster states. The wave function of the two-linear cluster state is given by:

$$|\psi\rangle = e^{i\hat{q}_1 \otimes \hat{q}_2} |p_1 = 0\rangle |p_2 = 0\rangle = \iint dx_1 dx_2 e^{ix_1 x_2} |x_1, x_2\rangle \tag{II.139}$$

and its associated graph representation is given in Fig. II.7(a). The Greenberger, Horne and Zeilinger (GHZ) state is also represented in Fig. II.7(b), and can be mathematically written as:

$$|\text{GHZ}\rangle = \int\int\int dx_1 dx_2 dx_3 e^{ix_1 x_2} e^{ix_2 x_3} e^{ix_3 x_1} |x_1, x_2, x_3\rangle \,. \tag{II.140}$$

These states have special interests owing to the difficulty to eliminate quantum entanglement via projective measurement in one node. In addition, GHZ states exhibit striking non-classical correlations [Greenberger et al., 1989] which have been used in quantum secret sharing protocol [Hillery et al., 1999].

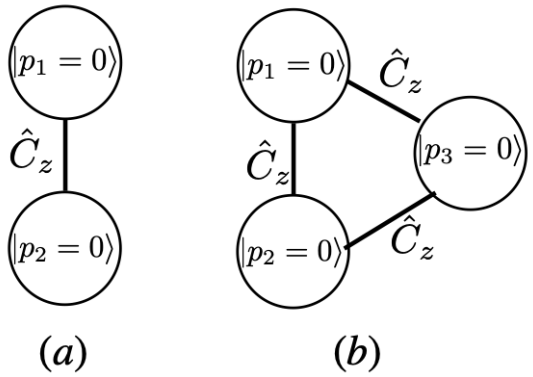

Figure II.7: Graph representation of two continuous variables cluster states, where each node is an ideal momentum squeezed state. (a) Two-linear cluster state. (b) GHZ cluster state.

Teleportation algorithm We examine how we can teleport Gaussian unitaries using the idea from CVCQC (see Ref. [Gu et al., 2009]). The entanglement between $|\psi\rangle = \int \psi(x)dx\,|x\rangle$ and the ideal squeezed state $|p_2 = 0\rangle$ is operated with the $\hat{C}_z$ gates, such as the full entanglement wave function can be written as:

$$\begin{aligned}\hat{C}_z\,|\psi\rangle\,|p_2 = 0\rangle &= \iint e^{ix_1x_2}\psi(x_1)\,|x_1\rangle_x\,|x_2\rangle_x\,dx_1dx_2 \\ &= \int \psi(x_1)\,|x_1\rangle_x\,|x_1\rangle_p\,dx_1. \end{aligned} \tag{II.141}$$

The measurement of the $\hat{p}$ quadrature with the associated result p gives:

$$|\psi\rangle = \int dx_1 e^{-ix_1p}\psi(x_1)\,|x_1\rangle_p = e^{-ip\hat{p}}\hat{F}\,|\psi\rangle\,. \tag{II.142}$$

Hence, the three steps described allow performing a Fourier transform followed by an additional displacement and is represented in Fig. II.8. The connectivity of the graph has special importance and quantifies how a given node of the graph is reachable from any way of the graph. Indeed, if the graph is "too" connected (see Ref. [Bacon and Flammia, 2009, Ellens and Kooij, 2013] for an accurate mathematical description), then measurement will affect all the nodes, which can destroy the entanglement of the remaining qumodes. In addition, the number of connections between each node quantifies the time to explore the entire graph. In general, we require that the graph is locally connected in two dimensions to realize universal quantum computation, as the rectangular geometry for instance. In general, we aim to have errors at the extremities of the graph which are not (less) connected to all the nodes, in order to avoid that errors propagate to the others nodes of the graph.

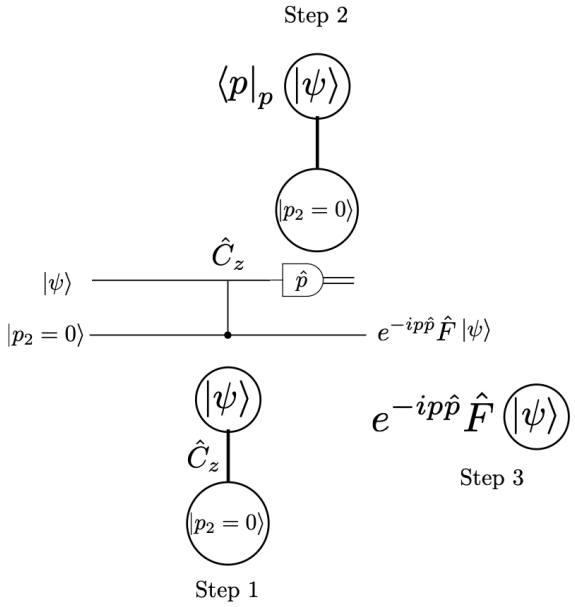

Figure II.8: Principle of teleportation of Gaussian operations. A homodyne detection in the spatial port one teleport the state $|\psi\rangle$ in the spatial port 2, along with two operations: Fourier transform $\hat{F}$ and displacement gate $e^{-ip\hat{p}}$.

Trace erasure error on a four linear cluster state We examine one possible example of operation on such a cluster state, a trace erasure one which happens at the extremity of a four-linear cluster state $|\psi\rangle = \hat{C}_{12}\hat{C}_{23}\hat{C}_{34}|0000\rangle_p$. The operator $\hat{C}_{ij}$ is the $\hat{C}_z$ gate applied on the i, j nodes. The associated density matrix can be written as:

$$\hat{\rho} = \int e^{ix_1x_2}e^{ix_2x_3}e^{ix_3x_4}e^{-ix_1'x_2'}e^{-ix_2'x_3'}e^{-ix_3'x_4'}|x_1, x_2, x_3, x_4\rangle\langle x_1', x_2', x_3', x_4'|. \tag{II.143}$$

We then take the partial trace of the fourth node, we obtain the state $\hat{\rho'} = \mathrm{Tr}_4(\hat{\rho})$, it gives:

$$\hat{\rho'} = \int e^{ix_1x_2}e^{ix_2x_3}e^{-ix_1'x_2'}e^{-ix_2'x_3}|x_1, x_2, x_3\rangle\langle x_1', x_2', x_3|\, dx_1dx_2dx_3dx_1'dx_2'dx_3 \tag{II.144}$$

which is a mixed state, and can be further written as:

$$\hat{\rho'} = \hat{C}_{23}\hat{C}_{12}(|00\rangle_p\langle 00|_p \int dx\,|x\rangle\langle x|)\hat{C}_{12}\hat{C}_{23}. \tag{II.145}$$

In order to recover a pure state, we have to perform a homodyne detection along the x-axis on the third node, which gives a two-linear cluster state with an additional momentum displacement operation with amplitude x:

$$\hat{\rho} = (\iint dx_1dx_2e^{ix_1x_2}e^{ix_2x}|x_1\rangle|x_2\rangle)(\iint dx_1dx_2e^{-ix_1x_2}e^{-ix_2x}\langle x_1|\langle x_2|). \tag{II.146}$$

In conclusion, the trace erasure operation, which consists to ignore one node of a cluster, on the extremity of a cluster state transforms the state to a mixed state. It is possible to preserve the purity and the entanglement of the remaining cluster state by sacrificing one squeezed state which is the *only* next neighbor of the node which was altered. If the same error occurs on the second or the third nodes of the four-linear cluster state, which are more connected, the total cluster state would be destroyed and the errors would flow drastically.

Conclusion To recap, what is hard to achieve experimentally with DVCQC is a deterministic entangled gate whereas the non-Clifford gates are easy to implement. In CVCQC, that is the contrary, which allows to experimentally generate large Gaussian entangled state. One way would be to go hybrid [Van Loock et al., 2008], by considering states which are entangled in discrete and continuous variables to combine both advantages of their encoding and to palliate to their respective limitations.

The way to implement quantum algorithms can be either by using the quantum circuit model, in DV and CV, or by using the measurement-based model with DVs or CVs system. Deutsh-Josza and Grover's algorithm [Su et al., 2018] for instance can be formulated with these models of quantum computation. While many algorithms in discrete variables are most common, the ones expressed with continuous variables are not numerous and are still a subject of research. Gaussian Boson Sampling allows to sample efficiently Haffnians [Hamilton et al., 2017], quantities which appear in Feynman's diagram calculation. The use of CV states could be useful in quantum simulation for instance. Indeed the mathematical description of physical systems in quantum field theory or condensed matter are naturally expressed with continuous variables. The deep success of qubit system encourages researchers to use them [Preskill, 2018], despite the fact condensed matter system are naturally described with continuous variables.

II.5 Quantum error correction over continuous variables

Quantum error correction (QEC) and fault tolerance require both finite-dimensional Hilbert space. Bosonic codes constitute a solution for defining QEC using the CV encoding: they are a class of quantum codes where logical qubits are encoded by defining a protected finite-dimensional system within an infinite-dimensional Hilbert space. One example of such codes is the so-called cat-code, which was the first one to be introduced [Cochrane et al., 1999] and possesses parity symmetry.

The GKP states, also called grid states, possess a translational symmetry. They are CVs states composed of a finite number of position peaks in an infinite Hilbert space. The width of both the peaks and their envelop depend on the number of photons of the state *i.e* on the squeezing. Narrow peaks and a wide envelop mean that the state has a high level of squeezing. Initial squeezing of 20.5 dB in a cluster with GKP ancillas states allows to a fault-tolerant measurement-based quantum computation as shown in [Menicucci, 2014]. These types of bosonic codes are designed to be robust against errors which are translational displacements in phase space. One can also use rotational symmetry as introduced in [Albert et al., 2020, Grimsmo et al., 2020]. As demonstrated in [Albert et al., 2018], GKP codes are also robust to protect against the pure-loss channel and over-perform the cat codes for a high number of photons, even though the cat codes are designed to protect against such errors. In addition, the deep interest of such states is motivated from its recent experimental realization in different platforms, such as superconducting cavities [Campagne-Ibarcq et al., 2020], the time-frequency variables at the

single photon level in an integrated photonic circuit [Fabre et al., 2020a] and trapped ions [Fluhmann et al., 2018].

In the following, we introduce the cat and GKP codes and how it is possible to correct errors from which they are designed to be robust against by mentioning different strategies.

II.5.1 Cat-code

Definition of the qubit cat code The logical zero and one qubit correspond to the two possible eigenstates of the parity operator $\hat{\Pi} = e^{i\pi\hat{a}^\dagger\hat{a}}$ with eigenvalues ± 1 which can be written as the coherent superposition of coherent states:

$$\left|\tilde{0}\right\rangle = \frac{1}{N_+}(|\alpha\rangle + |-\alpha\rangle),\ \left|\tilde{1}\right\rangle = \frac{1}{N_-}(|\alpha\rangle - |-\alpha\rangle), \tag{II.147}$$

where the normalization constant has been defined in Eq. (II.121). They are orthogonal states when α is large as soon as the condition $e^{-|\alpha|^2}\alpha^k \to 0$ is fulfilled and stay orthogonal under free dynamics. We note that, as the Wigner distribution, the cat-code is defined and possesses parity symmetry. Qubit cat codes are designed to correct against one photon loss. Photon losses cause errors that are equivalent to a bit flip, which can be corrected with a quantum error correction circuit [Ofek et al., 2016]. The most promising platform for generating such states is by using superconductivity cavities, but at the same time, this platform suffers from photons losses. It is called a biased noise channel as this error dominates over all the others.

Universal gate of set and error correction The universal gate set for the cat code is given by the one for qubit encoding. But the universality does not guarantee that the code is fault-tolerant. The knowledge of the structure of the noise can help to build the architecture of the code and thus to improve the threshold. Then, dependently on the main source of error of the experimental platform which produces the cat states, different codes have to be defined along with different gates to manipulate fault-tolerantly the code, which have in addition to be universal. One way would be to concatenate the cat code with a surface code and it was shown that it increases the accuracy threshold, compared to the DV encoding. This fact is a consequence of using an infinite Hilbert space of many harmonic oscillators.

It is possible to build a fault-tolerant set of a repetition code [Guillaud and Mirrahimi, 2019], where the based qubit are cat codes produced by superconducting cavities. The set of gates is given by $(\text{CNOT}, \hat{P}_{|\pm\rangle}, \hat{M}_X, \text{Toffoli}, \hat{X})$ and its universality is guaranteed by the Toffoli gate (see Fig. II.2). $\hat{M}_X$ is a measurement of the Pauli $\hat{X}$ matrix, and $\hat{P}_{|\pm\rangle}$ is the operation which designs the preparation of the coherent superposition $\left|\tilde{0,1}\right\rangle = \frac{1}{N_\pm}(|\alpha\rangle \pm |-\alpha\rangle)$.

It is not the unique strategy to increase the threshold, for instance in [Puri et al., 2020], they build a different repetition code which corrects dominant phase-flip error and is then concatenated with a CSS (Calderbank, Shor, Steane) code, which is a special type of stabilizer code.

The problem highlighted in this paper is that if the controlled gates have the $\hat{X}$ operator which does not commute with the dominant error, then the noise channel does not remain biased (or it said to depolarize the noise channel) and the advantages are lost. Since in the last reference, they have explicitly used the $\hat{X}$ operator, we then see that building universal and a fault-tolerant code using cat qubits is hot topics nowadays.

For a well prepared massive entangled cat state, one can perform quantum computation using the MBQC paradigm by doing sequential cavity measurement of superconductivities qudit cat-codes. [Joo et al., 2019].

II.5.2 GKP codes

An alternative solution for QEC is to encode information redundantly in a single system, namely by using quantum states which possess translational symmetry in rectangular phase space instead of duplicating qubit system. This state was introduced by Gottesman, Kitaev and Preskill (GKP) [Gottesman et al., 2001] in 2001. Their experimental realizations are very recent, we can cite the superconducting cavities [Campagne-Ibarcq et al., 2020], the trapped ions [Fluhmann et al., 2018] and the time-frequency continuous variables at the single photon level in an integrated photonic circuit [Fabre et al., 2020c], discussed in detail in this thesis.

The ideal square lattice GKP codes are the common eigenstates of the two commuting stabilizers:

$$\hat{S}_q = \hat{D}(\sqrt{2\pi}, 0), \tag{II.148}$$

$$\hat{S}_p = \hat{D}(0, \sqrt{2\pi}). \tag{II.149}$$

Since the stabilizers commute, it allows the simultaneous measurement of the position and momentum operators modulo $\sqrt{2\pi}$. The GKP states are made of an infinite Dirac peaks, their wave functions are explicitly given in the position basis:

$$\left|\overline{0}\right\rangle = \sum_{n\in\mathbb{Z}} \left|2n\sqrt{\pi}\right\rangle_q, \tag{II.150}$$

$$\left|\overline{1}\right\rangle = \sum_{n\in\mathbb{Z}} \left|(2n+1)\sqrt{\pi}\right\rangle_q. \tag{II.151}$$

They can correct displacement errors as long as $\sqrt{(\Delta q)^2 + (\Delta p)^2} \leq \sqrt{\pi}/2d$, where d is the dimension of the codespace. These states are non-physical, since their envelop is infinite and each peak is infinitively squeezed. We can build physical GKP state $|\tilde{\mu}\rangle$ where $\mu = 0, 1$, applying position and momentum noise, described by the single-Kraus operator $\hat{K}$:

$$|\tilde{\mu}\rangle = \hat{K}\,|\overline{\mu}\rangle = \iint dxdp e^{ix\hat{p}} e^{-ip\hat{x}} G_\sigma(x) G_\kappa(p)\,|\overline{\mu}\rangle\,, \tag{II.152}$$

which consists of multiplying displacement operators by Gaussian distributions $G_\sigma(x)G_\kappa(p)$ of mean value 0 and width σ. The application of displacement operator and the integration over momentum gives:

$$|\tilde{\mu}\rangle = \sum_n \int_{\mathbb{R}} dx G_\sigma(x - (2n+\mu)\sqrt{\pi}) G_{\kappa^{-1}}(x)\,|x\rangle\,. \tag{II.153}$$

We also define the coherent superposition of GKP states $|\tilde{+}\rangle = \frac{1}{\sqrt{2}}(|\tilde{0}\rangle \pm |\tilde{1}\rangle)$.

A Kraus map $\hat{K}$ is an operator describing the interaction between the state $\hat{\rho}$ and the environment (the channel) and can be expanded as:

$$\hat{K}\hat{\rho} = \int dudvdu'dv' F(u,v,u',v') e^{-iu\hat{p}} e^{-iv\hat{q}} \hat{\rho} e^{iv'\hat{q}} e^{iu'\hat{p}}, \tag{II.154}$$

where the F function characterizes the noise distribution. When F is a Gaussian function it is also called the Gaussian random channel. It is showed in Ref. [Noh et al., 2019] that GKP states are robust against Gaussian noise. After crossing such bosonic channel, the quantum state becomes a mixed one. Nevertheless, in the case of a very specific noise when F is separable as follows: $F(u,v,u',v') = F(u,v)F(u',v')$, the state stays pure. With such model, the Kraus operator is called the single Kraus operator [Motes et al., 2017] and can be employed to describe a physical GKP state.

An alternative way to build physical GKP states is by starting from the vacuum state, a Gaussian state centered at the origin of phase space, which is a physical state, and then applying displacement operators in order to create the comb structure. Such description is more adapted for the phase estimation protocol and is provided in[Albert et al., 2018, Baragiola et al., 2019, Noh et al., 2019].

We should note that another type of GKP states has been introduced and has a hexagonal geometry in phase space. The associated Wigner distribution is represented in Fig. II.9(b). The hexagonal GKP states can correct displacement errors as long as $\sqrt{(\Delta q)^2 + (\Delta p)^2} \leq \sqrt{\pi}/\sqrt{3}d$ then over perform the square GKP states. Both square and hexagonal GKP states are resilient against the bosonic pure-loss channel but the hexagonal one has a greater channel fidelity, defined as the overlap of the input state and the output state after the mentioned channel [Albert et al., 2018, Noh et al., 2019].

Universal set of gates The universal set of gates of the square lattice GKP code is given by [Noh et al., 2019]:

• The logical Pauli group $\hat{Z} = \exp(i\hat{q}\sqrt{\pi})$ and $\hat{X} = \exp(-i\hat{p}\sqrt{\pi})$. Logical CNOT gate can be realized with $\exp(-i\hat{p}_1 \otimes \hat{q}_2)$.

• The non-Clifford gate (or called the higher order Clifford gate [Campbell and Howard, 2017]) are for instance the T-gate $\exp\big(i\hat{q}^4/4\pi\big)$ [Noh et al., 2019] or the cubic phase gate [Gottesman et al., 2001]. It was shown recently that the non-Gaussianity brought by the cubic phase gate is not practical for achieving universal quantum computation with such a qubit state as such a gate can create peaks which are not in the GKP subspace [Hastrup et al., 2020].

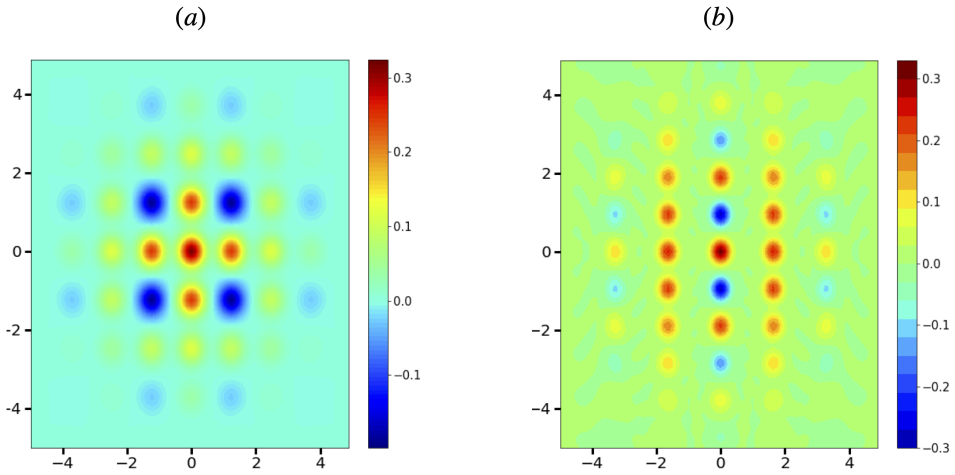

Figure II.9: Wigner distribution of the coherent superposition of GKP states $\left|\tilde{\pm}\right\rangle$ of two geometries. The two orthogonal axis are the position and momentum quadrature variables. (a) Square GKP state. (b) Hexagonal GKP state.

Error reduction We now discuss a noise reduction protocol for GKP states, and can also be applied for a Gaussian state, whose density matrix is noted $\hat{\rho}$ (see Ref. [Fabre et al., 2020b]). We start by coupling the density matrix to a GKP ancilla state $\left|\tilde{+}\right\rangle_x$ with the entangling operation $\hat{C}_z = e^{i\hat{q}_1\hat{q}_2}$, where $\hat{q}_{1/2}$ is the position operator and 1 and 2 denote each spatial port (see Fig. II.10). In the position representation, the total wave function can be written as:

$$|\psi\rangle = \iint e^{ix_1x_2}\psi(x_1)\psi_{\tilde{+}}(x_2)\,|x_1\rangle\,|x_2\rangle\,dx_1dx_2. \tag{II.155}$$

Then a homodyne measurement is performed on the p-quadrature on the spatial port 2. The state after these steps is:

$$\hat{\rho}' = \frac{\langle p|\,\hat{C}_z^{-1}\hat{\rho}\hat{C}_z\,|p\rangle_2}{\mathrm{Tr}(\langle p|\,\hat{C}_z^{-1}\hat{\rho}\hat{C}_z\,|p\rangle_2)}, \tag{II.156}$$

where p is the value measured of the homodyne detection and $\hat{\rho} = |\psi\rangle\langle\psi|$. As specified in Fig. II.10, an additional displacement gate $\hat{\mathcal{D}}(0,p)$ can be applied using the measurement result p of the homodyne measurement. The resulting state after such detection becomes:

$$\left|\psi'\right\rangle = \iint e^{ix_1x_2}e^{ix_2p}\psi(x_1)\psi_{\tilde{+}}(x_2)\,|x_1\rangle\,dx_1dx_2, \tag{II.157}$$

where $\hat{\rho}' = |\psi'\rangle\langle\psi'|$. After integration of the variable x_2, we obtain:

$$\left|\psi'\right\rangle = \int \psi(x_1)\tilde{\psi}_{\tilde{+}}(x_1+p)\,|x_1\rangle\,dx_1, \tag{II.158}$$

where $\tilde{\psi}_{\tilde{+}}(x)$ is the amplitude of the ancilla state in the p-representation given by a Gaussian comb. This protocol can be seen as the application of shifts errors (the momentum displacement of value p), which update the distribution of the noise described by $\psi(x+p)$ of the initial state and then projecting back the state in the GKP subspace by multiplying $\psi(x+p)$ by $\tilde{\psi}_{\tilde{+}}(x)$. Similar results expressed in terms of Wigner distribution have been obtained in [Baragiola et al., 2019]. Correction of the orthogonal quadrature is also possible repeating the protocol but using

the ancilla state $|\overline{+}\rangle_p = |\overline{0}\rangle_x$ in the spatial port 3 (see Fig. II.10) and performing a homodyne measurement in the orthogonal quadrature $\hat{x}$. In practice, when the initial state is a GKP state, these two steps have to be repeated to fully correct the state with different strategies as the one developed in [Wang, 2019] or with a Bayesian optimization procedure [Wan et al., 2019].

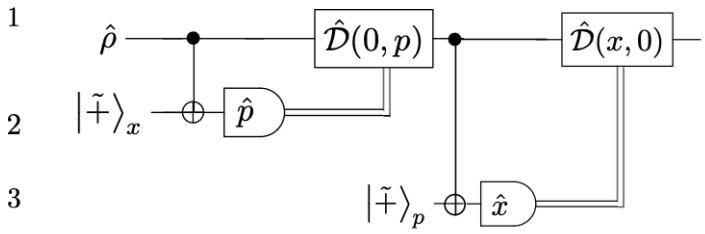

Figure II.10: Steane error correction scheme for a general density matrix $\hat{\rho}$ using as ancilla GKP states. The state $\hat{\rho}$ (upper rail) and the ancilla GKP state $|\tilde{+}\rangle_x$ are entangled by a $\hat{C}_Z$ gate followed by a homodyne detection on the spatial port 2. The measurement result p is used to perform a displacement operator denoted by $\hat{\mathcal{D}}(0,p)$. The procedure is then repeated but using as ancilla state $|\tilde{+}\rangle_p$ in spatial port 3 and a homodyne detection along the x-quadrature (extracted from [Fabre et al., 2020b].

The protocol applied to a coherent state using as an ancilla the state $|\tilde{+}\rangle_x$ results in the projection of the coherent state $\hat{\rho}$ on the GKP subspace. The initial coherent state becomes a random state on this subspace and can be used as a magic state to elevate GKP Clifford QC to fault-tolerant universal QC [Baragiola et al., 2019]. The protocol is a magic state distillation [Bravyi and Kitaev, 2005, Zhou et al., 2000]: the gate implemented corresponds to a quantum operation outside the set of Gaussian operations. The output state is a non-Gaussian one and by consequence is hard to simulate by classical means. The non-Gaussian resource comes from the ancilla GKP state itself and acts as a position-momentum filter.

Concatenation of GKP codes Again, achieving fault-tolerant quantum computation can be done with this type of qubit. The concatenation of the GKP code with a surface code such as the toric code in [Vuillot et al., 2019] improves the accuracy threshold compared to a DV encoding. When the toric code measurement and the GKP error correction (described above) are perfect, then the threshold for the surface code improves to 10 %, but decreases when the measurements are more realistic from both sides. The decoder strategy must be improved to increase this threshold and is the subject of current research.

Chapter III

Time-frequency continuous variables of single-photons

This chapter introduces the time-frequency continuous variables of single photons with a Hilbert space and a phase space approach. We emphasize their mathematical analogies with the quadrature position and momentum variables. We give a protocol showing the existence of quantum discord of a bipartite system constituted by two single photons with frequency degree of freedom, directly inspired by a protocol expressed with traditional quadrature position and momentum continuous variables and physically translated with our encoding.

III.1 Motivation

In the previous chapter, we have shown two ways to perform quantum computation with a photonic field. The first way is by using the discrete number degrees of freedom of single photons, which brought to define qubit and qudit states. The second way is by using CVs, and one instance of such variables is the quadrature position and momentum ones describing a multiphoton state. In summary of these two approaches, we conclude that a single-photon is a non-Gaussian information carrier which can have a discrete number of mode d.

The frequency degree of freedom of single photons can be used to define qubits [Lukens and Lougovski, 2017], where the two logical states correspond to two different frequencies. The same group has presented different gates for manipulating this "colored" qubit [Lu et al., 2019]. In Ref. [Kues et al., 2017], the group has used the arrival-time bin and the frequency of single photons for defining a qudit. Time-bin qubit has also been used for quantum key distribution (QKD) protocol [Marcikic et al., 2002, 2004]. We also note that time-energy entangled photons were produced by a micro-ring resonator (for instance see Ref. [Grassani et al., 2015]). The size of the full Hilbert space of N photons where each photon belongs to a Hilbert space of dimension d is d^N. So that the full Hilbert space scales exponentially with the number of photons and linearly with the size of each Hilbert space. This important remark has to remind us that the increasing size of the dimensionality of the modes of a single photon can not replace the ones induced by the increasing number of photons. In addition, for any quantum task, the

measurement of single photons destroys the state, and to perform complex calculation, one has in general to measure a part of the subsystem to know if errors happen, and then correct the remaining part of the quantum state. Hence, a quantum computation requires a large number of photons.

The frequency and time are robust degrees of freedom of single-photons in free space or in the atmosphere. Indeed, the spatial degree of freedom of single photons can be affected by turbulence effect, the reader can refer to Ref. [Hamadou Ibrahim et al., 2013] for a discussion and an experimental modelisation of this effect. For single-photons (or a classical field) propagating into an optical fiber or in the atmosphere, the dispersive effect induces a frequency quadratic phase which has to consequence to spread the temporal wave packet and can lead to errors if one encodes information in the arrival-time degree of freedom. The advantage compared to the polarization degree of freedom is that depolarization or polarization mode-dispersion in an optical fiber causes errors on polarization qubits at a faster rate than second-order dispersive effect on time-arrival qudits.

In this chapter, we will study single and two-photon states which have continuous time-frequency degrees of freedom. These states can be seen as qudit states by taking the limit $d \to \infty$. This limit leads to continuous time-frequency variables. We will show that the mathematical formalism between "quadrature position-momentum " and the "time-frequency" (or any other continuous degree of freedom of single photon) are close because we are considering the single photon subspace. Hence, many tools which are introduced for studying entanglement, quantum correlation, error correction in quadrature position-momentum CVs, among other tasks, can be reused with this type of CVs. The analogy does not work for the time-frequency CVs of classical fields.

Our formalism leads to the analogy between "single photon in multimode" and "many photons in one single-mode", which makes sense from a quantum computation perspective. We will show that frequency and time degrees of freedom of a single photon can be qualified as quantum continuous variables, as the position and momentum quadrature of an electromagnetic field. The proof of this mathematical analogy is shown by exhibiting an algebra of non-commuting operators, the time-frequency displacement ones. Such operators can be explicitly written using creation and annihilation operator of a single excitation of the electromagnetic field, which then do not have any classical counterpart. Nevertheless, the analogy has to be employed with caution because the physics is very different in the two cases. In quantum metrology, the analogy can be misleading. Indeed, the best estimation of a parameter can be made with an error given by the Cramer-Rao bound which scales as $1/N$, where N is the number of photons, but scales as the inverse of the square root of the number of modes. The described formalism in this chapter does not contradict this well-known fact, so the analogies between these two sets of continuous variables will be used again with caution in another contexts than quantum computation. Nevertheless, we should note a recent work [Zhuang et al., 2020], which introduces a

distributed sensing protocol using a network of local sensing nodes for parameter estimation. In this paper, it is shown that the variance of the parameter to measure scales as $1/M$, where M is the number of modes, when the nodes of the network are entangled quadrature continuous variables states. How this formalism and idea can be applied on entangled photons qudits pairs is one perspective, but could increase the strength of our analogy.

Universal quantum computation with transversal position-momentum degree of freedom of single photons was first proposed by Walborn and al. in [Tasca et al., 2011]. We provide the universal set for continuous time-frequency variables of single photons in Sec. III.4, or time-energy, enlightening the additional mathematical and physical difficulties related to the use of these variables. By using the finite or infinite dimensional degree of freedom of single photons, the universal set is composed of operations which act similarly on both a quantum (single photon here) and a classical field, because degrees of freedom are a common "clothes" for both these fields. Hence the operations of the universal set can be seen as a "mode engineering". It does not prevent the fact that the quantumness of our encoding resides in the single-photon field. The quantum computation power comes from entanglement and superposition of single-photon, and does not depend on the dimensionality of the engaged Hilbert space of single photons.

III.2 Description of time-frequency quantum state in Hilbert space

We start by providing a mathematical description of single photons with time-frequency continuous variables. A single-photon wave packet is described in quantum field theory as a field localized in space-time. It can also be described by a wave function [Smith and Raymer, 2007], as it is now presented [Fabre et al., 2020c].

III.2.1 Wave function of a single photon

The photon creation operator at frequency ω, $\hat{a}^\dagger(\omega)$, acts on the vacuum $|0\rangle$ as:

$$\hat{a}^\dagger(\omega)\,|0\rangle = |\omega\rangle\,. \tag{III.1}$$

The creation $\hat{a}^\dagger(\omega)$ (resp. annihilation $\hat{a}(\omega)$) operator increases (resp. decreases) the number of photons in the frequency ω mode by one. If we consider the frequency degree of freedom and other parameters such as the polarization or the direction of propagation denoted by the indices α, β, the creation and annihilation operator obey to the bosonic commutation relation:

$$[\hat{a}_\alpha(\omega), \hat{a}^\dagger_\beta(\omega')] = \delta(\omega - \omega')\delta_{\alpha,\beta}\mathbb{I}, \tag{III.2}$$

where $\mathbb{I}$ is the identity operator in the Hilbert space of the single-photon. The ladders operators obey to a Lorentz covariant commutation relation in the more general case where all degrees of

freedom are included [Roux and Fabre, 2020]. Analogously, we define the creation operator for a single photon at time t noted by $\hat{a}^\dagger(t)$ which is the Fourier transform of $\hat{a}^\dagger(\omega)$:

$$\hat{a}^\dagger(t) = \frac{1}{\sqrt{2\pi}} \int_{\mathbb{R}} d\omega e^{i\omega t} \hat{a}^\dagger(\omega), \tag{III.3}$$

where t is the time interval elapsed from its creation at the source and its arrival at the detector. A single photon at the arrival-time t is then defined by: $|t\rangle = |1_t\rangle = \hat{a}^\dagger(t)\,|0\rangle = \frac{1}{\sqrt{2\pi}} \int_{\mathbb{R}} d\omega e^{i\omega t}\,|\omega\rangle$. Since $\{|\omega\rangle\}_{\omega\in\mathbb{R}}$ is an orthogonal basis, we can expand a pure single photon state $|\Psi\rangle$ in this basis:

$$\hat{a}^\dagger(S)\,|0\rangle \equiv |\psi\rangle = \int_{\mathbb{R}} S(\omega) d\omega\,|\omega\rangle\,, \tag{III.4}$$

where $S(\omega) = \langle\omega|\psi\rangle$ is the amplitude spectrum of the single photon, with the normalization condition $\int_{\mathbb{R}} |S(\omega)|^2 d\omega = 1$. Rigorously, the integration range Eq. (III.4) should be $\mathbb{R}^+$. We have extended it to $\mathbb{R}$ as we consider experiments where the amplitude spectrum fulfills $S(\omega \leq 0) = 0$. In the experimental setup that we consider, $S(\omega)$ is typically non-zero only when $\omega \in [90, 110]$ THz. We can also argue that in our energy scale, there is no physical process which shifts to negative energy or close to zero.

We now consider single photons with a temporal structure, described by the state:

$$|\psi\rangle = \int_{\mathbb{R}} \tilde{S}(t) dt\,|t\rangle\,, \tag{III.5}$$

where $\tilde{S}(t) = \langle t|\psi\rangle$ is the Fourier transform of the spectrum of the source. We will later describe what is the meaning of t. We remind that a massless and non-relativistic particle could be described by a more general amplitude wavefunction $S(\vec{x}, t)$ with four variables - three positions and one time variable - or equivalently by its Fourier transform $\tilde{S}(\vec{k}, \omega)$, where $\vec{k}$ is the wave vector. Here, we consider a massless particle propagating along one direction of space, such as the dispersion relation is $\omega = c\left|\vec{k}\right|$. Since the photon moves at relativistic speed, the relation between its position and the proper time and given by the equation of motion: $x = ct$. The time and the longitudinal position of a relativistic particle are then not independent and count only as one degree of freedom. In that case, we can only describe the single photon propagating using the one dimensional function $S(\omega)$ or $\tilde{S}(t)$. The position variable of the single photon will be implicit in the following.

Example of spectral and temporal function The temporal pulse shape of single-photons produced by atomic decay is given by:

$$\tilde{S}(t) = -\gamma e^{-\gamma t/2}(1 - H(t)) \tag{III.6}$$

$$S(\omega) = \frac{1}{\sqrt{2\pi}} \frac{\sqrt{\gamma}}{i\omega - \gamma/2}. \tag{III.7}$$

γ is the inverse of the relaxation time between the excited and the ground state of the atom and $H(t)$ is the Heaviside function.

Dynamics The creation operator at time t can be written in free space: $\hat{a}_t^\dagger(\omega) = e^{-i\omega t}\hat{a}^\dagger(\omega)$, and the wave function at time t reads:

$$|\psi(t)\rangle = \int_{\mathbb{R}} \mathrm{S}(\omega) e^{-i\omega t} d\omega \, |\omega\rangle \, . \tag{III.8}$$

In general, the creation operator at time t, knowing the initial condition at t_0 is given by

$$\hat{a}(t) = \hat{U}^\dagger(t, t_0)\hat{a}(t_0)\hat{U}(t, t_0), \tag{III.9}$$

The unitary operator $U(t)$ (see after Eq. (II.4)) contains information about the Hamiltonian and possible jump operation, where this last does not have a classical analog. In order to be a valid bosonic operator, the new annihilation operator must satisfy the relation $[\hat{a}(t), \hat{a}(t')] = 0$ for $t, t' \geq t_0$.

In Ref. [Gersten, 1999], the equations of evolution of a single photon are in free space the Maxwell's equation, the $\hbar$ constant vanishes naturally. In other words, the field operators obey to the same equation, the Maxwell's one, as the classical envelope, when the medium of propagation has a linear response. If the single-photon field crosses a non-linear medium, the non-linear interaction can be described by a Hamiltonian developed into a power series of $\hbar$. N produced photons is mathematically translated by terms proportional to $\hbar^N$ in the Hamiltonian and have as consequence to decrease the probability of creation of many pairs. In classical non-linear optics, such interaction terms are written as a non-linear polarizability in the Maxwell's Ampere equation but $\hbar$ terms do not appear. The pump field is converted deterministically into two fields. It is hence very different from the quantum situation where photons pairs are created with a certain probability.

A dispersive medium is characterized by the dispersion relation developed into a Taylor series centered at the ω_0 frequency: $k(\omega) = k(\omega_0) + (\omega - \omega_0)\left(\frac{\mathrm{d}k}{\mathrm{d}\omega}\right)_{\omega_0} + \frac{1}{2}(\omega - \omega_0)^2 \left(\frac{\mathrm{d}^2 k}{\mathrm{d}\omega^2}\right)_{\omega}$. We will note $\left(\frac{\mathrm{d}^2 k}{\mathrm{d}\omega^2}\right)_{\omega} = k''(\omega_0)$. The first order term translates the temporal shift of the temporal wave packet while the second term translates its broadening. At the frequency which cancels the first order derivative, the annihilation bosonic operator at time t becomes:

$$\hat{a}(t) = e^{ik(\omega_0)L} \int_{\mathbb{R}} dt' \exp(-\frac{i(t-t')^2}{2\beta})\hat{a}(t'), \tag{III.10}$$

which is a Fresnel integral where $\beta = k''(\omega_0)L$ and L is the length of the dispersive medium. In the far-field limit $t^2/2\beta \ll 1$, the temporal profile is a spectral replica $\left|\tilde{S}(t)\right|^2 = |S(\omega = -t/\beta)|^2$, which is hence a way to perform a spectral intensity measurement of a single photon source. This tomographic technique is possible as soon as the condition $|\beta| = 1/\pi(\Delta f)^2$ is fulfilled, where Δf is the finest spectral detail.

Two photons case For a two photon state, the wave function can be written as:

$$|\psi\rangle = \iint d\omega_s d\omega_i \mathrm{JSA}(\omega_s, \omega_i) \, |\omega_s, \omega_i\rangle \, , \tag{III.11}$$

where the JSA is the Joint Spectral Amplitude and $\omega_s(\omega_i)$ is the frequency of the single photon called the signal and the idler. The wave function is normalized to one: $\iint d\omega_s d\omega_i |\mathrm{JSA}(\omega_s, \omega_i)|^2 = 1$. The Joint temporal amplitude JTA is defined as the Fourier transform of the JSA: $\mathrm{JTA}(t_s, t_i) = \iint d\omega_s d\omega_i e^{i\omega_s t_s} e^{i\omega_i t_i} \mathrm{JSA}(\omega_s, \omega_i)$. It corresponds to the amplitude of probability of the joint detection of a photon at time t_s and another at time t_i.

III.2.2 Localizability of single photons

Photons are relativistic particles and are hence not localizable [Newton and Wigner, 1949]. They do not have well-defined coordinate-space eigenstates, such that momentum (or frequency) and position (or time in 1D) amplitude wave function are not related by a Fourier transform. If it was the case, the wave function of the single-photon will not be locally connected to the electromagnetic field, will not transform as a geometrical object under Lorentz transformation and would behaves non-locally according to Ref. [Smith and Raymer, 2007].

As it was shown in [Fedorov et al., 2005], in the case of quasi-monochromatic spectrum*i.e* when the central frequency of the spectral distribution is larger than the spectral width, namely when $\omega_p \gg \Delta\omega$ condition is fulfilled, the temporal wave function and the spectral one are approximately related by a Fourier transform. The two experimental devices which produced single-photon and considered in this thesis verify this narrow-band condition, a fact which is certainly non-trivial (see Sec. IV.1.4).

III.2.3 Time and frequency operators

The way to introduce a correct time and frequency operator which is the closest to our formalism is given by the recent work of Ref. [Maccone and Sacha, 2020]. They are not necessary for the construction of the time-frequency phase space of single-photons, but they provide a simpler formalism to perform the analogies with the quadrature position and momentum continuous variables.

III.2.3.1 Introduction of the set of operators: a first attempt

In quantum physics, time is considered as a degree of freedom and not as an operator. In 1933, Pauli [W.Paul, 1933] showed that we cannot introduce a self-adjoint time operator which is canonically conjugate to the Hamiltonian operator whose spectrum is bounded from below. Many proposals to build such an operator can be found in the literature [Anastopoulos and Savvidou, 2017, Dias and Parisio, 2017, Halliwell et al., 2015, Muga et al., 2012]. In this section, we introduce a non-relativistic Hermitian time operator $\hat{\tau}$ canonically conjugated to the frequency operator $\hat{\omega}$, which is proportional to the free Hamiltonian as we will see. It prevents

us from defining different time operators for different Hamiltonians since we are physically constrained to verify the canonical commutation relation and by consequence the Heisenberg-type inequality. What's more, since $\hat{\omega}$ is not bounded from below, $\hat{\tau}$ is Hermitian.

The first proposal for a time operator is:

$$\hat{\tau} = \int_{\mathbb{R}} \tau d\tau \hat{a}^{\dagger}(\tau)\hat{a}(\tau) = \int_{\mathbb{R}} \tau d\tau \hat{n}(\tau). \tag{III.12}$$

The eigenvalue of this operator is the arrival time of the photon on a detector, or the creation time of a photon at time τ, we have the eigenvalue equation $\hat{\tau}\,|\tau\rangle = \tau\,|\tau\rangle$. $\hat{n}(\tau)$ enumerates the number of excitations which have the same arrival-time τ. The frequency operator in an integral representation can be written as:

$$\hat{\omega} = \int d\omega \hat{a}^{\dagger}(\omega)\hat{a}(\omega)\omega = \int d\omega \hat{n}(\omega)\omega, \tag{III.13}$$

and is also Hermitian so that it is an observable. The eigenvalues equation is $\hat{\omega}\,|\omega\rangle = \omega\,|\omega\rangle$ for a single photon at the frequency ω since the operator $\hat{n}(\omega)$ enumerate the number of excitation at frequency ω, and we have only one in the single photon subspace $\hat{n}(\omega)\,|\omega'\rangle = \delta(\omega - \omega')\,|\omega\rangle$. This operator can be view as the free Hamiltonian of the electromagnetic field in a continuous of mode (see Eq. (II.72)): $\hat{H} = \hbar \int d\omega \hat{n}(\omega)\omega$. But at the difference that $\hat{\omega}$ is not bounded from below.

The frequency operator on a state composed of n photons at the frequency ω in all the same mode a verifies the following eigenvalue equation:

$$\hat{\omega}\,|\omega, ..., \omega\rangle = n\omega\,|\omega, ..., \omega\rangle\,. \tag{III.14}$$

III.2.3.2 Second attempt: adding a quantum clock

The eigenvalues of the time operator given by Eq. (III.12) correspond to the proper time of the single photon. There is an underlying problem with such a definition according to Ref. [Maccone and Sacha, 2020]. In order to build an observable that leads to a time of arrival distribution, τ must be a constant of motion. The Born's rule states that $p(\tau|t) = |\langle\psi(t)|\tau\rangle|^2$, which means that the measurement at any time t must return the same outcome τ, while in quantum optics experiments, a detector "click" if and only if a photon is present. Then, we are lead to consider different times t and τ, which characterize different systems, the photon and a quantum clock as it was introduced in Ref. [Maccone and Sacha, 2020].

There is an additional argument, a classical one, from special relativity which leads us to not consider the proper time of a particle as an observable. The trajectory of a relativistic massive particle is constrained by the fact that the speed is bounded by the speed of light. The particle follows a trajectory given by a time-like geodesic, its tangent vector is inside the light cone which verifies the condition $\sum_{a,b} g_{ab}k^a k^b < 0$ where g_{ab} is the space-time metric and $k^a = dx^a/d\lambda$. λ is an arbitrary parameter which allows the reparametrisation for fixing the norm of the tangent

vector, by changing the frame. For a massive particle, it is possible to find an inertial frame such as, in that frame, the particle is at rest. It can be understood since the Lorentz transformations for $v \neq c$ are not singular. The temporal coordinate in that rest frame is called the proper time of the particle $\lambda \equiv \tau$. The movement of a massless particle, as the photon, follows a trajectory given by a null-like geodesic. The tangent vector k^a along the trajectory verifies the condition $\sum_{a,b} g_{ab} k^a k^b = 0$. In that case, we can not define a proper time of a photon as we no longer have the reparametrisation liberty.

These issues can be circumvented by considering time as a joint observable of the system and a quantum reference, described by a quantum clock, and does not lead to strange considerations with Born's rules. We now review the work presented in Ref. [Maccone and Sacha, 2020, **?**], adapted with the formalism described in this chapter.

A correct time operator The wave function describing the quantum state of the single-photon and the quantum clock (the detector) is the following tensorial product:

$$|\psi\rangle = \int dt \tilde{S}(t) \left|t\right\rangle_P \rightarrow \int dt \int_T dt' \tilde{S}(t) K(t,t') \left|t\right\rangle_P \left|t'\right\rangle_D , \tag{III.15}$$

where P labels the single-photon and D the detector. The integration range T of Eq. (III.15) is the temporal bandwidth of the detector. The function $K(t,t')$ can describe the possible time delay, due to an imperfect detector, between the actual arrival time of the single photon t and the time t' which is effectively recorded by an experimentalist. In the following, we will assume a perfect detector described by the function $|K(t,t')|^2 = \delta(t-t')$. The full wavefunction $|\psi\rangle$ is normalized as a consequence of the normalization of $\int dt \left|\tilde{S}(t)\right|^2 = 1$, at any time of the detection. The wave function Eq. (III.15) is not the one presented in Eq. (1) of Ref. [Maccone and Sacha, 2020], but does not lose its physical interpretation. The $\tilde{S}(t)$ function has to be understood as the amplitude of the time-arrival probability measured by a detector, *conditioned* to the presence of the single photon in the spatial range of the detector.

Based on this idea, a time-arrival POVM can be constructed as:

$$\hat{\Pi}_t = \left|t\right\rangle_D \left\langle t\right| \otimes P_d, \tag{III.16}$$

$$\hat{\Pi} = \mathbb{I} - \int dt \hat{\Pi}_t, \tag{III.17}$$

where we have defined the projector $P_d = \int_D dx \left|x\right\rangle_P \left\langle x\right|$ and D is the spatial domain of the detector. $\left|x\right\rangle_P$ denotes a single-photon at the spatial position x and its scalar product with the ket $\left|t'\right\rangle_P$ is formally given by $\langle t'|x\rangle = \langle t'|t/c\rangle \propto \delta(t-t')$. Hence the joint distribution of finding the photon at $x \in D$ and the detector clicking at t is given by the probability $p(t, x \in D) = \mathrm{Tr}(|\psi\rangle\langle\psi| \hat{\Pi}_t)$. The amplitude of probability $\langle t|\psi\rangle$ (see Eq. (III.5)) where t is wrongly interpreted as the proper time of a single-photon in the previous paragraph, must be understood as the quantity $\langle t, x|\psi\rangle$. t is in fact the time where the detector clicks, namely the arrival time of the photon and x is

the spatial position of the detector. Nevertheless, in the following the spatial x variable will be omitted to allege the notation, namely we will note $p(t, x \in D) \equiv |\langle t|\psi\rangle|^2 = \left|\tilde{S}(t)\right|^2$.

An arrival observable is defined by the time operator [Maccone and Sacha, 2020]:

$$\hat{T} = \int t dt \hat{a}^\dagger(t)\hat{a}(t) \otimes P_d + \mathbb{I}_C \otimes \int_{x \notin D} dx \, |x\rangle \langle x| \,, \tag{III.18}$$

where $\mathbb{I}_C$ is the identity on the clock of the Hilbert space. A correct time operator can not include the events which do not lead to clicks. Hence, it was proposed to split the operator $\hat{T}$ into two: $\hat{T} = (\hat{T}_1, \hat{T}_2)$. We have defined $\hat{T}_1 = \int t dt \hat{a}^\dagger(t)\hat{a}(t) \otimes P_d$, which describes the events which lead to single-photon detection. The second term of Eq. (III.18) is $\hat{T}_2$, and describes the events where nothing happens. Then, in the following, what we will note as the time operator is $\hat{T}_1 \equiv \hat{t}$.

Correct frequency operator An analog construction can be handled for building a correct frequency operator. It is defined as the tensorial product of two operators, one which applies on the Hilbert space of the photon and the other on the Hilbert space of the detector. The probability to obtain measurement value ω is conditioned to the presence of the photon in the spatial range of the detector. To allege the notation, we will note $p(\omega, x \in D) \equiv |S(\omega)|^2$.

III.2.3.3 Frequency-time Heisenberg inequality

For building the Heisenberg time-frequency inequality, the product $\hat{\omega}\hat{T}$ has to be defined, which is the case since both are now rigorously defined. Then, since the frequency and time are Hermitian operators and the two states $\hat{\omega}\hat{t}\,|\psi\rangle$, $\hat{t}\hat{\omega}\,|\psi\rangle$ are defined, the variances of each operator is defined and their product is bounded by:

$$\Delta\hat{\omega}\Delta\hat{t} \geq \frac{1}{2}\big|\langle[\hat{\omega}, \hat{t}]\rangle\big|, \tag{III.19}$$

which is called the Robertson inequalities [Robertson, 1929]. After evaluating the right-term of the last equation, we can prove the Heisenberg's inequality:

$$\Delta\hat{\omega}\Delta\hat{t} \geq \frac{1}{2}. \tag{III.20}$$

The equality holds for time-frequency Gaussian states, defined in more detail later. This relation is also valid for classical fields, since canonical conjugate variables is related by symplectic Fourier transform. The main and remarkable difference here is that we consider the single photon subspace. Thus, the mathematical reason for the non-commutativity of the introduced time and frequency operators is owing to the fact that that photons are bosons and obeys to Eq. (III.2) and does not have any counterpart with classical field. Moreover, we can relate the energy to the frequency by the relation $E = \hbar\omega$ only when single-photons fields are involved. The energy operator $\hat{E} = \hbar\hat{\omega}$ can hence be defined. The time-energy Heisenberg inequality can be then written as: $\Delta\hat{E}\Delta\hat{t} \geq \frac{\hbar}{2}$, which is not simply interpreted as the consequence of

Fourier-type inequality, but as the consequence of the non-commutation of bosonic operators which corresponds to a quantum origin.

III.2.4 Ladder operators and coherent-like basis

We can go a little step further by introducing ladders operators noted b and $\hat{b}^\dagger$ as the linear combination of time and frequency operators:

$$\hat{b} = \frac{1}{\sqrt{2}}(\hat{\Omega} + i\hat{T}), \tag{III.21}$$

$$\hat{b}^\dagger = \frac{1}{\sqrt{2}}(\hat{\Omega} - i\hat{T}). \tag{III.22}$$

We have introduced the dimensionless operators $\hat{\Omega}$ and $\hat{T}$, where the parameters chosen to define these operators depend on the considered energy-time scale. In our context and energy scale, we can define the dimensionless operators $\hat{\Omega} = \hat{\omega}/\Delta\omega$ and $\hat{T} = \hat{t}/\Delta t$ where $\Delta\omega$ is the frequency bandwidth and Δt is the temporal size of the single photon. In high-energy physics, for describing bosonic strings, such dimensionless time and frequency operators are also introduced, in a very different manner which is detailed in [Tong, 2012]. In such energy scale, the parameters which permit to introduce a dimensionless time and frequency operators are the Planck's energy and time $E_p = \sqrt{c^5\hbar/G}$, $t_p = \sqrt{\hbar G/c^5}$, which depend in addition to $\hbar$ the gravity constant G. So that the non-commutativity algebra of time-frequency operators can have an additional reason the curvature of space-time. But we will not consider such a regime.

The annihilation and creation-like operators do not commute: $[\hat{b}, \hat{b}^\dagger] = \mathbb{I}$ and they hence can be qualified as bosonic operators. The number operator $\hat{n} = \hat{b}^\dagger\hat{b}$ has integers eigenvalues which label the Fock-like basis $|\tilde{n}\rangle$, $\hat{n}\,|\tilde{n}\rangle = \tilde{n}\,|\tilde{n}\rangle$. With an analog construction as for the harmonic oscillator, the action of the annihilation and creation-like operator are:

$$\hat{b}\,|\tilde{n}\rangle = \sqrt{\tilde{n}}\,|\tilde{n}-1\rangle\,, \tag{III.23}$$

$$\hat{b}^\dagger\,|\tilde{n}\rangle = \sqrt{\tilde{n}+1}\,|\tilde{n}+1\rangle\,. \tag{III.24}$$

Despite the analogies of the mathematical structure between the Fock (see Eq. (II.76)) and the Fock-like basis, the interpretation of the integer $\tilde{n}$ as the number of excitation of a hypothetical "field" remains elusive. This is why the word "like" has its importance. The relation between the time basis $|t\rangle$ and the Fock-like basis is:

$$|t\rangle = \sum_{n\in\mathbb{N}} H_n(t)\,|\tilde{n}\rangle\,, \tag{III.25}$$

where $H_n(t)$ denotes the Hermite function (see Eq. (II.81)). The coherent-like state $|\beta\rangle$, or coherent-like time-frequency state is defined by the eigenvector of the annihilation-like operator:

$$\hat{b}\,|\beta\rangle = \beta\,|\beta\rangle\,, \tag{III.26}$$

which can be expressed in the Fock-like basis:

$$|\beta\rangle = e^{-|\beta|^2/2} \sum_{n\in\mathbb{N}} \frac{\beta^{\tilde{n}}}{\sqrt{\tilde{n}!}} |\tilde{n}\rangle \,. \tag{III.27}$$

The statistical property of a single photon is sub-Poissonian and so as $|\beta\rangle$ which is a particular single photon state. The Eq. (III.27) shows that the "quantized field" whose quanta are described by the Fock-like basis exhibits Poissonian statistics. Only experiments could answer the physical legitimacy to introduce such a field. More mathematical properties of the coherent-like time-frequency state expressed with physical time and frequency variables are given in Sec. V.1.1.

III.2.5 Heisenberg group

The Heisenberg group was first introduced for a single mode quantized radiation (see for instance Ref. [Brif and Mann, 1999]), modeled by an harmonic oscillator. The associated nilpotent 3-dimensional Lie algebra is defined by the set $\{\hat{Q}, \hat{P}, \mathbb{I}\}$ or by $\{\hat{a}, \hat{a}^\dagger, \mathbb{I}\}$. The operators verify the commutation equations $[\hat{X}, \hat{P}] = \mathbb{I}, [\hat{P}, \mathbb{I}] = [\hat{X}, \mathbb{I}] = 0$. The set of the three operators $\{\hat{t}, \hat{\omega}, \mathbb{I}\}$ also defines a Heisenberg algebra:

$$[\hat{t}, \hat{\omega}] = \mathbb{I}, \;\; [\hat{t}, \mathbb{I}] = [\hat{\omega}, \mathbb{I}] = 0, \tag{III.28}$$

which means that the Lie algebra is a non-abelian one. The group element of the Heisenberg group can be represented as:

$$\hat{D}_s(\omega, t) = e^{-i\omega\hat{t} + it\hat{\omega}}. \tag{III.29}$$

After applying the Baker-Haussdorf formula [Achilles and Bonfiglioli, 2012], we get:

$$\hat{D}_s(\omega, t) = e^{-i\omega\hat{t}} e^{it\hat{\omega}} e^{-i\omega t/2} \tag{III.30}$$

The exponential representation of the frequency displacement operator $\hat{\mathcal{D}}(t) = e^{it\hat{\omega}}$ permits to interpret the frequency operator, or equivalently the energy operator $\hat{E} = \hbar\hat{\omega}$ as the infinitesimal generator of the time translation. Since in addition it is an Hermitian operator, it is indeed a candidate for a physical property. In the same spirit, the time operator can be seen as the infinitesimal generator of frequency translation. Another representation of the time and frequency operators in the space $L^2(\mathbb{R})$ is given by:

$$(\hat{t}\psi)(t) = t\psi(t) \tag{III.31}$$

$$(\hat{\omega})(\psi)(t) = -i\frac{d\psi(t)}{dt}. \tag{III.32}$$

Time and frequency displacement operators do not commute, and so we obtain the Weyl relation,

$$\hat{D}(\mu)\hat{\mathcal{D}}(\tau) = e^{i\mu\tau}\hat{\mathcal{D}}(\tau)\hat{D}(\mu). \tag{III.33}$$

This non-commutative structure is more interesting than $[\hat{t}, \hat{\omega}] = \mathbb{I}$ as the time and frequency displacement operators in Eq. (III.33) are bounded operators [Le Bellac, 2013].

We also point out that the ladders-like operator $\hat{b}$, $\hat{b}^\dagger$ and the identity operator form a Heisenberg algebra. They can be used to express the time-frequency displacement operators as:

$$\hat{D}_s(\beta) = e^{-|\beta|^2/2} e^{\beta \hat{b}^\dagger} e^{-\beta^* \hat{b}}, \tag{III.34}$$

where we have noted the complex variable $\beta = \Omega + iT$, the sum of dimensionless frequency and time variables. The use of such complex variables can be in handy for some calculations. Note that the complex variable is not what is referred in the literature to a Wick's rotation $t \to -i\tau$, namely a $\pi/2$ rotation of time in a complex plane, since it involves both canonical conjugates variables.

III.3 Time-frequency phase space at the single particle level

In this section, we introduce the time-frequency phase space of a single-photon, following the mathematical construction of the quadrature position-momentum phase space.

III.3.1 Chronocyclic Wigner distribution for a single photon

Using the previously introduced bosonic operators, we can define the displacement mode operator in frequency as [Fabre et al., 2020c]:

$$\hat{D}(\mu) = \int_{\mathbb{R}} \hat{a}^\dagger(\omega + \mu)\hat{a}(\omega) d\omega, \tag{III.35}$$

As for Eq. (III.8), we have extended the range of integration from $\mathbb{R}^+$ to $\mathbb{R}$. Indeed, for the envisaged application, μ will be small enough so that the resulting displaced state amplitude spectra $S(\omega)$ will have its support in $\mathbb{R}^+$. Analogously, for the displacement in time we can write

$$\hat{\mathcal{D}}(\tau) = \int_{\mathbb{R}} \hat{a}^\dagger(t + \tau)\hat{a}(t) dt, \tag{III.36}$$

We have that $\hat{D}(\mu)\,|\omega\rangle = |\omega + \mu\rangle$ and $\hat{D}(\mu)\,|t\rangle = e^{i\mu t}\,|t\rangle$. In the literature, we can find another representation of the frequency displacement operators which deal with the issue of defining negative frequencies. These representations of the time and frequency displacement operators clarify the fact that we are considering the single photon subspace, which is not explicit in [Tasca et al., 2011].

Using the commutation relations, in analogy to the quadrature position-momentum phase space case, we can identify different possible orderings of the operators. At the single-photon level, this ordering refers to the position of the creation operator with respect to the destruction operator either in frequency or time. The normal order $\hat{D}_n(\mu, \tau) = \hat{D}(\mu)\hat{\mathcal{D}}(\tau)$ corresponds to the creation operator in frequency on the left and the annihilation operator in time on the right. The anti-normal order $\hat{D}_{an}(\mu, \tau) = \hat{\mathcal{D}}(\tau)\hat{D}(\mu)$ corresponds to the creation operator in time on the left and the annihilation operator in frequency on the left. The symmetric order is also

defined as, $\hat{D}_s(\mu,\tau) = \hat{D}(\mu)\hat{\mathcal{D}}(\tau)e^{-i\tau\mu/2}$. The symmetric displacement operator obeys to the Weyl's algebra:

$$\hat{D}_s(\mu_1,\tau_1)\hat{D}_s(\mu_2,\tau_2) = \hat{D}_s(\mu_1+\mu_2,\tau_1+\tau_2)e^{i(\tau_1\mu_2-\mu_1\tau_2)/2}. \tag{III.37}$$

By continuously varying the frequency and the time, in other words, in an adiabatic way, one can displace the system along a path (μ,τ). The total displacement along the path Γ can be written as:

$$\hat{D}_s = \hat{D}_s(\int_\Gamma d\mu d\tau)e^{i\int_\Gamma(\mu d\tau-\tau d\mu)/2}, \tag{III.38}$$

where we have used Eq. (III.37). If the path is closed, then $\int_\Gamma d\mu d\tau = 0$ and the total displacement is $\hat{D}_s = e^{i\phi}$ where:

$$\phi = \int_\Gamma(\mu d\tau - \tau d\mu)/2 = \iint_S \frac{dEdt}{\hbar} = \frac{S}{\hbar}, \tag{III.39}$$

where S is the geometrical area delimited by the path Γ. ϕ is called the geometric phase. This phase could be measured with an interference experiment. We have changed the variable $E = \hbar\omega$, which is only valid for a single photon field, to write explicitly the dependency of the geometrical phase with $\hbar$. The adiabatic displacement can be seen as a way of implementing a non-Abelian unitary matrix for doing quantum computation. It is called *holonomic* quantum computation [Sjöqvist, 2015]. One experimental implementation of such gates in the trapped ions platform, so that with quadrature position-momentum variables- and not by using degrees of freedom of single-photons-, was proposed in [Leibfried et al., 2003]. The existence of this phase arises from the non-commutative algebra of the ladder operators (see Eq. (III.2)) and is an optical analog of the Aharonov-Bohm effect. Note that such effect has its classical analog: a cyclic change along a path Γ in the polarization state of a classical field gives also a geometric phase, called the Pancharatnam's phase [Berry, 1987], which depends on the area enclosed by the path. The existence of this geometrical phase is a consequence of the wave nature of classical and quantum fields. They can be described by *two* parameters, amplitude and phase of the field, frequency and time here, are changed adiabatically, and the difference in the phase of the initial and final state is a signature of a non-zero holonomy of the Poincare sphere (in the Pancharatnam's phase example), the quantum time-frequency phase space (in the case of this chapter) or the traditional quadrature phase space. The holonomy quantifies the extent of the deviation of the angle between an initial vector and a final vector along a closed path by doing a parallel transport.

The unitary displacement operators $\hat{D}_\xi$, irrespectively of the ordering, $\xi = s, an, n$ are not Hermitian and obey to the following orthogonality relation:

$$\mathrm{Tr}[\hat{D}_\xi^\dagger(\mu,\tau)\hat{D}_\xi(\mu',\tau')] = \delta(\tau'-\tau)\delta(\mu'-\mu), \tag{III.40}$$

and the completeness relation:

$$\iint d\mu d\tau \hat{D}_\xi(\mu,\tau)\hat{D}_\xi^\dagger(\mu,\tau) = \mathbb{I}. \tag{III.41}$$

Using Eq. (III.40) and Eq. (III.41) we can expand all Hermitian matrices into this orthogonal basis, thus the density matrix reads:

$$\hat{\rho} = \iint \chi_{\hat{\rho}}^{\xi}(\mu,\tau)\hat{D}_{\xi}(\mu,\tau)d\mu d\tau. \tag{III.42}$$

The coordinate function $\chi_{\hat{\rho}}^{\xi}(\mu,\tau) = \mathrm{Tr}(\hat{\rho}\hat{D}_{\xi}^{\dagger}(\mu,\tau))$ is called the time-frequency characteristic function, it can be normal, anti-normal or symmetric depending on the ordering of the displacement operator. The Fourier transform of the characteristic function leads to a quasi-distribution probability. In particular, using the symmetric characteristic distribution, one can obtain the chronocyclic Wigner distribution,

$$W_{\hat{\rho}}(\omega,t) = \frac{1}{\pi}\int d\omega' e^{2i\omega' t}\left\langle \omega-\omega'\right|\hat{\rho}\left|\omega+\omega'\right\rangle. \tag{III.43}$$

The chronocyclic Wigner distribution gives the same information as the associated density matrix, following the completeness property. This distribution is also normalized: $\iint dtd\omega W_{\hat{\rho}}(\omega,t) = \mathrm{Tr}(\hat{\rho}) = 1$. In the case of a pure state $\hat{\rho} = |\psi\rangle\langle\psi|$ characterized by its amplitude spectrum $S(\omega)$ Eq. (III.4), the chronocylic Wigner distribution can be written as:

$$W_{\hat{\rho}}(\omega,t) = \frac{1}{\pi}\int d\omega' e^{2i\omega' t}S(\omega-\omega')S^{*}(\omega+\omega'). \tag{III.44}$$

Again, the chronocyclic Wigner distribution must be understood as a conditioned quasi-probability distribution, since the detector clicks at time t if the particle is present at position x. The marginals of the Wigner distribution leads to different physically measurable quantity as the spectrum of the source:

$$\int W_{\hat{\rho}}(\omega,t)dt = |S(\omega)|^2, \tag{III.45}$$

and the distribution of the arrival time of the photon of the source (using a fixed origin of time):

$$\int W_{\hat{\rho}}(\omega,t)d\omega = \left|\tilde{S}(t)\right|^2. \tag{III.46}$$

We can also see the chronocyclic Wigner distribution here as the average value of the displaced parity operator by applying the same methods as in [Royer, 1977] using the symmetric displacement operator $\hat{D}_s$:

$$W_{\hat{\rho}}(\omega,t) = \mathrm{Tr}(\hat{\rho}\hat{D}_s(\omega,t)\hat{\Pi}\hat{D}_s^{\dagger}(\omega,t)), \tag{III.47}$$

where $\hat{\Pi} = \int_{\mathbb{R}} d\omega\,|\omega\rangle\langle-\omega|$ is the parity operator which acts on a frequency state as $\hat{\Pi}\,|\omega\rangle = |-\omega\rangle$. We have again set the central frequency to zero and the extension range of the integral can be extended to $\mathbb{R}$. Consequently, measuring the chronocyclic Wigner distribution at the origin is a measurement of the average value of the parity operator. Finally, it can be shown that the chronocyclic Wigner distribution obeys the Stratonovich-Weyl rules [Brif and Mann, 1999, Tilma et al., 2016], which are fully detailed in Chap. VII.

To tackle the issue of negative frequencies, which again in our energy scale is not relevant, one could introduce the Affine Wigner distribution [Berge et al., 2019, Bertrand and Bertrand, 1992] which has two variables $\omega, t \in \mathbb{R}^{+} \times \mathbb{R}$. This distribution is built as the average value of

the displaced parity operator, where in that context, the displacement operators are composed of a time displacement operator and a frequency squeezing operation. Again in our energy scale, there are no physical processes which can lead to negative frequencies. The analog of the vacuum state in the time-frequency phase space is then no relevant to our study.

Since we are in the single-photon subspace, one could use the energy variable instead of the frequency one since we have $E = \hbar\omega$, which does not have any sense if one considers a classical field. We can conclude that the time-energy phase space is hence paved by a square lattice of area $\hbar/2$, as it is for the quadrature position and momentum phase space of a harmonic oscillator. A quantum state which is confined in a phase space of area $A = E \times T$ where A is the action, E and T are energy and time scale of the considered quantum state, can exhibit structure smaller than $\hbar^2/A \ll \hbar$ similarly to the counterintuitive results proved by Zurek [Zurek, 2001]. We will come back to this point in Chap. V.1.2, where we will introduce the frequency-time cat state.

Owing to the non-commutativity of the bosonic operator Eq. (III.2) and by consequence of the displacement operator Eq. (III.33), the time-frequency phase space of a single photon is quantized, as the quadrature position-momentum phase space. It leads to the analogy claimed at the introduction of the chapter between one single photon in many frequency modes and many photons in one frequency mode. The terminology from the continuous quadrature position-momentum variable can be reused for the continuous degree of freedom of a single photon, which is here the time-frequency (actually the longitudinal position-momentum one) but could also be the transversal position-momentum of a single photon. A fundamental consequence for quantum computing is that Gaussian frequency states whose chronocyclic Wigner distribution is Gaussian, namely time-frequency Gaussian state, can be efficiently simulated with a classical computer, whereas non-Gaussian time-frequency states cannot. Universal set of gates in this encoding is fully detailed in Sec. III.4. We should note that the continuous variables of a single photon encoding suffer from a scalability issue with the actual technology, compared to the quadrature position-momentum encoding. This limitation is not related to the dimensionality of the encoding, but to the quantum system which carries the encoding.

III.3.2 Wigner distribution of two photons and associated marginals

The introduced Wigner distribution can be generalized to the situation where more than one photon occupies different frequency modes. The Wigner distribution of a pure state Eq. (III.11) is:

$$W(\omega_s, \omega_i, t_s, t_i) = \frac{1}{\pi^2} \iint d\omega' d\omega'' e^{2i\omega' t_s} e^{2i\omega'' t_i} \left\langle \omega_s - \omega', \omega_i - \omega'' \middle| \psi \right\rangle \left\langle \psi \middle| \omega_s + \omega', \omega_i + \omega'' \right\rangle . \tag{III.48}$$

Integrating over the time-variables, we obtain one marginal of the two-photon Wigner distribution:

$$\iint W(\omega_s, \omega_i, t_s, t_i) dt_s dt_i = \mathrm{JSI}(\omega_s, \omega_i), \tag{III.49}$$

where $\mathrm{JSI}(\omega_s, \omega_i) = |\mathrm{JSA}(\omega_s, \omega_i)|^2$ is the Joint Spectral Intensity. We also have

$$\iint W(\omega_s, \omega_i, t_s, t_i) d\omega_s d\omega_i = \mathrm{JTI}(t_s, t_i), \tag{III.50}$$

where JTI is the Joint Temporal Intensity, which is the probability to measure a photon at an arrival time t_s in one detector and a photon at an arrival time t_i in another detector. We can also define two other "crossed" marginals: the probability to detect one photon at the arrival time t_s (resp. t_i) and the other at the frequency ω_i (resp. ω_s):

$$\mathrm{JTSI}(t_s, \omega_i) = \iint W(\omega_s, \omega_i, t_s, t_i) d\omega_s dt_i, \tag{III.51}$$

$$\mathrm{JSTI}(\omega_s, t_i) = \iint W(\omega_s, \omega_i, t_s, t_i) d\omega_i dt_s. \tag{III.52}$$

The measurement of the four marginals and the reconstruction of the JSA has been performed in [MacLean et al., 2019], this technique can not be applied on all optical system and depend on the frequency width of the considered JSA.

We can further generalize the chronocyclic Wigner distribution for the n-single photons case:

$$W_{\hat{\rho}}(\omega_1, t_1, ..., \omega_n, t_n) = \frac{1}{\pi^n} \int d\omega_1 dt_1 ... d\omega_n dt_n e^{2i(\omega'_1 t_1 + ... + \omega'_n t_n)} \langle \omega_1 - \omega'_1, ..., \omega_n - \omega'_n | \, \hat{\rho} \, | \omega_1 + \omega'_1, ..., \omega_n + \omega'_n \rangle . \tag{III.53}$$

So far, this last equation was not used, since such Wigner distribution would describe a system composed of different frequency entangled single photons, which is hard to produce experimentally.

III.3.3 Time-frequency Gaussian and cluster state

In this section, we describe frequency-time Gaussian states in terms of their covariance matrices. The frequency-time phase space of a single photon exhibits a non-commutative geometry owing to the relation Eq. III.2. Hence, we can use the formalism developed for position-momentum CVs in our encoding by changing the physical interpretation of the mathematical results. We introduce the column vectors which contain the time and frequency operators acting on different single-photons:

$$\hat{t} = \begin{pmatrix} \hat{t}_1 \\ \hat{t}_2 \\ \vdots \\ \hat{t}_n \end{pmatrix} , \; \hat{\omega} = \begin{pmatrix} \hat{\omega}_1 \\ \hat{\omega}_2 \\ \vdots \\ \hat{\omega}_n \end{pmatrix} , \; t = \begin{pmatrix} t_1 \\ t_2 \\ \vdots \\ t_n \end{pmatrix} , \; \omega = \begin{pmatrix} \omega_1 \\ \omega_2 \\ \vdots \\ \omega_n \end{pmatrix} \tag{III.54}$$

and also the vector of length $2n$: $\hat{X} = (\hat{\omega}, \hat{t})$ and $X = (\omega, t)$. The non-commutativity of the time and frequency operators has as consequence the relation:

$$[\hat{X}_j, \hat{X}_k] = i\hat{\Omega}_{jk}, \tag{III.55}$$

where $\hat{\Omega} = \begin{pmatrix} J & 0 \\ 0 & J \end{pmatrix}$ and $J = \begin{pmatrix} 0 & 1 \\ -1 & 0 \end{pmatrix}$.

Gaussian states A general time-frequency Gaussian state of n-photons can be written in terms of its wave function as [Arvind et al., 1995]:

$$\psi_{(u,v)}(\omega) = \pi^{-n/4}\det(u)^{1/4}e^{-\frac{1}{2}\omega^t(u+iv)\omega}, \tag{III.56}$$

which is normalized to one $\int d\omega^n \left|\psi_{(u,v)}(\omega)\right|^2 = 1$ and where the central frequency has been set to zero. The matrix u belongs to $S_n^{++}(R)$, the symmetric positive definite matrix. v is a symmetric matrix and describes for instance the spectral or temporal chirp and can lead to correlation between photons. Alternatively, in the time domain, the wave function of n-photons time-frequency Gaussian state is:

$$\psi_{(u,v)}(t) = \pi^{-n/4}\det(u)^{1/4}e^{-\frac{1}{2}t^t(u+iv)^{-1}t}, \tag{III.57}$$

where we have used the Gaussian integration: $\int_{\mathbb{R}} d\omega e^{i\omega\beta}e^{-\alpha\omega^2} = \sqrt{\frac{\pi}{\alpha}}e^{-\beta^2/4\alpha}$ where $\mathrm{Re}(\alpha) < 0$.

The time-frequency characteristic distribution $\chi^0_{\hat{\rho}}(\omega, t) = \mathrm{Tr}(\hat{\rho}\hat{D}^\dagger(\omega, t))$ of a time-frequency Gaussian state is Gaussian:

$$\chi_{\hat{\rho}}(\omega_1, t_1, ..., \omega_n, t_n) = (\frac{1}{2\pi})^n \exp\Big(-X^\top V X + AX\Big). \tag{III.58}$$

and is thus fully characterized by its first and second moments defined by:

$$A = \langle X \rangle, \tag{III.59}$$

$$V = \frac{1}{2}(\Delta X \Delta X^\top + (\Delta X \Delta X^\top)^\top). \tag{III.60}$$

A contains the first moments of the distribution and can be removed by a local displacement in the chronocyclic phase space, which is nevertheless a non-linear operation in frequency. The chronocyclic Wigner distribution of a frequency-time Gaussian states is also Gaussian and can be written as:

$$W_{\hat{\rho}}(\omega_1, t_1, ..., \omega_n, t_n) = (\frac{1}{2\pi})^n \exp\Big(-X^\top V^{-1} X + AX\Big), \tag{III.61}$$

V^{-1} is the inverse of the covariance matrix [Arvind et al., 1995]:

$$V^{-1}(u, v) = \begin{pmatrix} u + vu^{-1}v & vu^{-1} \\ u^{-1}v & u^{-1} \end{pmatrix}. \tag{III.62}$$

The covariance matrix of the quadrature position-momentum Wigner distribution contains the correlation of quadrature position-momentum Gaussian states in different modes, while here the time-frequency covariance matrix contains information about the time-frequency correlations between different single photons. The purity of the state is defined by $\mathrm{Tr}(\hat{\rho}^2) = \frac{1}{\sqrt{\det(V)}}$. Hence, the state is pure if $\det(V) = 1$ and mixed in other cases. The transformations that preserve the commutation relation of the time and frequency operator are symplectic transformations S defined as: $\Omega = S\Omega S^\top$. Gaussian unitaries acting on pure wave functions can be mapped in a one to one correspondence with symplectic transformations which act on the covariance matrix. Pragmatically, it means that Gaussian states, we can consider only their covariance matrix (in $\mathbb{R}^{2N}$) instead of considering their wavefunction (in $\mathbb{L}^2(R^{2N})$).

In our context, the time-frequency Heisenberg inequality of a single photon (see Eq. (III.20)) reads as:

$$V + iJ/2 \geq 0. \tag{III.63}$$

For a pure state, the covariance matrix can be written under the form: $V = \frac{1}{2}SS^\top$, which means that $SS^\top$ defines uniquely a Gaussian state as the covariance matrix V [Menicucci et al., 2011]. S can be cast as:

$$S = \begin{pmatrix} v^{-1/2} & 0 \\ uv^{-1/2} & v^{1/2}. \end{pmatrix}, \tag{III.64}$$

Graphical calculus of time-frequency Gaussian pure states can be handled in the same way as the quadrature position-momentum Gaussian pure states, by using the complex graph matrix:

$$Z = u + iv = \langle \hat{t}\hat{t}^\top \rangle^{-1} - \langle \hat{t}\hat{\omega}^\top \rangle, \tag{III.65}$$

which is the adjacency matrix of an undirect graph with complex values edge weight. In this encoding, the analog of "squeezing" is the temporal or spectral bandwidth of single-photons. The full machinery of graph calculus of cluster states could be generalized in our encoding, as the nullifiers formalism.

Time-frequency cluster state The measurement-based quantum computation is also a relevant approach for performing quantum computation with the time-frequency variables of single-photons. In DVCQC, each node is a polarization qubit state occupied by a single photon while in CVCQC, each node is a different mode of a multi-mode squeezed state. A two-linear cluster state is a EPR state, where the two modes are correlated (or anti-correlated) in position or momentum quadrature variables. The common point of both these encoding is that a node symbolizes a quantum field, a single-photon or a squeezed state.

Then, in our considered encoding, each node is occupied by a single photon, as in DVCQC. Nevertheless, owing to the fact that the degrees of freedom are continuous variables, the entanglement between the nodes is mathematically closer to the one of CVCQC, and not to DVCQC. A two-linear frequency cluster state is then written as:

$$|\psi\rangle = \hat{C}_X |t_1 = 0\rangle |t_2 = 0\rangle = \iint d\omega_1 d\omega_2 e^{i\omega_1\omega_2} |\omega_1\rangle |\omega_2\rangle , \tag{III.66}$$

which defines the gate $\hat{C}_X$ in this encoding. $|t = 0\rangle$ is the infinitely localized temporal peak, analogous to an infinitely squeezed state. Physically, the state $|\psi\rangle$ is radically different from Eq. (II.139): it retains the single-photon aspect from DVCQC and catches the continuous variables of CVCQC. Squeezing is a quantum characteristic and the frequency bandwidth is a common feature of classical and quantum fields. Nevertheless, it does not prevent that this graph state can be used for quantum application since we deal with single-photon states. The limitation of this quantum computation model is the same as for DVCQC. It is intrinsic to the fact that we are using single-photons: deterministic interactions between photons are difficult to realize experimentally. We should also note that transversal position-momentum single-photon cluster states were already defined in [Tasca et al., 2011].

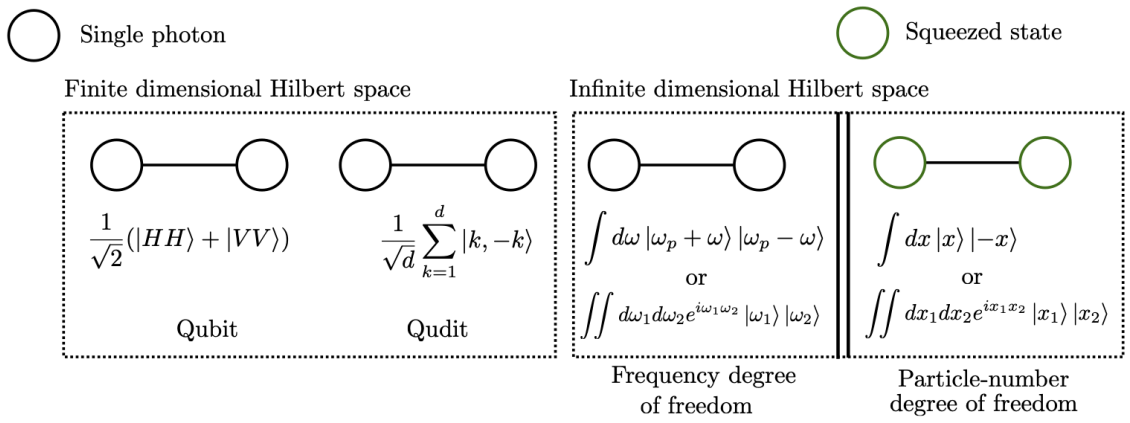

Figure III.1: Recap of the representation of different cluster states, with discrete or continuous degree of freedom of single-photons (black circle), or defined as a two-mode squeezed state.

III.3.4 Other time-frequency phase space distribution

The ordering of the time and frequency operators, or equivalently the ladder-like operators allows to define different time-frequency phase space distributions, in the same spirit as in Sec. II.4.3. The anti-normal (resp. normal) ordering corresponds to the case where the creation ladder-like operators (see Sec. III.2.4) are placed on the left (resp. on the right) and the annihilation ladders-like operators on the right (resp. left). In general, we define the s-ordered time-frequency characteristic distribution as:

$$\chi^s_{\hat{\rho}}(\omega,t) = e^{-is\omega t/2}\mathrm{Tr}(\hat{\rho}\hat{D}(\omega)\hat{\mathcal{D}}(t)). \tag{III.67}$$

The Fourier transform of the characteristic distributions labeled by s leads to different time-frequency phase space distributions. The anti-normal order ($s=-1$) leads to the time-frequency Husimi distribution [Husimi, 1940]:

$$Q_{\hat{\rho}}(\omega,t) = \frac{1}{\pi}\langle\omega,t|\,\hat{\rho}\,|\omega,t\rangle\,, \tag{III.68}$$

where $|\omega,t\rangle$ is a time-frequency coherent-like state. It is a single-photon with a Gaussian spectrum and is described in detail in Sec. V.1.1. The Fourier transform of the normal order time-frequency characteristic distribution ($s=-1$) leads to the P time-frequency distribution [Sudarshan, 1963]. While these distributions are sometimes used to represent classical intense laser fields, we highlight that in the single-photon subspace their mathematical constructions and their associated properties are different, owing to the non-commutative algebra of the bosonic operators Eq. (III.2). Experimental techniques to measure such distribution for classical fields can not be so easily translated for single-photon fields, as these techniques often require a non-linear interaction with the field to measure.

III.3.5 Time-frequency Gaussian measurement

A time-frequency Gaussian measurement produces a Gaussian probability distribution of the detection outcome for any input Gaussian state. The measurement of the frequency and the

arrival-time of single photons are then time-frequency Gaussian measurements if the response of the photodetector is a Gaussian temporal window. It is analogous to the measurement of two orthogonal quadrature using homodyne detection. But in this last case, any rotated marginal is accessible while the analog of this rotation in time-frequency Gaussian measurement is not known. The measurement of the JSI, JTI and the two other crossed marginals was done in [MacLean et al., 2019] and corresponds to Gaussian measurement if the temporal response of the detector is flat in the scale of the size of the single-photon wave packet.

A frequency Gaussian measurement can be done by letting a single-photon cross a dispersive medium and measuring its arrival-time probability distribution. The frequency distribution is recovered by the mapping from the time to the frequency induced by the dispersive medium, analog to a far-field measurement. There are other techniques which permit to amplify the signal using a coherent state as a seed, as the stimulated SPDC. Nevertheless, the amplified field is no longer a single photon field but has the same frequency distribution. This technique can also be called a frequency Gaussian measurement but since we are not anymore in the single-photon subspace, the amplified field can not be used for quantum application. An example of non-Gaussian time-frequency measurement can be obtained if the temporal window of the detector is non-Gaussian, with a rectangular shape for instance.

The rigorous treatment of a Gaussian measurement would be to consider the covariance matrix of the single-photon and the quantum clock, conditioned on the output of the detector. Again, if one considers a large Gaussian distribution compared to the wave packet of the single-photon, we conjecture that there is no additional feature of this rigorous mathematical and physical treatment.

III.4 Universal quantum computation with time-frequency degrees of freedom of single photon

In this section, we introduce the universal set of the time-frequency degrees of freedom of single photons. In Ref. [Tasca et al., 2011], such universal set was presented for the transversal position-momentum continuous variables degree of freedom of single-photons. But here, we present a rigorous mathematical proof by using the time and frequency or the creation and annihilation bosonic operators (see Eq. (III.3) and Eq. (III.2)). Indeed, these operators allow to reproduce the same algebra as the one of the position and momentum quadrature operators defined with the quantum harmonic oscillator. Our representation uses directly bosonic ladder operators and allows to be more transparent about the single photon subspace.

The universal set of quadrature position-momentum CVs manipulates the particle-number degrees of freedom of the same mode. Here, the number of photons is fixed to one since we are in the single photon subspace and the universal set manipulates the modes of single photons. It is actually usual: for polarization qubits, or time-frequency frequency bins (qudits) it is actually

the same situation. The universal set is an engineering of the modes so that we can think at first that these operations can be done classically. It is indeed the case, but we cannot have to forget that we consider the single photon subspace, and the considered algebra (see Eq. (III.3) and Eq. (III.2)) is purely quantum. Expressing the gates of the universal set by using time and frequency operators allows using the same mathematical proof than for quadrature position-momentum CVs. It precisely means that the concatenation of time-frequency Gaussian gates along with the non-Gaussian one permits to build any unitary time-frequency gates of the form $\exp(if(\hat{\omega},\hat{t}))$ where f is a polynomial function of time and frequency operators of arbitrary order. An example of a universal set is the time-frequency displacement gates, squeezing operations, two-photons gates, and the cubic phase gate. They are now presented.

III.4.1 Gaussian operations

We start by describing the Gaussian operations in this type of continuous variables. Again, they are mathematically the same as the quadrature position and momentum variables, but the physical interpretation is different.

Displacement operations The time-frequency displacements operations have been already described in Sec. (III.3.1).

Squeezing-type operation The squeezing terminology is obviously not adapted in this encoding, since it is related to the quadrature position-momentum variables on the number of photons of the field. The "squeezing" will refer here as the frequency or temporal bandwidth of single photons.

The squeezing or dilation operator is defined as, following [Moller et al., 1996]:

$$\hat{P}(r) = e^{-r/2} \int \hat{a}^\dagger(\omega e^{-r})\hat{a}(\omega)d\omega, \tag{III.69}$$

where $r \in \mathbb{R}$ is the squeezing parameter. It acts on a frequency state as $\hat{P}(r)\,|\omega\rangle = e^{-r/2}\,|\omega e^{-r}\rangle$. Equivalently by changing the variable $\lambda = e^{-r}$, the squeezing operator can be rewritten as $\hat{P}(\lambda) = \sqrt{\lambda}\int \hat{a}^\dagger(\lambda\omega)\hat{a}(\omega)d\omega$. It acts on a time state $\hat{P}(\lambda)\,|t\rangle = |\lambda t\rangle$. Let us consider the example of a physical state $|\psi\rangle = \int d\omega\psi(\omega)\,|\omega\rangle$ with $\psi(\omega)$ a Gaussian distribution of width σ. It corresponds to an elliptic Wigner distribution with width σ and σ^{-1} along the ω and t direction. After applying the squeezing operator $\hat{P}(\lambda)$ on the state $|\psi\rangle$, the amplitude spectrum $\psi(\omega)$ becomes a Gaussian distribution of width σ/λ, which justify the name of the operator $\hat{P}(\lambda)$.

Rotation gate A rotation in time-frequency phase space can be handled with a fractional Fourier transform. In particular the $\pi/2$-rotation is the Fourier transform, noted $\hat{F}$. More details will be given in Sec. V.5.

Two-photons gate The two-photons gate is the real experimental challenge in this encoding and its realization prevents for now large scale quantum computation using such CVs. It requires indeed a high non-linear effect for permitting an interaction between single-photons. The balanced controlled gate can be written under multiple forms. Its explicit representation in the single-photon subspace is:

$$\hat{C} = \iint d\omega_s d\omega_i \hat{a}^\dagger(\omega_s + \omega_i)\hat{a}^\dagger(\omega_s - \omega_i)\hat{a}(\omega_s)\hat{a}(\omega_i). \tag{III.70}$$

Since this gate is analogous to the balanced $\hat{C}_z$ in quadrature position and momentum CVs, we can write it using time and frequency operators:

$$\hat{C} = \exp(i(\hat{\omega}_1 \otimes \hat{T}_2 - \hat{T}_1 \otimes \hat{\omega}_2)), \tag{III.71}$$

with the subtlety that the time operator has to be "enhanced" by adding the ancilla quantum clock (see Sec. III.2.3.2), as for the other gates developed in this section. Nevertheless, it does not modify the commutation relation between the frequency and time operators acting on the quantum state.

III.4.2 Non-Gaussian gate

For instance, the frequency cubic phase gate is defined by:

$$\hat{C}(\gamma) = \int d\omega e^{i\gamma\omega^3} \hat{a}^\dagger(\omega)\hat{a}(\omega), \tag{III.72}$$

where $\gamma \in \mathbb{R}$. It can be written by using the frequency operator $\hat{C}(\gamma) = e^{i\gamma\hat{\omega}^3}$. Physically, this gate is the equivalent of the $\pi/8$ non-Clifford gate in DVs encoding. Higher order polynomial gates in time or frequency operators could also be defined.

To conclude, an example of universal time-frequency set of gates is $\{\hat{C}, \hat{P}(r), \hat{C}(\gamma), \hat{D}(0,\tau), \hat{F}\}$. We remind that the errors with this encoding are not related to the losses of photons. The absence of photons on a photo-detector is a non-event. A temporal error is related to the temporal broadening which increases the temporal bandwidth of a given peak. In addition, detectors have a finite resolution which depends on the frequency. The spectral tomography of the detectors briefly mentioned in Sec. VIII is one way to counter-balance this dependency which brings errors in our proposal for quantum computation.

III.5 Application: proposal of the measurement of time-frequency quantum correlations of two single photons

III.5.1 Classical and quantum entanglement

In this section, we aim to clarify the notion of entanglement, to convince of the ability of the time-frequency encoding to perform quantum tasks, as it is done with polarization of single-photon.

The notion of classical entanglement comes from the particular mathematical structure of a classical field of its degree of freedom [Aiello et al., 2015, Qian and Eberly, 2011]. For instance, the electromagnetic field $\vec{E}(x,y) = E_x(x,y)\vec{u}_x + E_y(x,y)\vec{u}_y$ presents a classical entanglement between the transversal position field $(E_x(x,y), E_y(x,y))$ and the polarization $(\vec{u}_x, \vec{u}_y)$. It was shown that such fields can violate Bell's like inequalities [Borges et al., 2010] or can bring a metrological classical advantage [Töppel et al., 2014]. Classical entanglement must not have been regarded as a quantum resource. This terminology is nevertheless kept as this special mathematical inseparability has provided fresh ideas for engineering a classical field to over perform already existing classical protocols.

The natural extension of classical intra-system entanglement is quantum *intra-system* entanglement and this type of correlation does not correspond to non-locality [Khrennikov, 2020]. A single photon which presents entanglement between polarization and transversal field is an example of quantum intra-system entanglement. Nevertheless, both of these correlations differ from a measurement perspective. In the classical regime intensity measurement is performed. A classical polarized field at 45° is a linear superposition of horizontal and vertical polarization and at each run of an experiment, we can measure the **intensity** of the field along two orthogonal directions. For a single photon in a coherent superposition of two orthogonal polarizations, after many runs of an experiment, we only have access to the **probability** that the state is polarized along one of the two orthogonal polarizations.

Quantum *inter-system* entanglement refers to one of possible quantum correlations between at least **two** different subsystems: pairs of single-photons or a two-mode squeezed state for instance. Non-locality and quantum discord are other examples of these quantum correlations. The existence of these quantum correlations does not depend on the dimensionality of the degrees of freedom of single-photons which is involved. Many experimental proofs of the existence of such quantum correlation with photonic qubits or qudits have been shown. A time-frequency EPR state, $|\psi\rangle = \int d\omega \, |\omega\rangle \, |-\omega\rangle$ could lead to violation of Bell's inequality and hence can be useful for QKD tasks. To the best of our knowledge, an experimental proof of such claim is lacking.

In the following, we will present a protocol which shows the existence of quantum discord using the time-frequency continuous variables of single-photons.

III.5.2 Quantum discord

In this section, we introduce the quantum discord which quantifies the excess of amount of information extractable in a measurement of a quantum state compared to a classical state. States with discord are valuable resources for achieving tasks that are unreachable with classical resources. A quantum state can display quantum discord without having entanglement.

For two classical random variables A and B, the total of correlation is measured by the mutual information defined by the two equivalent expressions:

$$I(A:B) = H(A) + H(B) - H(A,B), \tag{III.73}$$

$$J(A:B) = H(A) - H(A|B) = H(B) - H(B|A). \tag{III.74}$$

$H(X)$ is the Shannon entropy of the random variable X and $H(X|Y)$ is the conditional Shannon entropy. It is important to note the symmetry between the two variables A and B. The generalization of the mutual information $I(A:B)$ for a bipartite state $\hat{\rho}_{AB}$ is the quantity $I(\hat{\rho}_{AB}) = S(\hat{\rho}_A) + S(\hat{\rho}_B) - S(\hat{\rho}_{AB})$ where $S(\hat{\rho}) = -\mathrm{Tr}(\hat{\rho}\log(\hat{\rho}))$ is the Von-Neumann entropy. The density matrix of each subsystem after a partial trace operation is noted $\hat{\rho}_{A,B}$. $S(\hat{\rho}_{A,B})$ is known as the entropy of entanglement and is a quantifier of the loss of information when only a subsystem is accessed.

The generalization in the quantum case of the mutual information $J(A:B)$ is obtained by quantization of the expression based on conditional entropy. Nevertheless, the symmetry between the two subsystems is broken. We hence define two quantities depending on what subsystem is measured A or B: $J_A(\hat{\rho}_{AB}) = S(\hat{\rho}_A) - S_{\hat{\Pi}_j}(\hat{\rho}_{A|B})$ and $J_B(\hat{\rho}_{AB}) = S(\hat{\rho}_B) - S_{\hat{\Pi}_j}(\hat{\rho}_{B|A})$. In these expressions, $S_{\hat{\Pi}_j}(\hat{\rho}_{A|B}) = \sum_j p_j S(\hat{\rho}_{A|j})$ is the measurement-based quantum conditional entropy and $p_j = \mathrm{Tr}(\hat{\rho}_{AB}\hat{\Pi}_j)$ is the probability of obtaining the conditional state. $J_{A,B}(\hat{\rho}_{AB})$ depends on the POVMs, $\hat{\Pi}_j$ which describes the measurement performed on the subsystem A or B. The next step is to define a device independent quantity. The measure of the mutual information [Madsen et al., 2012] that quantifies the amount of classical correlation extractable by Gaussian measurement is:

$$J_A(\hat{\rho}_{AB}) = S(\hat{\rho}_B) - \min_{\hat{\Pi}_j}(S_{\hat{\Pi}_j}(\hat{\rho}_{A|B})), \tag{III.75}$$

where a minimization over all possible measurements of subsystem A is performed. The quantum A-discord is defined as the mismatch between the two equivalent expressions of the mutual information in classical information theory:

$$C_A(\hat{\rho}_{AB}) = I(\hat{\rho}_{AB}) - J_A(\hat{\rho}_{AB}). \tag{III.76}$$

The quantum A-discord is calculated for a certain class of quantum states, since the minimization depends on the considered quantum state and of the POVM. Here we restrict to the bipartite Gaussian state and the minimization is restricted to Gaussian measurements.

The motivation for characterizing and measuring such quantum correlation in time-frequency variables of a photon pair, is the apparent simplicity of the next proposed protocol, and was not done to our knowledge.

III.5.3 Quantum discord of time-frequency pure Gaussian states

The method in [Hosseini et al., 2014] consists of measuring the joint marginal distribution of the Wigner distribution of a bipartite Gaussian state thanks to homodyne detection along two orthogonal axes. Then, Bob (in B) measures two conditional marginal distributions corresponding to the positive or negative quadrature outcomes of Alice (in A). If the two peaks corresponding to the two marginals are separated, then the state displays a quantum discord.

We now generalize the method [Hosseini et al., 2014] to our context. The experimental method which allows verifying quantum discord for a bipartite two photons time-frequency Gaussian state is very similar. The initial Gaussian state produced by SPDC is described by the chronocyclic Wigner distribution: $W_{\hat{\rho}}(\omega_s, t_s, \omega_i, t_i) = \exp(-X^\top V^{-1} X)$, where the vector $X = (\omega_s, \omega_i, t_s, t_i)$ and the covariance matrix is:

$$V^{-1} = \begin{pmatrix} \delta_1 & 0 & L & 0 \\ 0 & 1/\delta_1 & 0 & 1/L \\ L & 0 & \delta_2 & 0 \\ 0 & 1/L & 0 & 1/\delta_2 \end{pmatrix}. \tag{III.77}$$

δ_1, δ_2 corresponds to the frequency width of the energy conservation function and of the phase-matching function respectively (see Chap. IV). We have defined $L = \delta_1\delta_2/(\delta_1 - \delta_2)$. The central frequency of the JSI has been set to zero. A frequency Gaussian state has non-zero discord if and only if $R \neq 0$ [Rahimi-Keshari et al., 2013]. If $R = 0$, it is indeed a product state. Alice and Bob share a time-frequency Gaussian state of two single photons, whose covariance matrix is given by Eq. (III.77). Then a frequency Gaussian measurement is performed and the JSI is measured. Then, depending on the negative or positive frequency outcomes of Alice, so there is classical communication, Bob evaluates the two conditioned quantities:

$$S_\pm(\omega_s) = \int_0^{\pm\infty} \pm \mathrm{JSI}(\omega_s, \omega_i) d\omega_i = \frac{1}{2} e^{-\omega_s^2/2S} e^{\omega_s^2 S/2L^2} [1 \pm \mathrm{erf}(\frac{\omega_s\sqrt{R}}{\sqrt{2\delta_1\delta_2}})], \tag{III.78}$$

where erf is the error function $\mathrm{erf}(x) = \int_0^x e^{-y^2} dy$ and $S = \delta_1\delta_2/(\delta_1 + \delta_2)$. We have also defined the ellipticity as the ratio: $R = (\delta_1 - \delta_2)/(\delta_1 + \delta_2)$ If the two peaks of $S_+(\omega_s)$ and $S_-(\omega_s)$ do not coincide, the time-frequency Gaussian state displays Gaussian discord.

We represent in Fig. III.2 the functions $S_\pm(\omega_s)$ for different ellipticity $R = 0, 0.96, 0.99$. For $R = 0$, the two curves $S_\pm$ (green and light blue) are identical and hence no supplementary correlations between the two fields are extractable. As R goes along 1, the curves $S_\pm(\omega_s)$ do not coincide and show the existence of quantum discord.

What is remarkable is that even with small time-frequency correlations, namely with $R \approx 0$, such a Gaussian state has non-zero discord. By measuring the JTI, this same method can also show the existence of quantum discord but we have to evaluate the conditional quantities $\tilde{S}_\pm(t_s)$, where the index $\pm$ refers to the outcomes $t_i < 0$ and $t_i > 0$. For $1/R \neq 0$, we arrive at the same conclusion for the presence of Gaussian quantum discord. In a more general case where the state displays correlations as $\langle \omega_{s,i} t_{s,i} \rangle$, we can show that the state presents also non-zero discord by

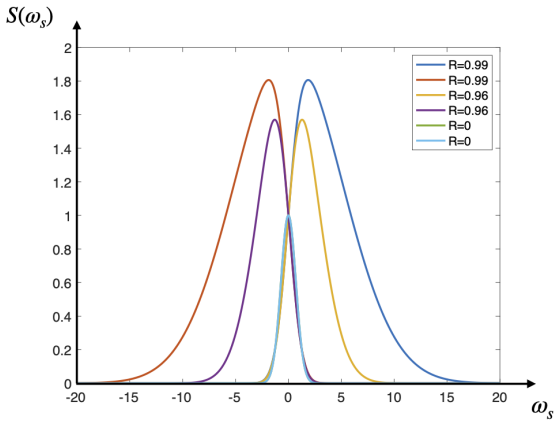

Figure III.2: $S_{\pm}(\omega_s)$ function for different ellipticity $R = 0, 0.96, 0.99$. The central frequency of the JSI has been set to zero. For $R = 0$, the discord is zero since the bipartite system is separable: the green and blue graph coincide. For $R \neq 0$, the state presents non-zero discord, since the purple and yellow function, and the blue and orange function do not coincide.

measuring the crossed marginal JTSI and JSTI (see Eq. III.51) presented in Ref. [MacLean et al., 2019]. For non-Gaussian time-frequency states, the separability of the conditioned quantities is only a sufficient condition for quantum discord [Hosseini et al., 2014]. The next step would be to perform this protocol experimentally.

Chapter IV

Generation of photon pairs by spontaneous parametric down conversion and their detection

In this chapter, we explain the generation of a frequency entangled photon pair by spontaneous parametric down conversion (SPDC), a non-linear process that can take place in bulk crystal or in integrated optical waveguides. The presence of frequency entanglement is assessed by using the Simon's criterion, which is a necessary and sufficient condition of entanglement of a bipartite Gaussian state. This criterion was introduced for quadrature position-momentum CV states and is translated in our encoding using the theoretical tools developed in Chap. III. The amount of entanglement is quantified using the Schmidt decomposition, as it is usually done in such context. Then, the detection of the photon pair is performed with the Hong, Ou and Mandel experiment, which allows to obtain signature of the particle's statistics, indistinguishability and the frequency entanglement of single photons.

IV.1 Presentation of SPDC

IV.1.1 General description of the wave function produced by SPDC

The SPDC process is a second order non-linear effect which consists of a three-wave mixing inside a bulk or a waveguide crystal. A coherent pump beam described by an electric field with central frequency ω_p called the degeneracy frequency, crosses a second-order non-linear crystal. One photon of the pump is annihilated and generates one pair constituted by two photons called the signal and the idler with frequencies ω_s and ω_i respectively. The generation of the pair is represented in Fig. IV.1 (a). There are also events where two photons of the pump generate two pairs which happen with a lower probability, along with multiphoton events. In the single photon regime, the signal and idler fields are simply single-photons. In the case where the multiphoton events are not negligible, the produced fields are rather called the signal and the idler modes. The semi-classical approximation is assumed which states that the pump is not to be significantly affected by the SPDC process.

For now, we assume to be in the multiphoton regime. The spectral distribution of the signal and idler modes are constrained by two conditions: the energy conservation (sketched in Fig. IV.1(a)) and the minimization of the phase matching condition along the z-direction, direction where the photons are generated. This last condition depends on the geometry of the crystal and the spatial pump profile. These two conditions will be precised in more detail for two specific waveguide geometries. In addition, three types of SPDC are defined depending on the polarization of the signal and idler modes. The type-0 (resp. type-I) SPDC corresponds to the case where the signal and idler fields have the same polarization (resp. orthogonal) to the pump while the type-II corresponds to the case where the signal and idler fields have orthogonal polarizations, noted a and b.

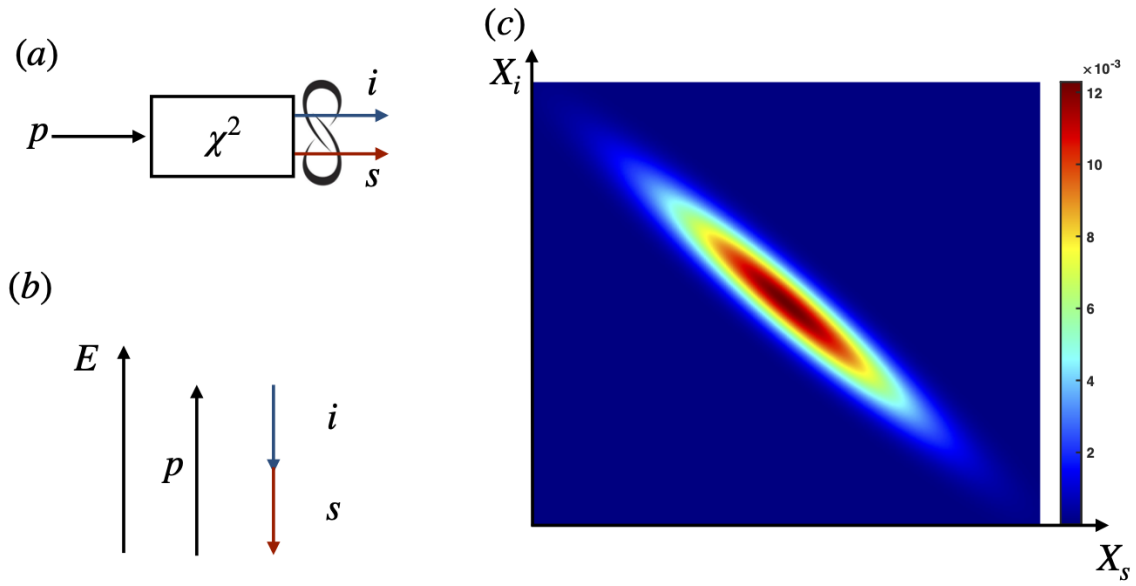

Figure IV.1: (a) Sketch of the generation of the signal and idler modes by SPDC in a second order non-linear medium. (b) Sketch of the energy diagram which traduce the energy conservation. Photons of the pump (p) are converted into idler (i) and signal (s) modes (c) Probability amplitude $|\psi(X_s, X_i)|^2$ of the two-mode squeezed state when $R > 1$. The two modes corresponds to two orthogonal polarization here.

Two-mode vacuum squeezed state We do not remind the full derivation of the wave function describing the signal and the idler modes. It is done for bulk systems in [Hong and Mandel, 1985, Walborn et al., 2010] and for the specific non-linear integrated device of our lab in Ref. [Boucher, 2016]. The quantum state generated by a type-II SPDC is a multi-mode vacuum squeezed state, where "multi-mode" refers to the transversal or spectral degree of freedom depending on the considered device. A given spectral mode for the signal and idler is described by the following wave function:

$$|\psi\rangle = \frac{1}{\cosh(r)} \sum_{n=0}^{\infty} \tanh(r)^n \, |n\rangle_s \, |n\rangle_i \,, \tag{IV.1}$$

where $0 < |r| < 1$ is the amplitude of squeezing determined by the pump power, the second order non-linearity of the crystal χ^2 and its length. $|n\rangle_{s/i}$ are Fock states for the signal and idler spectral modes and they are polarized horizontally and vertically respectively. We note that there is a perfect correlation between the number of photons of the signal and the idler modes. The specific structure of the involved frequency modes is going to be specified afterwards. The wavefunction Eq. (IV.1) includes infinitely higher order terms which contribute to multi-photon emissions. The state is also called a two-mode (signal and idler) EPR entangled state, because the amplitude of wave function expressed in quadrature position-momentum variables can be written as [Lvovsky, 2015]:

$$\psi(X_s, X_i) = \frac{1}{\sqrt{\pi}} e^{-(X_a+X_b)^2/4R^2} e^{-R^2(X_a-X_b)^2/4}, \tag{IV.2}$$

with $R = e^r$ and characterizes the ellipticity of the state in the (X_s, X_i) plane. The probability distribution of the wave function $|\psi(X_s, X_i)|^2$ is represented in Fig. IV.1 (c) and is ellipse elongated along the $X_- = X_s - X_i$ direction when $R \geq 1$. In the case where $r \to \infty$, the probability distribution is a line along the X_- axis and is an ideal EPR state, since the state is infinitely squeezed. The variances of the two-mode vacuum squeezed state are:

$$\Delta(\hat{X}_s - \hat{X}_i) = e^{-r} \tag{IV.3}$$

$$\Delta(\hat{P}_s + \hat{P}_i) = e^{r}, \tag{IV.4}$$

which means that if the state is anticorrelated along the $x_- = x_1 - x_2$ axis, it is correlated along the $p_+ = p_1 + p_2$ axis.

In the limit $|r| << 1$, Eq. (IV.1) can be developed as:

$$|\psi\rangle = \sqrt{1-|r|^2} \sum_{n=0}^{\infty} r^n |n\rangle_s |n\rangle_i = \sqrt{1-|r|^2} \exp(r\hat{a}^\dagger(\omega_s)\hat{b}^\dagger(\omega_i)) |0\rangle, \tag{IV.5}$$

where a and b denote two orthogonal polarizations. The previous wavefunction describes one frequency mode for the signal (ω_s) and the idler (ω_i). The full wave function which describes the signal and idler fields produced by SPDC is a tensorial product of Eq. IV.1 of different frequency modes. We now provide a proof of this result. By taking into account the spectral degree of freedom, the state produced by SPDC is the multi-mode vacuum squeezed state described by the wavefunction $|\psi(t)\rangle = \exp(i\hat{H}t/\hbar)|0\rangle$:

$$|\psi(t)\rangle = \exp(\frac{it}{\hbar} \iint d\omega_s d\omega_i F(\omega_s, \omega_i) \hat{a}^\dagger(\omega_s)\hat{b}^\dagger(\omega_i)) |0\rangle \tag{IV.6}$$

$$= \exp(\iint d\omega_s d\omega_i \mathrm{JSA}(\omega_s, \omega_i) \hat{a}^\dagger(\omega_s)\hat{b}^\dagger(\omega_i)) |0\rangle, \tag{IV.7}$$

where the $\mathrm{JSA}(\omega_s, \omega_i) = \frac{it}{\hbar} F(\omega_s, \omega_i)$ stands for the joint spectral amplitude and characterizes the frequency correlation of the signal and idler fields (see also Eq. (III.11)). Its specific shape will be detailed later. The time t is related to the length L of the non-linear medium: $t = L/c$. The Eq. (IV.7) is the multimode generalization of Eq. (IV.5). The JSA, after discretizing it and making a Schmidt decomposition can be written as: $\mathrm{JSA}(\omega_s, \omega_i) = \sum_{i=1}^{N} r_i f_i(\omega_s) g_i(\omega_i)$. f_i and

g_i are called Schmidt function and r_i are real positive numbers. This procedure will be described in more details in Sec. IV.3. N refers to the number of modes. Finally, the full wavefunction of the multimode squeezed state is:

$$|\psi\rangle = \prod_{i=1}^{N} \exp(r_m \iint d\omega_s d\omega_i f_i(\omega_s) g_i(\omega_i) \hat{a}^\dagger(\omega_s) \hat{b}^\dagger(\omega_i)) \, |0\rangle \, . \tag{IV.8}$$

It is now transparent that r_i is the squeezing parameter of each frequency mode labeled by m and is a particle-number sensitive variable. A development into a power series of the exponential in Eq. (IV.8) allows to write the state alternatively as:

$$|\psi\rangle = \bigotimes_{j=0}^{\infty} \sum_{n_j=0}^{\infty} r_j^{n_j} \, |n_j\rangle_s \, |n_j\rangle_i \, , \tag{IV.9}$$

where $|n_j\rangle_s = 1/\sqrt{n_j!}(\int_{\mathbb{R}} f_j(\omega_s)\hat{a}^\dagger(\omega_s)d\omega_s) \otimes \underbrace{...}_{n\text{times}} \otimes (\int_{\mathbb{R}} f_j(\omega_s)\hat{a}^\dagger(\omega_s)d\omega_s)\,|0\rangle$ and $|n_j\rangle_i = 1/\sqrt{n_j!}(\int_{\mathbb{R}} g_j(\omega_i)\hat{b}^\dagger(\omega_i)d\omega_i) \otimes \underbrace{...}_{n\text{times}} \otimes (\int_{\mathbb{R}} g_j(\omega_i)\hat{b}^\dagger(\omega_i)d\omega_i)\,|0\rangle$. We recognize that it is a tensorial product of two-mode squeezed states (see Eq. (IV.5)). The specific structure of the JSA and its modal decomposition determines the effective number of modes (see Sec. IV.3)

Quantum frequency comb The quantum frequency comb is a multimode squeezed state whose optical spectrum consists of a series of equally discrete space optical frequencies such that $\omega_n = \omega_p + n\overline{\omega}$. ω_p is the central frequency of the comb and $\overline{\omega}$ is the free spectral range, related to the length of the cavity L by $\overline{\omega} = c/2L$. In order to produce such state, the non-linear crystal which produces the signal and idler fields is placed into an optical cavity. The optical cavity shapes the spectral distribution of the signal and idler modes, namely the JSA. The state can be written as Eq. (IV.8), but with the difference that the Schmidt functions f_i, g_i are close to the ones imposed by the optical cavity. A demonstration of this fact in the biphoton regime is shown in Sec. IV.3. An important remark is that the quantum frequency comb has to be differentiated to the classical frequency comb. Indeed, the statistical property of the optical fields in each case is sub-Poissonian and Poissonian respectively.

Bringing new correlations between each frequency mode is an art and allows to build complex CV cluster states (see Sec. II.4.7), where each node of the cluster corresponds to one peak of the comb. For instance, by using a frequency comb pump synchronously pumped optical parametric oscillator (SPOPO) [Roslund et al., 2014] or by using an electro optic modulator, one can correlate different frequency signal and idler modes. Despite the deep interest in many experimental group of the quantum frequency comb [Asavanant et al., 2019, Cai et al., 2017, Chen et al., 2014, Larsen et al., 2019, Zhu et al., 2019], the impressive scalability of these states, the realization of non-Gaussian gates is only on his first step [Marshall et al., 2015] which is unavoidable for achieving universal quantum computation.

IV.1.2 Biphoton regime

The multiphoton regime is not the goal of this thesis. Instead, we will be interested in the depleted regime of the SPDC process, where each squeezing parameter fulfills the condition $|r_i = |r|| \ll 1$. The probability of having one photon is given by $P(1) = (1 - |r|^2)|r|^2$ and is limited to 25% for $|r| = 0.8$. Choosing such a value has as a consequence to degrade the number purity. Indeed, the ratio between the probability of having $n+1$ photons and n photons is: $P(n+1)/P(n) = |r|^2$ which depends linearly to the pump power. So a compromise has to be found in order to have a high single photon delivery $P(1)$ and to avoid higher photon emission terms. Experimentally, post-selection is performed to take into account only the two photons events and to rule out the higher order terms and the vacuum. The SPDC process allows to produce non-deterministically photon pairs, since the Eq. (IV.9) can be written at the first order of the squeezing parameter r_i:

$$\begin{aligned} |\psi\rangle &= \prod_i (|0\rangle + r_i |\psi_i\rangle + O(r_i^2)) \\ |\psi\rangle &= |0\rangle + \sum_j r_j |\psi_j\rangle + O(r^2), \end{aligned} \tag{IV.10}$$

where $\sum_j r_j |\psi_j\rangle = \sum_j r_j \iint d\omega_s d\omega_i f_i(\omega_s g_i(\omega_i) \hat{a}^\dagger(\omega_s)\hat{a}^\dagger(\omega_i)) |0\rangle = \iint d\omega_s d\omega_i \mathrm{JSA}(\omega_s, \omega_i)\hat{a}^\dagger(\omega_s)\hat{a}^\dagger(\omega_i) |0\rangle$. The state is then a non-Gaussian one, as it is a two-photon state. Since the particle-number is now fixed and we are restricted to the single photon regime, the continuous variables of interest are only the frequency ones. In addition, the performance of the source is also altered by the efficiency of the detectors which can depend on the frequency: but for the sake of simplicity in the following, we will consider that response is flat.

Spectral structure of the biphoton state produced by a non-linear crystal placed in free space We are now interested in the spectral structure of the photon pair, namely the JSA. The output biphoton state is:

$$|\psi\rangle = \iint \mathrm{JSA}(\omega_s, \omega_i) d\omega_s d\omega_i |\omega_s, \omega_i\rangle . \tag{IV.11}$$

The Joint spectral amplitude can be written as: $\mathrm{JSA}(\omega_s, \omega_i) = f_+(\omega_+) f_-(\omega_-)$, with $\omega_\pm = \omega_s \pm \omega_i$. The f_+ function is related to the energy conservation $\omega_s + \omega_i = \omega_p$ where ω_p is the frequency of the laser pump:

$$f_+(\omega_s, \omega_i) = \exp\left(-\frac{(\omega_s + \omega_i - \omega_p)^2}{4\Delta\omega_p^2}\right). \tag{IV.12}$$

The phase matching function f_- reflects the momentum conservation $\Delta\vec{k} = \vec{k}_p - (\vec{k}_s + \vec{k}_i)$, where $\vec{k}_{p,s,i}$ is the momentum of the pump, signal and idler photons respectively. In a bulk device, it is in general a sinc function which depends on the product $\Delta k z$, where z is the spatial coordinate of the direction of propagation. Satisfying $\Delta\vec{k} \approx 0$ is possible by choosing the right polarization of the pump and the orientation of the crystal. Nevertheless, the non-linear crystal is also birefringent. The wave vector of the extraordinary wave is not collinear to the Poynting vector of the field and leads to a beam walk-off and has the consequence to limit the nonlinear

optical efficiency. It is due to interference effects between signal and idler photons which are produced at different spatial locations inside the crystal. To compensate this walk-off and in the same time to respect the phase-matching condition, one solution consists to realize a *quasi*-phase matching condition where $\Delta\vec{k} \neq 0$ but with an alternance of layers of crystal whose non-linearity are of opposite signs. Without the alternance of these layers, the condition $\Delta\vec{k} \neq 0$ implies that the intensity of the signal and idler oscillates with respect to the length of the crystal. But by alternating the signs of the non-linearity of the layers, the intensity of the field can increase with respect to the length of the crystal.

For optical integrated devices, many other ways allow to achieve the quasi-phase matching condition [Orieux et al., 2017]. The function f_- is going to be explicitly expressed for two optical integrated devices and is assumed to have a Gaussian form, with a rigorous justification which will be given later. The JSI = |JSA| in that case is represented in Fig. IV.2(a). Note the mathematical resemblance with Fig. IV.1. In one case, there is a frequency anti-correlation of two single-photons (see Fig. IV.2(a)) and in the other, an anti-correlation in the particle-number distribution between two modes (see Fig. IV.1).

Spectral structure of the biphoton state in an optical cavity: microcomb When the non-linear crystal which generates the photon pairs is placed into an optical cavity, the JSA can be written as the product of four terms:

$$\mathrm{JSA}(\omega_s, \omega_i) = f_+(\omega_+) f_-(\omega_-) f_{\mathrm{cav}}(\omega_s) f_{\mathrm{cav}}(\omega_i). \tag{IV.13}$$

The effect of the cavity on the signal and idler photon is taken into account by the cavity function $f_{\mathrm{cav}}(\omega_{s/i})$ that acts as an imperfect frequency filter. The cavity functions are the Airy ones:

$$f_{\mathrm{cav}}(\omega) = \frac{\sqrt{1-R}e^{i\omega\tau/2}}{1-Re^{i\omega\tau}}, \tag{IV.14}$$

where R is the reflectivity of the cavity and $\tau = 2Ln/c$ is the time of one round-trip of a photon in the cavity, L is again the length of the cavity and n the refractive index of the medium inside the optical cavity. The function $|f_{\mathrm{cav}}(\omega)|$ is represented in the Appendix A.1: it is periodic and the frequency spacing between each peak is called the free spectral range $\overline{\omega} = c/2nL$. An important quantity is the finesse F defined as the ratio of the free spectral range and the half-width of the Airy functions. It can also be cast using the reflectivity factor: $F = \pi R^{1/2}/(1-R)$.

We will model the cavity function as a sum of Gaussians, which is a good approximation in the limit of a high finesse cavity:

$$f_{\mathrm{cav}}(\omega) = \sum_{n\in\mathbb{Z}} T_n(\omega), \tag{IV.15}$$

where $T_n(\omega) = \exp(-(\omega - n\overline{\omega})^2/(2\sigma^2))$. $\overline{\omega}$ represents the free spectral range and σ is related to the finesse, or the reflectivity. In the Appendix. A.1, we report for specific values of the

reflectivity, the width of the Gaussian peaks which minimizes the distance (defined as the norm-1) between the Gaussian comb and the Airy function. The frequency width σ reflects the finesse of the cavity. A high finesse corresponds to the condition $\overline{\omega} \gg \sigma$, the two photons state can be written in that case:

$$|\psi\rangle = \sum_{n,m\in\mathbb{Z}^2} \iint d\omega_s d\omega_i f_+(\omega_+) f_-(\omega_-) T_n(\omega_s) T_m(\omega_i) \, |\omega_s\rangle \, |\omega_i\rangle \, . \tag{IV.16}$$

The resulting state is as a grid state because of the cavity functions. The energy conservation and the phase-matching condition produce an envelope that limit the dimensions of the produced grid and is represented in Fig. IV.2(b). It is in general a frequency entangled state, since we can not be written the state as a product of two functions which depends only of ω_s and ω_i.

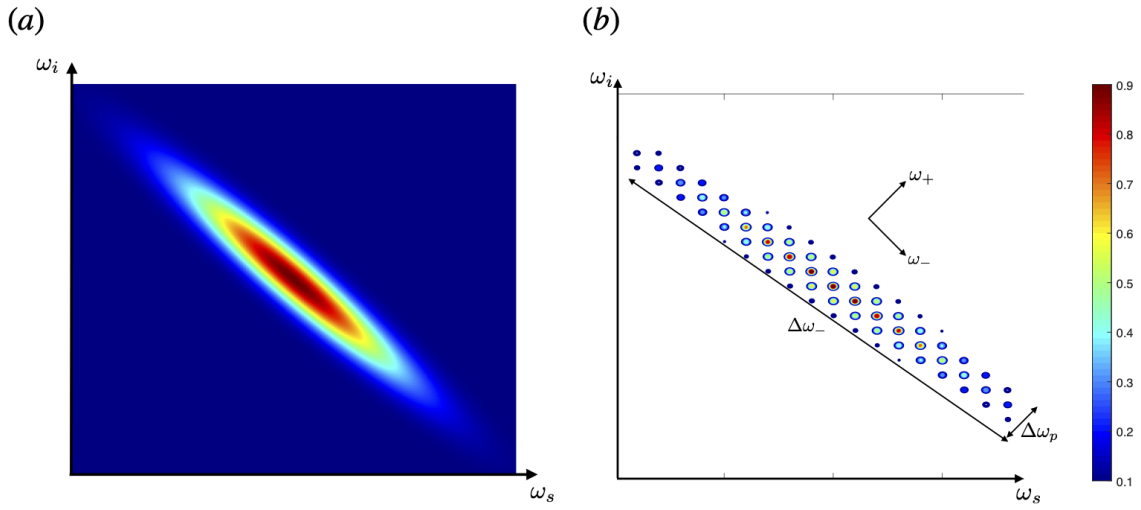

Figure IV.2: (a) Numerical simulation of the Joint Spectral Intensity for a two-photon source placed in a free space (b) and placed in an optical cavity, with arbitrary units. The size of the ellipse is delimited by the energy conservation (with a frequency width $1/\Delta\omega_p$) and the phase matching condition (with a frequency width of $1/\Delta\omega_-$). The center of the ellipse is the half of the degeneracy frequency ω_p. Here the state is said to be anti-correlated since $\Delta\omega_- > \Delta\omega_p$.

The frequency entanglement is reflected by the elliptical shape of the JSI. The ellipticity of the JSI is defined as $R = \frac{1/\Delta\omega_-^2 - 1/\Delta\omega_p^2}{1/\Delta\omega_-^2 + 1/\Delta\omega_p^2}$. A state with an arbitrary positive ellipticity is represented on the numerical simulation Fig. IV.2. The state is said to be correlated if the width of the energy conservation function f_+ is larger than the width of the phase matching function f_-: $1/\Delta\omega_- \gg 1/\Delta\omega_p$. Conversely the state is said to be anti-correlated, which is the case study of the next paragraph see Fig. IV.4(b), if $1/\Delta\omega_p \gg 1/\Delta\omega_-$.

Such states are called quantum micro-comb [Kues et al., 2019], because the average value of photon the number is one or two. It has to be differentiated with the quantum frequency comb, where squeezed states in different frequency modes are entangled. In Fig. IV.3, we sketch the frequency comb and the micro comb. They have the same frequency structure, but the frequency peaks are not populated by the same number of photons. For the frequency comb (see Fig. IV.3(a)), each frequency mode from each side of the central frequency is a two-mode

squeezed state. In Fig. IV.3(b), we represent the micro-comb where there is a photon number average of two. Quantum micro-combs are produced for instance by spontaneous four wave-mixing in a micro-ring cavity [Kues et al., 2019].

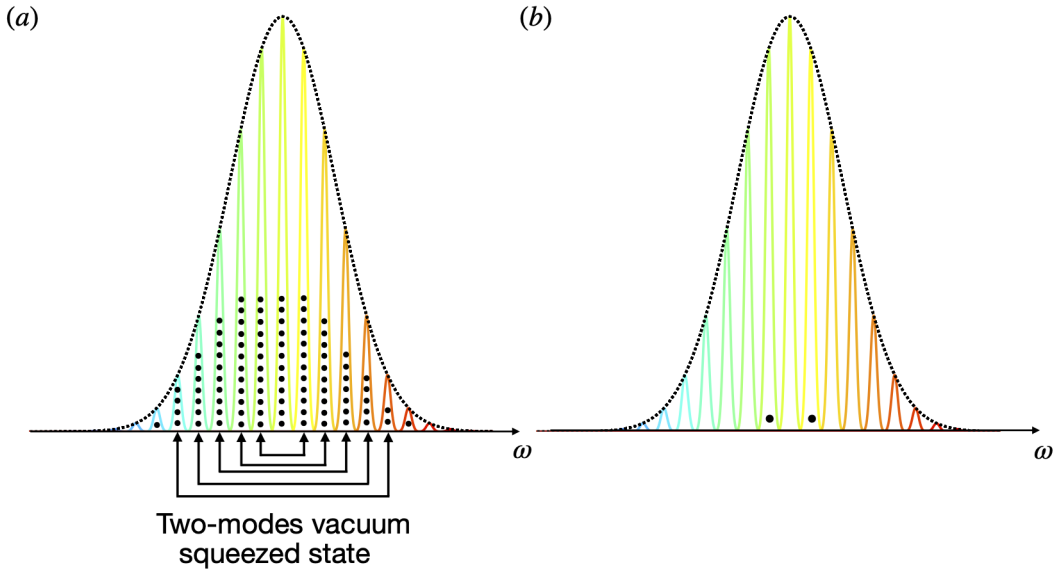

Figure IV.3: The modes structure are the same for (a) the frequency comb and (b) the micro-comb. During a detection event, the number of recorded photons for the two quantum states are not the same. The black dots represent the photons but do not represent their actual number in (a) and sketch only its difference with a micro-comb. Each connected arrow indicates that each pair is a two-mode vacuum squeezed state.

In the QITE experimental group of the Matériaux et Phénomènes Quantiques laboratory at Paris University, two different integrated waveguide optical devices have been built which can produce quantum micro-combs. The general advantages of such integrated optical circuits are their small size, stability, scalability and reconfigurability. An example of the advantage of integrated circuits over bulk systems, is that air conditioning deteriorates the stability of the generation of photon pairs when they are produced by a bulk system. It was demonstrated that single path-encoded qubit gates can be implemented with a high-fidelity [Qiang et al., 2018] in silicon integrated circuit. Many experimental demonstrations of Boson Sampling were also carried with integrated optical devices [Brod et al., 2019].

IV.1.3 Collinearly pumped integrated waveguide

The first device that we expose is an AlGaAs chip represented in Fig. IV.4(a). It consists of a Bragg reflection ridge waveguide optimized for efficient type-II SPDC [Maltese et al., 2020]. The pump beam is a transverse electric (TE) Bragg mode, whose wavelength is centered at 765 nm having a linewidth $\Delta\omega_p = 2\pi \times 100$ kHz. This leads to the generation of strongly anticorrelated photon pairs over a spectral band of $\Delta\omega_- = 2\pi \times 10.9$ THz centered around the frequency degeneracy as shown in the numerical simulations reported in Fig. IV.4 (b). The signal

and idler photons which are generated are TE and transverse magnetic (TM) in the C-telecom band. In such a device, the photons are indistinguishable since the JSA is centered at $\omega_- = 0$ and symmetric. The refractive index contrast between AlGaAs and air creates a cavity around the nonlinear medium, as the waveguide's facets play the role of mirrors, creating a Fabry-Perot cavity surrounding the non-linear medium. The free spectral range of the cavity is $\overline{\omega} = 2\pi \times 19.2$ GHz, yielding to a micro-comb with approximately 570 peaks.

In this case, the state is correlated and the Joint Spectral Amplitude is almost a line along the ω_- direction, and can be written as $\mathrm{JSA}(\omega_s, \omega_i) \simeq \delta(\omega_+ - \omega_p) f_-(\omega_-) f_{\mathrm{cav}}(\omega_s) f_{\mathrm{cav}}(\omega_i)$. The refractive index is polarization dependent such that $n_{\mathrm{TM}} \neq n_{\mathrm{TE}}$. Thus, the cavity functions of the signal and idler photons are described by different parameters, $\tau_{\mathrm{TM}}, \tau_{\mathrm{TE}}$ in the Airy function model and $\delta\omega_{\mathrm{TM}}, \delta\omega_{\mathrm{TE}}$ in the Gaussian model of the cavity. But we will consider that these parameters are equal for simplicity. Rigorous study can be found in [Maltese, 2019]. We will employ the Gaussian function to model the cavity. After performing the integration over the ω_+ variable in Eq. (IV.16), the wavefunction can be written as:

$$|\psi\rangle = \int d\omega_- f_-(\omega_-) f_{\mathrm{cav}}(\frac{\omega_p + \omega_-}{2}) f_{\mathrm{cav}}(\frac{\omega_p - \omega_-}{2}) \left| \frac{\omega_p + \omega_-}{2}, \frac{\omega_p - \omega_-}{2} \right\rangle. \tag{IV.17}$$

The $\mathrm{JSI}(\omega_s, \omega_i) = |\langle \omega_s, \omega_i | \psi \rangle|^2$ is experimentally obtained by the stimulated emission tomography technique (SET) [Eckstein et al., 2014, Liscidini and Sipe, 2013]. The Fig. IV.4 (c) shows the measurement of a portion of the JSI obtained with such method. This technique consists of using a TM polarized CW telecom laser as a seed to amplify the idler by difference frequency generation. Then, the frequency of the seed is changed to swept all the JSI [Francesconi et al., 2020, Maltese et al., 2020].

IV.1.4 Transversally pumped integrated waveguide

The second device is a semiconductor AlGaAs microcavity integrated source pumped transversally by a Ti:Sa laser with a central wavelength of 773 nm, with an incidence angle θ and waist w_p [Francesconi et al., 2020]. Two counter-propagating signal and idler photons are generated by SPDC in the telecom-band, and are in a superposition of TM and TE modes. Only the TM-polarized signal photon propagating along $z > 0$ and the TE-polarized idler photon propagating along the $z < 0$ is kept by placing two polarizers at each side of the crystal.

In addition, in the narrow pump bandwidth limit and neglecting the group velocity, the JSA can be cast under the form given by Eq. (IV.13). In such device, the phase matching function has the particular mathematical form [Francesconi et al., 2020]:

$$f_-(\omega_s, \omega_i) = \int_{-L/2}^{L/2} \mathrm{d}z \phi(z) e^{i\Delta k z}, \tag{IV.18}$$

where L is the length of the crystal and ϕ is the spatial field distribution of the pump beam along the z-axis (see Fig. IV.5 (a)) and is a Gaussian beam of width w_p (called the waist) which arrives at the center of the crystal with an angle θ. For a certain incidence angle, called the degeneracy

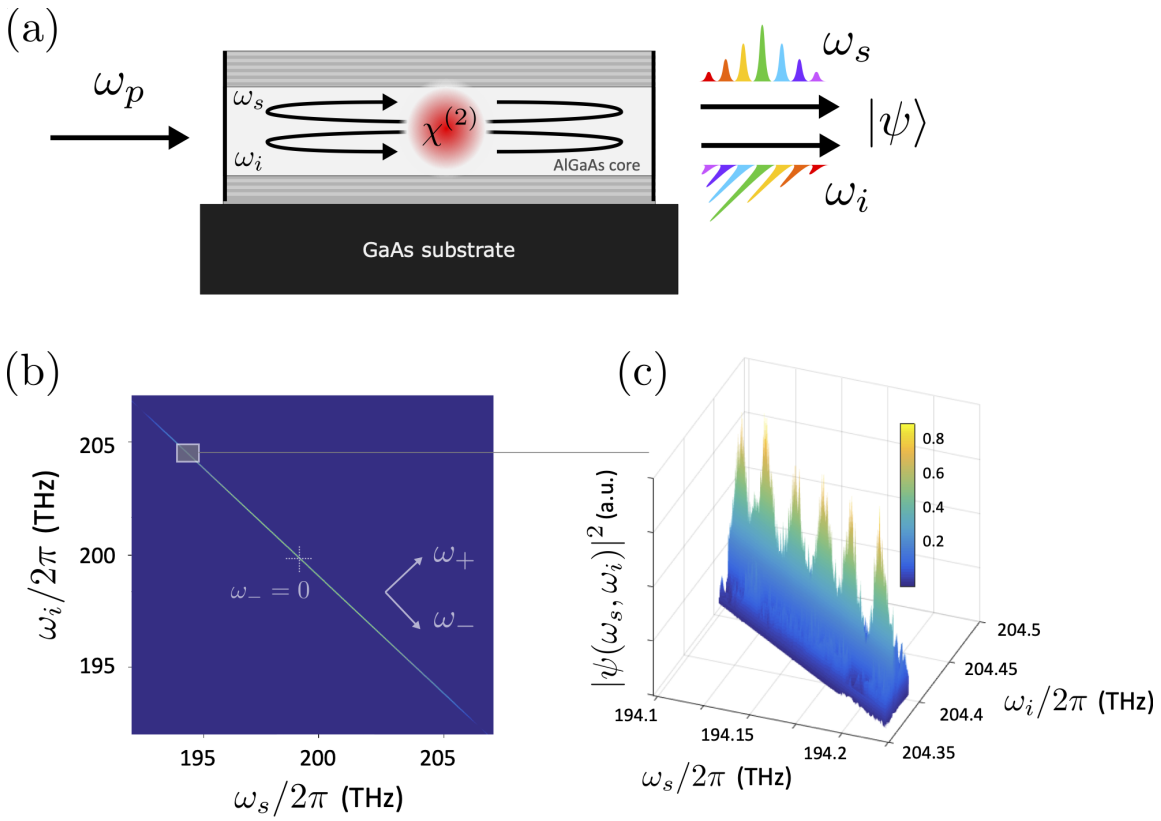

Figure IV.4: (a) A pump beam illuminates an AlGaAs waveguide where photon pairs are generated by SPDC. The difference in the refractive index between the air and the waveguide create an optical cavity effect. (b) Simulated JSI of the state emitted by the nonlinear cavity, using the nominal structure of the device. (c) Experimental JSI (detail). The figure is extracted from [Fabre et al., 2020c].

angle, the phase mismatch is $\Delta k = (\omega_s - \omega_i)/\overline{v}_g$ where the group velocity $\overline{v}_g = 2c/(n_{\mathrm{TE}} + n_{\mathrm{TM}})$ is assumed to be frequency independent. Again for this integrated device, we will consider that $n_{\mathrm{TE}} = n_{\mathrm{TM}}$. For $L \gg w_p$ we can extend the integral to the infinity and Eq. (IV.18) can be rewritten as:

$$f_-(\omega_s, \omega_i) = \exp\left(-\frac{(\omega_s - \omega_i)^2}{4\delta\omega^2}\right), \tag{IV.19}$$

where $\delta\omega = \frac{\overline{v}_g}{2w_p}$ and hence can be varied by changing with the waist of the pump beam w_p. It allows to modify the ellipticity of the JSI as it is shown in Fig. IV.5(b). The measurement of the JSI for this photon source is again obtained by stimulated emission tomography.

The narrow-band condition The two JSI of the photon pairs produced in the two presented integrated waveguides verify the narrow band condition described in Sec. III.2.2, a condition allowing to relate the spectral amplitude and the temporal amplitude by a Fourier transform. Indeed, the central frequency is larger that the spectral width of the source:

• For the collinearly pumped integrated waveguide: $\omega_p = 2.46 \cdot 10^{15}$ Hz $\gg 2\pi c\delta\lambda/\lambda_p^2 = 6.85 \cdot 10^{13}$ Hz. $\delta\lambda$ is the width of the quasi phase-matching condition.

• For the transversally pumped integrated waveguide: $\omega_p = 2.43 \cdot 10^{15}$ Hz $\gg 3.15 \cdot 10^{12}$ Hz.

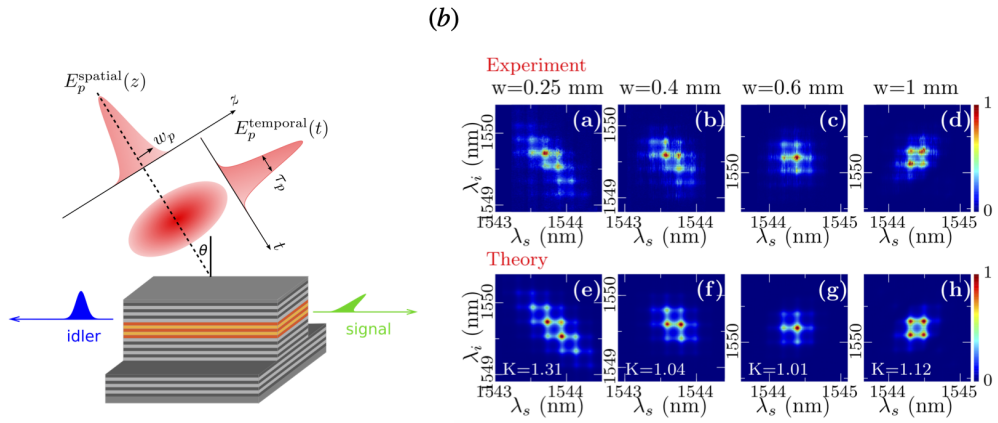

Figure IV.5: (a) A pump beam illuminates an AlGaAs waveguide where photons pairs are generated by SPDC. (b) JSI of the photon pairs obtained experimentally and numerically. Changing the value of the waist allows to modify the direction of the ellipse, from the ω_- axis (a) and (e) to the ω_+ axis (d) and (h). The figure is extracted from Ref. [Francesconi et al., 2020].

IV.1.5 Single photon source

The SPDC is a non-deterministic process which generates photons at random times. Nevertheless, for a type-II SPDC, the photon pair can be spatially split such that the detection of one of them heralds with high probability the presence of the second.

As it was demonstrated in [Belhassen et al., 2018], the non-linear waveguide pumped transversally can be used as a heralded single photon source. The advantage of this platform relies on the fact that the device works at room temperature and produces telecom wavelength photons. The purity of the source is the probability to have no more than one photon emitted by the source in each wave packet. It can be quantified by the second-order coherence g^2:

$$g^2(\tau) = \frac{\langle \hat{a}^\dagger(t)\hat{a}^\dagger(t+\tau)\hat{a}(t+\tau)\hat{a}(t)\rangle}{\langle \hat{a}^\dagger(t)\hat{a}(t)\rangle^2}, \tag{IV.20}$$

which is measured with a Hanbury, Brown and Twiss experiment [Brown and Twiss, 1956]. In that experiment, the field of interest is split into two spatial paths by a beam-splitter and the intensity correlation is measured on two detectors. τ corresponds to the delay time between the measured clicks of two detectors and t is a given reference time. Theoretically, $g^2(0) = 1 - 1/n$ where n is the number of photons, and it is equal to zero for a single-photon source. It is imperative to have the lowest $g^2(0)$ as possible for quantum application, to minimize the errors in quantum computation and simulation. Using the integrated waveguide [Belhassen et al., 2018], this factor is equal to $g^2(0) = 0.12$. Other devices can certainly have a lower $g^2(0)$ as mentioned in the next paragraph. But for the applications given in this thesis, we will be interested by the full pair and their spectral correlation.

Other platforms can create single-photons, as quantum dots in micro-pillar cavities which produce them with a highest purity $g^2(0) = 0.0028 \pm 0.0012$. But it is at the cost of working at low

temperature (4K) [Senellart et al., 2017] and with the additional difficulty of collecting the photons, which reduce the brightness of the single-photons. Another device which produces single-photons is the nitrogen vacancy centers in nano-diamond for instance see Ref. [Rodiek et al., 2017]. The ultimate goal for quantum computation is to create a source array producing identical single-photons. It was experimentally demonstrated that 20 identical pure single-photons can be produced using heralded single photon sources achieved using spontaneous four-wave mixing on a silica chip [Spring et al., 2017]. For quantum technology applications, it is important to have identical pure states. Indeed, the photon-photon interaction needed for two-photon gates lay on the purity of the controlled-photon into the other one. If the controlled-photon is in a mixed state, then it will create unwanted errors during quantum computation.

IV.2 Time-frequency continuous variable entanglement: Simon's criterion

States of continuous variables systems belong to a large Hilbert space and the characterization of entanglement is difficult to handle. A general CVs state is characterized by an infinite number of moments. We then restrict to Gaussian states which are fully characterized by their first and second moments and their entanglement are more easily characterized. This restriction in this subclass of CV states is not a limitation since they are useful in quantum computing and in quantum communication protocols.

The algebra of quadrature position-momentum variables possesses similar properties than the time-frequency one of single-photons, as explained in Chap. III. This mathematical analogy allows to use criteria developed in quadrature position-momentum variables to prove the separability of a bipartite state for a time-frequency biphoton state (see Eq.. (II.17) for the definition of separability).

The Simon's criterion [Simon, 2000] is a necessary and sufficient condition for bipartite Gaussian state entanglement and can be used to assess the presence of entanglement of time-frequency Gaussian states. We will directly explain and translate this criterion with the set of time-frequency continuous variables. In our context, the prefix "bi" refers to two photons present into two different modes and the Gaussianity refers that the moments of the chronocyclic Wigner distribution $W_{\hat{\rho}}(\omega_1, t_1, \omega_2, t_2)$ higher than two is zero. The Simon's criterion can be seen as a generalization of the Peres-Horodecki criterion [Peres, 1996], which is a necessary and sufficient condition for 2×2 and 2×3 dimensional system to be separable. If the eigenvalues of the partial transpose (with respect to any system) of $\hat{\rho}$ are non-negative, then the bipartite system is separable.

The equivalent operation of the partial transpose on one subsystem (let say the first one) when one consider not discrete but continuous variable is a reflection of the chronocyclic Wigner

distribution such as $W(\omega_1, t_1, \omega_2, t_2) \rightarrow W(-\omega_1, t_1, \omega_2, t_2)$. The covariance matrix changes as $V \rightarrow \Lambda^{-1} V \Lambda$, where $\Lambda = \mathrm{diag}(-1, 1, 1, 1)$. After the reflection a separable state fulfills the condition:

$$V + \frac{i}{2}\Lambda^{-1} J \Lambda \geq 0. \tag{IV.21}$$

The negativity of one of the eigenvalues of Eq. (IV.21) is a necessary and sufficient condition for Gaussian entanglement and constitute the Simon's criterion. The Heisenberg inequality $V + iJ/2 \geq 0$ after the reflection reads otherwise (see Eq. (19) in [Simon, 2000]). This criterion is now applied to characterize frequency entanglement of the biphoton state produced by SPDC placed in free space, since the state is a time-frequency Gaussian one.

First case: elliptical JSA A general joint spectral amplitude can be written as:

$$\mathrm{JSA}(\omega_s, \omega_i) = \frac{\Delta^{1/4}}{\pi^{1/2}} e^{-\frac{(\omega_p - \omega_s - \omega_i)^2}{4}} e^{-\frac{\Delta^2(\omega_s - \omega_i)^2}{4}}, \tag{IV.22}$$

where we have set $\Delta = \frac{\Delta\omega_p}{\delta\omega}$ which is the ratio between the frequency width of the energy conservation and the phase-matching condition. We now define the ellipticity by the ratio $E = \frac{1-\Delta^2}{1+\Delta^2}$. If the ellipticity is zero, the JSA is a circle and it is an ellipse in any others cases. The inverse of the covariance matrix is:

$$V^{-1} = \frac{1}{2}\begin{pmatrix} 1+\Delta^2 & 1-\Delta^2 & 0 & 0 \\ 1-\Delta^2 & 1+\Delta^2 & 0 & 0 \\ 0 & 0 & \frac{1+\Delta^2}{\Delta^2} & \frac{\Delta^2-1}{\Delta^2} \\ 0 & 0 & \frac{\Delta^2-1}{\Delta^2} & \frac{1+\Delta^2}{\Delta^2} \end{pmatrix}. \tag{IV.23}$$

For an elliptical JSA, the ellipticity is different than zero and the parameter $\Delta \neq 1$. The covariance matrix V is found numerically. The matrix $V + \frac{i}{2}\Lambda^{-1} J \Lambda$ has four eigenvalues. They are all positive or equal to zero for a null ellipticity. The first and the third eigenvalues are positive (resp. negative) for $\Delta \leq 0$ and negative (resp. positive) for $\Delta \geq 0$ (see Fig. IV.6).

When the ellipticity is zero, or when $\Delta = 1$, the JSA is circular. In that case, the covariance matrix is proportional to the identity, all the variances being equal. Hence the covariance matrix corresponds to a bipartite time-frequency coherent state (defined in details in Sec. V.1.1):

$$V = \frac{1}{2}\begin{pmatrix} 1 & 0 & 0 & 0 \\ 0 & 1 & 0 & 0 \\ 0 & 0 & 1 & 0 \\ 0 & 0 & 0 & 1 \end{pmatrix}. \tag{IV.24}$$

The Simon's criterion says that this state is separable, since the eigenvalues of $V + i\frac{\Lambda^{-1} J \Lambda}{2}$ are 0 or positive (see Fig. IV.6). Using Eq. (IV.24), we find the variances $(\Delta t)^2 = \frac{1}{2}$ and $(\Delta\omega)^2 = \frac{1}{2}$ and by consequence, we obtain $\Delta t . \Delta\omega = \frac{1}{2}$ which corresponds to the lower limit of the Heisenberg inequality, as it is for a time-frequency Gaussian state.

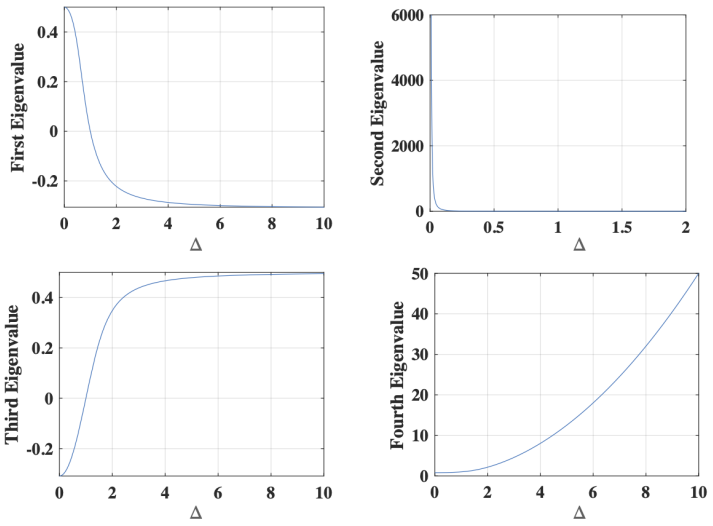

Figure IV.6: Eigenvalues of $V+i\frac{\Lambda^{-1}J\Lambda}{2}$. The second and the fourth eigenvalue are always positive, the third is negative for negative values of Δ and positive in the other case. For $\Delta = 1$, the eigenvalues are positive or equals to zero which means that the bipartite state is separable.

Elliptical JSA with a non-zero chirp For the sake of completeness, we introduce the effect of chirp, a quadratic time and frequency phase. The chirp is a time dependency of the instantaneous frequency of the optical signal and can be created by the chromatic dispersion and non-linearities due to the Ti-Sa crystal inside the cavity of the pump laser. This chirp brings new frequency correlation between the idler and the signal photon. Taking into account the chirp, the Joint spectral amplitude of the biphoton can be written as:

$$\mathrm{JSA}(\omega_s,\omega_i) = A\exp\left(-\frac{(\omega_s+\omega_i-\omega_p)^2}{4}\right)\exp\left(-\Delta^2\frac{(\omega_s-\omega_i)^2}{4}\right)\exp\left(-\frac{iC}{4}(\omega_s+\omega_i-\omega_p)^2\right), \tag{IV.25}$$

where A is a normalization factor obtained by normalization of the JSA and C is the chirp parameter. The inverse of the covariance matrix can be cast under the form:

$$V^{-1} = \frac{1}{2}\begin{pmatrix} 1+\Delta^2 & 1-\Delta^2 & C/2 & C/2 \\ 1-\Delta^2 & 1+\Delta^2 & C/2 & C/2 \\ C/2 & C/2 & \frac{1+\Delta^2}{\Delta^2} & \frac{\Delta^2-1}{\Delta^2} \\ C/2 & C/2 & \frac{\Delta^2-1}{\Delta^2} & \frac{1+\Delta^2}{\Delta^2} \end{pmatrix}. \tag{IV.26}$$

Chirp brings correlations between time and frequency, since $< t_s\omega_s > \neq 0$, $< t_s\omega_i > \neq 0$, $< t_i\omega_s > \neq 0$ and $< t_i\omega_i > \neq 0$. The eigenvalues of $V+i\frac{\Lambda^{-1}J\Lambda}{2}$ do not have an analytical expression and are found numerically. In Fig. IV.7, we display the four eigenvalues with respect to the chirp and the parameter Δ. This criterion does not answer the question of how much entanglement is brought by the chirp, other criteria have to be used for this purpose. But this example is presented as an additional example of our formalism. All the graphs of Fig. IV.6 are cuts at $C = 0$ of the graphs of Fig. IV.7.

Perspectives The criterion based on the entanglement of formation [Giedke et al., 2003] could also give a necessary and sufficient condition for the entanglement of time-frequency Gaussian

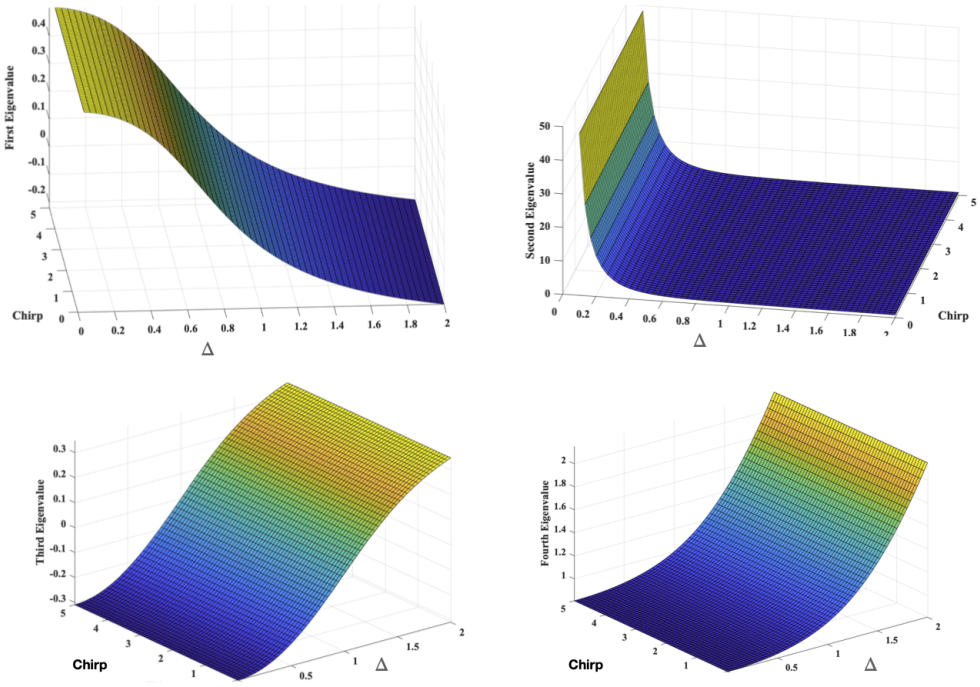

Figure IV.7: The first (resp. third) eigenvalue is negative (resp. positive) for an ellipticity inferior than one and is positive after. The second and the fourth are always positive. Even for a zero ellipticity and a non-zero chirp, the eigenvalues stay positive or zero.

states and is a witness for non-Gaussian time-frequency states, which are the quantum micro-comb for instance. But, in order to quantify the amount of entanglement, added by the chirp for instance, we have to use an entanglement measure such as the Schmidt decomposition.

IV.3 Quantifying entanglement using Schmidt decomposition

We now want to quantify the amount of entanglement between the signal and idler photons for different engineered spectrum by performing a Schmidt decomposition into the JSA. This mathematical tool can be used for a bipartite pure qudits system and not for a continuous one. Hence before introducing such decomposition, we explain how to express a continuous variable state into a discrete orthonormal one using the results presented in [Lamata and Leon, 2005].

IV.3.1 Decomposition into a set of orthogonal function

We can decompose the JSA by using two discrete and complete sets of orthogonal functions T_n of $L^2(\mathbb{R})$:

$$\mathrm{JSA}(\omega_s, \omega_i) = \sum_{n,m\in\mathbb{Z}^2} C_{n,m} T_n(\omega_s) T_m(\omega_i). \tag{IV.27}$$

The functions T_n verify two conditions, $\int T_n(\omega_s) T_m(\omega_s) d\omega_s = \delta_{n,m}$ and $\sum_m T_m(\omega) T_m(\omega') = \delta(\omega - \omega')$. The coefficients $C_{n,m}$ can be explicitly written as:

$$C_{n,m} = \langle n, m|\psi\rangle = \iint \mathrm{JSA}(\omega_s, \omega_i) T_n(\omega_s) T_m(\omega_i) d\omega_s d\omega_i, \tag{IV.28}$$

Then, the wave function is cast as:

$$|\psi\rangle = \sum_{n,m\mathbb{Z}^2} C_{n,m} |1_n\rangle |1_m\rangle , \tag{IV.29}$$

where the single photon state with spectrum T_n is:

$$|1_n\rangle = \int T_n(\omega_s) |\omega_s\rangle \, d\omega_s. \tag{IV.30}$$

The orthogonality condition is verified $\langle 1_n|1_m\rangle = \delta_{n,m}$ since the functions T_n are orthogonal. The Gaussian functions: $T_n(\omega_s) = \exp(-(\omega_s - n\Delta)^2/(2\sigma^2))$,·where σ is the width of the Gaussian and Δ the central frequency of the nth peak, are orthogonal when the condition $\Delta \gg \sigma$ is fulfilled. We can then numerically evaluate the matrix $C_{n,m}$ and perform the Schmidt decomposition of that matrix.

IV.3.2 Schmidt decomposition

We now introduce the Schmidt decomposition. A singular value decomposition is performed on the matrix $C_{n,m}$ which can be cast as $C = U\Lambda V$, where U and V are unitary matrices. It leads to the JSA:

$$\mathrm{JSA}(\omega_s, \omega_i) = \sum_{i=1}^{N} \lambda_i f_i(\omega_s) g_i(\omega_i), \tag{IV.31}$$

where the Schmidt coefficients $\lambda_i \in \mathbb{R}^+$ and since the JSA is normalized to one, we have $\sum_{i=1}^{N} |\lambda_i|^2 = 1$. The state is said to be separable when $\lambda_1 = 1$ and $\lambda_i = 0$ for $i \geq 2$. When $\lambda_1 \neq 1$ the state is said to be entangled. N is the number of truncated modes chosen such as $\lambda_i \geq 10^{-2}$. The Schmidt orthonormal functions are a linear combination of T_n: $f_i(\omega_s) = \sum_k U_{i,k} T_n(\omega_s)$ and $g_i(\omega_i) = \sum_k V_{k,i} T_m(\omega_i)$. The wave function can be finally written as:

$$|\psi\rangle = \sum_{n=1}^{N} \lambda_n |1_n\rangle_A |1_n\rangle_B , \tag{IV.32}$$

where $|1_n\rangle_A = \int d\omega_s f_n(\omega_s) |\omega_s\rangle$ and $|1_n\rangle_B = \int d\omega_i g_n(\omega_i) |\omega_i\rangle$.

We now define two entanglement quantifiers. The first is the Schmidt parameter

$$K = \frac{1}{\sum_i \lambda_i^4}, \tag{IV.33}$$

which describes the effective number of the populated eigenmodes. K is equal to one when the state is separable and is inferior to one otherwise. The inverse of K is related to the purity of a heralded single photon [Zielnicki et al., 2018] $P = \mathrm{Tr}(\hat{\rho}^2)$. The second is the Von-Neumann entropy:

$$S = -\sum_i \lambda_i^2 \ln(\lambda_i^2). \tag{IV.34}$$

For a separable state, the entropy is zero, which means that there is no acquired information when the mode 1 is observed. For an entangled state, the Von-Neumann entropy is then different from zero.

IV.3.3 Continuous variable Schmidt decomposition

It exists an alternative way to have directly the Schmidt decomposition from the JSA and to obtain both the Schmidt coefficients and the Schmidt modes functions. This technique was previously used by the experimental team of the QITE group [Orieux, 2012] and will be compared to the methods defined in the previous section. The Schmidt decomposition can be obtained by resolving the eigenvalues equation, or the kernel equation:

$$\iint d\omega_s d\omega_i \mathrm{JSA}(\omega_1, \omega_i)\mathrm{JSA}^*(\omega_i, \omega_s) = \lambda_n f_n(\omega_1), \tag{IV.35}$$

$$\iint d\omega_s d\omega_i \mathrm{JSA}(\omega_s, \omega_2)\mathrm{JSA}^*(\omega_s, \omega_i) = \lambda_n g_n(\omega_2), \tag{IV.36}$$

with again the normalisation condition for the Schmidt coefficients $\sum_{i=1}^{N} |\lambda_i|^2 = 1$. These equations are solved numerically with a singular value decomposition algorithm [Bogdanov et al., 2006], from which we access to λ_n, f_n, g_n. Only the significant values of the Schmidt modes are retained and we have chosen the condition $\lambda_n \geq 10^{-2}$ with a precision of 99 %. Both of the presented methods catch the phase of the Schmidt modes.

IV.3.4 Results

In this section, we present the Schmidt decomposition for a pure biphoton state for different values of ellipticity of the JSI and by taking into account the cavity effect when it is mentioned. The two introduced ways for obtaining the Schmidt decomposition of the JSA give the same values for the K parameter and the Von-Neumann entropy. In the case of an ellipticity of $E = 0.98$, the Schmidt modes basis in the two cases are the same, and it is verified numerically for the first four modes, with a fidelity of 0.99. It means that the solutions of the kernel equation (see Eq. (IV.35)) are actually Gaussian functions (see after Eq. (IV.15)). It can be understood because every function which composed the JSA is actually a Gaussian function. For different phase matching or cavity functions it can be otherwise. When we also consider the cavity effect, two subsequent Gaussian peak is chosen such as they are separated from one unit of frequency (normalized to the frequency width of the pump), and the frequency discretization of the JSA is chosen equal to 0.1.

The Schmidt decomposition is correct if the Schmidt coefficients converge to zero starting from a certain mode n. For that, the discretization length of the JSA has to be small enough. An equivalent statement is based on the entropy: from a higher value of the discretization length, we decrease this length until we arrive at a maximum value of entropy. When we arrive at this maximum, it means that the chosen discretization frequency length allows us to describe all the modes of the JSA.

IV.3.4.1 Schmidt decomposition of JSA with different ellipticity and zero chirp

***E* = 0.98** For such ellipticity, with or without the cavity, the Schmidt decomposition is the same (see Fig IV.8 (a) and (b)), and the Von Neumann entropy are identical in both cases

$S = 1.87$ bits. Despite that only integer multiples of the cavity can be emitted, the system keeps properties close to the continuous case, described by an infinitely high dimension Hilbert space. The cavity function is a separable function in frequency ω_s and ω_i and does not bring new frequency correlation. The first fourths modes $(f_i(\omega_s)g_i(\omega_i))_{1\leq i\leq 4}$ are represented in Fig. IV.9 without (a), (b), (c) and (d) and with (e), (f), (g), (h) the cavity functions. The forms of the modes functions are the same. In the first case, we see the increasing number of nodes 0, 1,2 and 3 for an increasing number of modes. The second case is the same but the Schmidt modes have been multiplied by mode functions.

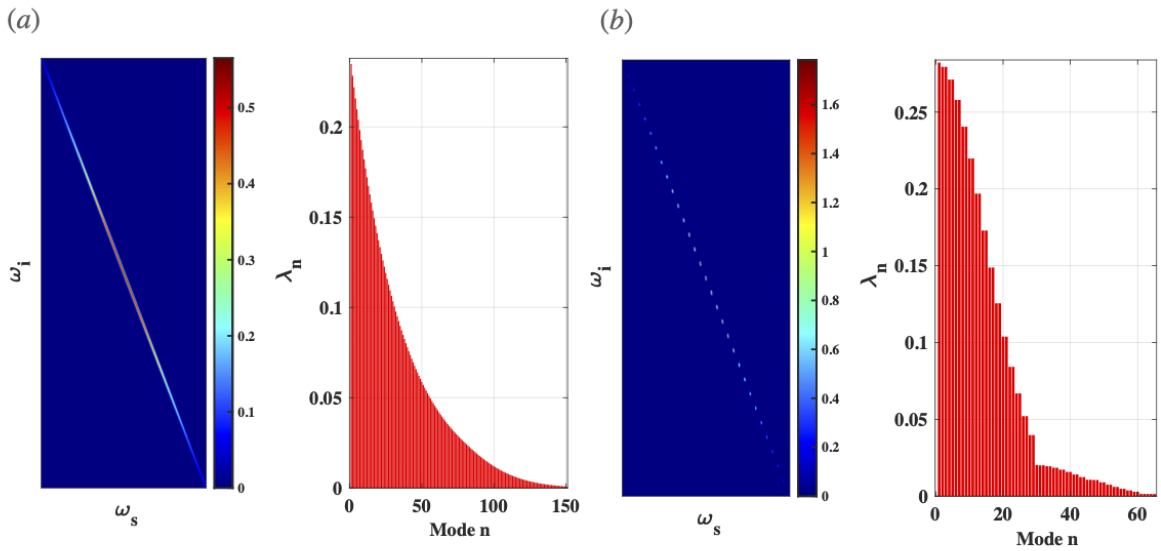

Figure IV.8: Joint spectral intensity with an ellipticity $E = 0.98$. and the associated Schmidt decomposition, without (on the left) and with the cavity effect (on the right).

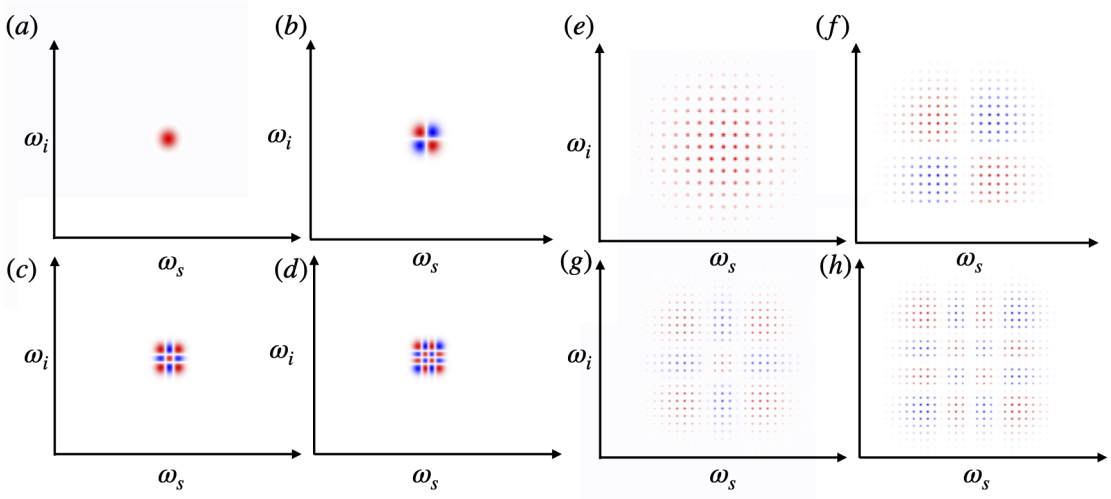

Figure IV.9: First fourth Schmidt modes for an ellipticity of $E = 0.98$. without (a), (b), (c) and (d) and with the cavity (e), (f), (g), (h). The scale is not the same in the two cases, a magnification has been applied on the right of the figure for a better visualization of the effect of the cavity.

$\boldsymbol{E = 0.99}$ For such ellipticity, the number of modes of the signal and idler photons is different if the cavity effect is taken into account. Indeed, the Von-Neumann entropy in the two cases

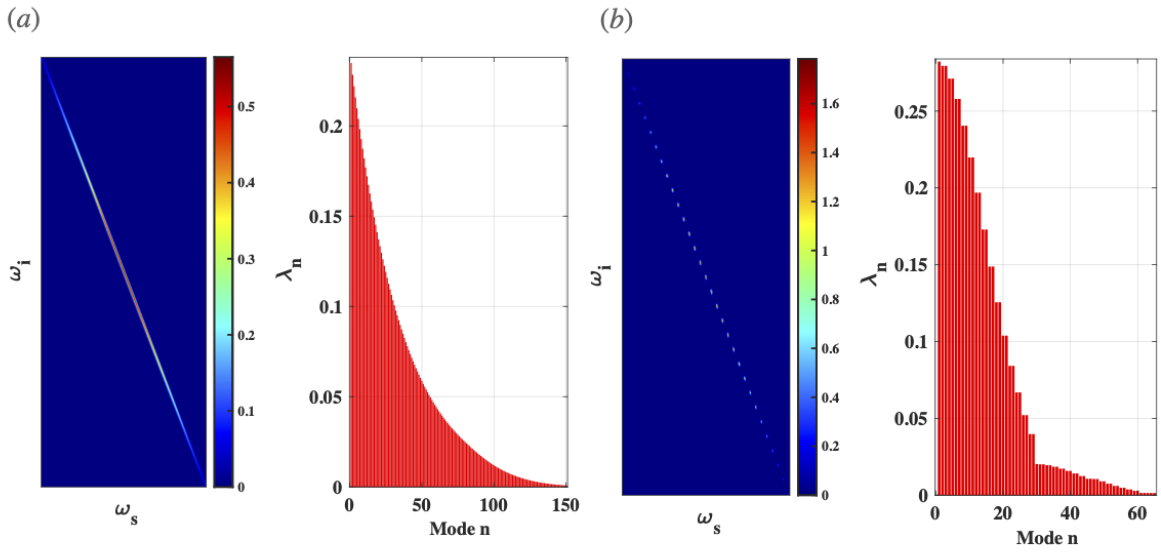

Figure IV.10: Joint spectral intensity with an ellipticity $E = 0.99$. and associated Schmidt decomposition. (a) without the effect of the cavity. (b) with the effect of the cavity. The number of modes increases from 13 to 180 when the ellipticity increases, which is a non-local operation.

is respectively $S_{\text{without cavity}} = 24.35$ bits and $S_{\text{with cavity}} = 8.12$ bits. This behavior is expected since the change in the ellipticity is a non-local operation in the frequency variables, the ellipse is "squeezed" along the ω_+ direction ($\omega_+ = \omega_s + \omega_i$ is a non-local variable) and extended along the ω_- direction.

In the presence of the cavity (see Fig IV.10(b)), each mode corresponds to one peak of the JSI. Also, we see a pairing phenomena: the central peak is alone and constitutes the first Schmidt mode, and then the two adjacent peaks form a pair and correspond to the second and third Schmidt mode which have the same amplitude. It allows to conclude that, as mentioned in Sec. IV.1.1, that the modes of the optical cavity impose the structure of the Schmidt functions.

In the absence of an optical cavity, we report in Fig. IV.11 (a) the values of the Von-Neumann entropy and the K factor. These quantities increase as the ellipticity reaches one. When the ellipticity goes to one, the state is a frequency EPR state.

IV.3.4.2 Adding time-frequency correlations with chirp

We do not consider the cavity effect in this section. We take into consideration the temporal chirp of the pump pulse, which brings new time-frequency correlation between the signal and idler photon [Brecht and Silberhorn, 2013]. This correlation cannot be seen by simple measurement of the JSI, but could be seen by measuring the full Wigner distribution or its crossed marginals. With a chirp different of zero, we expect to enhance the Schmidt number since the operation is not local in the collective variable ($\omega_s + \omega_i$) (see Eq. IV.25). We should notice that we have to be careful about the discretization since the number of Schmidt modes raise with the chirp. We decrease the discretization length until we reach a constant value of entropy. The

K parameter increases noticeably when the chirp increases when $\Delta \leq 1$ (see Fig. IV.11(b)), but remains constant when $\Delta \geq 1$. It can be interpreted by the fact that the chirp has an effect in the collective frequency variable ω_+.

Experimentally, we have only access to the measurement of the JSI = |JSA|. Then, we can apply the singular value decomposition to this last function which gives a lower bound to the Schmidt number [Eckstein et al., 2014].

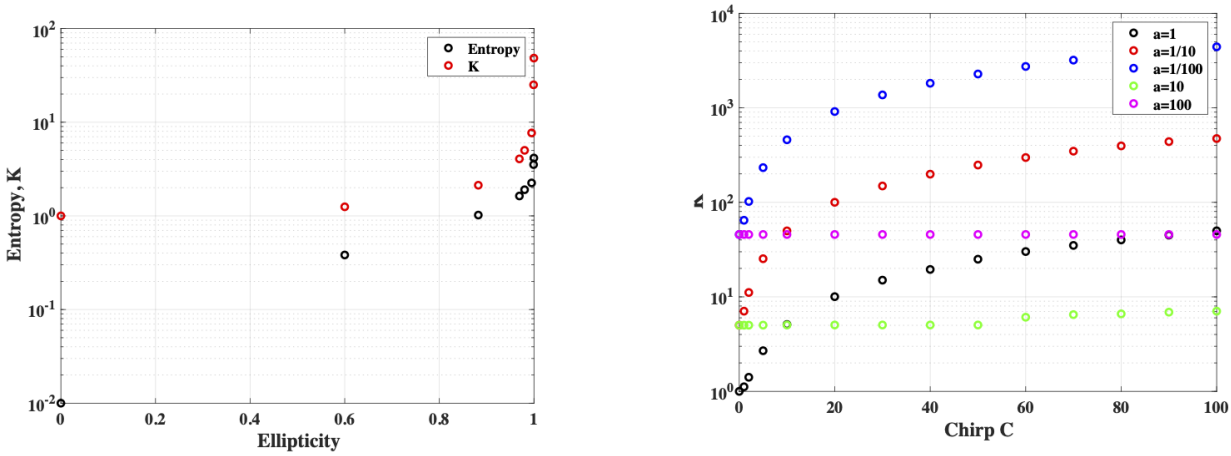

Figure IV.11: Evolution of the entropy and the K factor for different values of ellipticity. (b) Evolution of the entropy and the K factor with chirp for different values of ellipticity.

IV.4 The Hong, Ou and Mandel experiment

This section reviews the Hong, Ou and Mandel (HOM) experiment and how it can be used for a partial tomographic reconstruction of spectral distribution of a biphoton state. We also expose other experimental schemes to access different parts of the spectral distribution of a biphoton state, and explain the effect of the time-resolution of the detectors on the measurement result.

IV.4.1 Presentation of the experiment for different particle statistics

The Hong-Ou and Mandel experiment shows striking features of quantum optics and can be used to reveal different signatures of the statistics of quantum particles. We start by considering two indistinguishable particles, bosons, fermions or anyons, which impinges on a beam-splitter. They only differ in their spatial modes noted a and b, so the initial state of the two particles is:

$$|\psi\rangle = \hat{a}^\dagger \hat{b}^\dagger |0\rangle \,. \tag{IV.37}$$

Then the two particles impinge into a beam-splitter, modeled by the unitary matrix U acting on the spatial modes $U = \begin{pmatrix} t & r \\ r & t \end{pmatrix}$. r and t denote the reflection and the transmission coefficient related by the equation $|r|^2 + |t|^2 = 1$ which is a consequence of the energy conservation during the spatial separation of the particles. The beam-splitter (BS) is supposed to be balanced which

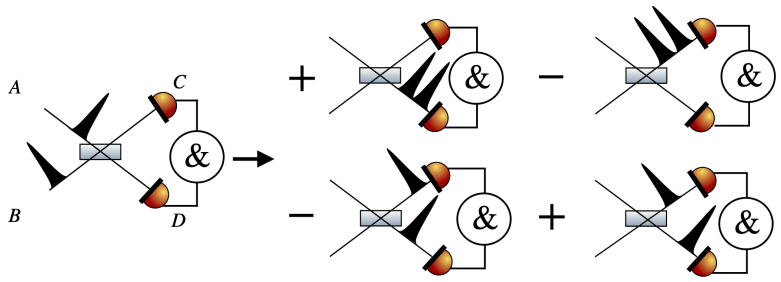

Figure IV.12: Sketch of the HOM experiment. Two indistinguishable particles depicted as black wavepacket are sent into the paths A and B. One of the particle is delayed of a time τ. After the beam-splitter, four possible cases are possible. Then coincidence measurement is performed, the only events recorded are those where there is one single photon at each spatial port C and D. The figure is extracted from [Fabre et al., 2020a].

means that $t = r = 1/\sqrt{2}$. The two particles state becomes after the BS:

$$|\psi\rangle = \frac{1}{2}((\hat{a}^\dagger)^2 + (\hat{b}^\dagger)^2 + \hat{a}^\dagger\hat{b}^\dagger - \hat{b}^\dagger\hat{a}^\dagger)\,|0\rangle\,. \tag{IV.38}$$

Two detectors are placed after the beam-splitter which allows to measure both single and coincidence counts. The measurement result depends on the statistics of the particles. If the particles are bosons, then the annihilation operators commute $\hat{a}^\dagger\hat{b}^\dagger = \hat{b}^\dagger\hat{a}^\dagger$ whereas if they are fermions, we have $\hat{a}^\dagger\hat{b}^\dagger = -\hat{b}^\dagger\hat{a}^\dagger$ and $(\hat{a}^\dagger)^2 = (\hat{b}^\dagger)^2 = 0$. For anyonic particle we have $\hat{a}^\dagger\hat{b}^\dagger = e^{i\phi}\hat{b}^\dagger\hat{a}^\dagger$, where ϕ is an angle. For $\phi = 0$ we recover the bosonic statistic and for $\phi = \pi$ we recover the fermionic one. For the three cases, the two-particles state after the beam-splitter is:

$$|\psi\rangle_B = \frac{1}{2}[(\hat{a}^\dagger)^2 + (\hat{b}^\dagger)^2]\,|0\rangle\,, \tag{IV.39}$$

$$|\psi\rangle_F = \hat{a}^\dagger\hat{b}^\dagger\,|0\rangle\,, \tag{IV.40}$$

$$|\psi\rangle_A = \frac{1}{2}[(\hat{a}^\dagger)^2(1+e^{i\phi}) + (\hat{b}^\dagger)^2(1+e^{i\phi}) + \hat{a}^\dagger\hat{b}^\dagger(1-e^{i\phi})]\,|0\rangle\,. \tag{IV.41}$$

Bosons bunche with equal probability when the beam-splitter is balanced either on spatial port C or on spatial port D. The coincidence probability is then zero and only single counts are recorded. This particle behavior is a pure quantum effect with no classical analogue. For bosons, this effect is visible when the particles are indistinguishable, because there is no way to say from which paths they came.

On the contrary, fermions antibunch which means that the coincidence probability is not zero and single counts are not recorded (see Eq. IV.40). The anyonic signature is quite different: we register both coincidence and single counts with probability $1/4(1-e^{i\phi})^2$ and $1/4(1+e^{i\phi})^2$ respectively (see Eq. (IV.41)). We will not analyze further the anyonic case and was just given for completeness.

We have only considered as a degree of freedom of the photon pair their spatial paths, namely the two arms of the interferometer. A time-delay in one arm of the interferometer can be added

which is a factor of indistinguishability of the two wavepackets which impinge on the beam-splitter. The coincidence probability as a function of the time delay τ is added in one arm of the interferometer before the beam-splitter, is a factor of indistinguishability. Such probability will exhibit a characteristic continuous dip when the photons are indistinguishable at $\tau = 0$, that smoothly disappears when τ moves away from zero. But more generally, photons distinguishability depends on several degree of freedom, as polarization, temporal mode [Ansari et al., 2017] and spectral mode [Sharapova et al., 2015].

IV.4.2 Study of the influence of the time-resolution on the coincidence probability

In this section, we explain the influence of the time-resolution of the photodetectors on the expression of the coincidence probability [Fabre et al., 2020a, Legero et al., 2006], which is a matter of importance for the HOM experiment described later.

The probability to measure one photon on a spatial port noted C at time t_1 and one photon at the port D at time t_2 (see Fig. IV.12 for instance) is given by the second order correlation function:

$$G^2(t_1, t_2, \tau) = \mathrm{Tr}(\overline{\hat{\rho}}(\tau)\hat{c}^\dagger(t_1)\hat{d}^\dagger(t_2)\hat{d}(t_2)\hat{c}(t_1)), \tag{IV.42}$$

where τ is the photon delay between the two arms of the interferometer. $\hat{c}(t_1)$ denotes the creation photon operator at time t_1 in the spatial port C. $\overline{\hat{\rho}}(\tau)$ is the state on the detector. The temporal size of the single photon wavepacket is noted δt. Any photodetector has a finite resolution T. Experimentally, we access to the probability to detect one photon in the interval $t_0 \pm T$ and the second in the interval $t_0' \pm T$:

$$I(t_0, t_0', \tau) = \int_{t_0-T}^{t_0+T} dt_1 \int_{t_0'-T}^{t_0'+T} dt_2 G^2(t_1, t_2, \tau). \tag{IV.43}$$

When $T \gg \delta t$, the range of the integral can be extended to the infinity and we obtain:

$$I(\tau) = \iint dt_1 dt_2 G^2(t_1, t_2, \tau). \tag{IV.44}$$

The coincidence probability can be rewritten as:

$$I(\tau) = \iint dt_1 dt_2 \iint dt_3 dt_4 \left\langle t_3, t_4 \right| \overline{\hat{\rho}}_\tau \hat{c}^\dagger(t_1)\hat{d}^\dagger(t_2)\hat{d}(t_2)\hat{c}(t_1) \left| t_3, t_4 \right\rangle. \tag{IV.45}$$

By applying the bosonic operators and after integration, the coincidence detection is $I(\tau) = \iint dt_1 dt_2 \left\langle t_1, t_2 \right| \hat{\rho}_\tau \left| t_1, t_2 \right\rangle$ which can be written alternatively, for a pure state $\overline{\hat{\rho}}_\tau = \left|\overline{\psi}_\tau\right\rangle \left\langle\overline{\psi}_\tau\right|$ using the closure relation:

$$I(\tau) = \iint d\omega_s d\omega_i \left|\left\langle\overline{\psi}_\tau\middle|\omega_s, \omega_i\right\rangle\right|^2. \tag{IV.46}$$

Looking at this last equation, it is equivalent to consider that the frequency response of the detectors is flat.

The coincidence probability in the case where $\delta t \gg T$ is this time:

$$I(\tau, \overline{\tau}) = \int G^2(t_0, t_0 + \overline{\tau}, \tau) dt_0, \tag{IV.47}$$

where t_0 is the time of the first detection which is integrated, τ being the optical delay between the two arms and the time-difference between two detections is noted $\overline{\tau}$. This result will be used in Sec. V.3.4.

IV.4.3 Generalized HOM experiment

From now on, we are in the non-time resolved limit. The HOM experiment is now described by taking into account the spectral and temporal degrees of freedom, as well as the spatial (or polarization) path one [Douce et al., 2013]. An initial wave function described by $|\psi\rangle = \iint d\omega_s d\omega_i \mathrm{JSA}(\omega_s, \omega_i) |\omega_s\rangle |\omega_i\rangle$ is generated by SPDC for the photonic case. The two particles of the pair after their generation are separated into two different paths where in the upper (resp. lower) path is placed a time delay τ (resp. a frequency shifter ν). The name of the generalized HOM experiment comes from the addition of a frequency shifter. The state becomes:

$$|\psi_{\mu,\tau}\rangle = \hat{D}(\mu, \tau) |\psi\rangle = \iint d\omega_s d\omega_i e^{i\omega_i \tau} \mathrm{JSA}(\omega_s + \mu, \omega_i) |\omega_s\rangle |\omega_i\rangle . \tag{IV.48}$$

The photon pair is then recombined into a balanced beam-splitter and the wave function is:

$$|\overline{\psi}_{\mu,\tau}\rangle = \frac{1}{2} \iint d\omega_s d\omega_i e^{i\omega_i \tau} \mathrm{JSA}(\omega_s + \mu, \omega_i) [\hat{a}^\dagger(\omega_s)\hat{a}^\dagger(\omega_i) - \hat{b}^\dagger(\omega_s)\hat{b}^\dagger(\omega_i) - \hat{a}^\dagger(\omega_s)\hat{b}^\dagger(\omega_i) + \hat{b}^\dagger(\omega_s)\hat{a}^\dagger(\omega_i)] |0\rangle . \tag{IV.49}$$

After the post-selection on the coincidence, the wave function $|\overline{\psi}_{\mu,\tau}\rangle_C$ can be written as,

$$|\overline{\psi}_{\mu,\tau}\rangle_C = \frac{1}{2} \iint d\omega_s d\omega_i [\mathrm{JSA}(\omega_s + \mu, \omega_i) e^{i\omega_i \tau} \mp \mathrm{JSA}(\omega_i + \mu, \omega_s) e^{i\omega_s \tau}] |\omega_s, \omega_i\rangle \tag{IV.50}$$

where the sign $\mp$ refers to bosonic or fermionic statistics. For a non-time resolved coincidence detection, the coincidence probability, which is now a function of the time delay and the frequency shift, can be now written:

$$I(\mu, \tau) = \frac{1}{2} [1 \mp \iint d\omega_s d\omega_i e^{2i\omega_- \tau} \mathrm{JSA}(\omega_s + \mu, \omega_i) \mathrm{JSA}^*(\omega_i + \mu, \omega_s)]. \tag{IV.51}$$

We take the example of a symmetric JSA, which means that under particle exchange we have the property: $\mathrm{JSA}(\omega_s, \omega_i) = \mathrm{JSA}(\omega_i, \omega_s)$ and set the frequency shift to zero $\mu = 0$. In Fig. IV.13, we represent coincidence probability of the bosons (blue) and the fermions (orange) choosing a Gaussian phase matching function. A dip and an anti-dip are observed for bosons and fermions at $\tau = 0$ as in the previous section. But as the optical path delay increases in absolute value the coincidence probability becomes zero and no longer quantum effect is observed.

The single count on port A and B for bosons particles, label by the subscript S can be written

$$|\psi_{\mu,\tau}\rangle_S = \frac{1}{2} \iint d\omega_s d\omega_i e^{i\omega_i \tau} \mathrm{JSA}(\omega_s + \mu, \omega_i) \hat{a}^\dagger(\omega_s) \hat{a}^\dagger(\omega_i) |0\rangle , \tag{IV.52}$$

$$|\psi_{\mu,\tau}\rangle_S = \frac{1}{2} \iint d\omega_s d\omega_i e^{i\omega_i \tau} \mathrm{JSA}(\omega_s + \mu, \omega_i) \hat{b}^\dagger(\omega_s) \hat{b}^\dagger(\omega_i) |0\rangle , \tag{IV.53}$$

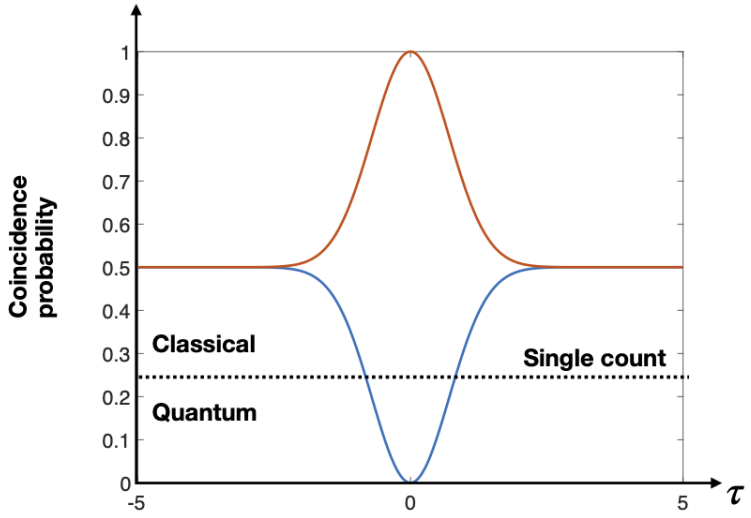

Figure IV.13: Coincidence probability of Gaussian (symmetric) function of bosons (blue) and fermions (orange) as a function of the delay time (with arbitrary units), which exhibits a dip and an anti-dip respectively. The dashed line for $I(\tau) = 1/4$ indicates the lower bound of classical fields.

and the single count probability $I_S = \iint d\omega_s d\omega_i \left|\langle \omega_s, \omega_i | \psi_{\mu,\tau} \rangle_S\right|^2$ does not depend on τ. The intensity is then 1/4 in the two cases and is represented by a dashed line in Fig. IV.13. For fermionic particles, the wavefunction of single count is zero for a symmetric spectrum as it is expected for such statistics.

Some particular values of the coincidence probability are physically meaningful. A coincidence probability below 1/4 can not be achieved with classical a field as demonstrated in [Ou et al., 1990] or in other words, a visibility larger than 50%. Using the manipulation of photonic degrees of freedom, such as the transverse spatial modes and polarization [Walborn et al., 2003], one can also use this anti-bunching process, revealed by an anti-dip with a coincidence probability above 1/2, that can be associated with a fermionic-like behavior [Francesconi et al., 2020] and is also an entanglement witness [Autebert et al., 2015, Douce et al., 2013, Eckstein and Silberhorn, 2008, Fedrizzi et al., 2009].

Case of a mixture From now on, we will consider only bosonic particles. The HOM experiment is also used for measuring the indistinguishability M of two single-photons [Senellart et al., 2017] produced by two different sources. The overlap between two single photon after they cross in a beam-splitter can be obtained by measuring the visibility of the HOM defined by: $V = (I_{\max} - I_{\min})/I_{\max}$. If the beam-splitter is balanced then we have $M = V$, which is now shown.

We investigate the case of two separable single-photons which are all in a frequency mixture for the sake of completeness. These two photons are obtained experimentally by heralding of two SPDC sources. A signature of the indiscernability of single-photons can be obtained by HOM interferometry. Indeed after the heralding of one photon of a pair, let us say the idler

photon labeled by the index i, the reduced density matrix is $\hat{\rho} = \mathrm{Tr}_i(|\psi\rangle\langle\psi|)$ and can be further written as:

$$\hat{\rho} = \iint \mathrm{JSA}(\omega_s, \omega_i)\mathrm{JSA}(\omega_s', \omega_i) |\omega_s\rangle \langle\omega_s'| \, d\omega_s d\omega_s' d\omega_i. \tag{IV.54}$$

After making a Schmidt decomposition of the JSA: $\mathrm{JSA}(\omega_s, \omega_i) = \sum_i \lambda_i f_i(\omega_s) g_j(\omega_i)$, the density matrix is now:

$$\hat{\rho} = \sum_{i,j} \lambda_i \lambda_j^* \int f_i(\omega_s) d\omega_s |\omega_s\rangle \int f_j^*(\omega_s') d\omega_s' \langle\omega_s'| \int g_i(\omega_i) g_j^*(\omega_i) d\omega_i. \tag{IV.55}$$

Since the Schmidt mode functions are orthogonal, then we have $\int g_i(\omega_i) g_j^*(\omega_i) d\omega_i = \delta_{i,j}$, and the reduced density matrix is hence:

$$\hat{\rho} = \sum_i |\lambda_i|^2 \int f_i(\omega_s) d\omega_s |\omega_s\rangle \int f_i^*(\omega_s') d\omega_s' \langle\omega_s'| \tag{IV.56}$$

and can not written as: $\hat{\rho} \neq |\psi\rangle\langle\psi|$ and is a mixed state $\hat{\rho} = \sum_i \alpha_i |\psi_i\rangle\langle\psi_i|$, with $|\psi_i\rangle = \int f_i(\omega_s) d\omega_s |\omega_s\rangle$ and $\alpha_i = |\lambda_i|^2$. In order to obtain a pure state after the heralding of the idler (or the signal), the JSA must be circular which corresponds to only one Schmidt mode.

The full density matrix of the two heralded single-photons can be cast under the form: $\hat{\rho} = \hat{\rho}_1 \otimes \hat{\rho}_2$ where $\hat{\rho}_{1/2}$ are under the form Eq. (IV.56). Hence the density matrix is $\hat{\rho} = \sum_{i,j} \alpha_i \beta_j |\psi_i\rangle\langle\psi_i| \otimes |\psi_j\rangle\langle\psi_j|$, where $|\psi_i\rangle \otimes |\psi_j\rangle = \iint d\omega_s d\omega_i f_i(\omega_s) g_j(\omega_i) |\omega_s, \omega_i\rangle$. The coincidence probability evaluated at the chronocyclic phase space point $(0,0)$ is:

$$I(0,0) = \frac{1}{2}(1 - \sum_{i,j} \alpha_i \beta_j \iint d\omega_s d\omega_i f_i(\omega_s) g_j(\omega_i) f_i^*(\omega_i) g_j^*(\omega_s)). \tag{IV.57}$$

If the state is pure, the coincidence probability is simply the overlap between the two single-photons spectrum:

$$I(0,0) = \frac{1}{2}(1 - \left| \int d\omega f(\omega) g^*(\omega) \right|^2). \tag{IV.58}$$

We now present some particular cases. If the single-photons are indistinguishable then $f = g$ and we recover the dip $I(0,0) = 0$. If the two photons are partially distinguishable, which means that they are not perfectly orthogonal $\int d\omega f(\omega) g^*(\omega) \neq 0$, then the dip does not reach the zero value. In the case of the mixture Eq. (IV.57) and if the single photon are indistinguishable then $f = g$, the coincidence probability is also zero according to the normalization condition $\sum_i |\lambda_i|^2 = 1$.

To conclude, we have seen that the measurement of coincidence probability allows to have a signature of the distinguishability of two single-photons.

IV.4.4 Measurement of the chronocyclic Wigner distribution of a photon pair

In the following we present alternative techniques for measuring the amplitude frequency distribution of a biphoton state, without the measurement of the marginals of the chronocyclic

Wigner distribution [MacLean et al., 2019] or by modulating the spectral phase of the single-photons [Beduini et al., 2014]. The presented techniques are based on HOM interferometry. In this section, we consider non-time resolved detectors.

IV.4.4.1 Measurement of the chronocyclic Wigner distribution W_-

We consider a photon pair produced by a type-II source, whose the JSA is assumed to be factorized as follows: $\mathrm{JSA}(\omega_s, \omega_i) = f_+(\omega_+)f_-(\omega_-)$. Hence, the associated chronocyclic Wigner distribution can be decomposed as $W_{\hat{\rho}}(\omega_s, t_s, \omega_i, t_i) = W_+(\omega_+, t_+)W_-(\omega_-, t_-)$, where:

$$W_\pm(\omega_\pm, t_\pm) = \int d\omega e^{2i\omega t_\pm} f_\pm^*(\omega_\pm + \omega) f_\pm(-\omega_\pm + \omega). \tag{IV.59}$$

Using Eq. (IV.51), the coincidence probablity $I(\mu, \tau)$ can be written as:

$$I(\mu,\tau) = \frac{1}{2}[1 - \mathrm{Re}(A \cdot \int d\omega_- e^{2i\omega_-\tau} f_-^*(\omega_- + \mu) f_-(-\omega_- + \mu))] = \frac{1}{2}(1 - A \cdot W_-(\mu,\tau)), \tag{IV.60}$$

where $A = \int d\omega_+ |f_+(\omega_+)|^2$ which does not depend on μ and τ. The measurement of the coincidence probability by varying both the frequency shift and the time delay allows to perform the full reconstruction of $W_-(\mu,\tau) = \mathrm{Tr}(\hat{\rho}_- \hat{D}^\dagger(\mu,\tau)\hat{\Pi}\hat{D}(\mu,\tau))$ distribution. In addition, if f_+ can be approximated by a Dirac distribution as it is the case for the integrated device described in Sec. IV.1.3, this technique allows the full tomography of the spectral amplitude of the biphoton state, since in that case the JSI is one dimensional along the ω_- direction.

The non-time resolved HOM experiment is a Gaussian measurement, since from a Gaussian phase-matching function input, we obtain a Gaussian output. We obtain directly point in the chronocylic phase space. Hence, for the tomographical reconstruction of the phase-matching function, there is no post-calculation to perform. It looks as the PNR detection in Sec. II.4.6 which allows accessing the histogram $\langle n|\,\hat{\rho}\,|n\rangle$. Then the average value of the parity (or the displaced one) operator is calculated afterward in a post-processing operation. PNR measurement does not measure phase space points and constitutes the crucial difference between these two experiments.

IV.4.4.2 Measurement of the chronocyclic Wigner distribution W_+

Information along the ω_+ axis of the JSI can not be obtained using only HOM interferometry, and another interferometric scheme has to be proposed to measure the W_+ function defined by Eq. (IV.59). We propose in this section an experimental scheme to measure the Chronocyclic Wigner distribution W_+, defined by Eq. (IV.59). Measuring this function for a device producing photons pairs with a Joint spectral distribution written as $\mathrm{JSA}(\omega_s, \omega_i) = f_+(\omega_+)f_-(\omega_-)$ allows to make the full tomographical reconstruction of the state, by adding the HOM experiment.

An initial state described by the wavefunction $|\psi\rangle = \iint d\omega_s d\omega_i \mathrm{JSA}(\omega_s, \omega_i)\,|\omega_s\rangle\,|\omega_i\rangle$, where the signal and idler photons are assumed to be produced by a type-II SPDC, have horizontal and vertical polarization and are in spatial port A/D. They have initially different polarization,

but they can be separated into two spatial paths using a PBS. The second step of the optical scheme consists in splitting each photon into two spatial paths noted A,B for the signal photon and C, D for the idler photon. The initial state $|\omega_s, \omega_i\rangle_{A,D}$ after the second step can be written as:

$$|\omega_s, \omega_i\rangle_{A,D} \rightarrow \frac{1}{2}(|\omega_s, 0\rangle_{A,B} - |0, \omega_s\rangle_{A,D})(|\omega_i, 0\rangle_{C,D} - |0, \omega_i\rangle_{C,D}). \tag{IV.61}$$

Then, two $\lambda/2$ waveplates are placed in port B and C, such as the single-photons in port A and C (resp. B and D) have horizontal polarization (resp. vertical). In the third step, we add time-frequency displacement operations in the four spatial ports which are specified in Fig. IV.14. They are explicitly $(\tau, \nu/2)$ in port A and C, $(-\tau, -\nu/2)$ in port B and D. Again, it can be realized with linear optical element for the time displacement (optical path delay) and with a non-linear element for the frequency displacement (EOM). The state Eq. (IV.61) becomes after these operations:

$$\begin{aligned}\frac{1}{2}(\Big|\omega_s + \frac{\nu}{2}, 0, \omega_i + \frac{\nu}{2}, 0\Big\rangle e^{i\tau\omega_+} - \Big|\omega_s + \frac{\nu}{2}, 0, 0, \omega_i - \frac{\nu}{2}\Big\rangle e^{i\omega_-\tau} \\ + \Big|0, \omega_s - \frac{\nu}{2}, \omega_i + \frac{\nu}{2}, 0\Big\rangle e^{-i\omega_-\tau} - \Big|0, \omega_s - \frac{\nu}{2}, 0, \omega_i - \frac{\nu}{2}\Big\rangle e^{-i\tau\omega_+})\end{aligned} \tag{IV.62}$$

The fourth step is to recombine the four spatial ports with a PBS. Horizontal photons are reflected while vertical photons are transmitted. The resulting state after the PBS is:

$$\begin{aligned}\frac{1}{2}(\Big|\omega_s + \frac{\nu}{2}, \omega_i + \frac{\nu}{2}\Big\rangle_{A,D} e^{i\tau\omega_+} - \Big|\omega_s + \frac{\nu}{2}, \omega_i - \frac{\nu}{2}; 0\Big\rangle_{A,D} e^{i\omega_-\tau} \\ + \Big|0; \omega_s - \frac{\nu}{2}, \omega_i + \frac{\nu}{2}\Big\rangle_{A,D} e^{-i\omega_-\tau} - \Big|\omega_i - \frac{\nu}{2}, \omega_s - \frac{\nu}{2}\Big\rangle_{A,D} e^{-i\omega_+\tau}).\end{aligned} \tag{IV.63}$$

After all these steps represented in Fig. IV.14, the full wave function, taking into account only the coincidence, can be written as:

$$|\psi\rangle_{\tau,\nu} = \frac{1}{2}\iint \mathrm{JSA}(\omega_s, \omega_i)(\Big|\omega_s + \frac{\nu}{2}, \omega_i + \frac{\nu}{2}\Big\rangle_{A,D} e^{i\tau\omega_+} - \Big|\omega_i - \frac{\nu}{2}, \omega_s - \frac{\nu}{2}\Big\rangle_{A,D} e^{-i\omega_+\tau}) d\omega_s d\omega_i \tag{IV.64}$$

Decomposing the JSA as $\mathrm{JSA}(\omega_s, \omega_i) = f_+(\omega_+)f_-(\omega_-)$ and by performing a change of variable inside the integral, we obtain:

$$|\psi\rangle_{\tau,\nu} = \frac{1}{2}\iint (f_+(\omega_+ - \nu)f_-(\omega_-)e^{i\tau(\omega_+ - \nu)} - f_+(\omega_+ + \nu)f_-(-\omega_-)e^{-i\tau(\omega_+ + \nu)}) \, |\omega_s, \omega_i\rangle_{A,C} \, d\omega_s d\omega_i \tag{IV.65}$$

The obtention of such wave function was the aim of all these operations: contrary to the HOM experiment, the phase depends on ω_+ and only the f_+ function are affected by the time-frequency displacement operations. The polarization of single-photons in the D arm can be again rotated of 90° to have the same polarization in the two arms. The coincidence measurement for a non-resolved time detection gives:

$$I(\tau, \nu) = \frac{1}{2}[1 - \mathrm{Re}(\int f_-(\omega_-)f_-^*(-\omega_-)d\omega_- \int f_+(\omega_+ - \nu)f_+^*(\omega_+ + \nu)e^{2i\omega_+\tau}d\omega_+)] \tag{IV.66}$$

Hence, we recognize the chronocyclic Wigner distribution W_+ and we can finally write:

$$I(\tau, \nu) = \frac{1}{2}(1 - B \cdot W_+(\tau, \nu)), \tag{IV.67}$$

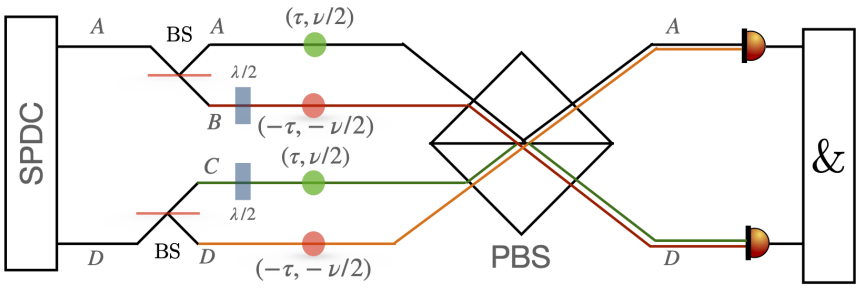

Figure IV.14: Sketch of the measurement of the chronocyclic Wigner distribution W_+. PBS stands for polarizing beam-splitter. Type II SPDC produced photon pairs with orthogonal polarization which are separated in two arms A and D. Successives operations are performed and a final coincidence measurement is done.

where $B = \mathrm{Re}(\int d\omega_- f_-(\omega_-) f_-^*(-\omega_-))$ is constant which does not depend on μ and τ. The mathematical expression which relates the coincidence probability and W_+ is the same as in the generalized HOM experiment (see Eq. (IV.60)).

IV.4.4.3 Rotation of the Wigner distribution

We discuss a method to perform a fractional Fourier transform in frequency-time variable based on an experimental technique that can be implemented on a chip in transverse pump configuration [Boucher et al., 2015, Orieux et al., 2013]. We will work in the non time-resolved detection limit $\delta t \gg T$ [Fabre et al., 2020a].

The aim of this section is to provide the analogous phase gate in position-momentum variable $\hat{P}(\theta) = \exp(i\theta\hat{X}^2)$ (where θ is the rotation angle and $\hat{X}$ is the position operator) in the collective frequency-time variable (ω_-, τ) of the biphoton state. We propose a solution using the integrated optical circuit described in Sec. IV.5 and [Autebert et al., 2015] by engineering the phase matching function so as to perform a rotation in the frequency-time phase space.
If the length of the circuit is much larger than the spatial width of the pump profile, the phase matching function is the Fourier transform of the spatial profile of the pump $A(z)$ [Autebert et al., 2015, Boucher et al., 2015]:

$$f_-(\omega_-) = \int_{\mathbb{R}} A(z) e^{i\omega_- z/v_g} dz, \tag{IV.68}$$

where v_g is the group velocity and z is the direction of the propagation of the two photons. According to [Boucher et al., 2015] and Eq. (IV.68) the spatial profile of the pump is the rescaled Fourier transform of the phase matching function $\tilde{f}(t_-) = A(t_- v_g)$. The adapted spatial profile to perform the rotation in the frequency-time phase space is:

$$A(z) = e^{-\frac{z^2}{2\Delta z^2}} e^{iz^2/a^2}, \tag{IV.69}$$

where Δz is the spatial width of the pump. The term e^{iz^2/a^2} can be obtained using a spatial light modulator (SLM) to produce a quadratic spatial phase with a curvature a that can be

experimentally controlled and varied. It can be viewed as a time chirp owing to the relation Eq. (IV.68). This frequency-time gate can also be considered as a time lens [Patera et al., 2018]. The chronocyclic Wigner distribution of the phase matching function is modified as follows:

$$W_{-}(\omega_{-},\tau) \rightarrow W_{-}(\omega_{-} - \tau\frac{v_g^2}{a^2},\tau). \tag{IV.70}$$

Since the coincidence probability is the measurement of the cut at $\omega_{-} = 0$ of the Wigner distribution, this solution enables the measurement of the full distribution without a frequency shift but rather by controlling the parameter a. Then, changing the value of a and repeating the OM experiment by varying τ, we can measure different cuts of the chronocyclic Wigner distribution corresponding to different frequency values.

For integrated or bulk optical system, this phase gate can be realized with a grating, which maps the frequency to spatial degree of freedom followed by a SLM and then another grating to return in the frequency domain [Mazzotta et al., 2016].

Chapter V

Generation and manipulation of single photon time-frequency state

This chapter introduces different single photon time-frequency states whose mathematical structure is the same as the ones defined in position-momentum quadrature variables. Experimental proposals for manipulating them and detect the signature of this manipulation, using for instance the HOM interferometer, are discussed.

V.1 Zoology of time-frequency states

First, let us remind that the considered time here is not the proper time of the photon but the time measured by an ancilla quantum clock (see Chap. III.2.3.2). Nevertheless, to lighten the notation, we will not repeat each time that we are considering the single photon state entangled with the quantum clock.

V.1.1 Coherent-like state in time-frequency continuous variable

Following the analogies between the pairs quadrature position-momentum and frequency-time variables, the coherent-like state in time-frequency variable corresponds to a single-photon with a Gaussian spectrum:

$$|\psi\rangle = \int d\omega e^{-(\omega-\omega_1)^2/(2\Delta\omega^2)} e^{i\omega\tau} |\omega\rangle = \left|\frac{\omega_1}{\Delta\omega} + i\Delta\omega\tau\right\rangle, \tag{V.1}$$

where ω_1 and τ are two parameters representing the average value of the chronocyclic Wigner distribution and $\Delta\omega$ is the spectral width of the Gaussian spectrum. We remind that a quadrature position-momentum coherent state can be written in the position basis $|\alpha = x_\alpha + ip_\alpha\rangle = |x_\alpha, p_\alpha\rangle = \int dx e^{-(x-x_\alpha)^2/2} e^{ixp_\alpha} |x\rangle$. As in the usual phase-space representation, the coherent-like state also forms an overcomplete basis as do not form an orthogonal basis:

$$\langle\omega_0, \tau_0|\omega_1, \tau_1\rangle = e^{-(\tau_0-\tau_1)^2\Delta\omega^2/4} e^{-(\omega_0-\omega_1)^2/4\Delta\omega^2} e^{i(\tau_0-\tau_1)(\omega_0+\omega_1)/2}. \tag{V.2}$$

The time-frequency like coherent state is also useful to build time-frequency Husimi and P-distribution as defined before, since such distributions are usually expressed in the coherent basis (see Sec. III.3.4) and can be useful for the tomography of single photon detectors (see the

conclusion of this chapter).

The physical interpretations of the coherent and coherent-like frequency time state are very different. The coherent state $|x_0, p_0\rangle$, also noted $|\alpha\rangle$ with $\mathrm{Re}(\alpha) = x_0$ and $\mathrm{Im}(\alpha) = p_0$, is the eigenvector of the annihilation operator $\hat{a}$ with the corresponding complex eigenvalue α. $|\alpha|^2$ is the average value of the photon number operator $\langle \hat{n} \rangle = \langle \hat{a}^\dagger \hat{a} \rangle$ of the monomode multi-photon field. The free evolution trajectory in the quadrature position-momentum phase space of a coherent state is a circle, a rotation of angle ωt induced by the Hamiltonian evolution $U(t) = e^{i\omega t(\hat{a}^\dagger \hat{a} + 1/2)}$, as mentioned in Chap. II.

For the coherent-like time-frequency state, the average value of the photon number is one, since the state is a single photon. The trajectory of its free evolution in time-frequency phase space is a translation along the time axis since such evolution is described by a time displacement operator. The denomination "coherent" in that case is not related to the photon number statistics of the state, which is sub-Poissonian for single photons but only due to the mathematical analog structure.

Also, close to the origin of the chronocyclic phase space, the frequencies are the radio one and are far from the regime that we consider in this thesis. We remind that we suppose the support of the distribution of the wave function centered at THz frequency and respect the narrowband condition (see Sec. III.2.2). The discussion of radiofrequency single photons and what happens for single photons at negative energy is irrelevant in our study and is beyond the framework of this thesis. The interpretation of the time-frequency coherent state (for short) as the displaced time-frequency vacuum state is our regime not relevant.

The aim of these remarks is to highlight the main physical differences between these two states, despite their mathematical analogies.

V.1.2 Time-frequency cat state

We define the time-frequency cat state as a single-photon state having a frequency distribution composed of two peaks centered around the frequencies $\omega_p + \omega_1$ and $\omega_p - \omega_1$ [Fabre et al., 2020a]. The corresponding wave function can be expressed as:

$$|\psi\rangle = \frac{1}{\sqrt{2}}\left(\int d\omega (f_{\omega_p+\omega_1}(\omega)e^{i\omega\tau} + f_{\omega_p-\omega_1}(\omega)e^{-i\omega\tau}\,|\omega\rangle\right) = \frac{1}{\sqrt{2}}(|\omega_p+\omega_1, \tau\rangle + |\omega_p - \omega_1, -\tau\rangle), \quad \text{(V.3)}$$

where $f_{\pm\omega_1}(\omega)$ is a Gaussian function centered at $\omega_p \pm \omega_1$ of width $\Delta\omega$. This definition is analogous to the usual Schrödinger cat state in position-momentum phase space (x, p), defined as the linear superposition of two macroscopically distinguishable coherent states $|\psi\rangle = \frac{1}{\sqrt{2}}(|\alpha\rangle + |-\alpha\rangle)$. The chronocyclic Wigner distribution of the time-frequency cat state is composed of three

terms:

$$W_-(\omega_-,\tau) = W_{\text{cat}}(\omega_-,\tau) = W_{12}(\omega_-,\tau) + W_{21}(\omega_-,\tau) + W_{\text{beating}}(\omega_-,\tau). \tag{V.4}$$

The first and second terms are Gaussian functions centered at $\omega_- = \omega_1 \mp \omega_2$ and $\tau = 0$:

$$\begin{aligned} W_{12}(\omega_-,\tau) &= \int d\omega' e^{2i\omega'\tau} f_{\omega_1-\omega_2}(\omega_- + \omega') f^*_{\omega_1-\omega_2}(-\omega' + \omega_-) \\ &= e^{-\tau^2\sigma^2} e^{-(\omega_- - (\omega_1+\omega_2))^2/\sigma^2}. \end{aligned} \tag{V.5}$$

The interference term has the form:

$$W_{\text{beating}}(\omega_-,\tau) = \int e^{2i\omega'\tau}(f_{\omega_1-\omega_2}(\omega_-+\omega') f^*_{\omega_2-\omega_1}(-\omega'+\omega_-) + f_{\omega_2-\omega_1}(\omega_-+\omega') f^*_{\omega_1-\omega_2}(-\omega'+\omega_-))d\omega'. \tag{V.6}$$

The chronocyclic Wigner distribution of this state is shown in Fig. V.9(c) and is the same as the Wigner distribution of a cat state in quadrature position-momentum variables (see Fig. II.5 (d)).

For the following discussion, let us change variables from the frequency one to the energy one in order to be more transparent in the presence of $\hbar$ when one considers a single photon field and not a classical field. The time-energy cat state is confined in an area in time-energy phase space $A = E \cdot T \gg \hbar$, which is the case in most experiments that we consider in this thesis. The time-energy phase space is paved with rectangles of area $\hbar/2$, according to the Heisenberg type inequality in these variables (see Eq. (III.20)). Hence, the time-energy cat state has structures in time-frequency phase space less than $\hbar$, called sub-Planck structures. As soon as the distance between the pulses is large enough, the areas smaller than the Sub-Planck equal to $\hbar/2$ grow. Such effect was also investigated for intense laser field [Austin et al., 2010]. But in this paper [Austin et al., 2010], the experiment is not performed in the quantum regime, so that the relation $E = \hbar\omega$ does not hold. In that case, the interference pattern created by the coherent superposition of two classical fields can not be understood as the one obtained for time-energy cat state. In the single photon regime, one could consider as perspectives to use such sub-Planck structures for quantum metrology as in [Toscano et al., 2006], since they are related to the Heisenberg-limited sensitivity to perturbations.

Such time-frequency cat-like state was introduced in [Boucher et al., 2015] along with experimental proposals to generate them using the non-collinear integrated waveguide described in Sec. IV.1.4. This time-frequency cat state, also called two-color photon state, was used for estimating time parameters to measure the thermal dilatation of an optical fiber [Chen et al., 2019] in an optical bulk circuit for instance. Time-frequency compass states which are coherent superpositions of four Gaussian spectrum states centered at four different points in chronocyclic phase space could in principle be produced using the transversally pumped integrated device [Boucher et al., 2015].

V.1.3 Time-frequency GKP state

In the following, we introduce the time-frequency grid state, also called the time-frequency GKP state and its application for quantum time-frequency error correction. Such state will be also called micro-comb, owing to its frequency comb structure but the adjective micro denotes that only one or two single photons are measured in a given detection event.

The grid state was first defined using quadrature position-momentum continuous variables [Duivenvoorden et al., 2017, Gottesman et al., 2001] and corresponds to a two-dimensional lattice in phase space where the area of the unit cell is a multiple of 2π. The time-frequency grid state also verifies this property, as periodic structures formed by the superposition of many modes and containing a single photon. Such states are mathematically equivalent to the quadrature position-momentum one's due to the non-commutative algebra of both time-frequency and quadrature position-momentum displacement operators.

More precisely (see [Fabre et al., 2020c]), the time-frequency grid state is defined as a common eigenstate with the eigenvalue $+1$ of the two commuting operators $\hat{D}(\omega)$ and $\hat{\mathcal{D}}(t)$ when the product of the two parameters verify $\omega t = 0 \mod 2\pi$. This property allows us to measure both time and frequency modulo 2π. The wave function of a general grid state can be written as:

$$|\psi\rangle = \sum_{n\in\mathbb{Z}} \left|\sqrt{\pi}(2n+\mu)\right\rangle_\omega , \tag{V.7}$$

where μ is an integer. The $+1$ eigenspace of the displacement operators is two-dimensional and allows to define a qubit taking for instance the values $\mu = 0$ and 1. It is developed in more detail in the following paragraph.

V.1.3.1 Ideal time-frequency GKP state

We start by providing the general framework to define single photon GKP states with many frequency modes. For such, we dichotomize the frequency mode space as follows: the two possible states of the qubit are the eigenstates (up to normalization) of the displacement operator $\hat{D}(2\overline{\omega}, 0)$, $\hat{\mathcal{D}}(\frac{2\pi}{2\overline{\omega}})$, the stabilizer of the code:

$$\left|\overline{0}\right\rangle_\omega = \sum_{n\in\mathbb{Z}} \left|\frac{\omega_p}{2} + 2n\overline{\omega}\right\rangle , \tag{V.8}$$

$$\left|\overline{1}\right\rangle_\omega = \sum_{n\in\mathbb{Z}} \left|\frac{\omega_p}{2} + (2n+1)\overline{\omega}\right\rangle . \tag{V.9}$$

In the above, $\overline{\omega}$ is the periodicity of the state and $\omega_p/2$ is the central frequency of the comb (see Fig. V.1). These states are called frequency-time square GKP states, because the time-frequency phase space representation of these states are square [Albert et al., 2018]. For simplicity, we will call them time-frequency GKP states.

Alternatively, as we show in Fig. V.1, we can use the time representation of the GKP states, (up to normalization):

$$\left|\overline{0}\right\rangle_\omega = \tau_{rt} \sum_{n\in\mathbb{Z}} e^{i\frac{\omega_p}{2}\frac{n\tau_{rt}}{2}} \left|\frac{n\tau_{rt}}{2}\right\rangle = \left|\overline{+}\right\rangle_t , \tag{V.10}$$

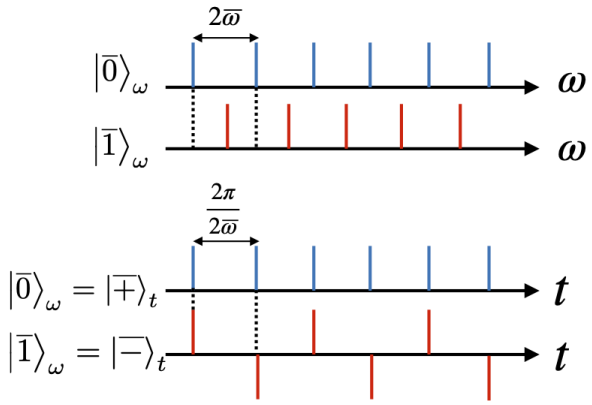

Figure V.1: Ideal frequency-time GKP state in the frequency and time basis. The figure is extracted from [Fabre et al., 2020c].

$$|\overline{1}\rangle_\omega = \tau_{rt} \sum_{n\in\mathbb{Z}} e^{i\frac{\omega_p}{2}\frac{n\tau_{rt}}{2}} (-1)^n \left|\frac{n\tau_{rt}}{2}\right\rangle = |\overline{-}\rangle_t \,, \tag{V.11}$$

where $\tau_{rt} = \frac{2\pi}{\overline{\omega}}$. We have used the equality $\sum_{n\in\mathbb{Z}} e^{2in\pi t/\tau_{rt}} = \tau_{rt} \sum_{n\in\mathbb{Z}} \delta(t - n\tau_{rt})$. We choose a system of units such that $\exp(i\frac{\omega_p}{2}\frac{n\tau_{rt}}{2}) = 1$: only in this case we can define a qubit as defined in the previous section. The $|\overline{0}\rangle_t, |\overline{1}\rangle_t$ logical time GKP state, eigenvectors of the stabilizer of the time displacement operator $\hat{\mathcal{D}}(0, \tau_{rt})$, are then (up again to normalization):

$$\begin{aligned} |\overline{0}\rangle_t &= \tau_{rt} \sum_{n\in\mathbb{Z}} \left|\frac{2n\tau_{rt}}{2}\right\rangle = |\overline{+}\rangle_\omega \,, \\ |\overline{1}\rangle_t &= \tau_{rt} \sum_{n\in\mathbb{Z}} \left|\frac{(2n+1)\tau_{rt}}{2}\right\rangle = |\overline{-}\rangle_\omega \,. \end{aligned} \tag{V.12}$$

Since the stabilizer $\hat{D}(\overline{\omega})$ translates the frequency by $\overline{\omega}$ and $\hat{\mathcal{D}}(0, \tau_{rt})$ translates the time by $2\pi/\overline{\omega}$, the code is designed to protect against shifts of values:

$$\begin{aligned} |\Delta\omega| &< \overline{\omega}, \\ |\Delta t| &< \pi/\overline{\omega}. \end{aligned} \tag{V.13}$$

The frequency-time phase space representation of the frequency-time GKP state is analogous to the GKP state in the (x, p) phase plane [Gottesman et al., 2001]. The wave function of the coherent superposition $|\psi\rangle = |\overline{+}\rangle_\omega$, for which the spectrum is $S(\omega) = \sum_{n\in\mathbb{Z}} \langle\omega|n\overline{\omega}\rangle = \sum_{n\in\mathbb{Z}} \delta(\omega - n\overline{\omega})$ possesses the following chronocyclic Wigner distribution:

$$\begin{aligned} W_{|\overline{+}\rangle_\omega\langle\overline{+}|_\omega}(\omega, t) &= \frac{1}{\pi} \int_{\mathbb{R}} d\omega' e^{2i\omega' t} S(\omega - \omega') S^*(\omega + \omega') \\ &= \frac{1}{\pi} \sum_{n,m\in\mathbb{Z}^2} (-1)^{nm} \delta(t - \frac{\pi}{\overline{\omega}} n) \delta(\omega - \frac{\omega_p}{2} - \frac{\overline{\omega}}{2} m). \end{aligned} \tag{V.14}$$

Experimentally, we have seen that the Hong-Ou and Mandel (HOM) interferometer allows to measure the cut of the chronocyclic Wigner distribution along the frequency axis [Douce et al., 2013] in the collective variable (ω, t) of a two photon pair. When the chronocyclic Wigner distribution is negative, namely when n, m are both odds, the HOM trace exhibits a dip above one half, which is a sufficient condition for entanglement.

V.1.3.2 Physical frequency-time GKP state

The time-frequency GKP states are not physical since we are summing over an infinite number of perfectly well defined frequency (or time) monochromatic modes. In this section, we will see how to formally describe physical (intrinsically noisy) time-frequency GKP states and how to physically interpret their number of peaks and the uncertainty of each mode. For that, we apply the formalism introduced in [Glancy and Knill, 2006].

Physical time-frequency GKP states are constructed by applying a Kraus-like operator $\hat{\xi}$ to the ideal time-frequency GKP state:

$$\left|\tilde{0}\right\rangle_{\omega} = \hat{\xi}\left|\overline{0}\right\rangle_{\omega} = \iint d\omega dt \xi(\omega,t)\hat{\mathcal{D}}(t)\hat{D}(\omega)\left|\overline{0}\right\rangle_{\omega}. \tag{V.15}$$

If we suppose that frequency and time noise are uncorrelated Gaussian distribution, we have that: $\xi(\omega,t) = G_{\delta\omega}(\omega)G_{\kappa}(t) = e^{-\omega^2/2\delta\omega^2}e^{-t^2/2\kappa^2}$. The physical interpretation of these two Gaussian noises becomes clearer after performing the time integral in Eq. (V.15), which leads to:

$$\left|\tilde{0}\right\rangle_{\omega} = \sum_{n\in\mathbb{Z}} \int T_{2n}(\omega)e^{-\omega^2\kappa^2/2}\left|\omega\right\rangle d\omega, \tag{V.16}$$

with $T_n(\omega) = \exp(-(\omega - n\overline{\omega})^2/(2\delta\omega^2))$ and we have used $\hat{\mathcal{D}}(t)\hat{D}(\omega)\left|\overline{0}\right\rangle_{\omega} = \sum_n e^{it(n\overline{\omega}+\omega)}\left|2n\overline{\omega}+\omega\right\rangle$. In our terminology, time noise creates an envelope, limiting the number of relevant frequency modes while frequency noise introduces an intrinsic width to each peak. Alternatively, we can construct the physical GKP state by permuting the time and frequency displacement operators. Since they are non-commuting operators, the state obtained by this procedure is not the same as Eq. (V.16). Such physical time-frequency GKP states are represented in Fig. V.2 (a).

For quadrature position-momentum GKP states, the Kraus operator applied on ideal GKP state [Glancy and Knill, 2006, Motes et al., 2017] models the finite width (which correspond to the finite amount of squeezing or its inherent noise) of each position peak and of the total envelope. Here, our Kraus-like operator modeled the bandwidth of the frequency peaks and the total envelope of the single photon state but could also be used to describe the bandwidth of a coherent state. In both cases -quadrature position-momentum variable for a multiphoton field or time-frequency degree of freedom of single photon- the Kraus operators are unitary and do not alter the purity of the state.

The physical origin of the finite width of the time and frequency distribution is considered in our formalism as errors that can be due to the propagation of single photons in a dispersive medium, as an optical fiber (see Fig. V.2 (b)). The effect of such an error is inducing bit-flips, since there is a probability to detect the one logical state, while the state is a zero logical one. Errors can also be related to time and frequency uncertainties inherent to the state preparation process.

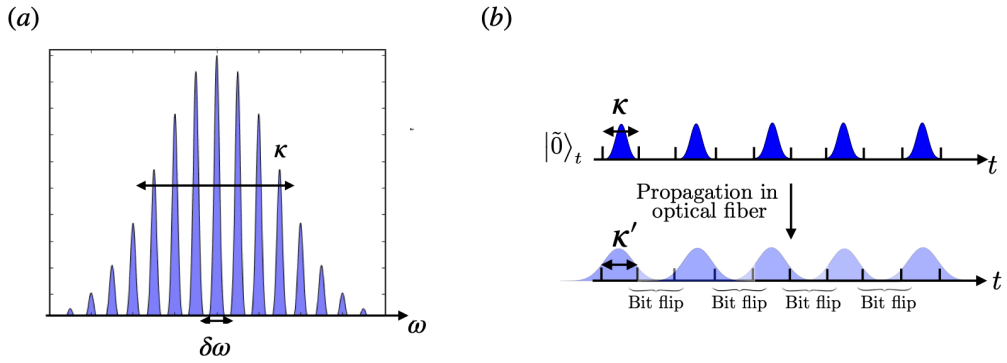

Figure V.2: (a) Physical frequency-time GKP state $|\tilde{0}\rangle_\omega$ in the frequency basis. (b) Effect of temporal broadening due to second order dispersive effect to the state $|\tilde{0}\rangle_t$, which can be considered as a bit-flip error in this encoding.

V.1.4 Mathematical description of 2D entangled time-frequency GKP state and time-frequency MBQC

In this section, we introduce 2D entangled time-frequency GKP states and show how they can be used to implement single-qubit gates and error correction [Fabre et al., 2020c, Menicucci, 2014].

We would like to transmit a qubit A, information which is encoded by a photon called the signal. A second qubit B is encoded by a second photon called the idler. We will show that qubit B can be used to correct errors in qubit A using a protocol in the same spirit of MBQC in quadrature position-momentum continuous variables (see Sec. II.4.7). First we create a continuous variable time-frequency entangled state, a so-called cluster state. Then we perform a single qubit measurement on the ancilla qubit B. Finally, a conditioned Gaussian type operation is performed on the remaining qubit, in order to reduce the time-frequency noise. We now introduce the basic notion of time-frequency continuous variable cluster state, which is motivated further by the experimental case studied in Sec. VII.4.

V.1.4.1 Preparation of a two-linear cluster state concatenated by GKP state

We start by considering an ideal separable two photon state, a two dimensional GKP state, that can be written as:

$$|\overline{+}\rangle_{\omega_s}|\overline{+}\rangle_{\omega_i} = \frac{1}{2}(|\overline{0}\rangle_{\omega_s}|\overline{0}\rangle_{\omega_i} + |\overline{0}\rangle_{\omega_s}|\overline{1}\rangle_{\omega_i} + |\overline{1}\rangle_{\omega_s}|\overline{0}\rangle_{\omega_i} + |\overline{1}\rangle_{\omega_s}|\overline{1}\rangle_{\omega_i}), \tag{V.17}$$

where the first/second qubit will be called the data and ancilla qubits respectively. Physical qubits can be constructed using the noise model introduced previously, and Kraus operators models frequency noises:

$$|\psi\rangle = \iint \hat{D}_{\mathrm{s}}(\omega)\hat{D}_{\mathrm{i}}(\omega')G_{\delta\omega}(\omega)G_{\delta\omega}(\omega')d\omega d\omega' \,|\overline{+}\rangle_{\omega_s}|\overline{+}\rangle_{\omega_i}\,. \tag{V.18}$$

The state has an intrinsic width for each peak of the grid, but does not have a finite envelope. For certain states produced experimentally, the time noise of the two photon state is correlated.

Frequency (or time) entanglement can be modeled as being produced by a symmetric CNOT operator $\hat{C}'$, (see [Parker et al., 2000] for its analogous in the quadrature of one mode of the electromagnetic field), which entangled the two photons:

$$\hat{C}' \left|t_s, t_i\right\rangle = \left|t_s + t_i\right\rangle \left|t_s - t_i\right\rangle . \tag{V.19}$$

This gate can also be interpreted as the action of a balanced beam-splitter that acts on the time degree of freedom. Indeed, we remind that the control-NOT gate $\hat{C}$ acts on the position quadrature $|x, y\rangle$ as follows $\hat{C}\,|x, y\rangle = |x + y, x - y\rangle$, and corresponds to the transform of a balanced beam-splitter. An example of possible photonic experimental realization is presented in Sec. VII.4. Another way to see the effect of this entangling operator is to apply it to the time displacement operator:

$$\hat{C}'\hat{\mathcal{D}}_{\mathrm{s}}(t)\hat{\mathcal{D}}_{\mathrm{i}}(t')\hat{C}'^{-1} = \hat{\mathcal{D}}_{\mathrm{s}}(\frac{t+t'}{2})\hat{\mathcal{D}}_{\mathrm{i}}(\frac{t-t'}{2}). \tag{V.20}$$

Since the time displacement operator and the entanglement gate do not commute, such operators ordering have to be taken into account. For this reason, we consider two types of entangled frequency-time GKP states which come from two different time-frequency noise models. The first one corresponds to applying the $\hat{C}'$ gate to the separable two dimensional described by Eq. (V.18) which gives the following wave function $|\psi\rangle_1 = \hat{C}' \left|\tilde{+}\right\rangle_\omega \left|\tilde{+}\right\rangle_\omega$. After performing a frequency change of variable, we obtain:

$$\begin{aligned} |\psi\rangle_1 = \iint dt dt' \hat{\mathcal{D}}_{\mathrm{s}}(t)\hat{\mathcal{D}}_{\mathrm{i}}(t') G_{1/\Delta\omega_p}(t) G_{1/\Delta\omega_-}(t') \\ \times \iint \hat{D}_{\mathrm{s}}(\omega)\hat{D}_{\mathrm{i}}(\omega') G_{\delta\omega_s}(\omega+\omega') G_{\delta\omega_i}(\omega-\omega') d\omega d\omega' \left|\overline{+}\right\rangle_{\omega_s} \left|\overline{+}\right\rangle_{\omega_i} . \end{aligned} \tag{V.21}$$

Hence, we showed that it is equivalent to apply the time-frequency beam-splitter gate $\hat{C}'$ on the separable 2D GKP state $\left|\tilde{+}\right\rangle_\omega \left|\tilde{+}\right\rangle_\omega$ or to start with frequency Gaussian correlated distribution for the two photons. After applying the time-frequency displacement operator and by integration on the time variable, the wave function becomes:

$$|\psi\rangle_1 = \iint d\omega_s d\omega_i G_{\Delta\omega_p}(\omega_+) G_{\Delta\omega_-}(\omega_-) G_{\delta\omega}(\omega_+) G_{\delta\omega}(\omega_-) \left|\omega_s, \omega_i\right\rangle . \tag{V.22}$$

The associated JSI of the state described by Eq. (V.22) is an ellipse elongated along the ω_+ or ω_- if $\Delta\omega_p < \Delta\omega_-$ or $\Delta\omega_- < \Delta\omega_p$ and is composed of circular cavity peaks of radius $\delta\omega$. This construction is analogous to the first step of a MBQC protocol, namely the construction of an entangled state (see Sec. II.4.7).

We now consider the second model of time-frequency noise. First, single-Kraus operators modeling the uncorrelated frequency noise between the signal and the idler is applied on the

ideal time-frequency GKP state: $|\psi\rangle = \iint \hat{D}_{\rm s}(\omega)\hat{D}_{\rm i}(\omega')G_{\delta\omega}(\omega)G_{\delta\omega}(\omega')d\omega d\omega' \left|\overline{+}\right\rangle_{\omega_s}\left|\overline{+}\right\rangle_{\omega_i}$. After applying the frequency displacement operator, we obtain the wave function:

$$|\psi\rangle = (\iint G_{\delta\omega}(\omega)G_{\delta\omega}(\omega')d\omega d\omega')\sum_{n,m}|n\overline{\omega}+\omega\rangle\left|m\overline{\omega}+\omega'\right\rangle. \tag{V.23}$$

The entangling gate described by Eq. (V.20), which equivalently corresponds to a correlated time noise, is then applied on the previous state:

$$|\psi_2\rangle = (\iint \hat{\mathcal{D}}_{\rm s}\left(\frac{t+t'}{2}\right)\hat{\mathcal{D}}_{\rm i}\left(\frac{t-t'}{2}\right)G_{1/\Delta\omega_p}(t)G_{1/\Delta\omega_-}(t')dtdt')\,|\psi_1\rangle. \tag{V.24}$$

The time displacement operators are then applied:

$$\begin{aligned}|\psi_2\rangle = &\iint G_{1/\Delta\omega_p}(t)G_{1/\Delta\omega_-}(t')dtdt'\iint G_{\delta\omega}(\omega)G_{\delta\omega}(\omega')d\omega d\omega'\\ &\times\sum_{n,m}e^{i(n\overline{\omega}+\omega)(t+t')/2}e^{i(m\overline{\omega}+\omega)(t-t')/2}\,|n\overline{\omega}+\omega\rangle\left|m\overline{\omega}+\omega'\right\rangle.\end{aligned} \tag{V.25}$$

We then integrate over the time variables, using the Fourier transform of Gaussian function:

$$\int dtG_{1/\Delta\omega_p}(t)e^{i((n+m)\overline{\omega}+\omega+\omega')t/2} = G_{\Delta\omega_p}(\frac{(n+m)\overline{\omega}+\omega+\omega'}{2}). \tag{V.26}$$

We thus obtain the following wave function:

$$\begin{aligned}|\psi_2\rangle = &\iint d\omega d\omega'\sum_{n,m}G_{\Delta\omega_p}(\frac{(n+m)\overline{\omega}+\omega+\omega'}{2})G_{\delta\omega}(\omega)G_{\delta\omega}(\omega')\\ &\times G_{\Delta\omega_-}(\frac{(n-m)\overline{\omega}+\omega-\omega'}{2})\,|n\overline{\omega}+\omega\rangle\left|m\overline{\omega}+\omega'\right\rangle.\end{aligned} \tag{V.27}$$

A final frequency variables change gives:

$$|\psi_2\rangle = \iint G_{\Delta\omega_p}(\omega_+)G_{\Delta\omega_-}(\omega_-)G_{\delta\omega}(\omega-n\overline{\omega})G_{\delta\omega}(\omega'-m\overline{\omega})d\omega d\omega'\,|\omega\rangle\left|\omega'\right\rangle. \tag{V.28}$$

All the steps described previously are presented in the quantum circuit in Fig. V.3(a). The gate ordering is chosen to obtain a special entangled GKP state which is the one produced experimentally in [Francesconi et al., 2020], where the envelope G is a function of the collective variable $\omega_\pm$ and the frequency noise distribution T_n of the local variable $\omega_{s/i}$.

It is interesting to notice that in the case where $G_{\Delta\omega_p}(\omega_+) = \delta(\omega_+)$ and $\overline{\omega}/\delta\omega \ll 1$, we can approximate $|\psi\rangle = \widetilde{|\overline{+}\rangle\,|\overline{+}\rangle} \simeq \hat{C}'\left|\tilde{+}\right\rangle\left|\tilde{+}\right\rangle$ where we have used Eq. (V.20). In this case, $|\psi\rangle$ is anti-correlated, and $\Delta\omega_p \ll \Delta\omega_-$. The JSI is shown in Fig. IV.4(b) and it is close to a line along the ω_- direction. We thus have that $\mathrm{JSA}(\omega_s,\omega_i) \simeq \delta(\omega_+ - \omega_p)f_-(\omega_-)f_{\rm cav}(\omega_s)f_{\rm cav}(\omega_i)$ and integration over ω_+ in Eq. (IV.16) leads to :

$$|\psi\rangle = \int d\omega_- f_-(\omega_-)f_{\rm cav}\left(\frac{\omega_p+\omega_-}{2}\right)f_{\rm cav}\left(\frac{\omega_p-\omega_-}{2}\right)\left|\frac{\omega_p+\omega_-}{2},\frac{\omega_p-\omega_-}{2}\right\rangle. \tag{V.29}$$

The two states described by Eq. (V.22) and Eq. (V.28) do not coincide in general. But in the case where the two conditions are fulfilled; $G_{\Delta\omega_p}(\omega_+) = \delta(\omega_+)$ and $\overline{\omega}/\delta\omega \ll 1$, the two states coincide with a fidelity close to one. The state described by Eq. V.29 consists of a two-linear time-frequency cluster state (see Fig. V.3 (c). It is defined by analogy with the cluster

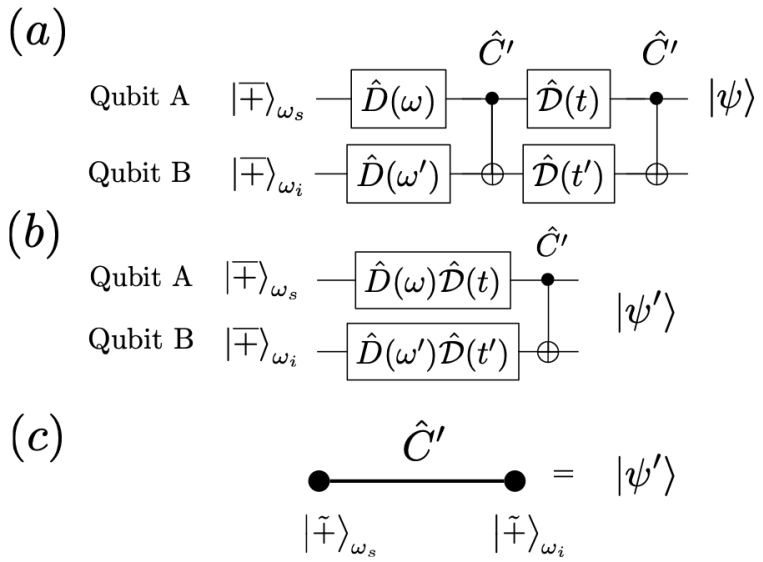

Figure V.3: Generation of entangled 2D time-frequency GKP state. The quantum circuit (a) and (b) are equivalent if the two conditions are verified: the ratio of the periodicity of the GKP state and the frequency noise width is smaller than one and if the envelope function of the collective variable ω_+ is a Delta distribution. (c) Two-linear time-frequency cluster state produced by SPDC into an optical cavity.

state in quadrature position-momentum variable for GKP state [Larsen et al., 2019]. Each node represents a physical time-frequency GKP state and each edge represents the application of an entangling gate $\hat{C}'$, as in [Menicucci, 2014]. In other words, it is a sum of time-frequency EPR pairs, owing to the frequency correlation imposed by the energy conservation.

V.1.4.2 Correction against temporal shift (MBQC)

The previously described 2D entangled time-frequency GKP state can be used to implement a measurement-based error correction protocol, which was previously defined for quadrature position-momentum continuous variables [Baragiola et al., 2019, Menicucci, 2014]. In this scenario, the result of a measurement performed on one qubit (say, B, encoded in the idler photon, also called the ancilla) is used to correct the error on the other qubit A, encoded in the signal photon, also called the data qubit). We remind the results presented in [Fabre et al., 2020c]

We will consider the effect of a time measurement on the ancilla qubit of state Eq. (IV.16). Since both qubits are entangled, measuring the ancilla qubit (B) has an effect on the data qubit (A), as shown in Fig. V.4 [Steane, 1996]. The operation realized in qubit B is teleported to qubit A, up to a known displacement on qubit A, which is given by the result of the measurement performed in qubit B. In the spirit of QEC, the interest of this approach is that, if noise corresponds to displacements in conjugate variables, as it is the case in the GKP code, one can show that, if qubit B is measured in one variable (time or frequency), its error in the measured variable is teleported to qubit A's error in the same variable. Thus, if qubit B's error is smaller

than A's, this scheme can be used to decrease the noise in physical GKP states of A [Menicucci, 2014].

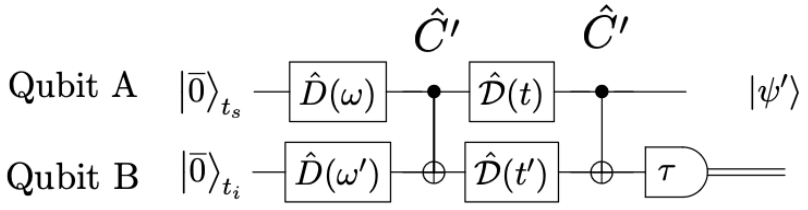

Figure V.4: The data qubit (signal) in arm A and the ancilla one (idler) in arm B are prepared in state $|\bar{+}\rangle_{\omega_s}|\bar{+}\rangle_{\omega_i} = |\overline{0}\rangle_{t_s}|\overline{0}\rangle_{t_i}$. After the time and frequency displacements and the $\hat{C}'$ gate, we perform a time measurement on the ancilla. The figure is extracted from [Fabre et al., 2020c].

While the described protocol is very general, the QEC of GKP states requires a specific and a certain ordering of optical elements. This protocol allows the correction of small displacements in phase space, for which the GKP is designed to be robust due to its comb structure. For the time-frequency GKP states that we consider in this chapter, the small displacement shifts are due to temporal broadening in a dispersive medium, and can cause an overlap between the $|\tilde{0}\rangle_t$ and $|\tilde{1}\rangle_t$ peaks of the logical qubit state. The possibility of correcting the "small" displacement which occurs in the GKP states is quantified thanks to a figure of merit developed in Ref. [Glancy and Knill, 2006, Shi et al., 2019].

Time-frequency error correction of an ideal time-frequency GKP state We start from a separable state, the data (signal) and the ancilla (idler) are initialized in the frequency $|\bar{+}\rangle_{\omega_s}|\bar{+}\rangle_{\omega_i}$ state:

$$|\psi\rangle = |\bar{+}\rangle_{\omega_s}|\bar{+}\rangle_{\omega_i} = |\overline{0}\rangle_{t_s}|\overline{0}\rangle_{t_i} = \sum_{n,m\in\mathbb{Z}^2} |nT\rangle|mT\rangle\,, \tag{V.30}$$

with $T = 2\pi\tau_{rt}$. Frequency and time Dirac distribution noises are assumed for both qubits:

$$|\overline{0}\rangle_{t_s}|\overline{0}\rangle_{t_i} \to \hat{\mathcal{D}}_s(t)\hat{\mathcal{D}}_i(t')\hat{D}_s(\omega)\hat{D}_i(\omega')|\overline{0}\rangle_{t_s}|\overline{0}\rangle_{t_i}\,, \tag{V.31}$$

then time noises are entangled with the $\hat{C}'$ operation:

$$\hat{C}'(\hat{\mathcal{D}}_s(t)\hat{\mathcal{D}}_i(t')\hat{D}_s(\omega)\hat{D}_i(\omega')|\overline{0}\rangle_{t_s}|\overline{0}\rangle_{t_i}) \tag{V.32}$$

$$= \hat{\mathcal{D}}_s(t+t')\hat{\mathcal{D}}_i(t-t')\hat{D}_s(\omega)\hat{D}_i(\omega')|\overline{0}\rangle_{t_s}|\overline{0}\rangle_{t_i} \tag{V.33}$$

$$= \sum_{n,m\in\mathbb{Z}^2} e^{in\omega T}e^{im\omega' T}|nT+t+t'\rangle|mT+t-t'\rangle\,. \tag{V.34}$$

We realize a time measurement on the ancilla (the idler). Let us say that the detector clicks at time τ, which can take only the values $\tau = t - t' + mT$. The initial state is projected into:

$$|\overline{0}\rangle_{t_s} \to e^{i\omega'(\tau-t+t')}\hat{\mathcal{D}}_s(t+t')\hat{D}_s(\omega)|\overline{0}\rangle_{t_s}\,. \tag{V.35}$$

The temporal shift of the data is entirely determined by the noise (shift) of the ancilla. The probability of success is given by $|t-t'| < \frac{\pi}{2\overline{\omega}}$, which means the probability to avoid to fall in another $\frac{\pi}{2\overline{\omega}}$ time window.

Gaussian distribution of the noise Now we consider that the time and frequency noise obeys to a Gaussian distribution and is written as:

$$|\psi\rangle = [\iint\iint G_{\delta\omega}(\omega)G_{\delta\omega}(\omega')G_{1/\Delta\omega_-}(t)G_{1/\Delta\omega_p}(t') \times \hat{\mathcal{D}}_s(t+t')\hat{\mathcal{D}}_i(t-t')\hat{D}_s(\omega)\hat{D}_i(\omega')dtdt'd\omega d\omega'] \left|\overline{0}\right\rangle_{t_s}\left|\overline{0}\right\rangle_{t_i}. \quad \text{(V.36)}$$

We then apply the time and frequency displacement operators on the GKP state:

$$|\psi\rangle = \iint\iint G_{\delta\omega}(\omega)G_{\delta\omega}(\omega')G_{1/\Delta\omega_-}(t)G_{1/\Delta\omega_p}(t') \times \sum_{n,m\in\mathbb{Z}^2} e^{in\omega T}e^{im\omega T}\left|nT+t+t'\right\rangle\left|mT+t-t'\right\rangle dtdt'd\omega d\omega'. \quad \text{(V.37)}$$

The Joint Temporal Amplitude of the state $\langle t_s, t_i|\psi\rangle = \mathrm{JTA}(t_s, t_i)$ is a circle whose radius is the frequency width $\overline{\omega}$, with elliptical peaks whose half axis are equal to $\Delta\omega_-$ and $\Delta\omega_p$ (see Fig. V.5). In the case where $\Delta\omega_- \gg \Delta\omega_p$, the JTA is a periodic (along t_-) but a set of lines along t_+: the periodicity along this direction is not visible owing to the time noise.

A time measurement on the ancilla is then performed, a click is detected at time τ and can take the value $\tau = mT + t - t'$. The new wavefunction $|\psi'\rangle = \langle\tau|\psi\rangle$ is, after performing an integration over t and after normalization:

$$\left|\psi'\right\rangle = \int d\omega'(\iint \sum_{n,m\in\mathbb{Z}^2} e^{i\omega nT}\frac{G_{\Delta\omega_-}(t'+\tau-mT)G_{\Delta\omega_p}(t')}{G_{\sqrt{\Delta\omega_-^2+\Delta\omega_p^2}}(\tau-mT)}\cdot G_{\delta\omega}(\omega')G_{\delta\omega}(\omega)e^{i\omega' mT} \times \left|(n-m)T+\tau+t')\right\rangle d\omega dt'). \quad \text{(V.38)}$$

After the time measurement of the ancilla (idler), the state is projected into a one dimensional GKP state. The time noise distribution of the signal is updated,

$$\frac{G_{\Delta\omega_-}(t'+\tau-mT)G_{\Delta\omega_p}(t')}{G_{\sqrt{\Delta\omega_-^2+\Delta\omega_p^2}}(\tau-mT)} = G_\delta(t'-t_m). \quad \text{(V.39)}$$

It is a normal distribution with variance $\delta^2 = \frac{\Delta\omega_-^2\Delta\omega_p^2}{\Delta\omega_-^2+\Delta\omega_p^2}$ and mean value $t_m = \frac{\Delta\omega_-^2}{\Delta\omega_-^2+\Delta\omega_p^2}(\tau+mT)$. The time noise of the data depends on both the noises of the ancilla and the data.

Hence the state can be written as:

$$\left|\psi'\right\rangle = \sum_{m\in\mathbb{Z}}\int dt'\iint d\omega d\omega' G_{\delta\omega}(\omega)G_\delta(t'-t_m)G_{\delta\omega}(\omega')e^{i\omega' mT}\hat{\mathcal{D}}_s(-mT+\tau+t')\hat{D}_s(\omega)\left|\overline{+}\right\rangle_{t_s}. \quad \text{(V.40)}$$

We point out that for time correlated photon meaning a very time noisy data $\Delta\omega_- \gg \Delta\omega_p$, the time distribution of the signal only depends on the noise of the idler, since $\delta \sim \Delta\omega_-$ and $t_m = \tau + mT$. Therefore the analysis is the same than in the previous section. We can understand this noise reduction on the Fig. V.5. When we perform a measurement on the t_- axis, the signal is projected into a less noisy state since the updated time distribution of the signal depends on the time distribution of the idler. The consequence is that, according to (V.39), the state becomes periodic along the t_+ direction, since the time width of each peak becomes $\Delta\omega_p$ (instead of $\Delta\omega_-$) which is smaller than $2\pi/\overline{\omega}$.

Note that, in order to come back to the previous analysis for anti-correlated photon, one has to measure the signal and not the idler.

We now discuss the experimental feasibility of the time quantum error correction. The Joint Temporal Intensity of the state given by Eq. (IV.16) is represented in Fig. V.5. The state is periodic (with periodicity of $2\pi/\overline{\omega} = 50$ ps) along the two orthogonal directions $t_{\pm}$. But since the inverse of the energy conservation width is much larger than the inverse of the free spectral range, the periodicity along the t_+ is not visible. A time measurement of the idler photon leads to the obtention of a random distribution which corresponds to the different peaks along the t_- axis. A single photon detector should have 50 ps time resolution to distinguish these peaks, which is possible with the actual technology. For instance superconducting single photon detector with a 3 ps time resolution is presented in [Esmaeil Zadeh et al., 2020] with a jitter inferior to 3 ps, which corresponds to the uncertainty of the arrival time of the photons, and hence does not affect the time error correction. Once the state is measured, further time or frequency correction operators could be applied on the data [Glancy and Knill, 2006].

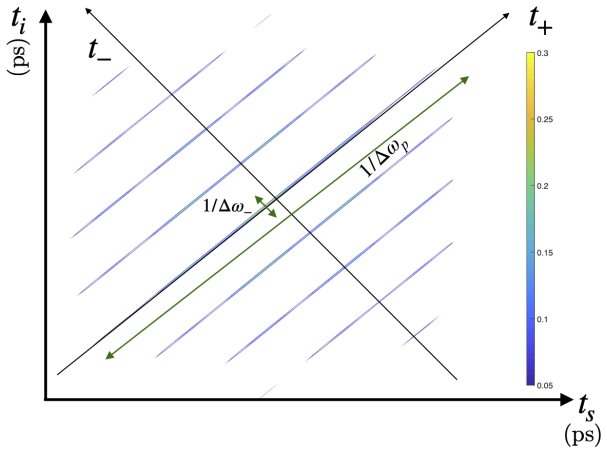

Figure V.5: Numerical simulation of the Joint Temporal Intensity of the time-frequency GKP states in the case $\Delta\omega_- \gg \Delta\omega_p$ with a 50 ps periodicity. It corresponds to the Fourier transform of the state shown in Fig. IV.4.(b). The state is periodic in both directions, but since the $1/\Delta\omega_p \gg 2\pi/\overline{\omega}$, we can not see the periodicity in the t_+ direction since the data qubit is very noisy. The figure is extracted from [Fabre et al., 2020c].

Error correction is also possible in frequency degrees of freedom, and it requires measuring one of the photons in the $\omega_{\pm}$ variables. This operation could be performed with non-linear devices implementing a controlled quantum gate in the frequency degrees of freedom.

An interesting aspect of using measurement-based techniques is that they provide an alternative to a deterministic two-qubit gate in single photon-based devices. As a matter of fact, implementing deterministic gates is a challenge in such set-ups, and starting from useful entangled resources can help achieving determinacy in different protocols. Possible ways to scale up the generation of time-frequency GKP states would be using on-demand production of pure

single photon states, reviewed in [Senellart et al., 2017] for instance. Such ideas can be combined to implement efficient frequency gates, which are currently realised with electro-optic modulators and pulse-shapers [Imany et al., 2018, Lukens and Lougovski, 2017]. We expect that the fast technological evolution of the integrated circuits physics will enable effective photon-photon interaction with higher probability in the near future.

In this section, we have presented the first principles of quantum error correction in time-frequency variables. Another application of the Steane error correction scheme presented above, with as input a Gaussian state and as ancilla a GKP state, permits producing distillable magic states and the universality in continuous variable encoding could be achieved without using non-Gaussian operation [Baragiola et al., 2019]. Finally, a time-frequency grid state could be used for metrological purposes as for the joint estimation of time and frequency parameters as developed in [Duivenvoorden et al., 2017].

V.2 Production and Manipulation of Time-frequency GKP state

V.2.1 Experimental production of time-frequency GKP state using SPDC process

We now recap the results of the previous section. The emitted quantum state described by Eq. (IV.16) for a general experimental bulk or integrated circuit inside an optical cavity in our case can be reformulated with single-Kraus-like operators in the spirit of Sec. V.1.3.2. In this framework, the SPDC process inside an optical cavity can be seen as two fictitious ideal GKP states which enter a Gaussian time-frequency noise channel, modeling the energy conservation and the phase matching condition (see Sec. V.1.3.2). The state becomes entangled thanks to a frequency beam-splitter operation. The width of the elliptically shaped JSI can be considered as time noise while the linewidth of the comb peaks as frequency noise.

This reinterpretation holds since the state described by the model Eq. (V.29) and the traditional description used for describing such state Eq. (IV.16) coincide. The produced state is an entangled time-frequency GKP state in one dimension along the ω_- direction. According to this formalism, the entangled time-frequency GKP state is hence suitable for QEC in the MBQC scenario as demonstrated before.

We now provide a simple example of a single one-photon gate, the time displacement operator and the signature of this operation is observed using the HOM experiment. Indeed, the coincidence probability measured thanks to the HOM experiment is a cut of the chronocyclic Wigner distribution in the correlated variables (ω_-, τ). This measurement is particularly adapted since the state is one dimensional and anti-correlated along the ω_- axis.

V.2.2 Experimental manipulation of time-frequency grid state: Single qubit gate

A possibility to manipulate frequency states such as defined by Eq. (V.29) is using electro-optical modulation (EOM), as demonstrated in [Lukens and Lougovski, 2017] for frequency-bin encoded qubits. Such techniques can also be used in the present context, with the difference that while in Ref. [Lukens and Lougovski, 2017] each frequency is manipulated independently, in the present encoding redundancy is a key aspect, and qubit manipulation requires acting on the whole frequency comb. It must then be manipulated as a whole, a situation that does not add any experimental complexity to the techniques demonstrated in [Lukens and Lougovski, 2017]. Interestingly, using EOM is not strictly necessary to manipulate time-frequency GKP

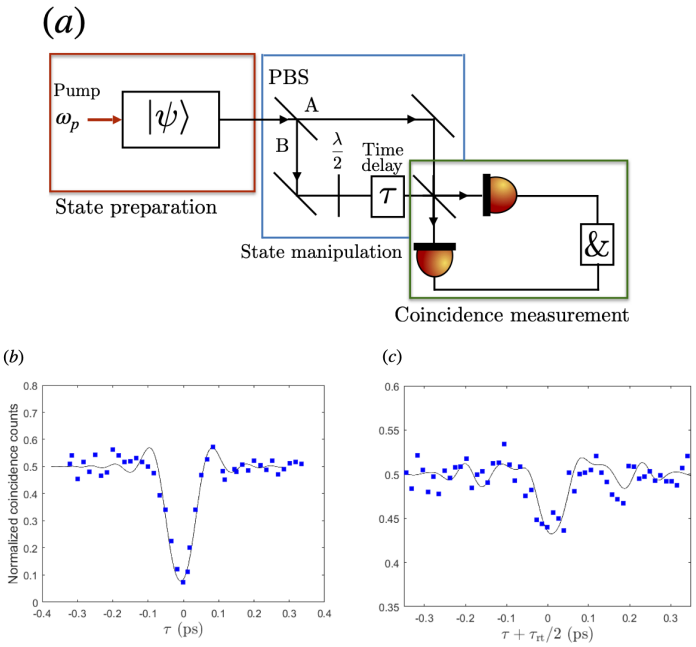

Figure V.6: (a) Hong-Ou-Mandel experiment enabling state manipulation and measurement. After being generated, signal and idler photons are separated to different arms of an interferometer with a polarizing beam-splitter (PBS). Time delay (τ) in one arm performs a $\hat{\mathbf{Z}}_{t_s}$ gate for $\tau = -\tau_{rt}/2$. In order to have the same polarization for the photons, a half-wave plate is added. State measurement can be done by recombining both photons in a second beam splitter and coincidence measurements for different values of τ. (b) Experimental coincidence measurements corresponding to state $\hat{C}' \left|\tilde{+}\right\rangle_{\omega_s} \left|\tilde{+}\right\rangle_{\omega_i}$. (c) Experimental coincidence measurements corresponding to state $\hat{C}'\hat{\mathbf{Z}}_{t_s} \left|\tilde{+}\right\rangle_{\omega_s} \left|\tilde{+}\right\rangle_{\omega_i}$. The continuous lines are numerical calculations obtained from AlGaAs chip taking into account the reflectivity and the birefringence of the signal and idler photons and the chromatic dispersion. The figure is extracted from [Fabre et al., 2020c].

states. We demonstrate here an experimentally simpler way to implement a quantum gate $\hat{Z}$ for time-frequency GKP states and obtain a signature of the manipulation using a Hong-Ou-Mandel (HOM) interferometer [Hong et al., 1987, Lu et al., 2003], that can be used for state measurement, as detailed in the following. The HOM setup is sketched in Fig. V.6 (a): signal and idler photons are sent to different arms of an interferometer, A and B. Introducing a time delay τ between the two arms, the two photons acquire a phase difference such that the biphoton

state arriving in the recombining beam-splitter is given by:

$$\left|\psi'\right\rangle = \int d\omega_- e^{-i(\omega_-+\omega_p)\tau/2} f_-(\omega_-) f_{\text{cav}}(\frac{\omega_p+\omega_-}{2}) f_{\text{cav}}(\frac{\omega_p-\omega_-}{2}) \left|\frac{\omega_p+\omega_-}{2}, \frac{\omega_p-\omega_-}{2}\right\rangle. \quad \text{(V.41)}$$

Without loss of generality for the present purposes, we consider $g(\omega_-) = f_-(\omega_-) f_{\text{cav}}(\frac{\omega_p+\omega_-}{2}) f_{\text{cav}}(\frac{\omega_p-\omega_-}{2})$ to be real. This function is also symmetric with respect to $\omega_- = 0$. The phase $e^{-i\omega_-\tau}$ corresponds to a displacement of τ in time, the conjugate variable to ω_-. It corresponds to the application of the $\hat{\mathcal{D}}_{t_s}(\tau)$ operator to the signal photon *before* the entangling operation $\hat{C}'$, such that state Eq. (V.41) can be written as $|\psi'\rangle = \hat{C}'\hat{\mathcal{D}}_{t_s}(\tau) \left|\tilde{+}\right\rangle_{\omega_s} \left|\tilde{+}\right\rangle_{\omega_i}$.

By choosing $\tau = -\tau_{rt}/2$ the n-th peaks of $g(\omega_-)$ with n even, remain unchanged, while for n odd, they gain a π phase and change signs, implementing the gate $\hat{\mathbf{Z}}_{t_s} \left|\tilde{+}\right\rangle_{\omega_s} = \left|\tilde{-}\right\rangle_{\omega_s}$ with a simple interferometric configuration and coincidence detection. We can argue that the time delay is a part of the interferometer itself and it is not a way to manipulate the state. Nevertheless, it is equivalent to consider a time displacement and then another from the measurement or only one time displacement as it is done here and represented in Fig. V.6 (a).

The signature of time displacement operator and the orthogonality of the two states can be detected by measuring coincidence with a HOM interferometer. As shown in [Douce et al., 2013], the HOM experiment is a direct measurement of the chronocyclic Wigner distribution of the phase-matching part of the JSA. In the experimental context discussed here, it gives access to a cut in the time-frequency phase space of the Wigner function associated to the global variable ω_-, $W(\mu, \tau)$, where μ is the amplitude of displacement of ω_- and τ the amplitude of displacement in time. The HOM experiment corresponds thus to the $\mu = 0$ plane, where τ is varied. The partial information obtained is enough to distinguish between the two orthogonal states.

We have implemented the setup of Fig. V.6 (a) on the state produced by our AlGaAs device. For $\tau = 0$, we expect a coincidence dip with a visibility fixed by the degree of indistinguishability of the emitted photon pairs : this corresponds to the state $\hat{C}' \left|\tilde{+}\right\rangle_{\omega_s} \left|\tilde{+}\right\rangle_{\omega_i}$. For $\tau = -\tau_{\text{rt}}/2$, we expect to observe a replica of the previous dip with a visibility given by a combination of facets reflectivity, birefringence and chromatic dispersion: this corresponds to the state $\hat{C}'\hat{\mathbf{Z}}_{t_s} \left|\tilde{+}\right\rangle_{\omega_s} \left|\tilde{+}\right\rangle_{\omega_i}$. The results of the corresponding measurements are shown respectively in Fig. V.6 (b) and (c). In the first (Fig. V.6 (b), $\tau = 0$) the visibility is 86%, while in the second case (Fig. V.6 (c), $\tau + \tau_{rt}/2 = 0$) we obtain a visibility of 12%, making these two states well distinguishable. The visibility of the adjacent peaks ($\tau \pm \tau_{rt}/2 = 0$) from the central dip ($\tau = 0$) could be enhanced with a higher reflectivity of the facets and using frequency filters before the beam-splitter.

We perform numerical simulations of the visibility of the second peak of the HOM experiment as a function of the cavity reflectivity and for different bandwidth of the filters placed before the beam-splitter presented in Fig. VII.8. The intersection of the dashed lines indicates the conditions of the realized experiment: a reflectivity of the facets of 0.3 without frequency filters, which leads to a theoretical prediction of 15% of visibility, which is in good agreement with the

experimentally observed result of 12%, see Fig. V.6 (c). Such visibility is enough to distinguish both possible GKP states. A possible way to enhance the visibility of the secondary peaks is to deposit a reflective coating on the facets, but this solution would equally enhance the negative effect of the cavity birefringence by making peaks corresponding to different polarizations more and more distinguishable. A usual solution for this is, in addition to coating, to add frequency filters, since the birefringence and the chromatic dispersion induced path distinguishably is less pronounced in the central part of the spectrum. This would thus permit to reach a higher value of the visibility (note that the total frequency bandwidth for about 500 peaks is 70 nm) (see Appendix of Ref. [Fabre et al., 2020c]). We note that the visibility reaches a maximum and then decreases when increasing the reflectivity, well illustrating our discussion on the antagonist roles of the reflectivity and the birefringence. It shows that a visibility of the order of 80 % is well within reach. Numerical and analytical results are presented in the Appendix of [Fabre et al., 2020c] for such values of reflectivity.

In summary, a visibility higher than 80% can be obtained by improving the reflectivity of the facets and filtering the produced spectrum, which would decrease the number of exploitable peaks and reduce the detection rate but would keep them of the order of a hundred.

Further possible manipulation of the time-frequency grid state has been proposed in Ref. [Maltese et al., 2020], where tuning the pump frequency permits to engineer the JSA symmetry. Compared to other schemes where the entire comb is manipulated [Imany et al., 2018, Lu et al., 2019], this technique enables to address the odd and the even peaks individually with low optical losses. In the formalism developed in Chap. III, the pump tuning corresponds to a frequency displacement operation on the signal and idler photon, see Fig. 2 of Ref. [Maltese et al., 2020], namely to non-linear operation without the need to introduce a non-linear material or EOM after the generation of the two-photon state.

V.2.3 Time-frequency gates for GKP manipulation

Separation of the even and odd frequency peaks In this part, we introduce how to separate spatially the odd and the even frequencies with a Mach-Zehnder type interferometer. Such scheme was already proposed for manipulating large cluster states (see Ref. [Alexander et al., 2016]).

A time-frequency GKP state composed of odd and even frequencies $\left|\tilde{+}\right\rangle$ is combined with the vacuum state on a beam-splitter. The spatial output port of the beam-splitter is noted A and B. The wave function can be written as:

$$|\psi\rangle = \frac{1}{\sqrt{2}}\left(\sum_{n\in\mathbb{Z}} c_n[|n\Delta\omega\rangle_A \otimes |0\rangle_B - |0\rangle_A \otimes |n\Delta\omega\rangle_B]\right), \tag{V.42}$$

where c_n is the envelope of the grid state and $|n\Delta\omega\rangle = \int d\omega T_n(\omega)\,|\omega\rangle$. In the spatial A port of the interferometer, a dispersive medium is introduced. The phase accumulated during a time t

by a photon of frequency $n\Delta\omega$ is $e^{in\Delta\omega t}$. Hence, before the second beam-splitter, the state is:

$$|\psi\rangle = \frac{1}{\sqrt{2}}(\sum_{n\in\mathbb{Z}} c_n[e^{in\Delta\omega t}\,|n\Delta\omega\rangle_A \otimes |0\rangle_B - |0\rangle_A \otimes |n\Delta\omega\rangle_B]). \tag{V.43}$$

After the second beam-splitter, keeping the same labels for the spatial port of the output, the wave function becomes:

$$|\psi\rangle = \frac{1}{2}\sum_{n\in\mathbb{Z}}[c_n(e^{in\Delta\omega t}-1)\,|n\Delta\omega\rangle_A \otimes |0\rangle_B - (e^{in\Delta\omega t}+1)\,|0\rangle_A \otimes |n\Delta\omega\rangle_B]. \tag{V.44}$$

Choosing the time t, or equivalently the length of the medium allows, thanks to interference effect, to suppress the odd or the even frequencies in one given spatial port. A π pulse, *i.e* taking an interaction time equal to $t = \pi/\Delta\omega$, gives rise to the wave function:

$$|\psi\rangle = \frac{1}{2}\sum_{n\in\mathbb{Z}}[c_n(e^{in\pi}-1)\,|n\Delta\omega\rangle_A \otimes |0\rangle_B - (e^{in\pi}+1)\,|0\rangle_A \otimes |n\Delta\omega\rangle_B] \tag{V.45}$$

The first term $(e^{in\pi}-1)$ is zero for even frequencies and -2 for odd frequencies. The second term $(e^{in\pi}+1)$ is 2 for even frequencies and 0 for odd frequency. Hence, we obtain:

$$|\psi\rangle = \sum_{n\in\mathbb{Z}} c_n(-\,|(2n+1)\Delta\omega\rangle_A\,|0\rangle_B + |0\rangle_A\,|2n\Delta\omega\rangle_B). \tag{V.46}$$

We thus obtain an analog of the polarizing beam-splitter for this frequency qubits, without non-linear optical elements. Once the odd and the even frequencies components are separated, it is possible to manipulate them separately. Nevertheless, the transformation is not unitary, the odd and even peaks can not be recombined with such interferometer.

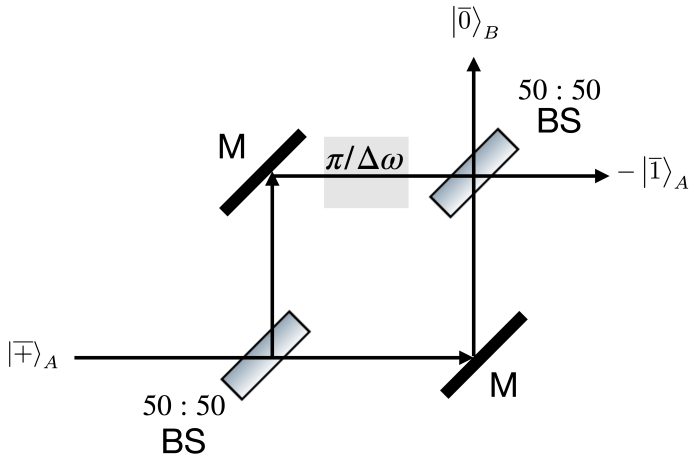

Figure V.7: Spatial separation of the odd and even peaks of the micro-comb with a Mach-Zehnder type interferometer. The temporal delay $\pi/\Delta\omega$ is the right delay for the separation.

Using Talbot effect The Talbot effect is a near field effect after a spatial grating and is characterized by the production of replicas at given propagation length. This effect has made a contribution for defining an universal set of gates for qudits [Farías et al., 2015]. In this paper, the considered state is composed of a series of peaks at a given location in the transversal plane

of the propagation of a single photon. This effect can also be used for doing a bit flip operation of GKP state as explained in the following.

Starting from the time-frequency grid state $|\overline{0}\rangle$ the near field interference have the effect to perform a $\hat{X}$ gate, at the Talbot distance defined by $z_T = l^2/\lambda$ where l is the periodicity of the grating and λ the wavelength of the field. The operator act as $|\overline{0}\rangle \rightarrow |\overline{1}\rangle$, along with $|\overline{1}\rangle \rightarrow |\overline{0}\rangle$ (see Fig. 1b in [Farías et al., 2015]. The papers [Barros et al., 2017, Farías et al., 2015] also give a set of gates for manipulating the transversal degree of freedom of single photons.

These tools can be implemented with the frequency variables. It requires first to map the frequency to an image, which can be done with a grating. Then, a $4f$ scheme is considered (see Fig. V.8), which are composed of two lenses and a spatial light modulator (SLM) placed at their focal planes. The inverse mapping from transversal to frequency degree of freedom is performed using another grating. The SLM allows to perform either phase modulation or amplitude one. The price to pay for this operation is the number of successive optical elements which decrease the intensity of single photon.

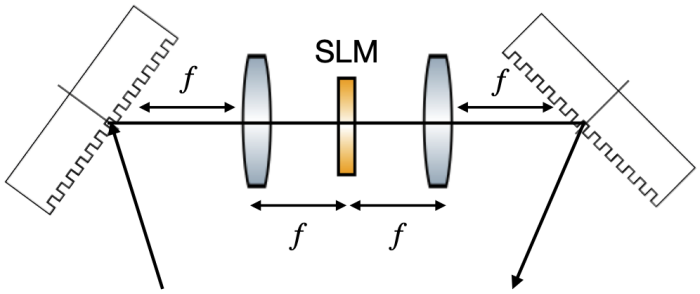

Figure V.8: $4f$ scheme used to manipulate time-frequency state. The first grating maps the frequency to transversal position variable, the SLM placed at the focal plane of the two lenses can perform any phase and amplitude modulation. Then the transversal position variable is mapped back to the frequency one.

V.3 Generation of time-frequency cat state by spectral post-selection

V.3.1 Reinterpretation of the OM experiment

We now provide an original interpretation of the Ou-Mandel experiment [Ou and Mandel, 1988] and show how it can be used to produce interesting nonclassical frequency states of photon pairs by spectral post-selection [Fabre et al., 2020a]. The OM experiment can be summarized as follows: an initial two-photon state is created by SPDC, whose Joint spectrum amplitude (JSA) is shown on the left of Fig. V.9 (a). After their generation, the two photons of the pair

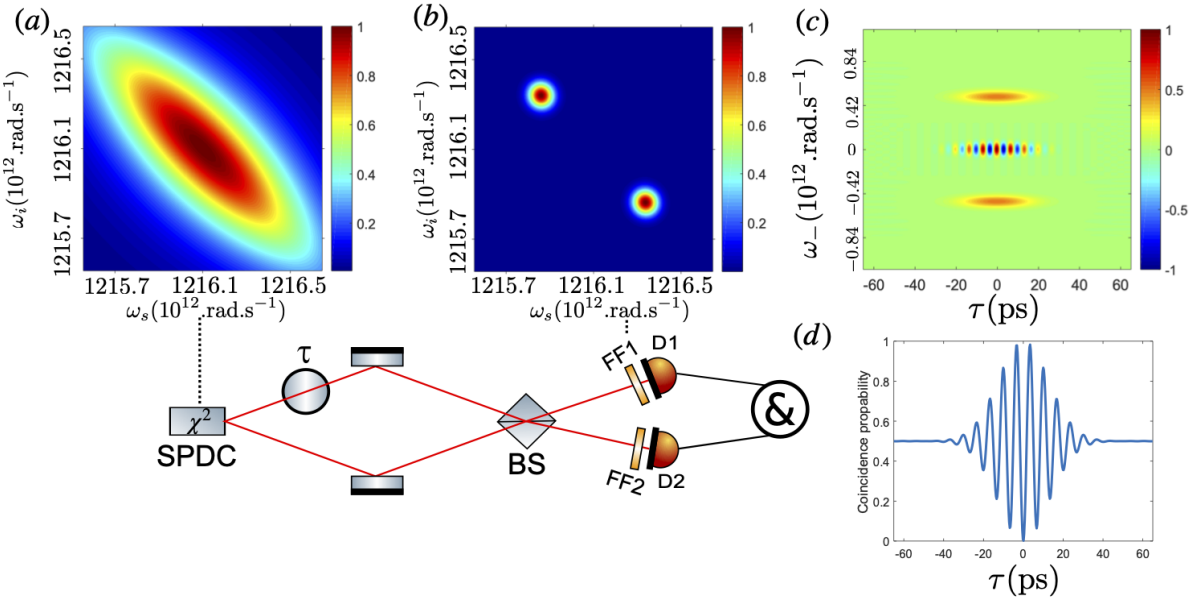

Figure V.9: Sketch of the experimental set-up of the Ou Mandel experiment: Photon pairs are generated via SPDC in a second order nonlinear crystal. One of the photon undergoes a temporal delay τ, the path of the two photons recombine in a balanced beam-splitter. Spectral filters are placed before the single photon detectors at the output ports of the beam-splitter. The numerical simulations correspond to the state generated in a transversally pumped AlGaAs waveguide: (a) Joint Spectral Amplitude of the frequency anti-correlated state generated by the AlGaAs chip; (b) Joint Spectral Intensity obtained after the action of the beam-splitter and the spectral filters (FF1, FF2) having a width of 50 pm and a separation of 0.6 nm; (c) corresponding chronocyclic Wigner distribution; (d) coincidence probability corresponding to the cut $\omega_- = 0$ in (c). The figure is extracted from [Fabre et al., 2020a].

are separated into two different paths and are then recombined in a balanced beam splitter as depicted in Fig. V.9. After the action of the balanced beam-splitter and the post-selecting done by the coincidence measurement, the two-photon state can be expressed as:

$$|\psi_\tau\rangle = \frac{1}{2}[\iint d\omega_s d\omega_i(\mathrm{JSA}(\omega_s,\omega_i)e^{-i\omega_i\tau} - \mathrm{JSA}(\omega_i,\omega_s)e^{-i\omega_s\tau})\,|\omega_s\rangle\,|\omega_i\rangle], \tag{V.47}$$

as in the usual HOM experiment. We now consider the effect of placing frequency filters before each detector. Each filter can be associated to a projector operator of the type:

$$\hat{F}(\omega_1,\sigma) = \int d\omega \overline{f}_{\omega_1}(\omega)\,|\omega\rangle\,\langle\omega|\,, \tag{V.48}$$

where $\overline{f}_{\omega_1}(\omega)$ is a Gaussian function centered at ω_1 of width σ. In the following, we will consider that the filters have the same spectral width. For standard Gaussian filters,

$$\overline{f}_{\omega_j}(\omega_\alpha) = \frac{1}{\sqrt{2\pi\sigma^2}}\exp(-\frac{(\omega_\alpha-\omega_j)^2}{2\sigma^2}), \tag{V.49}$$

with $j = 1,2$ and $\alpha = s,i$. The frequency state after spectral post-selection filtering and coincidence detection is:

$$|\psi_\tau\rangle = \frac{1}{2}\iint d\omega_s d\omega_i[\mathrm{JSA}(\omega_s,\omega_i)e^{-i\omega_i\tau} - \mathrm{JSA}(\omega_i,\omega_s)e^{-i\omega_s\tau}]f_{\omega_1}(\omega_s)f_{\omega_2}(\omega_i)\,|\omega_s\rangle\,|\omega_i\rangle\,. \tag{V.50}$$

The first term of Eq. (V.50) represents the situation where both photons are reflected by the beam-splitter and the second term represents the situation where both are transmitted. We have that the photon pairs passing through the filters are described by a quantum superposition of states having exchanged frequencies. In the case in which both photons are reflected, the signal photon with frequency ω_s is filtered by the filter centered at ω_1 and the idler with frequency ω_i is filtered by the filter centered at ω_2. If both are transmitted the opposite occurs. Thus, for $\omega_1 - \omega_2 \lesssim \Delta$ the state described by Eq. (V.50) corresponds to what we called a frequency-time cat-like state. These states correspond to two distinguishable states of signal and idler, since $\sigma \ll \Delta$; the quantum superposition comes from the paths interference produced by the beam-splitter.

For easier calculation, we write the product of the frequency function filter in the frequency collective variable:

$$\overline{f}_{\omega_1}(\omega_s)\overline{f}_{\omega_2}(\omega_i) = \frac{1}{2\pi\sigma^2}e^{-\frac{(\omega_+-(\omega_1+\omega_2))^2}{4\sigma^2}}e^{-\frac{(\omega_--(\omega_1-\omega_2))^2}{4\sigma^2}} = f_{\omega_1-\omega_2}(\omega_-)f_{\omega_1+\omega_2}(\omega_+). \tag{V.51}$$

f is a Gaussian function as $\overline{f}$ but differ by a factor two in the frequency width.

Finally, the wave function after the spectral filtering can be written as:

$$|\psi_\tau\rangle = \frac{A}{2}\int d\omega_-(f_-(\omega_-)e^{-i\omega_-\tau} - f_-(-\omega_-)e^{i\omega_-\tau})f_{\omega_1-\omega_2}(\omega_-)\,|\omega_-,-\omega_-\rangle\,, \tag{V.52}$$

with $A = f_{\omega_1+\omega_2}(0)$. We can notice that the state described by Eq. (V.3) and Eq. (V.52) are slightly different, if we consider their chronocyclic Wigner distribution. Indeed the state given

by Eq. (V.3) has the characteristic shape of the cat state in the frequency-time phase space (see Eq. (V.4) in the appendix) but the post-selected state Eq. (V.52) corresponds to a chronocyclic Wigner distribution with only the interference pattern (see Eq. (V.6)). We can now compute the coincidence rate as a function of the temporal delay $I(\tau) = \iint d\omega_s d\omega_i |\langle \omega_s, \omega_i | \psi_\tau \rangle|^2$, where we assumed that the photons are very short compared to the time resolution of the photodetectors (see Sec. **??**). After integration on the variable ω_+ taking into account that the frequency filters width is much narrower than the phase matching condition, $\sigma \ll \Delta$, we obtain:

$$I(\tau) = \frac{1}{2}(1 - \frac{1}{N}\mathrm{Re}[\int d\omega_- e^{-2i\omega_-\tau} |f_{\omega_1-\omega_2}(\omega_-)|^2]), \tag{V.53}$$

where N is a normalization constant. A last integration gives:

$$I(\tau) = \frac{1}{2}[1 - e^{-\tau^2\sigma^2}\cos(2\tau(\omega_2 - \omega_1))]. \tag{V.54}$$

A coincidence measurement shows a beating, with a period $\frac{2\pi}{\omega_2-\omega_1}$. Since we observe a coincidence probability for some values of τ that is greater than one half, this beating is a signature of frequency entanglement [Douce et al., 2013, Eckstein and Silberhorn, 2008] but is completely independent of the frequency entanglement of the initial state [Ou and Mandel, 1988]. In other words, the Ou and Mandel experiment can be seen as a measurement in a frequency entangled basis and as such, post-selects an entangled state. In the literature, the term of spatial beating is used to designate such oscillation in the coincidence measurement. Indeed the introduced optical path delay τ is a time shift since for a photon longitudinal position and time are proportional. Finally, this beating can not be obtained with a mixed state as shown in the Appendix **??**.

The above discussion provides a new interpretation of the oscillations shown in Fig. V.9. Indeed, according to [Douce et al., 2013], the coincidence probability Eq. (V.54) is the cut of the chronocyclic Wigner distribution $W_{\mathrm{cat}}(\omega_-, \tau)$ at the frequency $\omega_- = 0$ (see Eq. (V.6)). The measurement procedure corresponds to a measurement in a Schrödinger cat basis of the frequency state that has been initially generated by the SPDC crystal. We can conclude that the signal obtained by coincidence detection corresponds to the interference term of the frequency-time cat-like state:

$$I(\tau) = \frac{1}{2}(1 - W_{\mathrm{beating}}(0, \tau)). \tag{V.55}$$

Where $W_{\mathrm{beating}}(\omega, \tau)$ corresponds to the chronocyclic Wigner distribution of the phase matching function and is defined in Sec. V.4. We verified our results by performing numerical simulations (see Fig. V.9) on the state generated by SPDC using the experimental parameters for a transversally pumped semiconductor waveguide studied in [Orieux et al., 2013]. In this device, a pump beam around 775 nm impinging on top of a multilayer AlGaAs waveguide with an incidence angle θ generates by SPDC two orthogonally polarized signal/idler guided modes around 1.55 μm. Two Bragg mirrors provide a vertical microcavity for the pump beam increasing the conversion efficiency of the device [Orieux et al., 2011]. This geometry presents a particularly high degree of versatility in the control of the biphoton frequency correlations via the spatial engineering of the pump beam [Caillet et al., 2009, Francesconi et al., 2020]. In the numerical simulations

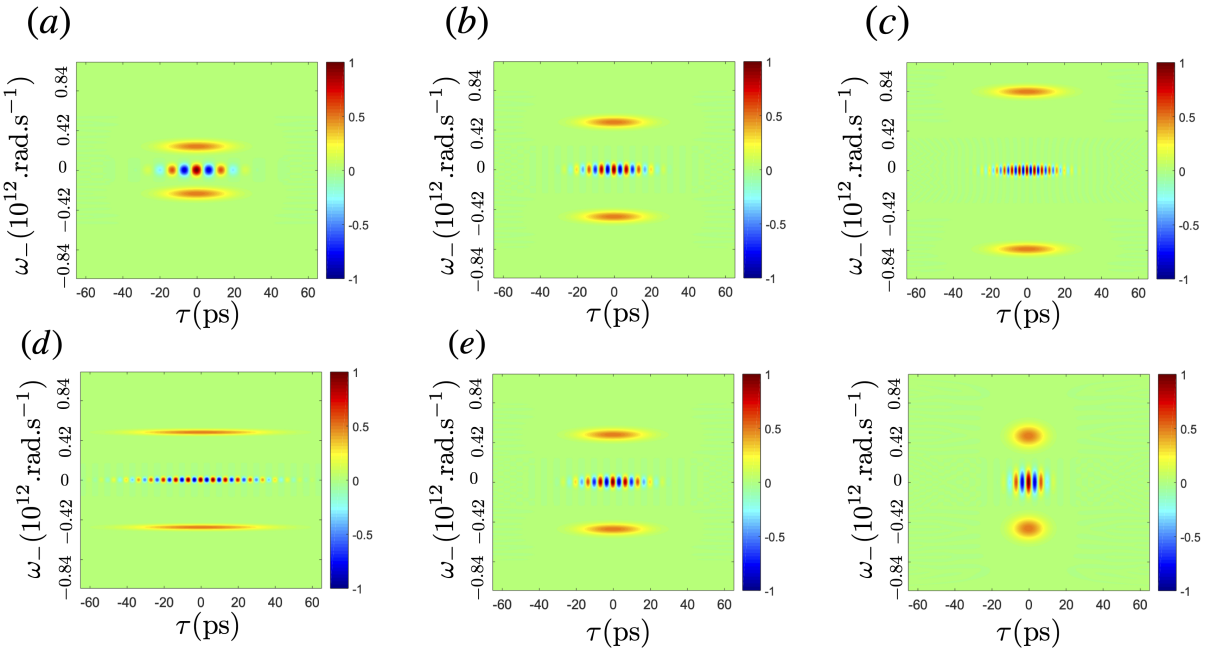

Figure V.10: Chronocylic Wigner distribution of the frequency-time cat-like state. Top: effect of the variation of the frequency separation $\omega_1 - \omega_2$ of the filters of 0.3 nm ($6.28{\cdot}10^{12}\mathrm{rad}.s^{-1}$) (a), 0.6 nm ($3.14{\cdot}10^{12}\mathrm{rad}.s^{-1}$) (b) and 1 nm ($1.88{\cdot}10^{12}\mathrm{rad}.s^{-1}$) (c), for a fixed spectral width of the filters of 50 pm ($37.6{\cdot}10^{12}\mathrm{rad}.s^{-1}$). Bottom: effect of the variation of the spectral width of the filters (25 pm ($75{\cdot}10^{12}\mathrm{rad}.s^{-1}$) (d), 50 pm ($37.6{\cdot}10^{12}\mathrm{rad}.s^{-1}$) (e) and 100 pm ($18{\cdot}10^{12}\mathrm{rad}.s^{-1}$) (f)) for a fixed spectral separation of 0.6 nm between the central wavelengths of the filters. The figure is extracted from [Fabre et al., 2020a].

reported in Fig. V.9, the pump beam has a Gaussian intensity profile with a waist 0.2 mm, pulses having a duration of 5 ps. This leads to the generation of a biphoton state with a JSA represented in Fig. V.9 (a). The spectral width of the JSA along the $\omega_+ = \omega_s + \omega_i$ axis is 1 nm ($1.88{\cdot}10^{12}\mathrm{rad}.s^{-1}$) and along the $\omega_- = \omega_s - \omega_i$ axis is 0.2 nm ($9.42{\cdot}10^{12}\mathrm{rad}.s^{-1}$).

In this section, we demonstrate that even starting from frequency anti-correlated photon pairs, which is the most common type of two-photon state produced by SPDC, the action of spectral filters allows to post-select Schrödinger cat-like states. The numerical simulation of the chronocyclic Wigner distribution of the filtered JSA and the coincidence probability of the OM experiment are shown in Fig. V.9 (c) and (d) respectively. They both match taking the cut $\omega_- = 0$ for the chronocyclic Wigner distribution. Notice that the observed oscillations appear irrespectively of the initial state produced by SPDC, since we are dealing here with a post-selection process. Finally, the larger the ratio $(\omega_1 - \omega_2)/\sigma$, the higher is the number of oscillations in the interference pattern of the frequency-time cat-like state, since this term is a measure of the size of the cat.

V.3.2 Effect of the filters parameters on the frequency cat state

In this section, we explain how to produce different types of frequency-time cat-like states by spectral post-selection. For such, we will use accordable frequency filters.

We start by studying the effect of the variation of the central frequency ω_1 and ω_2 of the filters while their width is fixed to 50 pm ($37.6{\cdot}10^{12}\text{rad}.s^{-1}$), see Fig. V.10 (a),(b),(c). If the central frequencies of the filters are equal, we do not obtain an interference pattern along the τ axis but rather a Gaussian function which is JSA. In that case, the photons are spectrally indistinguishable. When the central frequencies of the filters increases, the period of the beating oscillation $T = \frac{\pi}{\omega_1 - \omega_2}$ (see Eq. (V.54)) decreases and the number of oscillations increases.

We then investigate the influence of the spectral width of the filters, keeping fixed the frequency separation $\omega_1 - \omega_2$ of the filters at 0.6 nm ($3.14{\cdot}10^{12}\text{rad}.s^{-1}$), see Fig. V.10 (d),(e), (f). As the width decreases from 100 pm ($18{\cdot}10^{12}\text{rad}.s^{-1}$) to 25 pm ($75{\cdot}10^{12}\text{rad}.s^{-1}$), the coherence time of the wave packet increases, as a consequence of the Fourier-transform relation between frequency and time. Since the time-frequency phase space of a single photon are non-commutative, it can be interpreted as a true Heisenberg inequality.

V.3.3 Quantum eraser experiment

We now consider the experiment where each photon's path can be "marked" by placing frequency filters *before* the beam-splitter, a procedure that will destroy the previously observed beating and, depending on the degree of distinguishability between the photons, will lead to the appearance of dips with different visibility in the Hong, Ou and Mandel experiment [Hong et al., 1987]. There are different ways to implement a quantum eraser experiment with the HOM interferometer, using as a marker the polarization [Kwiat et al., 1992, Legero et al., 2004]. If the filtered frequencies are such that their difference, $|\omega_1 - \omega_2|$ is smaller than the width σ of the filters, this path-marking will not be totally effective and the two photons will spatially interfere after the beam-splitter. More specifically, as detailed in the following, the dip's visibility will depend on the ratio $|\omega_1 - \omega_2|/\sigma$, which is proportional to the distance between the distributions representing the "dead" and "alive" state of the cat.

Fig. V.11 (a), (b) reports the results of the numerical simulations of the chronocyclic Wigner distribution for an initial state represented in Fig. V.9 (a), with two frequencies filters placed before the beam-splitter. The analytical expression for the coincidence probability, demonstrated in the appendix of [Fabre et al., 2020a], is given by:

$$I(\tau) = \frac{1}{2}(1 - e^{-(\omega_1-\omega_2)^2/(2\sigma^2)} \cdot e^{-\tau^2\sigma^2/2}). \tag{V.56}$$

Expression (V.56) evidences that the larger the ratio $(\omega_1 - \omega_2)/\sigma$ the lower the visibility is, since the action of the filters makes the photons more distinguishable.

The described situation corresponds to selecting one of the two possible states of signal and idler described in the previous section, *i.e*, the one where $\omega_s = \omega_1$ and $\omega_i = \omega_2$. Thus, it corresponds to a Gaussian state in phase space, say, where the cat is alive. As shown in [Douce et al., 2013], the HOM coincidence measurement corresponds to a cut along the frequency axis in phase space. When $|\omega_1 - \omega_2| > \sigma$, the two photons have no spectral overlap, explaining a

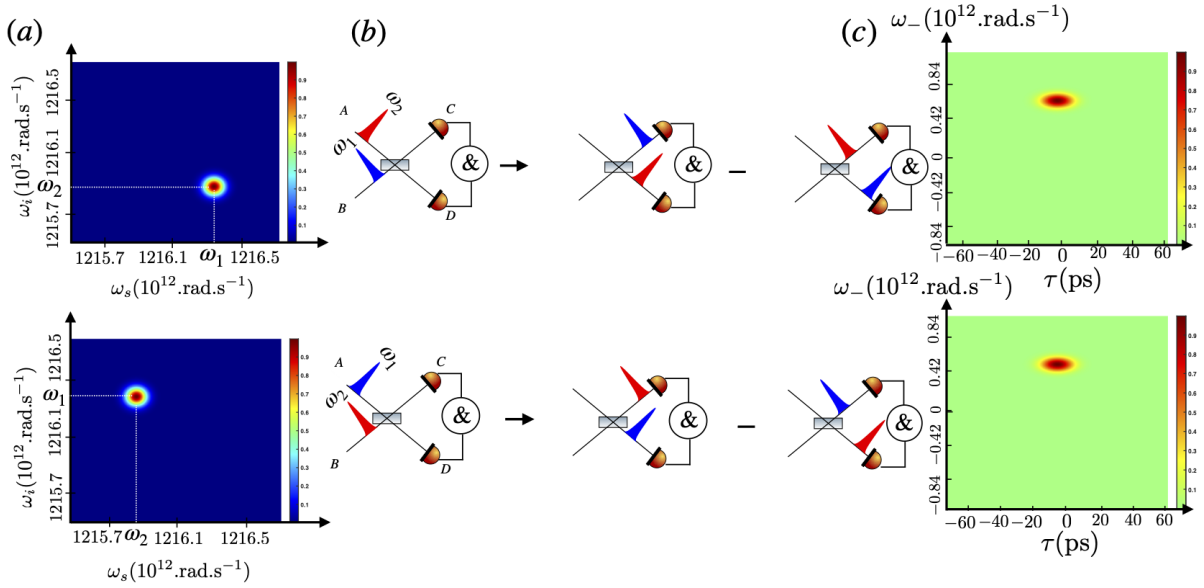

Figure V.11: (a) Joint Spectral Intensity of bicolor photon when the frequencies filters are placed before the beam-splitter and their corresponding diagrams. (b) Diagrams of the quantum state after the beam-splitter, taking into account only the coincidence events. (c) Chronocyclic Wigner distribution $W_-(\tau, \omega_-)$ of the two quantum state (b) when the time-resolution of the detectors is lower than the temporal size of the wave packet and $|\omega_1 - \omega_2| \neq 0$. The distribution is zero when $\omega_1 \gg \omega_2$. The figure is extracted from [Fabre et al., 2020a].

visibility that reaches 1/2, which is the classical statistical (uncorrelated) situation. In other words, the more signal and idler become distinguishable, the more the Wigner distribution corresponds to the one of a quantum superposition of two distinguishable states, since the Gaussians corresponding to each one of them become farther from the origin. In order to recover the dip representing the Gaussian chronocyclic Wigner distribution of a "quasi-classical" state, one possibility is using Electro Optical Modulators (EOM). But from our analogies, something simpler can be conceived. We can think, for instance, of displacing the filters central frequencies such that $\omega_1 \to \omega_1 - \mu$ and ω_2 remains constant. Then, the exponent in the exponential in Eq. (V.56) would be transformed as $\omega_1 - \omega_2 \to \omega_1 - \omega_2 - \mu$. Varying μ is a way to displace the frequency axis so that eventually it reaches the central point of the two-photon frequency distribution, given by $\mu = \omega_1 - \omega_2$. In this case, we recover photon indistinguishability, as if we had translated the origin of the frequency measurement to the central point of the Gaussian representing one of the two possible classical states, as is usually done in experiments.

To conclude this section, we described in detail a method to realize a quantum eraser experiment. It permits us to distinguish one of the two possible states that form the Schrödinger's cat-like state at the origin of the interference fringes described in Sec. V.3.1. What's more, this method can be generalized to measure the state described by a Gaussian in collective frequency-time phase space centered at the frequency $\mu = \omega_2 - \omega_1$. For such, one could simply change the frequency filters of the previous paragraphs, so that $\omega_s = \omega_2$ and $\omega_i = \omega_1$.

V.3.4 Effect of the time resolution of the photodetector

In this section, we will provide an analogy between the time-resolved HOM experiment and the Young two-slits experiment in the case of two anti-correlated photons in position. In the previous section, the temporal size of the wavepacket δ was much smaller than the integration time T of the photodetector. In this section, we investigate the other limit $\delta \gg T$ and reinterpret the measured spatial beating in coincidence measurement presented in the Refs. [Legero et al., 2004, 2006] in terms of the signature of a frequency-time cat-like state. In this limit, the probability of the joint detection is studied as a function of two temporal parameters, the optical delay between the two arms τ and the time-difference $\overline{\tau}$ between two detections:

$$I(\tau,\overline{\tau}) = \int dt_0 |\langle t_0, t_0+\overline{\tau}|\psi_\tau\rangle|^2. \tag{V.57}$$

The full derivation of this result is presented in Sec. IV.4.2. t_0 is the time of the first detection and $|\psi_\tau\rangle$ is the state after the beam-splitter:

$$|\psi_\tau\rangle = \frac{1}{2}\iint dt_s dt_i (\mathrm{JTA}(t_s-\tau,t_i) - \mathrm{JTA}(t_i-\tau,t_s))\,|t_s,t_i\rangle\,, \tag{V.58}$$

where JTA stands for Joint Temporal Amplitude and is the Fourier transform of the JSA. The coincidence detection probability given by Eq. (V.57) becomes:

$$I(\tau,\overline{\tau}) = \frac{1}{4}[\int dt_0 |\mathrm{JTA}(-\tau+t_0,t_0+\overline{\tau}) - \mathrm{JTA}(-\tau+t_0+\overline{\tau},t_0)|^2]. \tag{V.59}$$

We point out that for a vanishing time difference $\overline{\tau}$, the coincidence detection for any optical time delay and any wave function is zero, a situation which has no equivalent in the experiments described in the present article and is analyzed in [Legero et al., 2006].

We now consider again the experiment where two frequency filters are placed before the beam-splitter, as in the quantum eraser experiment described in Sec. V.3.3. When the optical path delay is set to zero, $\tau = 0$, the probability of the joint detection as a function of the time-difference $\overline{\tau}$ detection shows a spatial beating, as shown in Fig. 4 in Ref. [Legero et al., 2006]. We now explain the physical reason of this beating and interpret it again as the experimental evidence of a frequency-time cat-like state. We start by giving the analytic expression of the coincidence detection probability. The expression of the JTA for two frequency anti-correlated photons, when two spectral filters are placed before the beam-splitter is:

$$\mathrm{JTA}(\overline{\tau}) = e^{-(\omega_1-\omega_2)^2/4\sigma^2} e^{-\overline{\tau}^2\sigma^2/4} e^{-i\overline{\tau}(\omega_1-\omega_2)}, \tag{V.60}$$

where the JTA depends only on the time difference $\overline{\tau} = t_s - t_i$ owing to the anti-correlation in frequencies. Taking into account Eq. (V.59), the joint detection measurement $I(\overline{\tau}) \propto |\mathrm{JTA}(\overline{\tau}) - \mathrm{JTA}(-\overline{\tau})|^2$ becomes:

$$I(\overline{\tau}) = \frac{1}{4}[|\mathrm{JTA}(\overline{\tau})|^2 + |\mathrm{JTA}(-\overline{\tau})|^2 - 2\mathrm{Re}(\mathrm{JTA}(\overline{\tau})\mathrm{JTA}^*(-\overline{\tau}))]. \tag{V.61}$$

Finally using Eq. (V.60) and after normalization, we obtain:

$$I(\overline{\tau}) = \frac{1}{2} e^{-\overline{\tau}^2\sigma^2}(1-\cos(2\overline{\tau}(\omega_1-\omega_2)). \tag{V.62}$$

Alternatively the joint detection can be written as $I(\overline{\tau}) = |\langle\overline{\tau}|\psi\rangle|^2$, where the probability amplitude $\langle\overline{\tau}|\psi\rangle$ is the Fourier transform of the sum of the spectral function of the filters. This measurement gives the marginal of the chronocyclic Wigner distribution $\int d\omega W_{-}(\omega, \overline{\tau}) = I(\overline{\tau})$ and in that sense is perfectly analogous to the intensity measured in a biphoton Young experiment as we shall see in the next section, except for the sign in front of the interference term which comes from the reflectivity of the beam-splitter. The joint detection measurement is represented on Fig. V.12. It shows an oscillatory behavior, which is the marginal of the chronocyclic Wigner distribution of a frequency-time cat-like state along the time axis.

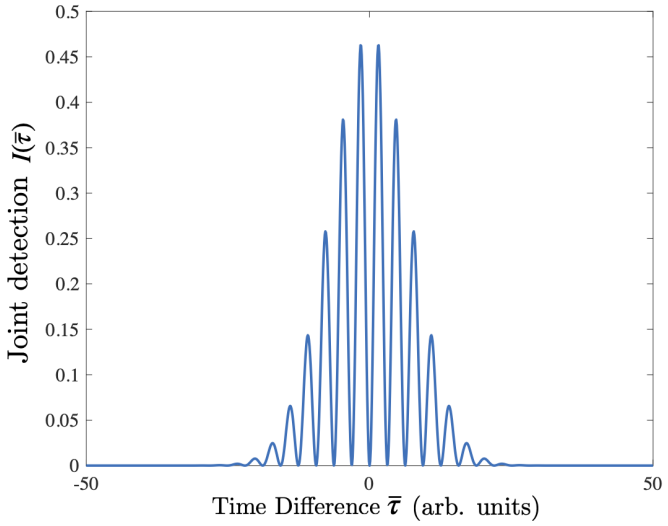

Figure V.12: Joint detection probability $I(\overline{\tau})$ as a function of the time difference $\overline{\tau}$ in arbitrary units. It corresponds to the marginal of the chronocyclic Wigner distribution of a frequency (odd) cat state and differ from the non-resolved HOM experiment (see Fig. V.9 (d)) where the cut of the chronocyclic Wigner distribution is actually obtained. The figure is extracted from [Fabre et al., 2020a].

V.3.5 Double-slit experiment with a biphoton state

We now develop the analogy between the biphoton Young's experiment and the time-resolved HOM experiment. This analogy is useful to understand the previous experiment in terms of frequency-time cat-like state. A similar experiment to the one described below can be found in Refs. [Menzel et al., 2013].

We consider two-position anti-correlated photons which are polarized and sent through two slits: a vertically (V) polarized photon can pass only in the lower slit and a horizontally (H) photon in the upper slit as indicated in Fig. V.13 (c). The spatial degree of freedom in the HOM experiment corresponding to the two ports of the interferometer is translated in the Young's experiment into the polarization since they both constitute discrete degrees of freedom. In the far-field regime using the Fraunhofer approximation, propagation leads to the Fourier transform of the photonic transverse spatial variables [Leibfried et al., 1998, Santos et al., 2018]. Thus, the two slits experiment with anti-correlated photons leads to the generation of position-momentum cat states without post-selection, see Fig. V.13.

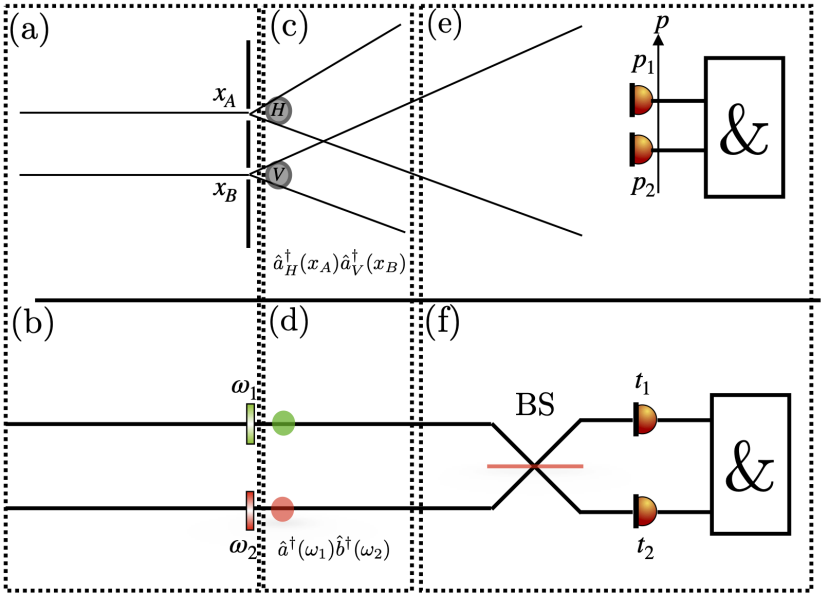

Figure V.13: Analogy between the biphoton Young's experiment and the time-resolved Hong Ou and Mandel interferometer. (a) A biphoton with polarization H/V crosses the slits centered at x_A/x_B. (b) A biphoton state in port A/B cross the filter centered at frequency ω_1/ω_2. (c) Propagation of the biphoton in the near field. (d) Propagation of the biphoton (the dispersion in free space being neglected). (e, f) An even (resp. odd) cat state is produced in the far-field (resp. after the beam-splitter (BS in the figure)) where joint detection measurement is performed. The detection parameters are noted in the two experiments $p_{1/2} = kx_{1/2}/z$ and $t_{1/2}$ but only their difference matter. The figure is extracted from [Fabre et al., 2020a].

Formally, the two-photon cat state can be described by the wave function after the two slits:

$$|\psi\rangle = \iint dx_1 dx_2 F(x_1, x_2) f_{x_A+x_B}(x_+) f_{x_A-x_B}(x_-) \hat{a}_H^\dagger(x_1) \hat{a}_V^\dagger(x_2) \, |0\rangle \, , \tag{V.63}$$

where $F(x_1, x_2)$ is the transverse distribution of the two photon state before the two slits. $\hat{a}_{H/V}^\dagger(x_i)$ is the creation operator of a single photon at position x_i with polarization H/V. The two slits behave as a position filter that can be modeled by a Gaussian function $f_{x_{A/B}}(x) = \exp(-(x - x_{A/B})^2/(2\sigma^2))$, with σ the spatial width of the filter which is analogous to the width of the frequency filter as in Eq. (V.49). We also employed the notation used for the factorized form of the function filters $f_{x_A}(x_1) f_{x_B}(x_2) = f_{x_A+x_B}(x_+) f_{x_A-x_B}(x_-)$ where $x_\pm = x_1 \pm x_2$. We will consider again the factorization $F(x_1, x_2) = \delta(x_+) f_-(x_-)$ and the condition $\sigma \ll \Delta$, where Δ is the width of the slit of f_-. In the near field, we observe two Gaussian peaks which are the slits transmittance.

In the far-field, two detectors are placed at position x_i, $i = 1, 2$ and at a distance from the slits z. Propagation in the far field ($z \gg kx_1^2$) plays the role of the beam-splitter: due to the diffraction, each detector detects photons coming from either slits, forming a coherent superposition of both possible polarized photons that propagated until z. With the same calculation of the previous section, the joint detection $I(\overline{p}) = |\langle \overline{p} | \psi \rangle|^2$ is:

$$I(\overline{p}) = \frac{1}{2} e^{-\overline{p}^2 \sigma^2} (1 + \cos(2\overline{p}(x_A - x_B)), \tag{V.64}$$

where $\overline{p} = k(x_1 - x_2)/z$ which shows the signature of the creation of an even position-momentum cat. Again the amplitude of probability $\langle \overline{p}|\psi\rangle$ corresponds to the coherent sum of the Fourier transform of the transmittance of the slits. This biphoton Young experiment can be considered as a "momentum resolved" detection scheme, where the detection parameter $\overline{p}$ is analogous to the time difference $\overline{\tau}$ in the time-resolved HOM experiment.
The propagation can also be viewed as a $\pi/2$ rotation in the position-momentum phase space, or a Fourier transform. Accessing the marginals of the Wigner distribution between these two limits corresponds to implementing fractional Fourier transform to the state.

V.4 Pump engineering: Fermionisation

In this section, we explain how to engineer the antisymmetry of the JSA of a photon pair with a transversally pumped optical integrated device (see Sec. IV.1.4). A phase mask realized with a SLM is placed before the pump enters the integrated circuit, as represented in Fig. V.14.

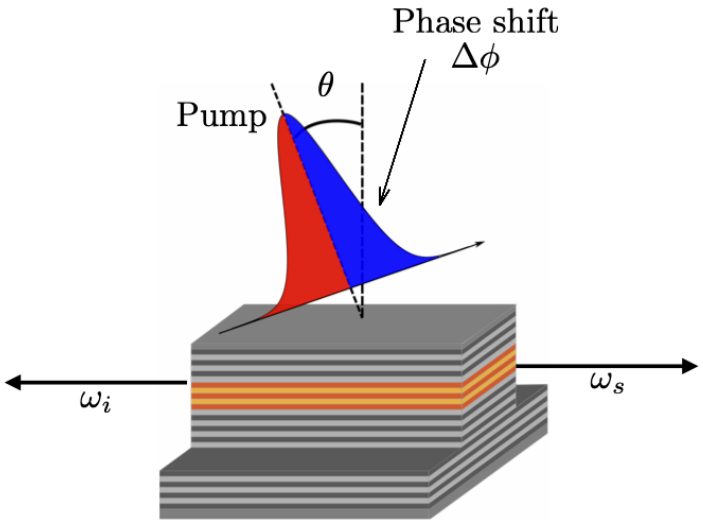

Figure V.14: Sketch of the pumping geometry before the integrated waveguide. Two photons are generated by SPDC whose Joint spectral Amplitude is modified accordingly to the phase shift.

To model the phase mask, the pump amplitude can be written as $\mathcal{A}_p(z) = F(z)e^{-z^2/w_p^2}e^{ikz}$, where F is the transparency of the SLM and w_p is the spatial width of the pump. In our case, it can be written under the form $F(z) = 1$ for $z < 0$ and $F(z) = e^{i\Delta\varphi}$ for $z > 0$. The phase-matching function can be written as (see Sec. IV.1.4):

$$\phi_{\mathrm{PM}}(\omega_s,\omega_i) = \int_{-L/2}^{0} dz\, e^{-z^2/w_p^2} e^{i(\omega_s-\omega_i)z/v_g} e^{i(k-k_{\mathrm{deg}})z} + e^{i\Delta\phi}\int_{0}^{L/2} dz\, e^{-z^2/w_p^2} e^{-i(\omega_s-\omega_i)z/v_g} e^{i(k-k_{\mathrm{deg}})z}. \tag{V.65}$$

After performing a change of variable in the first integral $z \to -z$ and pumping at the degenerescence angle, meaning the condition $k = k_{\mathrm{deg}}$, the phase-matching function becomes:

$$\phi_{\mathrm{PM}}(\omega_s,\omega_i) = f(\omega_s,\omega_i) + e^{i\Delta\phi} f(\omega_i,\omega_s), \tag{V.66}$$

with $f(\omega_s, \omega_i) = \int_0^{L/2} dz e^{-z^2/w_p^2} e^{i(\omega_s - \omega_i)z/v_g}$. Note that we can not continuously evolve from bosons statistics to fermions statistic since for phase between zero and π, the phase matching function does not satisfy the condition $\phi_{\mathrm{PM}}(\omega_s, \omega_i) = e^{i\Delta\phi}\phi_{\mathrm{PM}}(\omega_i, \omega_s)$, required to produce anyonic statistisc (see also Eq. (IV.41)). Another phase pattern has to be found to simulate such statistics and will be the subject of further work.

For such frequency spectrum, the two photons are antisymmetric by the exchange of the frequencies: $\mathrm{JSA}(\omega_s, \omega_i) = -\mathrm{JSA}(\omega_i, \omega_s)$, since the f_+ is always symmetric under the exchange of frequencies. The photon pairs are in different paths and have different polarization, they are hence distinguishable. The symmetrization postulate does not apply on this step, the full wave function being antisymmetric under the permutation of the photons, it does not contradict the fact they are bosons. With such a spectrum, we can obtain the signature of fermionic statistics. There is no actual physical transformation that changes the nature of the particle. But with such a spectrum, writing the state as $|\psi\rangle = \iint \mathrm{JSA}(\omega_s, \omega_i)\hat{a}^\dagger(\omega_s)\hat{a}^\dagger(\omega_i)d\omega_s d\omega_i$ and applying the permutation operator P gives: $P|\psi\rangle = -|\psi\rangle$, and using the fact that photons are bosons (see IV.4.1). Alternatively, the same wavefunction could be obtained with a symmetric spectrum and with fermions. For that reason, the engineering of the antisymmetry of the frequency spectrum of the photons pairs is called fermionisation. A similar operation but using the transversal degree of freedom of single photons was done the first time in [Walborn et al., 2003] in bulk optical medium and then [Jin et al., 2018], it was then realized using integrated waveguide in [Matthews et al., 2013].

To go further analytically, we can evaluate the previous integral since the size of the circuit L is such that $L \gg w$. The bound of the integral is thus set from 0 to the infinity. The phase matching function can be written as:

$$\phi_{\mathrm{PM}}(\omega_s, \omega_i) = w[e^{i\Delta\phi}\mathrm{fadf}(\frac{\omega_- w}{v_g}) - (\mathrm{fadf}(\frac{\omega_- w}{v_g}) - 2e^{-(\omega_- w_p/v_g)^2/4})], \tag{V.67}$$

where fadf is the faddeeva function defined by $\mathrm{fadf}(x) = e^{-x^2}\mathrm{erfc}(-ix)$, erfc being the complex error function.

The coincidence measurement measured with the HOM experiment allows obtaining the signature of the symmetry of the JSA. Modifying the phase of the SLM, the exchange particle statistic evolves (not continuously) from a Bose-Einstein ($\Delta\phi = 0$) to a Fermi-Dirac one ($\Delta\phi = \pi$).

The coincidence probability as a function of the JSA of the signal and idler photons is given by Eq. (IV.51). If the JSA is symmetric under the exchange of the photons, then $I(\tau) = \frac{1}{2}(1 - \mathrm{Re}\iint d\omega_s d\omega_i \mathrm{JSI}(\omega_s, \omega_i)e^{i\omega_-\tau})$. At zero delay $I(\tau = 0) = 0$ which means that for a symmetric spectrum the photons bunched and the absence of coincidence is the signature of the bosonic statistic. If the JSA is antisymmetric under the exchange of particle

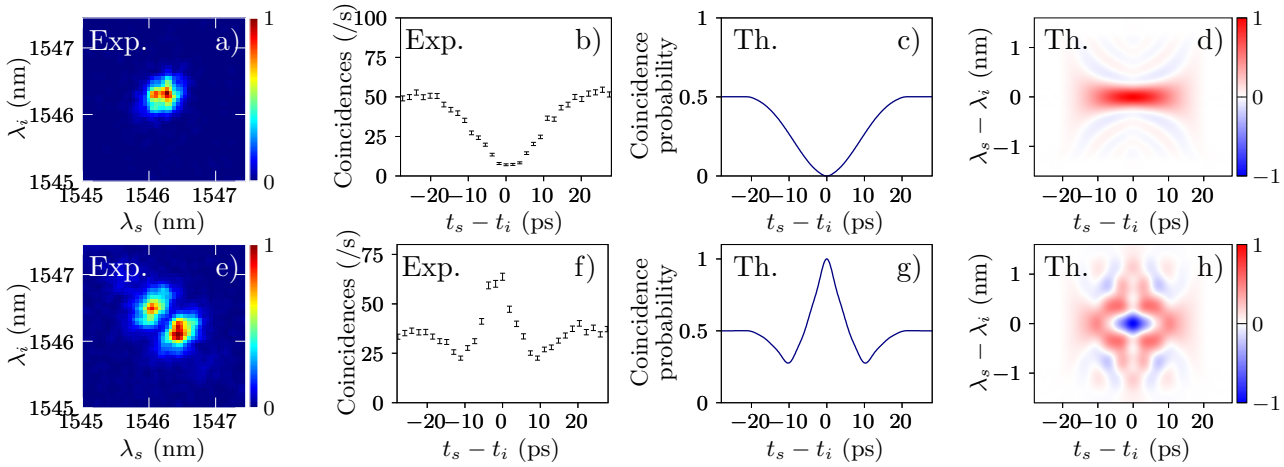

Figure V.15: (a) Measured JSI for a Gaussian pump beam, leading to a symmetric frequency-entangled state. (b) Corresponding measured and (c) calculated coincidences in a Hong-Ou-Mandel experiment, and (d) calculated chronocyclic Wigner function W_- (normalized so that ± 1 corresponds to a HOM dip (peak) of full visibility). (e-h) Same as (a-d) but when applying a π phase step at the center of the pump beam, leading to an antisymmetric frequency-entangled state (reproduced from Ref. [Francesconi et al., 2020])

$I(\tau) = \frac{1}{2}(1 + \mathrm{Re}\iint d\omega_s d\omega_i \mathrm{JSI}(\omega_s, \omega_i) e^{i\omega_- \tau})$, then at zero time delay $I(\tau = 0) = 1$, the photons antibunched and we obtain the signature of fermionic statistic.

The experimental results are presented in Fig. V.15(b)(f) along with the theoretical prediction (c),(g) for a symmetric and antisymmetric JSA. The negativity of the chronocyclic Wigner distribution, or equivalent having a coincidence probability higher than 1/2 (see Fig. V.15) is a necessary condition for entanglement of time-frequency variables of the photons pairs, and more precisely it constitutes a non-Gaussian entanglement witness. The full tomographical reconstruction of W_- can be done using a frequency shift as mentioned in IV.4.4.1. W_+ could be also measured using the device presented in IV.4.4.2, but it also requires an EOM. The measurement of the full Wigner distribution, without measuring the JSA could be done in principle. Nevertheless, in the case of this counter-propagating device, changing the pump incidence allows us to scan the full Wigner distribution W_-, and is hence less demanding in terms of optical material than an EOM.

V.5 Proposal of experimental realization of time-frequency gates

The goal of this part is also to provide the possible experimental implementation of time-frequency gates realized in various experimental groups. The aim is not to give all the experimental details, but to provide possible experimental implementations.

V.5.1 Single photon gate

We start by considering single photon gates, introducing both Gaussian and non-Gaussian time-frequency gates.

Time and frequency displacement operators Time and frequency displacement operators can be implemented thanks to linear phase in frequency or time. Free propagation of a single photon during a time t_0 in a linear media creates a temporal shift ($\phi(\omega) = \omega t_0$) and implements the time displacement operator $\hat{\mathcal{D}}(t_0)$. The Chronocyclic Wigner distribution becomes $W_{\hat{\rho}}(\omega, t) \rightarrow W_{\hat{\rho}}(\omega, t - t_0)$. Such an elementary gate is used in the HOM experiment, as described previously.

A frequency shift of the order of MHz, needed for our experiment, could be realized with an EOM, for implementing the frequency displacement operator $\hat{D}(\omega_0)$. The phase modulation over time is a linear ramp $\phi(t) = \omega_0 t$, such that the Chronocyclic Wigner distribution becomes $W_{\hat{\rho}}(\omega, t) \rightarrow W_{\hat{\rho}}(\omega - \omega_0, t)$. Frequency translation in fiber using four-wave mixing process was proposed [McGuinness et al., 2011], But the efficiency of the generation process is quite low. Any measurement which demonstrated a similar manipulation is for now classical, since it requires a coherent seed pump to amplify the signal of a single photon, as it is frequently the case in this encoding. In [McGuinness et al., 2011], frequency displacement was proposed by using an active beam-splitter, *i.e* whose the reflectivity and the transmissivity depend on the frequency.

Rotation in phase space: Fractional Fourier transform Realizing a Fractional Fourier transform in transversal position and momentum (x, p) variables can be done in three successive steps [Tasca et al., 2011, 2009]. First, a free propagation along the z axis, which introduces a quadratic phase in momentum as $e^{i\pi\lambda z p^2}$ (in the paraxial approximation). A second step consists of placing a lens of focal length f' which introduces a quadratic position phase $e^{-i\pi x^2/\lambda f}$. The final and third step is again a free propagation. The Wigner distribution becomes after these three steps:

$$W_{\hat{\rho}}(x', p') \rightarrow W_{\hat{\rho}}(x'\cos(\theta) + p'\sin(\theta), -x'\sin(\theta) + p'\cos(\theta)), \tag{V.68}$$

where the rescaled position and momentum variables are defined by $x' = x/d_\theta$, $p' = d_\theta p$ with $d_\theta = \sqrt{f'\sin(\theta)/k}$ and the parameters $z = 2f\sin^2(\theta)/2$, $f = f'/\sin(\theta)$. In the case where $z = f'$, we obtain $\theta = \pi/2$ which corresponds to a Fourier transform, a rotation of $\pi/2$ in the phase plane of transversal position and momentum variables. For any other values of θ, a fractional Fourier transform is performed, namely a θ rotation in the transversal position and momentum phase space of a single photon. Mapping the frequency into transversal degree of freedom using a grating could allow to use the presented technique to perform the fractional Fourier transform.

Alternatively, in order to realize a Fractional Fourier transform in time-frequency variables (ω, t), we proceed to three steps. First, we have to introduce a quadratic frequency phase, second a quadratic time phase and then another quadratic frequency phase, and is represented in Fig. V.16. The quadratic frequency phase can be realized with an optical fiber making use of the second order dispersive effect. The device presented in Ref. V.2.3 is more efficient for controlling such phase. The advantage to use these three successive steps is to avoid errors due to the positioning of the optical elements.

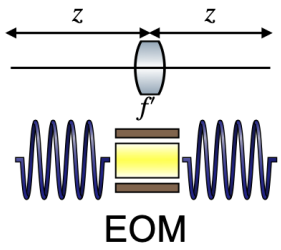

Figure V.16: Fractional Fourier transform in transversal position-momentum and its equivalent with time-frequency variables. The free propagation in transversal position momentum variables is equivalent to the second order dispersive effect in an optical fiber. The action of the lens is analogous to the experimentally controlled modulation of an EOM.

Squeezing-type operation We are now discussing some experimental implementation of this operation. By changing the incidence angle of the pump spectrum in the counter-propagating integrated device presented in Sec. IV.1.4, the ratio between the minor and major axis of the elliptical JSA can be modified. Hence the "squeezing" of this analog two-modes squeezed state. Such operation can be performed in different optical devices which produce photons pairs with techniques depending on the considered platform, or directly on a single photon state.

We also mention an original proposal to perform this squeezing operation by moving a beam-splitter which makes use of the Doppler effect in [Raymer et al., 2010]. Optical alignment is an issue in such experiments, as well as the spatial overlap of the two input crossing beams and the considered mirror velocity.

Cubic phase gate Finally, non-Gaussian gates in this CV can be done easily experimentally. The $4f$ optical scheme described in Sec. V.2.3 can be used to implement a quadratic and cubic phase gate (or higher-order) The SLM allows simulating higher-order dispersion, or alternatively, it can be used to compensate such effect and could be considered as error correction. A signature of third-order dispersive effect can be observed with HOM interferometry [Mazzotta et al., 2016]. Such a phase creates small shoulders on the left of the central dip of the HOM trace. It happens when the phase-matching width is larger than the pump width with at least a factor 20. When it is not the case, the HOM trace is symmetric. The effect of the cubic phase is well known on an intense laser field and is an issue for producing short femtosecond pulses as it broadens the spectrum of the laser field and does not remain symmetric with respect to the central frequency.

V.5.2 Two-photons gate

We have seen in Sec. V.2.1 that the non-linear interaction of the integrated source can performed the gate $\hat{C} = \iint d\omega_s d\omega_i \hat{a}^\dagger(\omega_s+\omega_i)\hat{a}^\dagger(\omega_s-\omega_i)\hat{a}(\omega_s)\hat{a}(\omega_i)$ on a fictitious time-frequency grid state.

We can note that of the experimental demonstration of the combination of two single photons converted into a single photon of higher energy by sum-frequency generation [Guerreiro et al., 2014], with an efficiency of 10^{-8}. But the measurement of the frequency spectrum of the generated photon is classical because a seed is used to amplify the sum-frequency generated single photon. It is nevertheless encouraging for experiments in the quantum regime.
Other experimental proof of two photons gate was also performed. Frequency entanglement swapping was also realized in [Merkouche et al., 2018]. In [Lukens and Lougovski, 2017], the authors defined a frequency qubits as two different colors. Two-photons gates were performed by optimizing successive pulse shaper and electro-optic modulator. While it sounds very promising, the losses are quite important mainly due to the fact that such optical schemes require many optical elements. Frequency domains beam-splitter are based on a second-order nonlinear optical effect in a periodically-poled lithium niobate waveguide with a strong pump light, and can also be combined to create frequency domain Mach-Zender interferometer as demonstrated in [Kobayashi et al., 2017].

Chapter VI

Combining time-frequency and particle-number degree of freedom: a functional phase space approach

The aim of this chapter is to provide a full description of a photonic quantum state which combines both frequency spectrum and quadrature position-momentum continuous variables. In general, it can be done with three approaches, as it generally is in quantum mechanics. The first one is by using a functional space approach as in this recent paper [Roux, 2018], the second with a path-integral approach. The third one is by using a functional phase space approach [Roux, 2020b] and is going to be studied in detail in this chapter. This chapter is mainly based on the results presented in [Roux and Fabre, 2020].

VI.1 Motivation

The Wigner functional phase space quasi-probability distribution for bosonic and fermionic field was introduced in Ref. [Mrowczynski, 2013, Mrowczynski and Mueller, 1994] in particle physics and for describing the electromagnetic field in [Bialynicki-Birula, 2000]. We review the full derivation of such distribution from a general functional quantization procedure and its application in quantum optics. The point is that this description combines both the frequency spectrum and the particle-number degree of freedom of the field. The point of this chapter is to consider the spectral function $F(\omega)$ as a continuous variable itself. We give some examples of the functional Wigner distribution for multimode usual states in Sec. VI.4. An important point is that this functional distribution can be considered as the *mother* of all Wigner quasi-probability distributions. Indeed, we show by fixing the frequency mode or by fixing the particle-number of the functional Wigner distribution, we can recover the CV Wigner distribution (see Eq. II.89) and the chronocyclic Wigner one respectively, shown in Sec. VI.5. It comes from the fact all the considered phase spaces are symplectic.

One motivation for such a study is for quantifying the high dimensional entanglement between different continuous variables degree of freedom [Roux, 2020b] of state produced by SPDC,

as the transversal and particle number CV. Further motivations for quantum simulation and computation is given in the conclusion of this chapter.

VI.2 Functional space approach for describing multiphoton state with continuous degree of freedom

To fix our notation, we start by giving an introduction of the Functional space approach to describe a quantum multi-photon state with a frequency spectrum continuous variable degree of freedom, inspired by [Roux, 2018]. In [Roux, 2018, Roux and Fabre, 2020] the formalism is more general since it includes all spatio-temporal degrees of freedom. We first show how a functional space approach can be useful for studying a single-photon in many continuous modes. It will allow setting the notation for this chapter. Then, we will combine the particle-number and the frequency spectrum degree of freedom by first considering Fock states and quadrature position-momentum states with a continuous variable spectrum. Then, we introduce the bosonic coherent state which is a coherent state with a continuous mode spectrum, useful for building the functional phase space.

VI.2.1 Single-photon with a continuous multi-spectrum

As described in Chap. III, a single-photon with an amplitude-frequency spectrum $S \in L^2(\mathbb{R})$ is described by the wave function $|S\rangle = \int d\omega S(\omega) |\omega\rangle$ as in Eq. (III.4). We may consider the possible uncertainty of the generation process of the spectrum of a single-photon source, intrinsic to a given experimental device. Such motivation was first formulated [Roux, 2017] for describing the quantum state of a frequency comb. This uncertainty could have a possible consequence in metrology. But the presented functional aspect of the space to describe such state with continuous spectrum was not used in this paper and it is the aim of what it follows.

Let us consider an experimental device which produces a single-photon with different spectrum S_i, which are not necessarily orthogonal. The wave function could be written as $|\psi\rangle = \psi_1 |S_1\rangle + \psi_2 |S_2\rangle + ... = \sum_i \psi_i |S_i\rangle$. The sum can be compactly written as:

$$|\psi\rangle = \int_{L^2(\mathbb{R})} \mathcal{D}[S]\psi[S] |S\rangle , \tag{VI.1}$$

where $\mathcal{D}[S]$ stands for the functional integration and reads as a sum over a set of orthogonal complex modes function $\mathcal{D}[S] = \int \prod_i \frac{1}{\pi} d\mathrm{Re}S_i \mathrm{Im}S_i$ where again $S_i \in L^2(\mathbb{R})$. The set of functions which are summed can be of a finite or infinite cardinal. We are considering the spectral function as continuous variables. We remind that a continuous variable is any variable defined on the real line. An infinite number of continuous degrees of freedom can be either a countable infinite set of continuous degrees of freedom or an uncountable (in other words, continuous) infinite set of continuous degrees of freedom. We say a set A is countably infinite if $\mathbb{N} \equiv A$ which means that A has the same cardinality as the natural numbers. We say that A is countable if it is finite

or countably infinite.

The infinity set of functions can be either Dirac distributions, since $\delta \in L^2(\mathbb{R})$, or we can sum over the Laguerre polynomials for instance. In the second case, each orthogonal mode S_i can also be decomposed into monochromatic modes δ, which compose the interior of each polynomial, but they are not the one which are summed.

The scalar product $\langle S|\psi\rangle = \psi[S]$ corresponds to a sum of the overlap of S with all S_i of the wave function. The notation between braket [ ] denotes that the quantity is a functional, a function of function. $\psi[S]$ is then a functional, which takes as argument a function and maps it into a complex value number.

In order to make this decomposition Eq. (VI.1), we have assumed that $|S\rangle$ is an overcomplete basis (since it is not orthogonal): $\int \mathcal{D}[S]\,|S\rangle\langle S| = \mathbb{I}$, which is now demonstrated. We first can write $\int_{L^2(\mathbb{R})} \mathcal{D}[S]\,|S\rangle\langle S| = \int \mathcal{D}[S] \iint d\omega d\omega' S(\omega)S^*(\omega')\,|\omega\rangle\langle\omega|$. The functional integral can be calculated if we impose the equivalent of completeness condition over the space of function [Roux, 2018]:

$$\int_{L^2(\mathbb{R})} \mathcal{D}[S]S(\omega)S^*(\omega') = \delta(\omega - \omega'), \tag{VI.2}$$

which is valid if we are summing over a set of functions with a finite cardinal and not an infinite one as shown in Ref. [Roux, 2020a]. Indeed, by integrating over ω and ω', the left-hand side of the equation is equal to $\int \mathcal{D}[S]$ which is equal to the cardinality of the considered set of function. The right-hand side gives:

$$\int_{\mathbb{R}} \delta(0)d\omega = \Omega \tag{VI.3}$$

which is associated with the cardinal of the countable infinite. Hence, if the sum is taken with respect to an infinite cardinal set, the two sides of Eq. VI.2 can not be equal. It is the main difficulty in this type of continuous variables $S(\omega)$: if the sum is handled over an infinite set of square normalizable functions, many mathematical results from quadrature position-momentum CVs can not be reused in that context . We will precise when it is the case and when it can be circumvented.

VI.2.2 Fixed-spectrum Fock states

We now define the fix-spectrum Fock states [Roux, 2018] which are Fock states with a spectral frequency distribution S considered as a continuous variable. As we will see, the fix-spectrum Fock states do not have the mathematical property to be a convenient building block for building other states which combine both particle-number and spectrum degrees of freedom. In Fig. VI.1, we represent the general approach. how from a single-photon with a functional description of its degree of freedom, we lift the restriction of the single-photon subspace to study multiphoton indistinguishable state, because each photon will have the same spectrum S.

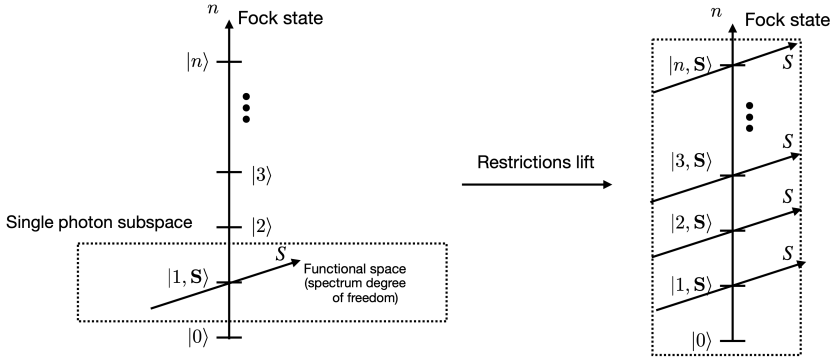

Figure VI.1: We start from a single-photon with a continuous multi-spectrum, which leads to a functional space description of the state. We then study all degrees of freedom of a quantum field, without restriction on its particle number. The axis directed by S represents the spectral function degree of freedom, which is a continuous one.

Quantum system of bosonic identical particles is described by the tensorial product of Hilbert space h as follows $H = \bigotimes_{i=1}^{n} h_i$. Each particle has its states in h. As in Chap. III for the study of a single-photon, the Hilbert space h is $L^2(\mathbb{R})$, the space of square normalizable function, describing the frequency degree of freedom or in our study the frequency spectrum. The number of photons here is fixed, so that the full Hilbert space is not a Fock space. We consider that each photon is indistinguishable and characterized by the same spectrum $S \in L^2(\mathbb{R})$. Such fix-spectrum Fock states can be written as:

$$|n, \mathbf{S}\rangle = \frac{1}{\sqrt{n!}}(\hat{a}^\dagger[S])^n |0\rangle = \frac{1}{\sqrt{n!}} |1, \mathbf{S}\rangle \otimes ... \otimes |1, \mathbf{S}\rangle . \tag{VI.4}$$

The bold letter $\mathbf{S}$ is used to indicate that the variables in the ket is a mode function. Each photon possesses a discrete degree of freedom labeled by a, which denotes the polarization degree of freedom or any other. The scalar product of two Fock states with different spectrum is:

$$\langle n, \mathbf{S} | m, \mathbf{S}' \rangle = \delta_{n,m}(\langle \mathbf{S} | \mathbf{S}' \rangle)^n, \tag{VI.5}$$

which means that the fix-spectrum Fock states are not orthogonal but they are normalized since we have the condition $\langle n, \mathbf{S}|n, \mathbf{S}\rangle = 1$. The next step would be to expand a wave function using the fix-spectrum Fock states $|\psi\rangle = c[S_1] |n, \boldsymbol{S}_1\rangle + c[S_2] |n, \boldsymbol{S}_2\rangle + ... = \int_{L^2(\mathbb{R})} \mathcal{D}[S] c[S] |n, \boldsymbol{S}\rangle$ which corresponds to an infinite coherent superposition of a fix-number Fock state with different spectrum. It would be an extension of the usual result in the monochromatic limit: $|\psi\rangle = \sum_n c_n |n\rangle$, where $c_n \in l^2(\mathbb{N})$. But this mathematical expansion is not valid. Indeed, the completeness relation of the fix-spectrum Fock states is not verified as demonstrated in [Roux, 2018]:

$$\int_{L^2(\mathbb{R})} \mathcal{D}[S] \sum_n |n, \mathbf{S}\rangle \langle n, \mathbf{S}| \neq \mathbb{I}. \tag{VI.6}$$

It comes from the fact that once the functional integration over S is handled, it gives a number depending on n, which once it is summed, it does not give the identity [Roux, 2020a]. In conclusion, the fixed-Fock states $|n, \mathbf{S}\rangle$ do not form a basis. Mathematically speaking, it means that

we can not translate all the results, mathematical tricks involving the Fock states developed in the quantum optics formalism in our context.

In the case where the n photons have distinguishables spectra, its wave function can be written under the form $|1,\mathbf{S_1}\rangle \otimes ... \otimes |\mathbf{1},\mathbf{S_n}\rangle$ where the first photon has a spectrum S_1, the second S_2 etc. The action of annihilation and creation operators $\hat{a}[S]$ and $\hat{a}^\dagger[S]$ of spectrum S on such multiphoton state is:

$$\hat{a}[S]\,|1,\mathbf{S_1}\rangle \otimes ... \otimes |1,\mathbf{S_n}\rangle = (n+1)^{1/2}\,\langle 1,\mathbf{S}|1,\mathbf{S_1}\rangle\;\; |\mathbf{1},\mathbf{S_2}\rangle \otimes ... \otimes |1,\mathbf{S_n}\rangle \tag{VI.7}$$

$$\hat{a}^\dagger[S]\,|\mathbf{1},\mathbf{S_1}\rangle \otimes ... \otimes |1,\mathbf{S_n}\rangle = n^{-1/2}\,|1,\mathbf{S}\rangle\,|1,\mathbf{S_1}\rangle \otimes ... \otimes |1,\mathbf{S_n}\rangle\,. \tag{VI.8}$$

Since all the photons are uncorrelated, namely a tensor product, we can develop a wave function in a functional space describing the frequency spectrum for each single photon:

$$|\psi\rangle = \int_{L^2(\mathbb{R})} \mathcal{D}[S_1]\psi[S_1]\,|1,\boldsymbol{S}_1\rangle \otimes ... \otimes \int_{L^2(\mathbb{R})} \mathcal{D}[S_n]\psi[S_n]\,|1,\boldsymbol{S}_n\rangle\,, \tag{VI.9}$$

since this expansion does not need the completeness relation of the fixed-number Fock states but only the completeness relation for the spectrum (see Eq. (VI.2)).

We now demonstrate some relations on the action of the creation and annihilation operator at frequency ω on the fixed-spectrum Fock state. We have:

$$\hat{a}(\omega)\,|n,\mathbf{S}\rangle = S(\omega)\sqrt{n}\,|n-1,\mathbf{S}\rangle\,, \tag{VI.10}$$

where we have used the bosonic commutation relation Eq. (III.2). The number operator $\hat{n}(\omega) = \hat{a}^\dagger(\omega)\hat{a}(\omega)$ of photons at frequency ω acts on a number Fock state with amplitude spectrum $S(\omega)$ as:

$$\hat{n}(\omega)\,|n,\mathbf{S}\rangle = nS(\omega)\hat{a}^\dagger(\omega)\,|n-1,\mathbf{S}\rangle = nS(\omega)\,|n-1,\mathbf{S};1,\omega\rangle\,, \tag{VI.11}$$

where we have used the commutation relation $[n(\omega),\hat{a}^\dagger(\omega')] = \delta(\omega-\omega')\hat{a}^\dagger(\omega)$. From these two last equations, we deduce the action of the annihilation operator $\hat{a}^\dagger(\omega)$ on a fixed-spectrum Fock state is:

$$\hat{a}^\dagger(\omega)\,|n,\mathbf{S}\rangle = \sqrt{n+1}\,|n,\mathbf{S};1,\omega\rangle\,. \tag{VI.12}$$

The photon number operator with spectrum S is defined by $\hat{n}[S] = \hat{a}^\dagger[S]\hat{a}[S]$ and verifies the eigenvalues equation:

$$\hat{n}[S]\,|n,\mathbf{S}\rangle = n(\int_{\mathbb{R}} d\omega|S(\omega)|^2)\,|n,\mathbf{S}\rangle = n\,|n,\mathbf{S}\rangle\,, \tag{VI.13}$$

which is proven in Appendix A.2.2. From this last relation, we deduce that a photon number sensitive detector, described crudely by $\hat{n}[S]$, which has a frequency resolution characterized by a Gaussian spectrum S is able to count n photons. If the detector has a spectral characteristic S' different from the state to measure, which is generally the case in the experiment, the number of photons detected will be less than n, as we have:

$$\hat{n}[S']\,|n,\mathbf{S}\rangle = n(\int_{\mathbb{R}} d\omega S(\omega)S'^*(\omega))\,|n,\mathbf{S}\rangle\,. \tag{VI.14}$$

This overlap $(\int d\omega S(\omega)S'^*(\omega))$ causes an error which reduces the number of photons effectively detected.

VI.2.3 Fixed-entangled-spectrum Fock state

In the previous section, we assume that the n photons of the fix-spectrum Fock states had the same spectrum S or that they had different spectrum $(S_i)_{1\leq i\leq n}$. In order to complete the landscape of the n photons state with spectral distribution degree of freedom, we now consider a n particle state which is entangled in frequency, characterized by the distribution F, as follows:

$$|F_n\rangle = \frac{1}{n!}\int_{\mathbb{R}} d\omega_1 ... \int_{\mathbb{R}} d\omega_n F(\omega_1, ..., \omega_n)\hat{a}^\dagger(\omega_1)...\hat{a}^\dagger(\omega_n)\,|0\rangle\,, \tag{VI.15}$$

where F is a symmetric function of the frequency and the normalisation of the state reads $\frac{1}{n!}\iint d\omega_1 ... d\omega_n |F(\omega_1, ..., \omega_n)|^2 = 1$. There are $n!$ different terms: n particles can have the frequency ω_1 and $n-1$ with ω_1 and 1 with ω_2 and so on. This state can not be factorized into a product of single-photon states, where each one of them has a normalized spectrum S as in the previous section. In practice, the state can have additional degrees of freedom that distinguish the photons, such as polarization or spatial path. An example with $n = 2$ is given by the biphoton state produced by a type-II SPDC (see Sec. III.11) where the indiscernability factor $1/n!$ is not present in that case since the pair has different polarization.

VI.2.4 Fixed-spectrum quadrature position-momentum basis

We provide in this section the position-momentum basis which contains also the spectrum continuous degree of freedom. The position and momentum quadrature operators for a monochromatic field at frequency ω are defined by:

$$\hat{Q}(\omega) = \frac{1}{\sqrt{2}}(\hat{a}(\omega) + \hat{a}^\dagger(\omega)), \tag{VI.16}$$

$$\hat{P}(\omega) = \frac{1}{\sqrt{2}i}(\hat{a}(\omega) - \hat{a}^\dagger(\omega)), \tag{VI.17}$$

which corresponds to the usual quadrature position-momentum operators in quantum optics, *i.e* when considering a harmonic oscillator which vibrates at frequency ω, where the frequency label is always implicit. They obey to the commutation equation:

$$[\hat{Q}(\omega), \hat{P}(\omega')] = i\delta(\omega - \omega'). \tag{VI.18}$$

The generalization of the quadrature operators in the polychromatic case, the fixed-spectrum quadrature position-momentum quadrature operators, *i.e* for a physical frequency mode, is:

$$\hat{Q}[S] = \frac{1}{\sqrt{2}}(\hat{a}[S] + \hat{a}^\dagger[S]), \tag{VI.19}$$

$$\hat{P}[S] = \frac{1}{\sqrt{2}i}(\hat{a}[S] - \hat{a}^\dagger[S]). \tag{VI.20}$$

They are also called Segal operators [Combescure and Robert, 2012] and they do not correspond to a direct integration of Eq. (VI.16). The fixed-spectrum quadrature operators verify the commutation equation:

$$[\hat{Q}[S], \hat{P}[S']] = i\mathrm{Im}(\langle \mathbf{S}|\mathbf{S}'\rangle). \tag{VI.21}$$

The fixed-spectrum position-momentum basis is defined by:

$$|\mathbf{q}\rangle = \hat{C}[q]\,|0\rangle\,, \tag{VI.22}$$

$$|\mathbf{p}\rangle = \hat{C}[p]\,|0\rangle\,, \tag{VI.23}$$

with the creation operators $\hat{C}[q/p]$ operators are given by:

$$\hat{C}[q] \propto \exp\left(-\tfrac{1}{2}|q|^2 + \hat{a}^\dagger[q] - \hat{b}^\dagger\right), \tag{VI.24}$$

$$\hat{C}[p] \propto \exp\left(-\tfrac{1}{2}|p|^2 + i\hat{a}^\dagger[p] + \hat{b}^\dagger\right), \tag{VI.25}$$

where

$$\hat{a}^\dagger[q] = \sqrt{2}\int_{\mathbb{R}} \hat{a}^\dagger(\omega)q(\omega)d\omega, \tag{VI.26}$$

$$\hat{a}^\dagger[p] = \sqrt{2}\int_{\mathbb{R}} \hat{a}^\dagger(\omega)p(\omega)d\omega, \tag{VI.27}$$

$$\hat{b}^\dagger = \frac{1}{2}\int_{\mathbb{R}} \hat{a}^\dagger(\omega)\hat{a}^\dagger(\omega)d\omega, \tag{VI.28}$$

and

$$|q|^2 = \int_{\mathbb{R}} d\omega |q(\omega)|^2,\ |p|^2 = \int_{\mathbb{R}} d\omega |p(\omega)|^2. \tag{VI.29}$$

The generalization of these last operators for all spatio-temporal degrees of freedom is provided in [Roux, 2020a, Roux and Fabre, 2020]. The proportional sign $\propto$ in Eq. (VI.24) indicates a non-trivial normalization condition owing to the existence of combinatorial terms, which are specified in [Roux and Fabre, 2020]. The bold character $|\mathbf{q}\rangle$ in the ket means that the state describes both particle-number degree of freedom and the spectral distribution one, in order to distinguish it from the quadrature position ket $|q\rangle$ where q is only sensitive to the particle-number degree of freedom. The fixed-spectrum quadrature position and momentum basis are the eigenstates of the operators defined by Eq. (VI.16):

$$\hat{Q}(\omega)\,|\mathbf{q}\rangle = q(\omega)\,|\mathbf{q}\rangle \tag{VI.30}$$

$$\hat{P}(\omega)\,|\mathbf{p}\rangle = p(\omega)\,|\mathbf{p}\rangle\,. \tag{VI.31}$$

Note that we have $\hat{P}(\omega) = -i\frac{d}{dq(\omega)}$, where the derivative is in our context a functional one. The completeness condition of the fixed-spectrum quadrature position and momentum basis holds and reads:

$$\int_{L^2(\mathbb{R})} \mathcal{D}[q]\,|\mathbf{q}\rangle\langle\mathbf{q}| = \mathbb{I},\ \int_{L^2(\mathbb{R})} \mathcal{D}^\circ[p]\,|\mathbf{p}\rangle\langle\mathbf{p}| = \mathbb{I}. \tag{VI.32}$$

Note the important change in the functional integration: $\mathcal{D}^\circ[p] = \mathcal{D}[p]/(2\pi)^\Omega$. The factor $(2\pi)^\Omega$ is important to ensure the completeness relation (see Ref. [Roux, 2020a]) where $\Omega = \int \delta(0)d\omega$ is the cardinality of a countable infinite set. The fixed-spectrum quadrature position and momentum basis is also orthogonal as proven in Ref. [Roux, 2018, 2020a]. The eigenstates $|\mathbf{q}\rangle$ and $|\mathbf{p}\rangle$ are related by a functional Fourier transform:

$$|\mathbf{q}\rangle = \int_{L^2(\mathbb{R})} e^{i\int q(\omega)p(\omega)d\omega}\,|\mathbf{p}\rangle\,\mathcal{D}^\circ[p]. \tag{VI.33}$$

Hence, the fixed-spectrum quadrature position and momentum are a mutually unbiased basis since we have the relation: $\langle \boldsymbol{p}|\boldsymbol{q}\rangle = \exp(-i\int_{\mathbb{R}} d\omega p(\omega)q(\omega))$. Following the completeness relation of such basis, a multimode wavepacket is defined by summing over different functions $q(\omega)$, using the functional integral:

$$|\psi\rangle = \int_{\mathbb{L}^2(\mathbb{R})} \mathcal{D}[q]\psi[q]\,|\mathbf{q}\rangle\,, \tag{VI.34}$$

where $\psi[q] = \langle \mathbf{q}|\psi\rangle$ is a functional ($\mathbb{L}^2(\mathbb{R}) \to \mathbb{C}$). The same wavepacket can also be built using the momentum $|\mathbf{p}\rangle$ basis as:

$$|\psi\rangle = \int_{L^2(\mathbb{R})} \mathcal{D}^{\circ}[p]\tilde{\psi}[p]\,|\mathbf{p}\rangle\,. \tag{VI.35}$$

where again $\tilde{\psi}[p]$ is a functional. Both these wavepackets describing quantum state belong to the functional Hilbert space defined as $\mathcal{L}^2(L^2(\mathbb{R})) = \{\psi[S] \in C^{\infty}, S \in L^2(\mathbb{R})/\int \mathcal{D}[S]|\psi[S]|^2 < \infty\}$, and owing to the normalization of the wave function and the orthogonality relation of the fixed-spectrum position-momentum basis, we have $\int_{L^2(\mathbb{R})} \mathcal{D}^{\circ}[p]\left|\tilde{\psi}[p]\right|^2 = \int_{L^2(\mathbb{R})} \mathcal{D}[q]\left|\tilde{\psi}[q]\right|^2 = 1$.

What is surprising is that even if the decomposition basis is not orthogonal $\langle S|S'\rangle \neq 0$, the fixed-spectrum position-momentum basis are. The functional integral runs over all the square normalizable functions and not only the set of mutually orthogonal functions [Roux, 2020a].

VI.2.5 Fock states expressed in the fixed-spectrum position-momentum basis

In the following, we give the explicit expression of the matrix element $\langle \mathbf{q}|n,\omega\rangle$ which makes naturally appear the Hermite functional, in the same way that the matrix element $\langle q|n\rangle$ depends on the Hermite function. First, the expression of the ground state can be found using the equation: $\langle \mathbf{q}|\,\hat{a}(\omega)\,|0\rangle = 0 = \langle \mathbf{q}|\,(\hat{Q}(\omega) + i\hat{P}(\omega))\,|0\rangle$ which gives:

$$(q(\omega) + \frac{\partial}{\partial q(\omega)})\psi_0[q] = 0, \tag{VI.36}$$

where we have introduced $\psi_0[q] = \langle \mathbf{q}|0\rangle$. Its expression is the following Gaussian functional:

$$\psi_0[q] = \exp(-\frac{1}{2}\int_{\mathbb{R}} q^2(\omega)d\omega) \tag{VI.37}$$

and corresponds to the ground state of a quantum oscillator in a continuum of frequency modes. If the field $q(\omega)$ can be written under the form $q^2(\omega) = \delta(\omega - \omega_0)q^2$, where q denotes the usual quadrature position variable, the state is projected into the monochromatic ω_0 subspace. Indeed, we recover the Gaussian ground state of the monochromatic quantum oscillator, the vacuum state: $\psi_0[\boldsymbol{q} = \delta(\omega - \omega_0)q] = \psi_0(q) = \exp(-q^2/2)$.

The higher-order Hermite polynomial functional can be found using the same technique:

$$\langle \mathbf{q}|n,\omega\rangle = \psi_n[q] = \frac{1}{\sqrt{2^n n!}}(q(\omega) + \frac{\partial}{\partial q(\omega)})^n\psi_0[q] \tag{VI.38}$$

$$= \frac{1}{\sqrt{2^n n!}}\psi_0[q]H_n[q], \tag{VI.39}$$

where the Hermite functional $H_n[q]$ is defined by (under the reserve of its existence):

$$H_n[q] = (-1)^n\exp(\int_{\mathbb{R}} d\omega|q(\omega)|^2)\frac{d^n}{d[q]^n}\exp(-\int_{\mathbb{R}} d\omega|q(\omega)|^2). \tag{VI.40}$$

VI.2.6 Bosonic coherent state

In this section, we define the bosonic coherent state which is the continuous multimode generalization of the coherent state $|\alpha\rangle$. The introduced formalism is generally used to express transition matrix element or Green function in path-integral formalism or for a general phase space quantization.

The bosonic coherent states $|\boldsymbol{\psi}\rangle$ are defined as the eigenstates of the annihilation field operator $\hat{a}(\omega)$ [Combescure and Robert, 2012]:

$$\hat{a}(\omega)\,|\boldsymbol{\psi}\rangle = \psi(\omega)\,|\boldsymbol{\psi}\rangle\,. \tag{VI.41}$$

Such states are also called continuous-mode coherent states or scalar field coherent states. Again, the bold character $|\boldsymbol{\psi}\rangle$ in the ket means that the state contains the description of particle-number degree of freedom and the frequency spectrum one. The bosonic coherent state has the property of being the right eigenstate of the annihilation operator since we have $\hat{a}^\dagger(\omega)$ with the eigenvalues $\psi^*(\omega)$. The bosonic coherent state can be explicitly written as:

$$|\boldsymbol{\psi}\rangle = \exp(\hat{a}^\dagger[\psi] - \hat{a}[\psi])\,|0\rangle\,, \tag{VI.42}$$

where the creation (resp. annihilation) bosonic operator are defined by

$$\hat{a}^\dagger[\psi] = \int_{\mathbb{R}} \psi(\omega)\hat{a}^\dagger(\omega)d\omega, \tag{VI.43}$$

$$\hat{a}[\psi] = \int_{\mathbb{R}} \psi^*(\omega)\hat{a}(\omega)d\omega. \tag{VI.44}$$

The bosonic coherent state $|\boldsymbol{\psi}\rangle$ is also the left eigenvalues of the creation bosonic operator $\hat{a}[\psi']$:

$$\hat{a}[\psi']\,|\boldsymbol{\psi}\rangle = (\int_{\mathbb{R}} d\omega\psi'^*(\omega)\psi(\omega))\,|\boldsymbol{\psi}\rangle\,, \tag{VI.45}$$

which can be obtained by integration of Eq. (VI.41). Despite the mathematical similarity with Eq. (III.4), $\psi(\omega) \in L^2(\mathbb{R})$ is not the amplitude spectrum of a wave function of a single-photon because it contains the particle-number degree of freedom. Indeed, the average value of number operator of spectrum ψ with respect to the bosonic coherent state is:

$$\langle\boldsymbol{\psi}|\,\hat{n}[\psi]\,|\boldsymbol{\psi}\rangle = (\int_{\mathbb{R}} |\psi(\omega)|^2 d\omega)^2, \tag{VI.46}$$

where $\hat{n}[\psi] = \hat{a}^\dagger[\psi]\hat{a}[\psi]$. Thus, if it is equal to one that means that we consider a bosonic coherent state with a mean value of photon equal to one. It does not mean that the state is a single-photon one either. Hence, $\psi \in L^2(\mathbb{R})$ but is not square normalizable to one to take into account the particle-number degree of freedom. Nevertheless, the full wave function $|\boldsymbol{\psi}\rangle$ is normalized to one. In quantum field theory the fact that the field is not normalized is related in that context to the non-conservation of the number of particles during high-energy processes.

We then mention other properties of the bosonic coherent states. Annihilation and creation bosonic operator verify the commutation equation:

$$[\hat{a}[\psi], \hat{a}^\dagger[\psi]] = (\int d\omega |\psi(\omega)|^2)\mathbb{I}. \tag{VI.47}$$

The action of the creation field operator $\hat{a}^\dagger(\omega)$ on a bosonic coherent state is:

$$\hat{a}^\dagger(\omega)\,|\boldsymbol{\psi}\rangle = \frac{\partial}{\partial\psi(\omega)}\,|\boldsymbol{\psi}\rangle\,. \tag{VI.48}$$

The bosonic coherent state can be alternatively written using the fixed-spectrum Fock state:

$$|\boldsymbol{\psi}\rangle = \exp(-\frac{1}{2}\int_{\mathbb{R}} d\omega|\psi(\omega)|^2)\sum_{n=0}^{\infty}\frac{1}{\sqrt{n!}}\,|n,\psi\rangle\,, \tag{VI.49}$$

which is demonstrated in [Combescure and Robert, 2012]. In particular, the probability to have n particles with spectrum $\psi(\omega)$ is given by $\frac{1}{n!}\left|\int\psi(\omega)d\omega\right|^{2n}\exp(-\int d\omega|\psi(\omega)|^2)$. We then recognize the Poisson's distribution, in this continuous multimode case.

Bosonic coherent states are not orthogonal, since the overlap of two such states is given by:

$$\langle\boldsymbol{\psi'}|\boldsymbol{\psi}\rangle = \exp(-\int\left|\psi(\omega)-\psi'(\omega)\right|^2 d\omega)\exp(-i\mathrm{Im}(\langle\boldsymbol{\psi'}|\boldsymbol{\psi}\rangle)), \tag{VI.50}$$

which also shows that the state is normalizable. As demonstrated in [Roux, 2020a] they form an overcomplete basis as the coherent state,

$$\mathbb{I} = \int_{L^2(\mathbb{R})}\mathcal{D}^\circ[\psi]\,|\boldsymbol{\psi}\rangle\langle\boldsymbol{\psi}|\,, \tag{VI.51}$$

where again $\mathcal{D}^\circ[\psi] = \mathcal{D}[\psi]/(2\pi)^\Omega$. Generally, in condensed matter theory when such states are considered, the sum is taken with respect to a finite cardinal's set of functions, so that the cardinality of the countable infinite does not appear.

Alternatively, we can decompose the amplitude of the bosonic coherent state $\psi(\omega)$ into its real and imaginary parts, namely the two quadrature functions $q(\omega)$ and $p(\omega)$: $\psi(\omega) = \frac{1}{\sqrt{2}}(q(\omega)+ip(\omega))$, where these two last functions are real valued. We recall that the field $\psi(\omega)$ is analogous to α and hence the function $p(\omega), q(\omega)$ are mathematically analogous to the continuous variable p, q. The bosonic coherent state using the position-momentum quadrature $\hat{Q}(\omega)$ and $\hat{P}(\omega)$ operators can be written as:

$$|\boldsymbol{\psi}\rangle = |\boldsymbol{q},\boldsymbol{p}\rangle = \exp(i\int d\omega[p(\omega)\hat{Q}(\omega) - q(\omega)\hat{P}(\omega)])\,|0\rangle\,, \tag{VI.52}$$

where we have used Eq. (VI.16). It is the continuous multimode generalization of Eq. (II.111).

The bosonic coherent state can describe the field of a laser neglecting the dissipation and the noise due to spontaneous emission in the atomic laser medium [Van Enk and Fuchs, 2001]. Different temporal noise distributions can be used to model different types of laser, as the phase diffusing one for instance.

Stellar functional and Bargmann-Segal functional space A multiphoton state with a continuous multi-spectrum can be written in the bosonic coherent basis:

$$|\phi\rangle = \int_{L^2(\mathbb{R})} \mathcal{D}^\circ[\psi]\phi[\psi]\,|\boldsymbol{\psi}\rangle\,. \tag{VI.53}$$

$\phi[\psi]$ is called the Stellar functional distribution by the multimode generalization of the Stellar distribution introduced in [Chabaud et al., 2020, Gagatsos and Guha, 2019, Nonnenmacher and Voros, 1997]. This functional distribution can be considered as the square root of the functional Husimi distribution, if and only if the state is pure, which will be defined later (see Eq. (VI.86)). The stellar distribution is an element of the Bargmann-Segal functional space which is the space of holomorphic functional such as

$$\int_{L^2(\mathbb{R})} |\phi[\psi]|^2 e^{-|\psi|^2}\mathcal{D}^\circ[\psi] < \infty. \tag{VI.54}$$

This space (functional or not) is mapped to the Hilbert space by a double modified Weierstrass transform. We do not develop the stellar representation and was just given for the sake of completeness.

P-functional distribution Finally, we introduce the expansion of a density matrix in the diagonal basis of bosonic coherent states, called also the P-representation, as:

$$\hat{\rho} = \int_{L^2(\mathbb{R})} \mathcal{D}^\circ[\psi]P_{\hat{\rho}}[\psi]\,|\boldsymbol{\psi}\rangle\,\langle\boldsymbol{\psi}|\,, \tag{VI.55}$$

where $P_{\hat{\rho}}[\psi]$ is the functional Glauber-Surdashan P-distribution. We now give an example of such distribution for the continuous spectrum multimode thermal state:

$$P_{\hat{\rho}}[\psi] = \frac{1}{\pi\overline{n_\psi}} e^{-|\psi|^2/\overline{n_\psi}}, \tag{VI.56}$$

where $\overline{n_\psi}$ is the number of photons with spectrum ψ. This choice is motivated because it is a functional Gaussian state [Barnett and Radmore, 2002] and because the following probability distribution $P_n[S] = \langle n,[S]|\,\hat{\rho}\,|n,[S]\rangle$ is the Bose-Einstein one. Indeed, such probability distribution can be written as:

$$P_n[S] = \int_{L^2(\mathbb{R})} \mathcal{D}^\circ[\psi]P_{\hat{\rho}}[\psi]|\langle n,[S]|\psi\rangle|^2, \tag{VI.57}$$

$$= \frac{1}{\pi\overline{n_\psi}} \int_{L^2(\mathbb{R})} \mathcal{D}^\circ[\psi] e^{-|\psi|^2/\overline{n_\psi}} \frac{|\langle S|\psi\rangle|^{2n}}{n!} e^{-|\psi|^2}. \tag{VI.58}$$

Inside the integral, there are Gaussian functional multiplied by monomials in ψ, namely $|\langle S|\psi\rangle|^{2n}$. We can nevertheless come back to a Gaussian functional integral detailed in the Appendix (see Eq. (A.3)), the probability has a Bose-Einstein distribution form, as one would expect,

$$P_n[S] = \frac{\overline{n_\psi}^n}{1+\overline{n_\psi}^{n+1}} \tag{VI.59}$$

and does not depend on S. $P_{\hat{\rho}}[\psi]$ is not the continuous version of the multimode (discrete) thermal state described by the distribution: $\prod_{k=1}^M \frac{1}{\pi\langle n_k\rangle} e^{-|\alpha|^2/n_k}$, which is a normally distributed distribution for each mode. The next step would be to show that the functional distribution $P_{\hat{\rho}}[\psi]$ allows to reproduce all the n-order correlation function of the thermal state and observe what $\psi \in L^2(\mathbb{R})$ permit to represent a multimode thermal state.

Different way of writing the bosonic coherent state In the literature, one can found a variant of the bosonic coherent state, written as : $|\boldsymbol{\psi}\rangle = \exp(\hat{a}^\dagger[\psi])\,|0\rangle$. This choice is reminiscent of the normal ordering, detailed in this formalism later. This bosonic coherent state is not normalizable, because of the missing factor $e^{-\int d\omega|\psi(\omega)|^2/2}$ and the overlap between two bosonic coherent state is $\langle\beta|\psi\rangle = e^{\int d\omega\psi(\omega)\beta^*(\omega)}$. A supplementary condition is imposed in that case: $\int_{\mathbb{R}} d\omega\psi(\omega)\beta^*(\omega) < \infty$, condition obtained using the Cauchy-Schwartz inequality. One factor has to be added $e^{-\int_{\mathbb{R}} d\omega|\psi(\omega)|^2}$ in order to that state fulfills the completeness relation: $\int_{L^2(\mathbb{R})} \mathcal{D}[\psi]\,|\boldsymbol{\psi}\rangle\,\langle\boldsymbol{\psi}|\,e^{-\int d\omega|\psi(\omega)|^2} = \mathbb{I}$. Note that this discussion is also valid for coherent states.

VI.3 Functional phase space

After the description of a quantum state in a functional Hilbert space, we are naturally led to describe it in a functional phase space, by generalization of the construction presented in Chap. II, where only one frequency mode was considered. Further motivations are mentioned at the end of the chapter.

VI.3.1 Bosonic displacement operator

The bosonic displacement operator, is one representation of the Heisenberg group, can be written as [Combescure and Robert, 2012] :

$$\hat{D}[\psi] = \exp(\hat{a}^\dagger[\psi] - \hat{a}[\psi]) = \exp(\hat{a}^\dagger[\psi])\exp(-\hat{a}[\psi])\exp(-\frac{1}{2}\int_{\mathbb{R}} d\omega|\psi(\omega)|^2), \tag{VI.60}$$

where we have used the Glauber formula: $\exp(\hat{A}+\hat{B}) = \exp(\hat{A})\exp(\hat{B})\exp(-\frac{1}{2}[\hat{A},\hat{B}])$, valid when the operators $\hat{A}$ and $\hat{B}$ commute with their commutator $[\hat{A},\hat{B}]$. The bosonic coherent state can be written using the displacement bosonic operator $|\boldsymbol{\psi}\rangle = \hat{D}[\psi]\,|0\rangle$. The bosonic displacement operators satisfy the Weyl algebra:

$$\hat{D}[\psi]\hat{D}[\psi'] = \exp(-i\mathrm{Im}(\langle\boldsymbol{\psi}\mid\boldsymbol{\psi'}\rangle))\ \hat{D}[\psi+\psi'], \tag{VI.61}$$

where we have used the relation $\hat{a}^\dagger[\psi+\psi'] = \hat{a}^\dagger[\psi] + \hat{a}^\dagger[\psi']$ which comes from Eq. (VI.43). The displacement operator is unitary $\hat{D}^\dagger[\psi]\hat{D}[\psi] = \mathbb{I}$, since we have $\hat{D}^\dagger[\psi] = \hat{D}[-\psi]$. The displacement operator $\hat{D}[\gamma]$ applied on a bosonic coherent state $|\boldsymbol{\psi}\rangle$ gives:

$$\hat{D}[\gamma]\,|\boldsymbol{\psi}\rangle = \exp(-i\mathrm{Im}(\langle\boldsymbol{\psi}\mid\boldsymbol{\gamma}\rangle))\ \ |\boldsymbol{\psi}+\boldsymbol{\gamma}\rangle\,. \tag{VI.62}$$

We can define the bosonic displacement operator in quadrature position-momentum with fixed-spectrum variables:

$$\hat{D}[q,p] = \exp(i\int_{\mathbb{R}} d\omega[p(\omega)\hat{Q}(\omega) - q(\omega)\hat{P}(\omega)]) \tag{VI.63}$$

and the state Eq. (VI.52) can be rewritten as $\hat{D}[q,p]\,|0\rangle = |\mathbf{q},\mathbf{p}\rangle$. We have also the relation:

$$\hat{D}^\dagger[\psi]\hat{a}[\psi']\hat{D}[\psi] = \hat{a}[\psi'] + \langle\boldsymbol{\psi}|\boldsymbol{\psi'}\rangle, \tag{VI.64}$$

$$\hat{D}^\dagger[\psi]\hat{a}^\dagger[\psi']\hat{D}[\psi] = \hat{a}[\psi'] - \langle\boldsymbol{\psi'}|\boldsymbol{\psi}\rangle. \tag{VI.65}$$

More generally, as for a monochromatic field or for a single-photon field in many frequency modes (see Chap. III), we can define different version of the displacement operators index by $s \in [-1, 1[$:

$$\hat{D}_s[\psi] = \exp(\frac{1}{2}s|\psi|^2)\hat{D}[\psi], \tag{VI.66}$$

$$= \sum_{n,m} \frac{1}{n!m!}\{(\hat{a}^\dagger[\psi])^n \hat{a}[\psi]^m\}_s. \tag{VI.67}$$

s is related to the ordering of ladders operators when one considers average values of operators cast into polynomials of creation and annihilation operators. $\{(\hat{a}^\dagger[\psi])^n \hat{a}^m[\psi]\}_s$ is the s-ordered products of the ladder's operators defined by generalization of the results in Ref. ([Cahill and Glauber, 1969]). The normal and anti-normal ordered products are distinguished by the values $s = \pm 1$: it corresponds to have all annihilation (resp. creation) operators on the left of the creation (resp. annihilation) ones. The symmetric order corresponds to the value $s = 0$: for instance with $n = m = 1$, this ordering corresponds to the symmetric product $(1/2)\{\hat{a}[\psi]\hat{a}^\dagger[\psi] + \hat{a}^\dagger[\psi]\hat{a}[\psi]\}$. The operators $\hat{D}_1[\psi] = \exp(\hat{a}^\dagger[\psi])\exp(-\hat{a}[\psi])$ and $\hat{D}_{-1}[\psi] = \exp(-\hat{a}[\psi])\exp(\hat{a}^\dagger[\psi])$ are the normally and anti-normally ordered displacement operators.

Functional characteristic distribution The functional characteristic distribution labeled by s is defined as the Fourier transform of the displacement operators:

$$C^s_{\hat{\rho}}[\psi] = \langle \hat{D}_s[\psi] \rangle = \mathrm{Tr}(\hat{\rho}\hat{D}_s[\psi]). \tag{VI.68}$$

The functional characteristic distribution can be written explicitly using the Glauber identity:

$$C^s_{\hat{\rho}}[\psi] = \mathrm{Tr}(\hat{\rho} e^{\hat{a}^\dagger[\psi]} e^{-\hat{a}[\psi]}) e^{(s-1)\langle \boldsymbol{\psi}|\boldsymbol{\psi}\rangle}. \tag{VI.69}$$

The trace stands for a functional integration: $\mathrm{Tr}(\hat{\rho}\hat{D}[\psi]) = \int_{L^2(\mathbb{R})} \mathcal{D}^\circ[\psi'] \langle \boldsymbol{\psi'}|\hat{\rho}\hat{D}[\psi]|\boldsymbol{\psi'}\rangle$. We point out that we have the following identity: $C^s_{\hat{\rho}}[0] = \mathrm{Tr}(\hat{\rho}) = 1$, where to demonstrate this result, we have used the completeness relation of the bosonic coherent state.

Discussion of the multimode discrete limit The case of a discrete set of monochromatic modes can be recovered by decomposing the spectrum as: $\psi(\omega) = \sum_k \alpha_k \delta(\omega - \omega_k)$, where α_k is the particle-number sensitive parameter of each mode labeled by k. Then, the bosonic operator $\hat{a}^\dagger[\psi]$ is after integration $\hat{a}^\dagger[\psi] = \sum_k \alpha_k \hat{a}^\dagger(\omega_k) = \sum_k \alpha_k \hat{a}^\dagger_k$. For each frequency mode labeled by k, we obtain the usual commutation relation:

$$[\hat{a}_k, \hat{a}^\dagger_j] = \delta_{j,k}\mathbb{I}. \tag{VI.70}$$

Then, we can recover the multimode discrete displacement operator from $\hat{D}[\psi]$ using the decomposition of the amplitude spectrum introduced in this paragraph. Indeed, we obtain for n modes:

$$\hat{D}[\psi] \equiv \hat{D}(\alpha_1, ..., \alpha_n) = \exp(\sum_{k=1}^{n} (\alpha_k \hat{a}^\dagger_k - \alpha^*_k \hat{a}_k)). \tag{VI.71}$$

This discussion can be extended for n-orthogonal modes which are not necessarily monochromatic.

VI.3.2 Multimode Squeezed state

We consider the multimode functional squeezed operator defined by

$$\hat{S}[\beta] = \exp(\int_{\mathbb{R}} d\omega \beta(\omega)\hat{a}^\dagger(\omega)\hat{a}^\dagger(-\omega) - \beta^*(\omega)\hat{a}(\omega)\hat{a}(-\omega)), \tag{VI.72}$$

where $\beta(\omega)$ is called the squeezing function parameter. This state can be produced by a type-I SPDC, since we suppose that the signal and idler modes have the same polarization noted a, with a JSA under the form $\text{JSA}(\omega_s, \omega_i) = \delta(\omega_s + \omega_i)\beta(\omega_s - \omega_i)$. The most general form of a multimode squeezed state is given by Eq. IV.7. The two modes are anti-correlated in frequency. A different multimode squeezed state, with different frequency correlation between the signal and idler modes produced by a type-II SPDC, was provided in [Roux, 2020b].

The functional squeezed vacuum state is then described by applying the multimode functional squeezed operator on the vacuum state $|\boldsymbol{\beta}\rangle = \hat{S}[\beta]\,|0\rangle$. We will be interested more specifically to the functional squeezed coherent state which corresponds to the displaced squeezed vacuum state described by the wave function:

$$|\boldsymbol{\psi}, \boldsymbol{\beta}\rangle = \hat{D}[\psi]\hat{S}[\beta]\,|0\rangle\,. \tag{VI.73}$$

We point out that the relation $\hat{D}[\psi]\hat{S}[\beta] = \hat{S}[\beta]\hat{D}[\gamma]$ holds as in the monomode case. For showing this, we demonstrate in Appendix A.2.3 the expressions of creation and annihilation operators present in the displacement operator $\hat{D}[\gamma]$:

$$\hat{a}[\gamma] = \int_{\mathbb{R}} d\omega[\psi(\omega)\hat{a}(\omega)\text{ch}(|z(\omega)|) - \psi^*(-\omega)\hat{a}^\dagger(\omega)e^{i\theta(\omega)}\text{sh}(|z(\omega)|)], \tag{VI.74}$$

$$\hat{a}^\dagger[\gamma] = \int_{\mathbb{R}} d\omega[\psi^*(\omega)\hat{a}^\dagger(\omega)\text{ch}(|z(\omega)|) - \psi(-\omega)\hat{a}(\omega)e^{-i\theta(\omega)}\text{sh}(|z(\omega)|)]. \tag{VI.75}$$

It corresponds to a Bogoliubov transformation of the operators $\hat{a}[\psi]$ and $\hat{a}^\dagger[\psi]$, with $\beta(\omega) = z(\omega)e^{i\theta(\omega)}$. The field $\gamma(\omega)$ associated to the bosonic coherent state $|\boldsymbol{\gamma}\rangle = \hat{D}[\gamma]\,|0\rangle = \exp(-\hat{a}[\gamma] + \hat{a}^\dagger[\gamma])\,|0\rangle$, after rearranging the terms in the integral, can be written in function of the amplitude of the coherent state $\psi(\omega)$ and the squeezing parameter $\beta(\omega)$ as: $\gamma(\omega) = \psi(\omega)\text{ch}(|z(\omega)|) - \psi(-\omega)e^{-i\theta(\omega)}\text{sh}(|z(\omega)|)$. In addition, squeezed coherent states form an overcomplete basis:

$$\iint_{L^2(\mathbb{R})} |\boldsymbol{\psi}, \boldsymbol{\beta}\rangle\langle\boldsymbol{\psi}, \boldsymbol{\beta}|\,\mathcal{D}^\circ[\psi]\mathcal{D}[\beta] = \mathbb{I}, \tag{VI.76}$$

where the functional integration is taken with respect to both functions ψ and β.

VI.3.3 Functional quasi-probability distribution on phase space

The functional Wigner quasi-probability distribution is defined by the functional Fourier transform of the symmetric ($s = 0$) characteristic functional:

$$\mathcal{W}_{\hat{\rho}}[\psi] = \int_{L^2(\mathbb{R})} \exp(2i\text{Im}(\int_{\mathbb{R}} d\omega \psi^*(\omega)\psi'(\omega)))C^0_{\hat{\rho}}[\psi']\mathcal{D}[\psi']. \tag{VI.77}$$

Its mathematical structure is very similar to the monomode Wigner distribution $W_{\hat{\rho}}(\alpha)$ (see Eq. II.97). We can also perform a change of variable to obtain the functional Wigner distribution in position-momentum variables:

$$\mathcal{W}_{\hat{\rho}}[q,p] = \int_{L^2(\mathbb{R})} \mathcal{D}[q'] \exp(-2i \int_{\mathbb{R}} p(\omega) q'(\omega) d\omega) \left\langle \mathbf{q} - \mathbf{q}' \right| \hat{\rho} \left| \mathbf{q} + \mathbf{q}' \right\rangle, \tag{VI.78}$$

and we obtain the Wigner distribution as it was first introduced in a quantum field theory context [Mrowczynski and Mueller, 1994]. We observe the similarity in the mathematical structure with the CV Wigner distribution Eq. (II.89). The functional Wigner quasi-probability distribution is normalized to one:

$$\int_{L^2(\mathbb{R})} \mathcal{D}[q] \int_{L^2(\mathbb{R})} \mathcal{D}^\circ[p] \mathcal{W}_{\hat{\rho}}[q,p] = 1, \tag{VI.79}$$

where we have used the functional Dirac distribution $\delta[q] = \int_{L^2(\mathbb{R})} \mathcal{D}[p] e^{-i \int p(\omega) q(\omega) d\omega}$. The marginals of the functional Wigner quasi-probability distribution is given by:

$$\int_{L^2(\mathbb{R})} \mathcal{D}^\circ[p] \mathcal{W}_{\hat{\rho}}[q,p] = \langle \mathbf{q} | \hat{\rho} | \mathbf{q} \rangle, \tag{VI.80}$$

$$\int_{L^2(\mathbb{R})} \mathcal{D}[q] \mathcal{W}_{\hat{\rho}}[q,p] = \langle \mathbf{p} | \hat{\rho} | \mathbf{p} \rangle. \tag{VI.81}$$

We recover the diagonal matrix element of the density matrix, and corresponds to what it is generally called the *correct* marginals. In addition, the functional Wigner quasi-probability distribution can be written as the expectation value of the displacement parity operator:

$$\mathcal{W}_{\hat{\rho}}[q,p] = \langle \hat{D}_s^\dagger[q,p] \hat{\Pi} \hat{D}_s[q,p] \rangle, \tag{VI.82}$$

where the parity operator $\hat{\Pi}$ is here defined as: $\hat{\Pi} = \int_{L^2(\mathbb{R})} \mathcal{D}[q] \left| \mathbf{q} \right\rangle \left\langle -\mathbf{q} \right|$. The introduced distribution satisfies hence all the Stratonovich-Weyl rules for building a valid phase space distribution [Khvedelidze and Abgaryan, 2017, Stratonovich, 1956], which will d detailed in Chap. VII. In addition, the functional Wigner distribution can be negative, as the Wigner distribution, and hence corresponds to a quasi-probability functional distribution.

Finally, the functional Wigner distribution for a bipartite state, where the prefix *bi* refers to two spatial or polarization modes, can be written as:

$$\mathcal{W}_{\hat{\rho}}[q_1,p_1,q_2,p_2] = \iint_{L^2(\mathbb{R})} \mathcal{D}[q'] \mathcal{D}[q''] e^{-2i \int p_1(\omega) q_1'(\omega) d\omega} e^{-2i \int p_2(\omega) q_2'(\omega) d\omega} \times \left\langle \mathbf{q}_1 - \mathbf{q}_1', \mathbf{q}_2 - \mathbf{q}'_2 \right| \hat{\rho} \left| \mathbf{q}_1 + \mathbf{q}'_1, \mathbf{q}_2 + \mathbf{q}'_2 \right\rangle. \tag{VI.83}$$

High-dimensional entanglement of photon pairs is analyzed using the Schmidt decomposition and the functional Wigner formalism in [Roux, 2020b]. The partial trace over the idler mode can lead to a mixed state if the initial state $\hat{\rho}$ is entangled, which means in our context that the quasi-probability functional distribution is not separable as follows $\mathcal{W}_{\hat{\rho}}[q_1,p_1,q_2,p_2] \neq \mathcal{W}_{\hat{\rho}}[q_1,p_1] \mathcal{W}_{\hat{\rho}}[q_2,p_2]$.

VI.3.4 s-ordered phase space quasi-probability distribution and average value of operator

s-ordered phase space distribution The general s-ordered phase space quasi-probability distribution is defined as:

$$W_{\hat{\rho}}[\psi, s] = \mathrm{Tr}(\hat{\rho}\hat{T}_s[\psi]), \tag{VI.84}$$

which corresponds to the expectation value of the operator $\hat{T}_s[\psi]$ defined by the Fourier transform of the s-order displacement operator:

$$\hat{T}_s[\psi] = \int_{L^2(\mathbb{R})} \hat{D}_s[\psi]\exp(2i\mathrm{Im}(\int_{\mathbb{R}} d\omega\psi^*(\omega)\xi(\omega)))\mathcal{D}^\circ[\psi]. \tag{VI.85}$$

The operator $\hat{T}_s[\psi]$ verifies the orthogonality relation $\mathrm{Tr}(\hat{T}_s[\psi]\hat{T}_s^\dagger[\psi']) = \delta[\psi - \psi']$. For $s = 1$ $W_{\hat{\rho}}([\psi], 1)$ is the P-functional distribution $P_{\hat{\rho}}[\psi]$, introduced in Eq. (VI.55), and for $s = -1$ the functional Husimi distribution:

$$W_{\hat{\rho}}([\psi], -1) \equiv Q_{\hat{\rho}}[\psi] = \langle \boldsymbol{\psi} | \, \hat{\rho} \, | \boldsymbol{\psi} \rangle \, . \tag{VI.86}$$

Average value of operators A bounded operator $\hat{O}$ can be expanded into a power series of $\hat{a}(\omega)$ and $\hat{a}^\dagger(\omega)$ in the s-ordered form as follows $\hat{O} = \sum_{n,m} o_{n,m}\{(\hat{a}(\omega))^n(\hat{a}^\dagger(\omega))^m\}_s$. Its matrix element between two bosonic coherent states reads:

$$\langle \boldsymbol{\psi} | \, \hat{O} \, | \boldsymbol{\psi'} \rangle = \sum_{n,m} o_{n,m} e^{-\int d\omega\psi(\omega)\psi'^*(\omega)}\{(\psi(\omega))^n(\psi'^*(\omega))^m\}_s. \tag{VI.87}$$

Note that the expansion of an operator into a power series of the ladders operators $\hat{a}[\gamma]$ and $\hat{a}^\dagger[\gamma]$, using $\{(\hat{a}^\dagger[\psi])^n\hat{a}^m[\psi]\}_s$ lead to a similar result by replacing $\psi(\omega)$ by $\int d\omega\gamma(\omega)\psi^*(\omega)$ and $\psi'(\omega)$ by $\int d\omega\gamma^*(\omega)\psi'(\omega)$, following Eq. (VI.45).

VI.3.5 Relation between the different probability distribution

This section provides relations between probability distributions, similarly to the monochromatic case described in Chap. II. These distributions are related by a Weierstrass transform, which in other words, corresponds to the functional convolution with the Husimi or Wigner distribution of the functional vacuum state (see Fig. VI.2). More explicitly, the Husimi functional distribution is related to the Wigner distribution and the P-functional distribution by:

$$Q_{\hat{\rho}}[\alpha] = \int_{L^2(\mathbb{R})} \mathcal{D}[\beta]P_{\hat{\rho}}[\beta]e^{-|\alpha-\beta|^2} = P_{\hat{\rho}}[\alpha] \circledast Q_{|0\rangle}[\alpha] \tag{VI.88}$$

$$Q_{\hat{\rho}}[\alpha] = \int_{L^2(\mathbb{R})} \mathcal{D}[\beta]W_{\hat{\rho}}[\beta]e^{-2|\alpha-\beta|^2} = W_{\hat{\rho}}[\alpha] \circledast W_{|0\rangle}[\alpha], \tag{VI.89}$$

$$W_{\hat{\rho}}[\alpha] = \int_{L^2(\mathbb{R})} \mathcal{D}[\beta]P_{\hat{\rho}}[\beta]e^{-2|\alpha-\beta|^2} = P_{\hat{\rho}}[\alpha] \circledast W_{|0\rangle}[\alpha], \tag{VI.90}$$

where the star $\circledast$ denotes the convolutional product. $W_{|0\rangle}[\alpha] = 2e^{-2|\alpha|^2}$ and $Q_{|0\rangle}[\alpha] = e^{-|\alpha|^2}$ are the functional Wigner (resp. Husimi) distribution of the vacuum state, demonstrated in the next section. We remind that $|\alpha - \beta|^2 = \int |\alpha(\omega) - \beta(\omega)|^2 d\omega$. In [Koczor et al., 2020], a

more general formula is presented which relate all the s-ordered phase space quasi-probability distribution F, and holds in our functional formalism:

$$F_{\hat{\rho}}([\alpha], s+s'-1) = F_{|0\rangle}([\alpha], s') \circledast F_{\hat{\rho}}([\alpha], s). \tag{VI.91}$$

This formula shows that the inverse Weierstrass transform is not possible. From the Husimi functional distribution we cannot obtain the Wigner functional one. We now demonstrate only Eq. (VI.89) and the other relations are straightforward. The anti-normal and symmetric characteristic functional distribution are related by the equation $C^{-1}_{\hat{\rho}}[\beta] = e^{-|\beta|^2/2} C^{0}_{\hat{\rho}}[\beta]$ which becomes after applying the Fourier transform and expressing the symmetric functional characteristic as the Wigner functional:

$$\begin{aligned}
\int_{L^2(\mathbb{R})} \mathcal{D}^{\circ}[\beta] C^{-1}_{\hat{\rho}}[\beta] e^{\beta^*\alpha - \alpha^*\beta} &= \int_{L^2(\mathbb{R})} \mathcal{D}^{\circ}[\beta] e^{-|\beta|^2/2} C^{0}_{\hat{\rho}}[\beta] e^{\beta^*\alpha - \alpha^*\beta}, \\
Q_{\hat{\rho}}[\alpha] = \int_{L^2(\mathbb{R})} \mathcal{D}^{\circ}[\lambda] W_{\hat{\rho}}[\lambda] &\int_{L^2(\mathbb{R})} e^{\beta^*(\lambda-\alpha)} e^{-\beta(\lambda^*-\alpha^*)} e^{-|\beta|^2/2} \mathcal{D}^{\circ}[\alpha], \\
Q_{\hat{\rho}}[\alpha] &= \int_{L^2(\mathbb{R})} \mathcal{D}^{\circ}[\lambda] W_{\hat{\rho}}[\lambda] e^{-2|\alpha-\lambda|^2},
\end{aligned} \tag{VI.92}$$

where we finally used the functional Gaussian integration Eq. (A.3). We have also used the simplified notation, with for instance $\beta^*\alpha = \int d\omega \beta^*(\omega)\alpha(\omega)$.

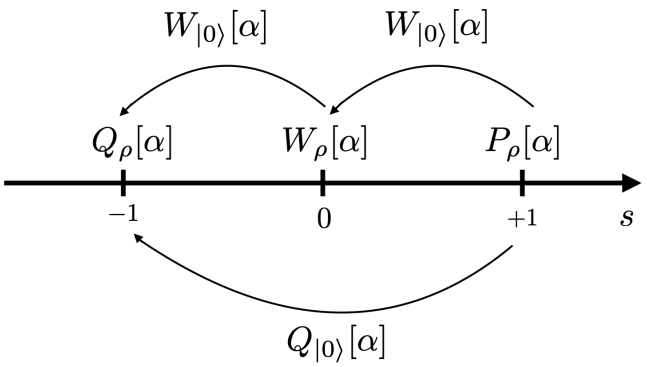

Figure VI.2: Sketch of the different functional phase space quasi-probability distributions. The arrows means how to obtain the considered distribution (placed on the line) with a convolution functional product of the functional Wigner or Husimi quasi-probability distribution of the vacuum state.

VI.4 Examples of functional Wigner quasi-probability distribution of multimode multi-photon state

We now calculate the functional Wigner quasi-probability distribution of different continuous frequency spectrum multiphoton states, which are the generalization of discrete multimode states introduced in quantum optics. Analytical calculation is possible using the Gaussian functional integration. The presented approach for calculating the functional Wigner quasi-probability

distribution from the characteristic functional is based on the work in [Barnett and Radmore, 2002]. Also, the fixed-spectrum Fock states are not a complete basis and for that reason, we will make use of the relation between different functional distributions (see Sec. VI.3.5) for calculating the Wigner functional of multimode thermal states.

VI.4.1 Bosonic coherent and vacuum state

The characteristic function of the bosonic coherent pure state $\hat{\rho} = |\boldsymbol{\beta}\rangle \langle\boldsymbol{\beta}|$ is:

$$C^0_{|\boldsymbol{\beta}\rangle}[\psi] = \langle\boldsymbol{\beta}| \hat{D}[\psi] |\boldsymbol{\beta}\rangle = \exp(-2i\mathrm{Im}(\langle\boldsymbol{\beta}|\boldsymbol{\psi}\rangle))\exp(-|\psi|^2/2). \tag{VI.93}$$

After performing the Gaussian functional integration (see Eq. (A.3) in the Appendix), the Functional Wigner quasi-probability distribution is:

$$W_{|\beta\rangle}[\psi] = \exp(-2\int_{\mathbb{R}} d\omega|\psi(\omega) - \beta(\omega)|^2). \tag{VI.94}$$

In the quadrature position and momentum variables, the functional Wigner distribution of the bosonic coherent state can be written as:

$$\mathcal{W}_{\hat{\rho}}[q,p] = \exp(-2\int_{\mathbb{R}} (q(\omega) - \overline{q}(\omega))^2 d\omega) \times \exp(-2\int_{\mathbb{R}} (p(\omega) - \overline{p}(\omega))^2 d\omega), \tag{VI.95}$$

where $\mathrm{Re}(\beta(\omega)) = \overline{q}(\omega)$ and $\mathrm{Im}(\beta(\omega)) = \overline{p}(\omega)$.

For $\beta = 0$, the Eq. (VI.95) leads to the functional Wigner quasi-probability distribution of the vacuum state $|0\rangle$:

$$W_{|0\rangle}[\psi] = \exp(-2\int_{\mathbb{R}} d\omega|\psi(\omega)|^2), \tag{VI.96}$$

which is a Gaussian functional centered at the origin of the functional phase space, as expected.

VI.4.2 Squeezed state

The functional characteristic of the squeezed coherent state $|\boldsymbol{\alpha},\boldsymbol{\beta}\rangle = \hat{D}[\alpha]\hat{S}[\beta]|0\rangle$, $C^0_{|\boldsymbol{\alpha},\boldsymbol{\beta}\rangle}[\psi] = \langle 0| \hat{S}^\dagger[\beta]\hat{D}^\dagger[\alpha]\hat{D}[\psi]\hat{D}[\alpha]\hat{S}[\beta]|0\rangle$ is, using the completeness relation Eq. (VI.76):

$$\begin{aligned} C^0_{|\boldsymbol{\alpha},\boldsymbol{\beta}\rangle}[\psi] &= \langle 0| \hat{D}[\gamma] |0\rangle \exp(-2i\mathrm{Im}(\int_{\mathbb{R}} d\omega\psi(\omega)\alpha(\omega))) \\ &= e^{-\frac{1}{2}\langle\boldsymbol{\gamma}|\boldsymbol{\gamma}\rangle} e^{-2i\mathrm{Im}(\langle\boldsymbol{\psi}|\boldsymbol{\alpha}\rangle)}, \end{aligned} \tag{VI.97}$$

where $|\boldsymbol{\gamma}\rangle$ has been defined after Eq. (VI.74). The functional Wigner quasi-probability distribution is,

$$W_{|\boldsymbol{\alpha},\boldsymbol{\beta}\rangle}[\psi] = \exp(-2\int_{\mathbb{R}} d\omega\Big|(\psi(\omega) - \alpha(\omega))\mathrm{ch}(z(\omega)) + (\psi^*(\omega) - \alpha^*(\omega))e^{i\theta(\omega)}\mathrm{sh}(z(\omega))\Big|^2), \tag{VI.98}$$

where we have again used the Gaussian functional integration. We then consider the case of the squeezed vacuum state by setting the displacement shift value $\alpha = 0$. The functional Wigner quasi-probability distribution of the squeezed vacuum state is:

$$W_{|\boldsymbol{\beta}\rangle}[\psi] = \exp(-2\int_{\mathbb{R}} d\omega\Big|\psi(\omega)\mathrm{ch}(z(\omega)) + \psi^*(\omega)e^{i\theta(\omega)}\mathrm{sh}(z(\omega))\Big|^2), \tag{VI.99}$$

with again $\beta(\omega) = z(\omega)e^{i\theta(\omega)}$ and corresponds to a shear transformation of the Wigner functional of the vacuum state Eq. (VI.96). Another example of the functional Wigner of a two-mode functional squeezed state is presented in [Roux, 2020b].

VI.4.3 Thermal state

We now evaluate the functional Wigner quasi-probability distribution of the multimode thermal state defined by Eq. (VI.56) and by using Eq. (VI.90),

$$W_{\hat{\rho}}[\psi] = \int_{L^2(\mathbb{R})} D^{\circ}[\beta] \frac{1}{\pi \overline{n_S}} e^{-|\beta|^2/\overline{n_S}} e^{-2|\psi-\beta|^2}. \tag{VI.100}$$

After using the functional Gaussian integration (see Eq. (A.3)), the functional Wigner quasi-probability distribution of the thermal state is:

$$W_{\hat{\rho}}[\psi] = \exp(-\frac{2}{2\overline{n}_s+1} \int_{\mathbb{R}} d\omega |\psi(\omega)|^2). \tag{VI.101}$$

The functional Wigner distribution of the multimode thermal state has the same form as the thermal state in CV variables (see Ref. [Barnett and Radmore, 2002]) but here we have a functional Gaussian distribution.

VI.4.4 General Gaussian state

Finally, to wrap up our results, we present the general functional characteristic of a functional Gaussian state,

$$C^0_{\hat{\rho}}[q,p] = \exp(-\frac{1}{2} \int_{\mathbb{R}} d\omega \int_{\mathbb{R}} d\omega' X^{\top}(\omega) \Sigma(\omega,\omega') X(\omega')) \tag{VI.102}$$

and the functional Wigner quasi-probability distribution can be cast under the form:

$$\mathcal{W}_{\hat{\rho}}[q,p] = \exp(-\frac{1}{2} \iint d\omega d\omega' X^{\top}(\omega) \Sigma^{-1}(\omega,\omega') X(\omega') + X^{\top}(\omega) Y(\omega)), \tag{VI.103}$$

where $X(\omega) = \begin{pmatrix} q(\omega) \\ p(\omega) \end{pmatrix}$, $\Sigma^{-1}(\omega,\omega')$ the inverse of the covariance matrix. $Y(\omega)$ contains the first moments of the distribution. In the case of the thermal state (see Eq. (VI.101)), the covariance matrix is "diagonal":

$$\Sigma^{-1}_{\text{th}}(\omega,\omega') = \delta(\omega-\omega') \begin{pmatrix} 1/(2\overline{n}_s+1) & 0 \\ 0 & 1/(2\overline{n}_s+1) \end{pmatrix}. \tag{VI.104}$$

For the bosonic functional state (see Eq. (VI.95)), the covariance matrix is also diagonal and equal to the identity $\Sigma^{-1}_{\text{coh}}(\omega,\omega') = \delta(\omega-\omega')\mathbb{I}$ and the first moments are given by $Y(\omega) = (\overline{x}(\omega), \overline{p}(\omega))$.

The utility of the introduction of the covariance matrix is to consider the possible generalization of the research which was done to assess Gaussian entanglement in our context. The Simon's criterion is one of them.

VI.4.5 Fixed-spectrum n-Fock state

The fixed-spectrum Fock state $|n, \mathbf{S}\rangle$ does not verify the completeness relation, and the technique for calculating the Wigner functional from the characteristic functional does not work in this

formalism. The calculation is nevertheless possible with another strategy, developed in [Roux and Fabre, 2020] and gives the following result:

$$W_{|n,\mathbf{S}\rangle}[\psi] = (-1)^n L_n(4|\langle S|\boldsymbol{\psi}\rangle|^2)\exp(-2\int_{\mathbb{R}} d\omega|\psi(\omega)|^2). \tag{VI.105}$$

The difference with the monochromatic case (see Eq. (II.109)) is that there is an overlap between the spectrum $S \in L^2(\mathbb{R})$ of the state and the phase space function variable ψ in the Laguerre functional L_n (under the reserve of its existence) defined by Eq. (II.110).

VI.5 Projection of the Wigner functional quasi-probability distribution

VI.5.1 Projection of the Wigner functional quasi-probability distribution into a fixed-particle number degree of freedom distribution

In this section, we provide how we obtain the chronocyclic Wigner distribution from the Wigner functional, by fixing the particle-number degree of freedom. The expectation value of the annihilation operator $\hat{a}(\omega)$ is given by:

$$\langle \hat{a}(\omega)\rangle = \int_{L^2(\mathbb{R})} \alpha(\omega) Q_{\hat{\rho}}[\alpha]\ \mathcal{D}^\circ[\alpha], \tag{VI.106}$$

and the correlation function $C(\omega',\omega) = \langle \hat{a}^\dagger(\omega')\hat{a}(\omega)\rangle$:

$$C(\omega',\omega) = \int_{L^2(\mathbb{R})} \alpha^*(\omega')\alpha(\omega) Q[\alpha]\ \mathcal{D}^\circ[\alpha]. \tag{VI.107}$$

These expressions can be applied to the case of the fixed-spectrum bosonic coherent state defined by Eq. (VI.42),

$$\langle \boldsymbol{\psi}|\, \hat{a}(\omega)\, |\boldsymbol{\psi}\rangle = \psi(\omega), \tag{VI.108}$$

$$C(\omega',\omega) = \psi^*(\omega')\psi(\omega), \tag{VI.109}$$

where we have used the Gaussian functional integration Eq. (A.3). After performing the inverse Weyl transform on Eq. (VI.109), we obtain the chronocyclic Wigner distribution of the field ψ,

$$W_{\hat{\rho}}(\omega,t) = \int_{\mathbb{R}} d\omega' e^{2i\omega' t}\langle \hat{a}^\dagger(\omega+\omega')\hat{a}(\omega-\omega')\rangle, \tag{VI.110}$$

$$= \int_{\mathbb{R}} d\omega' e^{2i\omega' t}\psi^*(\omega+\omega')\psi(\omega-\omega'). \tag{VI.111}$$

If ψ is square normalizable to one, it corresponds to a bosonic coherent state with a mean number photon value of one. In that case, we recover a similar chronocyclic Wigner distribution defined by Eq. (III.44). Despite the mathematical similarity in the structure of these chronocyclic Wigner distributions, a bosonic coherent state with an average photon value of one is not a single-photon. They have indeed the same chronocyclic Wigner distribution, but these two electromagnetic fields differ by their statistical property, one is sub-Poissonian the other is Poissonian as mentioned in Chap. II.

VI.5.2 Projection of the functional phase space into the monochromatic limit

In this section, we explain how to recover the usual Wigner distribution (see Eq. (II.89)) from the functional one, by fixing the spectral degree of freedom. First, we discuss how we can recover the coherent state from the bosonic coherent one. Starting from the bosonic coherent field $|\boldsymbol{\alpha}\rangle = \exp(-\int(\alpha(\omega)\hat{a}^\dagger(\omega) - \alpha^*(\omega)\hat{a}(\omega))d\omega)$, the coherent state $|\alpha\rangle$ can be recovered, by choosing a spectrum α under the form $\alpha(\omega) = \alpha\delta(\omega)$. It corresponds to the case of a laser beam with fixed frequency ω_0 without spectral noise, using the terminology of Chap. V. The amplitude α is the particle-number sensitive variable. Indeed, we obtain in that case:

$$|\boldsymbol{\alpha}\rangle \equiv |\alpha\rangle = \exp(-\alpha\hat{a}^\dagger(\omega) + \alpha^*\hat{a}(\omega))\,|0\rangle\,, \tag{VI.112}$$

where the label ω of the ladders operators in the quantum optics formalism is always implicit. This example provides another case that the spectrum S is not normalized to one owing to the particle-number sensitive parameter α, as in quantum field theory (see Ref. [Mrowczynski and Mueller, 1994]).

We now consider the functional Wigner distribution of the bosonic coherent state $|\boldsymbol{\alpha}\rangle$, which is described by Eq. (VI.95) and consider the following spectrum $\alpha^2(\omega) = \alpha^2\delta(\omega)$. The functional Wigner distribution is a function of function, so to go to the phase space from the functional one, the Wigner functional has to be evaluated at the "point" $\beta^2(\omega) = \beta^2\delta(\omega)$. There is no square on the Dirac distribution to avoid mathematical divergence. The functional Wigner distribution is now simply the Wigner distribution:

$$W_{|\alpha\delta_\omega\rangle}[\boldsymbol{\beta} = \beta\delta_\omega] \equiv W_{|\alpha\rangle}(\beta) = \exp(-2|\alpha - \beta|^2), \tag{VI.113}$$

which is indeed the Wigner distribution of the coherent state $|\alpha\rangle$. Let us consider that the frequency variable ω_1 of the coherent state and the frequency of the Wigner distribution ω are different so that the amplitude spectrum of the coherent state is $\beta^2(\omega) = \beta^2\delta(\omega - \omega_1)$. We are again in phase space (not functional) and obtain the following Wigner distribution:

$$W_{|\alpha\delta_\omega\rangle}[\boldsymbol{\beta} = \beta\delta_{\omega_1}] = \exp(-2|\beta|^2 - 2|\alpha|^2). \tag{VI.114}$$

Hence, there is no overlap between the variable of phase space and the field of the density matrix since they are in orthogonal frequency modes. The state described Eq. (VI.114) corresponds to the vacuum state multiplied by a constant factor. Despite the apparent simplicity of the results, it is not possible to obtain it with the Wigner distribution formalism described in Chap. II. It helps us to remind that the phase space has also a spectrum variable here denoted δ_ω which is in quantum optics always forgotten, in addition to the particle sensitive variable α. This spectrum is centered at the same frequency mode as the one of the considered quantum state.

VI.6 Discussion and perspectives

This chapter provides a functional phase space description of quantum states which combines both particle-number and spectral distribution degree of freedom. We perform the calculation of usual functional Wigner distribution for functional Gaussian states, along with the fixed-spectrum Fock state one. It shows that their functional Wigner distribution has the same mathematical form as the Wigner distribution in the monochromatic limit. The difference is that the scalar variable of the distribution is replaced by a function.

The future goal of this formalism is not to naively generalize everything. The use of such formalism for studying and performing the tomographical reconstruction of a multimode photonic or phononic field may not be useful. In many cases, a frequency cut-off or a mode cutoff is wide enough, and information is not lost using such cuts. Meanwhile, the formalism shows its utility for quantifying high dimensional entanglement. By continuity of this first paper [Roux, 2020b], a generalization of the Simon's criteria could be considered, as an entanglement witness in continuous multimode variables among many other criteria, which would be based on the functional entropy of formation for instance and is a work in progress.

We now give perspectives of the functional formalism in quantum simulation and computation. As the squeezed bosonic state corresponds to the ground state of the Bardeen–Cooper–Schrieffer theory [Bardeen et al., 1957], creating it with flying photons and manipulating could be useful for quantum simulation. We mention that the bosonic coherent state is used in condensed matter theory. Indeed, the Green's function in condensed matter which is the n-order correlation function in quantum optics is defined as:

$$G(x_1,t_1,...,x_n,t_n,x'_n,t'_n,...,x'_1,t'_1) = \langle 0|\,\hat{T}\hat{a}(x_1,t_1)...\hat{a}(x_n,t_n)\hat{a}^\dagger(x'_n,t'_n)\hat{a}^\dagger(x'_1,t'_1)\,|0\rangle \quad \text{(VI.115)}$$

where $\hat{T}$ refers to the time-ordering operator, which orders the ladders operators in a manner to have the future time on the left and the past time on the right. The ladders (or field) operators are expressed in the Heisenberg's picture $\hat{a}(x_1,t_1) = e^{-i\hat{H}t_1}\hat{a}(x_1)e^{i\hat{H}t_1}$, where $\hat{H}$ is the Hamiltonian of the system. The Green's function can be expressed using the generating functional:

$$Z[\psi] = \langle 0|\,\hat{T}\exp(i\int d^3xdt(\hat{a}^\dagger(x,t)\psi(x,t) + \psi^*(x,t)\hat{a}(x,t)))\,|0\rangle \quad \text{(VI.116)}$$

where we recognize the overlap of the bosonic coherent state (when all degrees of freedom are considered) with the vacuum state,

$$G(x_1,t_1,...,x_n,t_n,x'_n,t'_n,...,x'_1,t'_1) = (-i)^{n+n'}\frac{\delta^{n+n'}Z[\psi]}{\delta\psi^*(x_1,t_1)\delta\psi^*(x_n,t_n)...\delta\psi(x'_n,t'_n)\delta\psi(x'_1,t'_1)}. \quad \text{(VI.117)}$$

The generating functional describes the probability amplitude that a vacuum state remains the vacuum when it is in contact with multiple electromagnetic external sources $\psi(x,t)$. Despite the apparent difficulty to produce and to perform operations on such bosonic coherent states,

this remark on the Green's function shows that how the formalism introduced in this chapter could be used to use flying photons for simulating complex quantum systems.

The functional phase space could find application for representing hybrid CV-CV quantum states as detailed in the conclusion of the previous chapter. Moreover, we only focus on a bosonic optical field, one could also investigate the extension of the current formalism to fermionic fields developed in [Mrowczynski, 2013] but for quantum optic applications.

Finally, the study of the classical limit, using the Hepp's method [Combescure and Robert, 2012, Hepp, 1974, Hepp and Lieb, 1973] along with the Moyal's formulation [Roux and Fabre, 2020] in terms of deformation quantization [Berra-Montiel and Molgado, 2020] could bring a new light for the quantum optics and information community to help understand what are the implications of a non-commutative algebra in a phase space formulation.

Chapter VII

Wigner distribution on a double cylinder phase space

This last chapter provides a novel description of quantum states in a double cylinder phase space, which is particularly adapted for systems exhibiting translational symmetry such as the GKP states. Visualization into that specific phase space of quantum error correction protocol of GKP state is given along with two ways for measuring this distribution. This chapter is mainly based on Ref. [Fabre et al., 2020b].

VII.1 Symmetries of phase space and bosonic code

Phase space quasi-probability distributions are valuable tools for understanding and visualizing quantum states. R.L Stratonovich was the first to use an axiomatic approach to build a distribution in phase space [Stratonovich, 1956]. The Stratonovich-Weyl rules correspond to the set of properties that a valid phase space distribution $W_{\hat{\rho}}(\Omega)$ must satisfy [Brif and Mann, 1998, Tilma et al., 2016], where Ω denotes the chosen parametrization. The distribution is built from the generalized Weyl rule, $W_{\hat{\rho}}(\Omega) = \mathrm{Tr}(\hat{\rho}\hat{\Delta}(\Omega))$, where $\hat{\Delta}(\Omega)$ is called the kernel, point phase space operator, Stratonovich-Weyl quantizer. The restricted version of the Stratonovich-Weyl correspondence states [Tilma et al., 2016]:

• There is a one-to-one correspondence between the Wigner distribution and the density matrix. That means the mapping between the two is informationally complete.

• $W_{\hat{\rho}}(\Omega)$ is normalized *i.e* the integral of the Wigner distribution over the phase space is one $\int W_{\hat{\rho}}(\Omega)d\Omega = \mathrm{Tr}(\hat{\rho}) = 1$.

• The kernel is Hermitian, so that $W_{\hat{\rho}}(\Omega)$ is real.

• $W_{\hat{\rho}}(\Omega)$ is self-conjugate; the overlap formula Eq. (II.94) holds.

• The covariance condition states that if $\hat{\rho}$ is invariant under global unitary operations then the associated Wigner distribution also checks this property.

When the parametrisation Ω corresponds to the position and momentum variables, the phase space is rectangular as developed in Chap. II and the kernel $\hat{\Delta}(x, p)$ is the displaced parity operator (see Eq. (II.95)). The Wigner distribution of qudits systems, where the associated phase

space is a torus, also verifies these properties (see Chap. II). Other phase space geometries exist, such as cylinder, sphere and the associated Wigner distributions also verify this set of rules. The parametrisation is chosen depending on the symmetries of the quantum state of interest.

The Wigner distribution, like bosonic codes, is constructed from symmetry considerations. Therefore, symmetries can be particularly adapted to describe each code. For instance, when the dynamical group is a $\mathbb{SU}(2)$ symmetry [Klimov et al., 2017, Tilma et al., 2016], the phase space is a 2-sphere whereas for the Heisenberg-Weyl and the cylindrical group, the phase space is rectangular and cylindrical respectively.

Defining two lattices along with the position and momentum variables with periodicity l and $2\pi/l$, we can define modular variables (MVs). MVs are a specific class of observables that are periodic and have been introduced in [Aharonov et al., 1969] to explain non-local properties of quantum states. They are now used in quantum information protocols to identify discrete structures in continuous variable states [Carvalho et al., 2012, Ketterer et al., 2016, Tollaksen et al., 2010]. MVs are particularly adapted in situations where the considered quantum state has a periodic structure. We also note the recent interest of the high energy community of this formalism for understanding quantum gravity or metastring theory[Freidel et al., 2017, Yargic, 2020, Yargic and Geiller, 2020].

We propose in this chapter to study systems with translational symmetry. For such, we define a four dimensional phase space and define a quasi-probability distribution, obeying the Stratonovich-Weyl [Khvedelidze and Abgaryan, 2017] rules, with two pairs of azimuthal-angular variables. The associated angular variables correspond to the MVs. It leads to the construction of a double cylinder phase space. We then generalize the results obtained on the rotational Wigner distribution on a single cylinder phase space, as introduced in [Bizarro, 1994, Gonzalez et al., 2003, Potoček and Barnett, 2015, Rigas et al., 2008], or for the phase-number Wigner distribution one [Moya-Cessa, 2003, Vaccaro and Pegg, 1990]. The representation of a quantum state in a double cylinder phase space is totally equivalent to the rectangular phase space. But it turns out to be the most adapted one for states exhibiting translational symmetry. We show only in two specific examples, that codes which exhibit the same symmetry than the one underlying the construction of a phase space have a similar Wigner distribution. In particular, Schrödinger cat codes which have parity symmetry are represented in the rectangular phase space by two peaks and an oscillation pattern perpendicular to the peaks. The GKP states have translational symmetry and remarkably they have the same shape in a double cylindrical phase space, which we introduce in this chapter. We further propose to study a quantum error correction protocol relying on the use of a position-momentum GKP state as ancilla and visualize the correction in this phase space.

VII.2 Modular variables formalism

In this section, we describe an alternative representation of quantum states using modular variables, which is well adapted for physical systems with translational symmetry. For such, we will introduce the Zak's transform, an operation that takes as input a function of one variable (which belongs to $\mathbb{R}$) and produces as output a function of two variables (which belong to the torus $\mathbb{S}^1 \times \mathbb{S}^{1*}$). The modular basis and its canonically conjugate one are defined. In the following, we set $\hbar = 1$.

VII.2.1 Modular basis and the Zak's transform

As shown in [Aharonov et al., 1969, Ketterer et al., 2016], the pairs of canonically conjugate variable $\hat{x}$ and $\hat{p}$, related by the commutation relation $[\hat{x}, \hat{p}] = i$ can be decomposed into :

$$\hat{x} = \hat{N}_x x_0 + \hat{\overline{x}} \ , \ \hat{p} = \hat{N}_p p_0 + \hat{\overline{p}}, \tag{VII.1}$$

where $\hat{N}_x$ and $\hat{N}_p$ are operators with integers eigenvalues n_x and n_p which define a lattice along the x and p-axis, with period x_0 and p_0 respectively (see Fig. VII.1). $\hat{\overline{x}}$ and $\hat{\overline{p}}$ are bounded operators which spectra lie on the intervals $\frac{1}{2}[-x_0, x_0[$, $\frac{1}{2}[-p_0, p_0[$ respectively. In order to quantize the phase space, as we will see, it is not possible to have operators which are discontinuous as the bounded operator $\hat{\overline{x}}$ and $\hat{\overline{p}}$. Instead, we can choose smooth versions of these operators, such as their cos, sin or the exponential versions [Ruetsche, 2011]. The exponential form corresponds to displacement operators defined by $\hat{\mathcal{D}}(x, p) = e^{i(\hat{x}p - \hat{p}x)}$. It was shown in [Busch and Lahti, 1986, Schroeck, 1989] that if $x_0 p_0 = 2\pi$, the commutator of the two displacements operators vanishes:

$$[\hat{\mathcal{D}}(2\pi, 0), \hat{\mathcal{D}}(0, 2\pi)] = 0, \tag{VII.2}$$

Hence, the quantum algebra of modular variables differs from the classical algebra one, since the corresponding Poisson brackets of Eq. (VII.2) is not zero [Freidel et al., 2017]. In the following, we choose the values $x_0 = l$ and $p_0 = \frac{2\pi}{l}$. When the previous condition (see Eq. (VII.2)) is fulfilled, we can define the modular basis $|\overline{x}, \overline{p}\rangle$, which are the common eigenstates of the displacement operators:

$$\begin{aligned} \exp\big(i\hat{\overline{x}}\mu\big) \, |\overline{x}, \overline{p}\rangle &= \exp(i\overline{x}\mu) \, |\overline{x}, \overline{p}\rangle \, , \\ \exp\big(i\hat{\overline{p}}\alpha\big) \, |\overline{x}, \overline{p}\rangle &= \exp(i\overline{p}\alpha) \, |\overline{x}, \overline{p}\rangle \, , \end{aligned} \tag{VII.3}$$

for $\mu \in \frac{1}{2}[-\frac{\pi}{l}, \frac{\pi}{l}[$ and $\alpha \in \frac{1}{2}[-l/2, l/2[$. The MV basis is orthogonal since we have: $\langle \overline{x}', \overline{p}' | \overline{x}, \overline{p}\rangle = \delta_l(\overline{x} - \overline{x}')\delta_{\frac{2\pi}{l}}(\overline{p} - \overline{p}')$ (where δ_l is the Dirac comb of period l) and also satisfy the completeness relation: $\iint d\overline{x} d\overline{p} \, |\overline{x}, \overline{p}\rangle \langle \overline{x}, \overline{p}| = \mathbb{I}$. The integer operators do not commute and verify the relation:

$$[\hat{N}_x, \hat{N}_p] = \frac{i}{2\pi}\mathbb{I} - \frac{1}{l}[\hat{\overline{x}}, \hat{N}_p] - \frac{l}{2\pi}[\hat{N}_x, \hat{\overline{p}}], \tag{VII.4}$$

which is a consequence of the commutation relation $[\hat{x}, \hat{p}] = i$ [Gneiting and Hornberger, 2011, Ketterer et al., 2016]. From this equation, we conclude that we cannot build a basis with

the integers eigenvalues of the operators $\hat{N}_x, \hat{N}_p$. The two other commutators which appear in Eq. (VII.4) are different from zero and are:

$$[\hat{\overline{x}}, \hat{N}_p] = \frac{il}{2\pi}(\mathbb{I} - l\int_{-\pi/l}^{\pi/l} d\overline{p}\,|l/2, \overline{p}\rangle\,\langle l/2, \overline{p}|), \tag{VII.5}$$

$$[\hat{N}_x, \hat{\overline{p}}] = \frac{i}{l}(\mathbb{I} - \frac{2\pi}{l}\int_{-l/2}^{l/2} d\overline{x}\,|\overline{x}, \pi/l\rangle\,\langle \overline{x}, \pi/l|), \tag{VII.6}$$

where the second term on the right-hand side of the two previous equations are a sum of projectors on modular eigenstates. These relations constitute an additional proof of the distinction between the integers operators $\hat{N}_x$ and $\hat{N}_p$ and the angular momentum operators $\hat{N}$ and $\hat{M}$ defined by Eq. (VII.17). They prevent the construction of a basis built with the common eigenstates of $\hat{N}_x, \hat{N}_p$. Nevertheless, if we do not impose that the period of the x-lattice and the period of the p-lattice are related as before (periodic boundary condition), it would be possible to build such basis.

The Zak's transform (also called Weyl-Brezin-Zak transform [Gonzalez et al., 2003]) is a map-

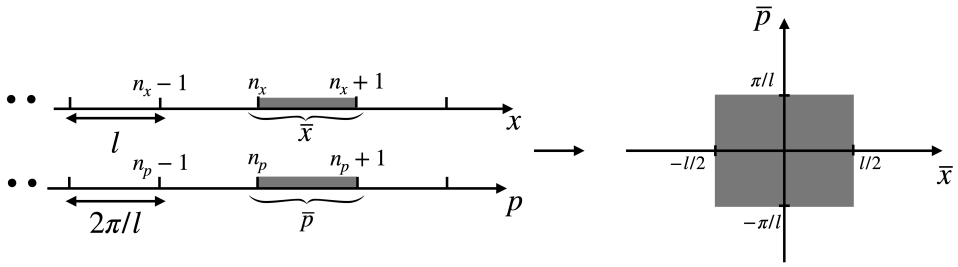

Figure VII.1: Schematic representation of the position and momentum lattices, with period $x_0 = l$ and $p_0 = 2\pi/l$. The integers n_x, n_p label the cells along the x,p axis and the modular variables $\overline{x}, \overline{p}$ correspond to the position and momentum values inside one cell. The figure is extracted from [Fabre et al., 2020b].

ping from $L^2(\mathbb{R}) \to L^2(\mathbb{S}^1 \times \mathbb{S}^{1*})$ (where $\mathbb{S}^{1*}$ is the dual of the circle $\mathbb{S}^1$) which permits the representation of a position or momentum function by a two-dimensional function [Gneiting and Hornberger, 2011, Ketterer et al., 2016]. For a position state, it can be written in the following form:

$$|x\rangle = |\overline{x} + ml\rangle = \int_{-\frac{\pi}{l}}^{\frac{\pi}{l}} d\overline{p} e^{-im\overline{p}l}\,|\overline{x}, \overline{p}\rangle\,, \tag{VII.7}$$

and for the inverse of the Zak's transform,

$$|\overline{x}, \overline{p}\rangle = \sum_{m\in\mathbb{Z}} e^{im\overline{p}l}\,|\overline{x} + ml\rangle\,. \tag{VII.8}$$

In the p-representation, the Zak's transform can be written as:

$$|p\rangle = |\overline{p} + \frac{2\pi}{l}n\rangle = e^{-i\overline{x}\cdot\overline{p}}\int_{-l/2}^{l/2} d\overline{x} e^{2i\pi n\overline{x}/l}\,|\overline{x}, \overline{p}\rangle\,, \tag{VII.9}$$

The modular basis being orthogonal, we can decompose a wave function $|\psi\rangle = \int_{\mathbb{R}} dx\psi(x)\,|x\rangle$ as:

$$|\psi\rangle = \int_{-\frac{\pi}{l}}^{\frac{\pi}{l}} \int_{-l/2}^{l/2} \psi(\overline{x},\overline{p})\,|\overline{x},\overline{p}\rangle\, d\overline{x}d\overline{p}, \tag{VII.10}$$

$$\psi(\overline{x},\overline{p}) = \sum_{n\in\mathbb{Z}} \psi(\overline{x}+nl)e^{-in\overline{p}l}. \tag{VII.11}$$

$\psi(\overline{x},\overline{p})$ is called the modular wave function and can be represented in a torus $\mathbb{S}^1 \times \mathbb{S}^{1*}$. The modular wave function is quasi-periodic in $\overline{x}$ and periodic in $\overline{p}$:

$$\psi(\overline{x}+l,\overline{p}) = e^{il\overline{p}}\psi(\overline{x},\overline{p}), \tag{VII.12}$$

$$\psi(\overline{x},\overline{p}+\frac{2\pi}{l}) = \psi(\overline{x},\overline{p}) \tag{VII.13}$$

The modular wave function is uniquely defined by its restriction to the unit square (the unfolded torus). The quasi-period is reminiscent of the Aharanov-Bohm potential [Aharonov and Bohm, 1959].

VII.2.2 Fourier transform of the modular variable basis

The canonical conjugate basis of the modular basis is defined by the double Fourier series [Englert et al., 2006],$\{(\overline{x},\overline{p})/\overline{x}\in\mathbb{S}^1,\overline{p}\in\mathbb{S}^{1*}\}\to\{(\frac{2\pi}{l}n,ml)/n,m\in\mathbb{Z}\}$:

$$|\overline{x},\overline{p}\rangle = \sum_{n,m\in\mathbb{Z}^2} |n,m\rangle e^{-i(\frac{2\pi}{l}n\overline{x}-ml\overline{p})}. \tag{VII.14}$$

is called the integer Zak's basis or the discrete Zak's basis. The inverse relation is the Fourier transform of the two bounded integrals:

$$|n,m\rangle = \int_{-\frac{l}{2}}^{\frac{l}{2}} \int_{-\frac{\pi}{l}}^{\frac{\pi}{l}} d\overline{x}d\overline{p}e^{i(\frac{2\pi n}{l}\overline{x}-ml\overline{p})}\,|\overline{x},\overline{p}\rangle \tag{VII.15}$$

This basis is also orthogonal since $\langle n',m'|n,m\rangle = \delta_{n,n'}\delta_{m,m'}$ and satisfies the closure relation $\sum_{n,m\in\mathbb{Z}^2}|n,m\rangle\langle n,m| = \mathbb{I}$. The scalar product of the two canonically conjugate basis is:

$$\langle n,m|\overline{x},\overline{p}\rangle = e^{i(\frac{2\pi n}{l}\overline{x}-ml\overline{p})}, \tag{VII.16}$$

which means that they are mutually unbiased. We define the two integers operators $\hat{N},\hat{M}$ with discrete spectrum $n,m\in\mathbb{Z}^2$:

$$\hat{N}\,|n,m\rangle = n\,|n,m\rangle \;\;,\;\; \hat{M}\,|n,m\rangle = m\,|n,m\rangle\,, \tag{VII.17}$$

and they necessarily commute $[\hat{N},\hat{M}]=0$. Thus, we cannot identify these operators to $\hat{N}_x,\hat{N}_p$. Even though we can know with an infinite precision the eigenvalues of the bounded operators, $\hat{\overline{x}}$, $\hat{\overline{p}}$, $\hat{N}$ and $\hat{M}$ this is not the case for the integers eigenvalues of $\hat{N}_x,\hat{N}_p$. They cannot be known simultaneously as a consequence of Heisenberg's inequality [Englert et al., 2006].

The only nonzero commutator between the four operators Eq. (VII.3) and Eq. (VII.17) are: $[\hat{N},\exp(i\hat{\overline{x}}\mu)] = \mu\exp(i\hat{\overline{x}}\mu)$ and $[\hat{M},\exp(i\hat{\overline{p}}\alpha)] = \alpha\exp(i\hat{\overline{p}}\alpha)$, with similar results in [Bizarro,

1994, J.Tosiek and Przanowski, 1995]. Hence $(\overline{x}, n)$ and $(\overline{p}, m)$ form a couple of independent azimuth-angular variables. We can hence write the wave function in the integer's basis:

$$|\psi\rangle = \sum_{n,m\in\mathbb{Z}^2} \psi_{n,m} |n, m\rangle . \tag{VII.18}$$

The relations between the modular wave function and the integer wave function are:

$$\psi_{n,m} = \int_{-\frac{\pi}{l}}^{\frac{\pi}{l}} \int_{-l/2}^{l/2} \psi(\overline{x}, \overline{p}) e^{-i(\frac{2\pi n}{l}\overline{x} - m\overline{p}l)} d\overline{x} d\overline{p}, \tag{VII.19}$$

$$\psi(\overline{x}, \overline{p}) = \sum_{n,m\in\mathbb{Z}^2} e^{i(\frac{2\pi n}{l}\overline{x} - m\overline{p}l)} \psi_{n,m}. \tag{VII.20}$$

The integer wave function defined by Eq. (VII.19) can be seen as a bipartite qudit state. $\psi_{n,m}$ is non-separable if it cannot be written under the form $\psi_{n,m} = f_n g_m$. Usual tools for understanding and quantifying non-separability of pure bipartite qudit system, with for instance the Schmidt decomposition, can be used in this context [Nielsen and Chuang, 2011].

The transformation relating the x-representation to the integer-representation is:

$$|x\rangle = |\overline{x} + ml\rangle = \sum_{n,m'\in\mathbb{Z}^2} \mathrm{sinc}((m - m')\pi) e^{-in2\pi\overline{x}/l} \left|n, m'\right\rangle , \tag{VII.21}$$

and the inverse relation is:

$$|n, m\rangle = \int_{-l/2}^{l/2} \sum_{m'\in\mathbb{Z}} e^{in2\pi\overline{x}/l} \mathrm{sinc}((m - m')\pi) \left|\overline{x} + m'l\right\rangle d\overline{x}, \tag{VII.22}$$

where we used the formula $\int_{-\pi/l}^{\pi/l} e^{-inl\overline{p}} e^{iml\overline{p}} d\overline{p} = \pi \mathrm{sinc}((m - n)\pi)$. We can also find the relation from the p-representation to the integer one in an analogous way. Thanks to these relations, it becomes more clear why it is not possible to identify the integer which labels the position in the Hilbert space x here noted m' in Eq. (VII.22) and the integer m which is the eigenvalue of the angular momentum operator $\hat{M}$.

We can also define two other hybrid basis with two variables, where one of them is bounded and the other is an integer, as $|\overline{x}, m\rangle$ or $|n, \overline{p}\rangle$. They constitute an orthogonal basis such that $\langle\overline{x}, n|\overline{x}', n'\rangle = \delta(\overline{x} - \overline{x}')\delta_{n,n'}$ and they are also complete. The two hybrid basis are mutually unbiased since:

$$\langle\overline{x}, m|n, \overline{p}\rangle = e^{i(\frac{2\pi n}{l}\overline{x} - ml\overline{p})}. \tag{VII.23}$$

The wave function can be expressed in the basis $|\overline{x}, m\rangle$, for instance, as:

$$|\psi\rangle = \sum_{m\in\mathbb{Z}} \int_{-l/2}^{l/2} d\overline{x} \psi(\overline{x}, ml) \left|\overline{x}, ml\right\rangle , \tag{VII.24}$$

where the amplitude $\psi(\overline{x}, \overline{p})$ is given by

$$\psi(\overline{x}, ml) = \int_{-\pi/l}^{\pi/l} \psi(\overline{x}, \overline{p}) e^{im\overline{p}l} d\overline{p}. \tag{VII.25}$$

The other relations between the various wave functions can be deduced straightforwardly in an analogous fashion. The relations between the different choices of basis are presented in Fig. VII.2 together with the different commutation relation between the associated operators.

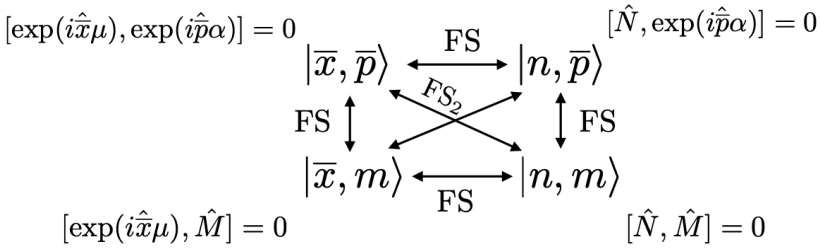

Figure VII.2: Relation between the different choices of basis. FS stands for Fourier series and FS_2 for double Fourier series. The figure is extracted from [Fabre et al., 2020b].

VII.2.3 Modular time-frequency bosonic creation and annihilation operator

In this section, we introduce the modular bosonic creation and annihilation operator of continuous variables of single photons, which can be the position and momentum or the frequency and time variables. For instance, the modular annihilation bosonic operator $\hat{a}(\overline{\omega}, \overline{t})$, which is the annihilation operator of a photon at frequency $\overline{\omega}$ and time $\overline{t}$ can be defined using the Zak's transform of the creation bosonic operator at frequency $\omega = \overline{\omega} + n\Delta$,

$$\hat{a}(\overline{\omega}, \overline{t}) = \sum_{n\in\mathbb{Z}} e^{-in\Delta\overline{t}} \hat{a}(\overline{\omega} + n\Delta). \tag{VII.26}$$

The last equation can be inverted to obtain the relation:

$$\hat{a}(\omega) = \hat{a}(\overline{\omega} + n\Delta) = \int_{-\Delta}^{\Delta} e^{in\Delta\overline{t}} \hat{a}(\overline{\omega}, \overline{t}) d\overline{t}. \tag{VII.27}$$

The modular time-frequency creation operator can be analogously defined and applied to the vacuum state: it corresponds to the creation of a a single photon state with the bounded frequency and time: $\hat{a}^\dagger(\overline{\omega}, \overline{t}) |0\rangle = |\overline{\omega}, \overline{t}\rangle$. We can show that the modular time-frequency creation and annihilation bosonic operators verify the same commutation relations than the creation and annihilation bosonic operators:

$$[\hat{a}(\overline{\omega}, \overline{t}), \hat{a}(\overline{\omega'}, \overline{t'})] = 0 \tag{VII.28}$$

$$[\hat{a}^\dagger(\overline{\omega}, \overline{t}), \hat{a}^\dagger(\overline{\omega'}, \overline{t'})] = 0, \tag{VII.29}$$

$$[\hat{a}(\overline{\omega}, \overline{t}), \hat{a}^\dagger(\overline{\omega'}, \overline{t'})] = \delta(\overline{\omega} - \overline{\omega'})\delta(\overline{t} - \overline{t'})\mathbb{I} \tag{VII.30}$$

The modular basis is defined by $\hat{a}^\dagger(\overline{\omega}, \overline{t}) |0\rangle = |\overline{\omega}, \overline{t}\rangle$ and is orthogonal since $\langle \overline{\omega}, \overline{t} | \overline{\omega}, \overline{t}\rangle = \delta(\overline{\omega} - \overline{\omega'})\delta(\overline{t} - \overline{t'})$. Hence, we can develop the wave function into the modular time-frequency basis:

$$|\psi\rangle = \iint d\overline{\omega} d\overline{t} \psi(\overline{\omega}, \overline{t}) |\overline{\omega}, \overline{t}\rangle, \tag{VII.31}$$

$$\psi(\overline{\omega}, \overline{t}) = \sum_{n\in\mathbb{Z}} \psi(\overline{\omega} + n\Delta) e^{in\Delta\overline{t}}. \tag{VII.32}$$

We can generalize to the many photons case without difficulty. For the sake of completeness, we can introduce the frequency modular operator as well as the time modular one as:

$$\hat{\overline{\omega}} = \iint d\overline{\omega} d\overline{t} \overline{\omega} \hat{a}^\dagger(\overline{\omega}, \overline{t}) \hat{a}(\overline{\omega}, \overline{t}) \tag{VII.33}$$

$$\hat{\overline{t}} = \iint d\overline{\omega} d\overline{t} \overline{t} \hat{a}^\dagger(\overline{\omega}, \overline{t}) \hat{a}(\overline{\omega}, \overline{t}), \tag{VII.34}$$

$$\tag{VII.35}$$

which allows to reproduce the commutation algebra of the position-momentum quadrature operators $[\hat{\overline{\omega}}, \hat{\overline{t}}] = 0$. For a quantization procedure, the exponential version of these operators has to be considered. As mentioned in Chap. III, the time modular operator has to be supplemented by an ancilla quantum clock. The aim of this section is also to show that when considering continuous variables degree of freedom of single photons, there is no need to introduce time and frequency (or position and momentum operators) to define modular variables. They can be considered as "parameters" of creation and annihilation bosonic operators, and the non-commutative algebra comes from the ladders operators. The modular variables used in the following can describe quadrature position-momentum variables as well as continuous variables of single photons.

VII.3 Some instances of modular wave functions

This section provides examples of probability distributions of modular wave function of quantum states.

VII.3.1 Coherent state

The wave function of a coherent state centered in the rectangular phase space at position x_0 and momentum p_0 can be written in the form as:

$$|\psi\rangle = \int_{\mathbb{R}} \frac{dx}{\sqrt{2\pi\sigma^2}} e^{-\frac{(x-x_0)^2}{2\sigma^2}} e^{ip_0(x-x_0)} |x\rangle \,, \tag{VII.36}$$

where σ is the width of the Gaussian function. In the modular basis, the corresponding modular wave function is [A.Ketterrer, 2016]:

$$\phi(\overline{x}, \overline{p}) = G_\sigma(\overline{x}) \Theta_3(\frac{l(\overline{p} - p_0)}{2} - i\frac{l(\overline{x} - x_0)}{2\sigma^2}, G_\sigma(l)), \tag{VII.37}$$

where l is the length of the lattice and Θ_3 is the third elliptic theta-function:

$$\Theta_3(x, y) = \sum_{n \in \mathbb{Z}} y^{n^2} e^{-2inx}. \tag{VII.38}$$

This distribution is also called the wrapped Gaussian distribution. The state is not separable into two functions which would depend on the modular variables $\overline{x}, \overline{p}$. We can study the state in two limits, choosing the values $x_0 = p_0 = 0$. In the case where $l \gg \sigma$, the Gaussian state in the modular basis can be approximated by:

$$\phi(\overline{x}, \overline{p}) \simeq N(\sigma, l) G_\sigma(\overline{x}) H_{2\pi/l}(\overline{p}), \tag{VII.39}$$

whereas in the other limit $\sigma = l$,

$$\phi(\overline{x}, \overline{p}) \simeq N'(\sigma, l) G_\sigma(\overline{p}) H_{2\pi/l}(\overline{x}), \tag{VII.40}$$

where $N(\sigma, l)$ and $N'(\sigma, l)$ are two normalization factors and $H_{2\pi/l}(\overline{p})$ is the rectangular function centered at zero of width $2\pi/l$. In this approximate form, the modular wave function is separable $\phi(\overline{x}, \overline{p}) \simeq f(\overline{x}) g(\overline{p})$ and is a localized state in the modular variable $\overline{x}$ but delocalized in the other

$\overline{p}$. It can be understood here as a consequence of the non-periodicity property of the amplitude wave function of the state in the x-representation. These two states are represented in Fig. VII.104(a) and (c). In Fig.VII.104(b), we represent an intermediate case where the Heaviside function is changing its direction.

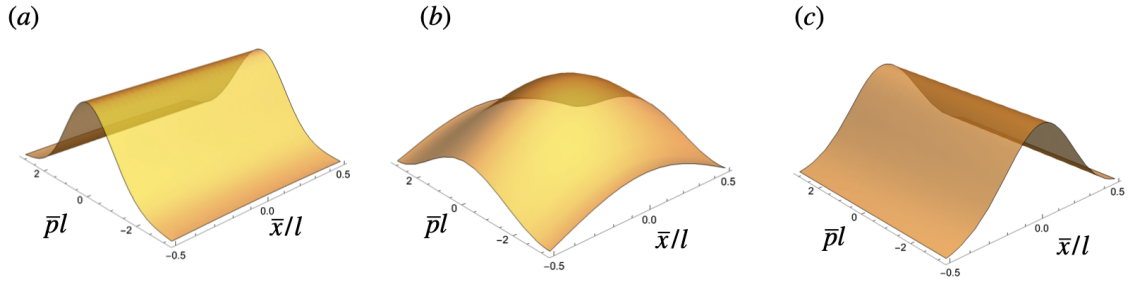

Figure VII.3: Plots of the probability distribution of wave function of the coherent state in the modular plane for the parameters $x_0 = p_0 = 0$. (a) $\sigma = l$ (b) $2\sigma = l$ (c) $5\sigma = l$.

VII.3.2 Ideal GKP states

In this section, we recall a few properties of GKP states [Albert et al., 2018, Gottesman et al., 2001], which are translational symmetric bosonic codes and express them using the modular representation.

In order to define the GKP qubit using continuous variables, we start by defining a lattice along the x-axis with an interval length $l = \sqrt{\pi}$. This corresponds to a lattice along the p-axis of length $2\sqrt{\pi} = 2\pi/\sqrt{\pi}$ as in the case of modular variables. The $\left|\overline{0}\right\rangle$ logical state of the qubit is defined as the translationally invariant comb with period $2\sqrt{\pi}$, where each peak is centered in each interval. The $\left|\overline{1}\right\rangle$ logical state is defined by the translation of the $\left|\overline{0}\right\rangle$ logical state of a $\sqrt{\pi}$ length. The GKP states are non-physical, since they are composed of infinitively squeezed peaks with an infinite large envelope as represented on Fig. VII.4. The two logical states can be written as two localized states in the modular plane:

$$\left|\overline{0}\right\rangle_x = |\overline{x} = -\frac{l}{4}, \overline{p} = 0\rangle = \sum_{n\in\mathbb{Z}} |-\frac{l}{4} + nl\rangle, \tag{VII.41}$$

$$\left|\overline{1}\right\rangle_x = |\overline{x} = \frac{l}{4}, \overline{p} = 0\rangle = \sum_{n\in\mathbb{Z}} |\frac{l}{4} + nl\rangle. \tag{VII.42}$$

It explicits the interest of using the modular basis to describe these states. The $\left|\overline{0}\right\rangle$ (resp. $\left|\overline{1}\right\rangle$) logical state is a point centered at $\mp l/4$ on the left (resp. right) modular half-plane (see Fig. (VII.1)). We also define the linear superposition $|\overline{\pm}\rangle_x = \frac{1}{\sqrt{2}}(\left|\overline{0}\right\rangle_x \pm \left|\overline{1}\right\rangle_x) = \left|\overline{0}, \overline{1}\right\rangle_p$ where the last equality stands only if the periodicity of the GKP states is $\sqrt{\pi}$.

In the integer Zak's basis, the GKP states are delocalized. This can be intuitively understood, since the modular and the integer Zak's basis are related by a Fourier series transform and is

written as:

$$\left|\overline{0}\right\rangle_x = \sum_{n,m\in\mathbb{Z}^2} e^{-i\pi n/2} \left|n,m\right\rangle \tag{VII.43}$$

$$\left|\overline{1}\right\rangle_x = \sum_{n,m\in\mathbb{Z}^2} e^{i\pi n/2} \left|n,m\right\rangle \tag{VII.44}$$

The fact that the integer wave function does not depend on m is a consequence of the non-normalizability of the state. It will be interpreted in the next section.

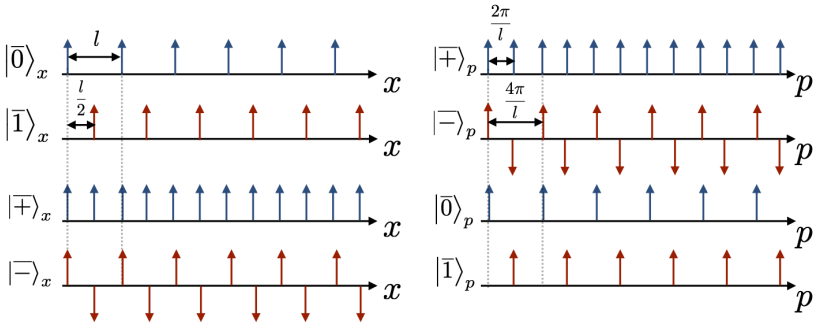

Figure VII.4: Schematic plot of the wave function of the GKP state in the two orthogonal quadratures. The vertical arrows represent the Dirac comb. In the x-representation, the $\left|\overline{0}\right\rangle_x$ (in blue) and $\left|\overline{1}\right\rangle_x$ (in red) logical state has a l periodicity and correspond to the $|\overline{+}\rangle_p$ and $|\overline{-}\rangle_p$ logical states in the p-representation. The figure is extracted from [Fabre et al., 2020b].

Alternatively we can define the lattice along the p-quadrature exchanging the definition of $\left|\overline{0}\right\rangle_p$ by $|\overline{+}\rangle_p$. This remark will be useful for Sec. VII.5.1.1.

VII.3.3 Gaussian Comb and physical GKP state

The wave function of a finitely squeezed Gaussian peak of width Δ and with an total envelop of width κ can be written in the position representation as:

$$\psi(x) = \frac{N}{(\pi\Delta^2)^{1/4}} e^{-(x\kappa)^2/2} \sum_{n\in\mathbb{Z}} e^{-(x-nl)^2/2\Delta^2} \tag{VII.45}$$

In the large comb limit $\Delta/l \gg 1$ and $\kappa l \gg 1$, the modular wavefunction is separable:

$$\psi(\overline{x},\overline{p}) = C_\Delta(\overline{x}) C_\kappa(\overline{p}) \tag{VII.46}$$

where C_Δ is the Gaussian comb which isdefined by

$$C_\Delta(\overline{x}) = \frac{1}{(\pi\Delta^2)^{1/4}} \sum_{n\in\mathbb{Z}} e^{-(\overline{x}-nl)^2/2\Delta^2} \tag{VII.47}$$

where the used the Poisson sum formula $\sum_{n\in\mathbb{Z}} f(t+nl) = \frac{1}{l}\sum_{n\in\mathbb{Z}} \tilde{f}(m\omega)e^{im\omega t}$, where $\omega = 2\pi/l$. This Gaussian comb can be used to define a qubit, which corresponds to a physical GKP state.

Each interval of the position lattice is divided by two, and the ideal GKP state, the $\left|\overline{0}\right\rangle$ and $\left|\overline{1}\right\rangle$ are the center of these two half-planes. The ideal comb is fed by applying displacement operators multiplied by Gaussian function, as mentioned in Sec. II.5.2. The effect of each single Kraus operation is represented in Fig. VII.5 in the position axis as well as in the modular plane. Finally, the superposition of physical GKP states $\left|\tilde{\pm}\right\rangle_x = \frac{1}{\sqrt{2}}(\left|\tilde{0}\right\rangle_x \pm \left|\tilde{1}\right\rangle_x)$ can be written as:

$$\left|\tilde{\pm}\right\rangle_x = \frac{\tilde{N}(l,\kappa,\Delta)}{\sqrt{2}}(\int_{-\frac{\pi}{l}}^{\frac{\pi}{l}} d\overline{p} \int_{\frac{-l}{2}}^{\frac{l}{2}} d\overline{x}(G_\Delta(\overline{x}-l/4)G_\kappa(\overline{p}) \pm G_\Delta(\overline{x}+l/4)G_\kappa(\overline{p}))\left|\overline{x},\overline{p}\right\rangle), \quad \text{(VII.48)}$$

where the non-trivial normalization $\tilde{N}(l/\sigma) = 1/(\left|\left\langle\tilde{0}\middle|\tilde{0}\right\rangle + \left\langle\tilde{1}\middle|\tilde{1}\right\rangle \pm 2\left\langle\tilde{0}\middle|\tilde{1}\right\rangle\right|^{1/2})$ with $\left\langle\tilde{0}\middle|\tilde{0}\right\rangle = \left\langle\tilde{1}\middle|\tilde{1}\right\rangle = 2\text{erf}(\frac{\kappa\pi}{l}) \cdot (\text{erf}(\frac{l}{4\Delta}) + \text{erf}(\frac{3l}{4\Delta}))$ and $\left\langle\tilde{0}\middle|\tilde{1}\right\rangle$ is given by:

$$\left\langle\tilde{0}\middle|\tilde{1}\right\rangle_x = \frac{\text{erf}(\frac{\kappa\pi}{l}).e^{-(l/4\Delta)^2}\text{erf}(l/2\Delta)}{\text{erf}(3l/4\Delta) + \text{erf}(l/4\Delta)} \quad \text{(VII.49)}$$

The two states become orthogonal in the limit $l \gg \Delta$. The real GKP states are represented on Fig. (VII.5)(a) and (b) in the modular plane (resp. over the real line x) when $l \gg \Delta$ and $2\pi/l \gg \kappa$, which are the conditions assumed here. Finally, following Ref. [Glancy and Knill, 2006], the modular wave function for GKP states can be interpreted as the amplitude of probability of having an error of u (resp. v) in the x-quadrature (resp. p) if $|u|, |v| < \sqrt{\pi}/6$.

In the limit of infinite squeezing, we recover the non-physical state described by an ideal GKP state, or a Dirac comb, which can be described by the modular wave function $\psi(\overline{x},\overline{p}) = \delta(\overline{x})\delta(\overline{p})$.

The state described by Eq. (VII.92) can be written in the integer representation: $\left|\tilde{0}\right\rangle = \sum_{n,m\in\mathbb{Z}^2} f_n g_m \left|n,m\right\rangle$ with $f_n = \int_{-l/2}^{l/2} d\overline{x} e^{-i\frac{2\pi}{l}n\overline{x}} G_\Delta(\overline{x}+l/4)$ and $g_m = \int_{-\pi/l}^{\pi/l} d\overline{p} G_\kappa(\overline{p}) e^{im\overline{p}l}$ that are calculated in details in Appendix A.5. When we consider ideal GKP states (see Eq. (VII.43)), the envelope of the position comb is infinite and this is why g_m does not depend of m.

VII.3.4 Set of logical of gates for the GKP qubit

We now introduce the set of Pauli matrices adapted for this qubit encoding [Ketterer et al., 2016]. It corresponds to the displacement operators:

$$\hat{X} = \hat{\mathcal{D}}(\frac{l}{2},0) = \int_{-l/2}^{l/2} d\overline{x} \int_{-\pi/l}^{\pi/l} d\overline{p} e^{2i\pi\overline{x}/l} \hat{\sigma}_x(\overline{x},\overline{p}), \quad \text{(VII.50)}$$

$$\hat{Z} = \hat{\mathcal{D}}(0,\pi/l) = \int_{-l/2}^{l/2} d\overline{x} \int_{-\pi/l}^{\pi/l} d\overline{p} e^{-i\overline{p}l} \hat{\sigma}_z(\overline{x},\overline{p}), \quad \text{(VII.51)}$$

with the Pauli matrices

$$\hat{\sigma}_x(\overline{x},\overline{p}) = e^{-i\overline{p}l/2}\left|\overline{x},\overline{p}\right\rangle\left\langle\overline{x}+\frac{l}{2},\overline{p}\right| + e^{i\overline{p}l/2}\left|\overline{x}+\frac{l}{2},\overline{p}\right\rangle\left\langle\overline{x},\overline{p}\right|, \quad \text{(VII.52)}$$

$$\hat{\sigma}_y(\overline{x},\overline{p}) = i(e^{i\overline{p}l/2}\left|\overline{x}+\frac{l}{2},\overline{p}\right\rangle\left\langle\overline{x},\overline{p}\right| - e^{-i\overline{p}l/2}\left|\overline{x},\overline{p}\right\rangle\left\langle\overline{x}+\frac{l}{2},\overline{p}\right|), \quad \text{(VII.53)}$$

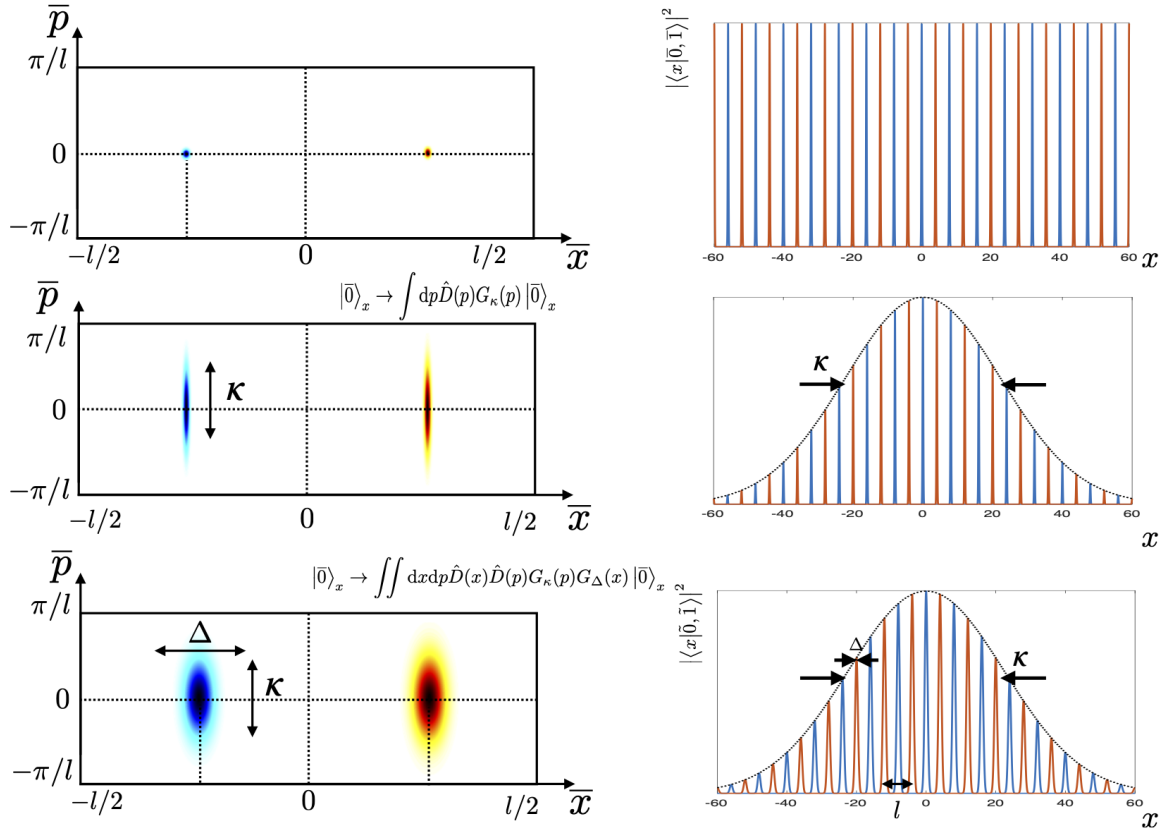

Figure VII.5: (a) Probability density of the 0 (blue) and 1 (red) physical GKP state in the modular plane, which are Gaussian in the variable $\overline{x}$ and $\overline{p}$. (b) Wave function of the GKP state in the x-representation.

$$\hat{\sigma}_z(\overline{x},\overline{p}) = |\overline{x},\overline{p}\rangle\langle\overline{x},\overline{p}| - |\overline{x}+\frac{l}{2},\overline{p}\rangle\langle\overline{x}+\frac{l}{2},\overline{p}|. \tag{VII.54}$$

These gates are not hermitian and that $\hat{Z}^2 \neq \mathbb{I}$ and $\hat{X}^2 \neq \mathbb{I}$. Operators $\hat{X}$ and $\hat{Z}$ are not elements of the basis of the $\mathbb{SU}(2)$ Lie algebra. In [Ketterer et al., 2016], it was shown that we can introduce modular readout observables $\hat{\Gamma}_\beta$, which are hermitian and constructed by analogy with the logical Pauli operators. They are defined by:

$$\hat{\Gamma}_\beta = \int_{-l/2}^{l/2} d\overline{x} \int_{-\pi/l}^{\pi/l} d\overline{p} \hat{\sigma}_\beta(\overline{x},\overline{p}), \tag{VII.55}$$

with $\beta = x, y, z$ and with the modular Pauli matrices $\hat{\sigma}_\beta(\overline{x},\overline{p})$. These operators will be useful for the tomographic reconstruction of the modular Wigner distribution in Sec.VII.7.

VII.4 Quantization in a double cylinder phase plane

In this section, after introducing the displacement and point operator [Miquel et al., 2002, Wootters, 2004] on a double cylinder phase space, we build the associated Wigner distribution.

VII.4.1 Displacement operator and phase point operator on a double cylinder

VII.4.1.1 Modular Displacement operator

The modular variables $\overline{x}, \overline{p}$ are angle coordinates and are canonically conjugated to the integers variable n, m which are the angular momentum variable. We define the modular displacement operator as:

$$\hat{D}(n, \overline{x}, m, \overline{p}) = e^{i(\overline{x}\frac{2\pi\hat{N}}{l} + \hat{\overline{x}}\frac{2\pi n}{l} - \overline{p}l\hat{M} + \hat{\overline{p}}ml)}. \tag{VII.56}$$

Owing to the commutation relations between the different operators (see Fig. VII.2), the pairs $(n, \overline{x})$ and $(m, \overline{p})$ are dynamical variables of two independent degrees of freedom, as pointed out in [Englert et al., 2006]. The modular displacement operator can hence be written as the product of unitary operators $\hat{D}(n, \overline{x}, m, \overline{p}) = \hat{D}(n, \overline{x})\hat{D}(m, \overline{p})$, with for instance $\hat{D}(n, \overline{x}) = e^{i(\overline{x}\frac{2\pi\hat{N}}{l} + \hat{\overline{x}}\frac{2\pi n}{l})}$.

The modular displacement operator can be rewritten in an integral or sum representation. First, in the integer Zak's basis,

$$\hat{D}(n, \overline{x}, m, \overline{p}) = \sum_{r,s\in\mathbb{Z}^2} e^{i\overline{x}(r+n/2)\frac{2\pi}{l}} e^{-i\overline{p}(s+m/2)l} \left|r+n, m+s\right\rangle \left\langle r, s\right|. \tag{VII.57}$$

And then in the modular basis,

$$\hat{D}(n, \overline{x})\hat{D}(m, \overline{p}) = e^{-in\frac{2\pi}{l}\overline{x}/2} e^{iml\overline{p}l/2} \int_{-l/2}^{l/2} d\overline{x_1} \int_{-\pi/l}^{\pi/l} d\overline{p}_1 e^{i\frac{2\pi}{l}\overline{x_1}n} e^{-i\overline{p}_1 l} \left|\overline{\overline{x_1}+\overline{x}}, \overline{\overline{p}_1+\overline{p}}\right\rangle \left\langle \overline{x_1}, \overline{p}_1\right|. \tag{VII.58}$$

The product of two modular displacement operators is equivalent to a modular displacement operator where the variables are summed up to a phase factor called the cocycle:

$$\begin{aligned}\hat{D}(n, \overline{x}, m, \overline{p})\hat{D}(n', \overline{x'}, m', \overline{p'}) & e^{-i(\overline{x}n'/2 - \overline{x'}n/2)\frac{2\pi}{l}} e^{-i(\frac{\overline{p}m'}{2} - \overline{p'}m/2)l} \\ &= e^{\pm iH(\left|\overline{x}-l\pm\overline{x'}\right|)\frac{(n+n')}{2}} e^{\mp iH(\left|\overline{p}-\frac{\pi}{l}\pm\overline{p'}\right|)\frac{(m+m')}{2}} \\ &\quad \times \hat{D}(n+n', \overline{\overline{x}+\overline{x'}}, m+m', \overline{\overline{p}+\overline{p'}}),\end{aligned} \tag{VII.59}$$

where we have used the relation $\overline{\overline{x}+\overline{x'}} = \overline{x} + \overline{x'} \mp lH(\left|\overline{x} - l/2 \pm \overline{x'}\right|)$ for $\overline{x} \gtrless 0$ [Mukunda, 1979] and $H(x)$ is the Heaviside function which is zero for negative values of x and equals to one if not. The modular displacement operator forms an orthogonal basis:

$$\mathrm{Tr}(\hat{D}^\dagger(n', \overline{x'}, m', \overline{p'})\hat{D}(n, \overline{x}, m, \overline{p})) = \delta(\overline{x} - \overline{x'})\delta(\overline{p} - \overline{p'})\delta_{n',n}\delta_{m',m}, \tag{VII.60}$$

where we have used the formula $\sum_{n\in\mathbb{Z}^2} e^{in(\overline{x}-\overline{x'})} = \delta(\overline{x}-\overline{x'})$ and satisfy the completeness relation:

$$\sum_{n,m\in\mathbb{Z}^2} \int_{-l/2}^{l/2} d\overline{x} \int_{-\frac{\pi}{l}}^{\frac{\pi}{l}} d\overline{p}\hat{D}(n, \overline{x}, m, \overline{p})\hat{D}^\dagger(n, \overline{x}, m, \overline{p}) = \mathbb{I}. \tag{VII.61}$$

Any operator can be expanded into such a complete basis. In particular the density matrix reads:

$$\hat{\rho} = \int_{\frac{-l}{2}}^{\frac{l}{2}} \int_{-\frac{\pi}{l}}^{\frac{\pi}{l}} \sum_{n,m\in\mathbb{Z}^2} \hat{D}(n, \overline{x}, m, \overline{p})\chi(n, \overline{x}, m, \overline{p}) d\overline{x} d\overline{p}, \tag{VII.62}$$

where we introduced the modular characteristic function $\chi(n, \overline{x}, m, \overline{p}) = \mathrm{Tr}(\hat{\rho}\hat{D}^\dagger(n, \overline{x}, m, \overline{p}))$.

VII.4.1.2 Point operator on a double cylinder phase space

In this section, we introduce the point operator on a double cylinder phase space from its definition on the one cylinder phase space. It is defined as the symplectic Fourier transform of the displacement operator [Bizarro, 1994, Rigas et al., 2008, 2010],

$$\hat{\Delta}(n,m,\overline{x},\overline{p}) = \int_{-\frac{\pi}{l}}^{\frac{\pi}{l}} \int_{-l/2}^{l/2} d\overline{x'} d\overline{p'} \sum_{q,s\in\mathbb{Z}^2} e^{i\frac{2\pi q}{l}\overline{x}} e^{is\overline{p}l} e^{-i\frac{2\pi n}{l}\overline{x'}} e^{-im\overline{p'}l} \hat{D}(q,\overline{x'},s,\overline{p'}). \tag{VII.63}$$

An operator which can be expanded into a product of polynomial of $\hat{\overline{x}}, \hat{\overline{p}}, \hat{N}, \hat{M}$ can be written in many ways depending on the choice of the operators ordering. In Eq. (VII.63), the Weyl ordering has been considered [J.Tosiek and Przanowski, 1995]. The variables of the point operator label the phase space and do not correspond to the variables of the integer Zak's basis. The point operator verifies the finite norm condition:

$$\sum_{n,m\in\mathbb{Z}^2} \int_{-\frac{\pi}{l}}^{\frac{\pi}{l}} \int_{-l/2}^{l/2} d\overline{x} d\overline{p} \hat{\Delta}(n,m,\overline{x},\overline{p}) = \mathbb{I}. \tag{VII.64}$$

Point and parity operators are related by the equation

$$\hat{\Delta}(0,0,0,0) = \hat{\Delta} = \hat{\Pi}, \tag{VII.65}$$

$\hat{\Pi}$ being the parity operator defined by $\hat{\Pi} = \int dx \, |x\rangle \langle -x|$. $\hat{\Pi}$ is a reflection along the x-axis and can also be written in the modular basis:

$$\hat{\Pi} = \int_{-\frac{\pi}{l}}^{\frac{\pi}{l}} \int_{-l/2}^{l/2} d\overline{x} d\overline{p} \, |\overline{x},\overline{p}\rangle \langle -\overline{x},-\overline{p}| \,, \tag{VII.66}$$

where we used Eq. (VII.7). The parity operator can also be seen as an inversion about the origin in the modular plane. In the integer representation, the parity operator has a similar form, $\hat{\Pi} = \sum_{n,m\in\mathbb{Z}^2} |n,m\rangle \langle -n,-m|$.

We point out that the point operator $\hat{\Delta}(n,m,\overline{x},\overline{p})$ is also separable in the two pairs of azimuth-angular momentum variables, owing to the commutation relation invoked in VII.2.2:

$$\hat{\Delta}(n,m,\overline{x},\overline{p}) = \hat{f}(n,\overline{x})\hat{g}(m,\overline{p}) \tag{VII.67}$$

which can be written, using Eq. (VII.57), in the integer Zak's basis as:

$$\hat{f}(n,\overline{x})\hat{g}(m,\overline{p}) = \sum_{n',r,m',r'\in\mathbb{Z}} \int_{-l/2}^{l/2} \int_{-\pi/l}^{\pi/l} d\overline{x'} d\overline{p'} e^{i\overline{x'}\frac{2\pi}{l}(r+n'/2)} e^{-i(n'\overline{x}-n\overline{x'})\frac{2\pi}{l}} e^{-i\overline{p'}l(r'+m'/2)} e^{i(m'\overline{p}-m\overline{p'})l} \times |r+n',r'+m'\rangle \langle r,r'| \,. \tag{VII.68}$$

After integration, we obtain:

$$\hat{f}(n,\overline{x})\hat{g}(m,\overline{p}) = \sum_{n',m'\in\mathbb{Z}^2} e^{\frac{2i\pi}{l}\overline{x}(n-n'/2)} e^{i\overline{p}(m-m'/2)l} |n+\frac{n'}{2}, m+\frac{n'}{2}\rangle\langle n-\frac{m'}{2}, m-\frac{m'}{2}|. \tag{VII.69}$$

Then, we can express the point operator under the covariant form:

$$\hat{\Delta}(n,m,\overline{x},\overline{p}) = \hat{D}(n,\overline{x},m,\overline{p})\hat{\Delta}\hat{D}^{\dagger}(n,\overline{x},m,\overline{p}). \tag{VII.70}$$

where $\hat{\Delta} = \hat{\Pi}$ from Eq. (VII.65). In summary, the phase space described in this section is the cartesian product of two cylinders $(S^1 \times \mathbb{Z})^2$, since we have two independent pairs of canonically conjugate azimuthal-angular variable.

VII.4.2 Lie algebra of the cylindrical group

For the sake of completeness, we define the generators of the Lie algebra of the cylindrical group $\mathbb{S}^1 \times \mathbb{Z}$ are the set of the three operators:

$$\hat{A}_1 = e^{i2\pi\hat{\overline{x}}/l} \ , \ \hat{A}_{-1} = e^{-i2\pi\hat{\overline{x}}/l} \ , \ \hat{R}_1 = il\frac{d}{d\overline{x}} \tag{VII.71}$$

where $\hat{R}_1$ is the generator of rotations and $\hat{A}_1$ and $\hat{A}_{-1}$ are two generators of translation (in opposite direction) into the cylinder. The three operators satisfy the circular canonical commutation relation [Ruetsche, 2011]:

$$[\hat{A}_1, \hat{A}_{-1}] = 0 \ , \ [\hat{R}_1, \hat{A}_1] = i\hat{A}_{-1} \ , \ [\hat{R}_1, \hat{A}_{-1}] = -i\hat{A}_1 \tag{VII.72}$$

which forms the Lie algebra of the cylindrical group. The spectrum of R_1 is composed of integers and hence corresponds to the operator $\hat{N}$ defined by Eq. (VII.17).

Then, the generators of a Lie algebra of two independent cylinders are:

$$\{e^{i2\pi\hat{\overline{x}}/l}, e^{-i2\pi\hat{\overline{x}}/l}, \hat{N}, e^{i\overline{p}l}, e^{-i\overline{p}l}, \hat{M}\}. \tag{VII.73}$$

VII.4.3 Modular Wigner distribution

The expectation value of the point operator [Ercolessi et al., 2007, Miquel et al., 2002, Wootters, 2004], also called the symbol of the density matrix, is the quasi-probability distribution in a double cylinder phase space $(S^1 \times \mathbb{Z})^2$ whose variables are noted $(n, \overline{x})$ and $(m, \overline{p})$. We call it the Modular Wigner distribution and is defined as [Bizarro, 1994, Rigas et al., 2008]:

$$W_{\hat{\rho}}(n, m, \overline{x}, \overline{p}) = \mathrm{Tr}(\hat{\rho}\hat{\Delta}(n, m, \overline{x}, \overline{p})). \tag{VII.74}$$

Due to the hermiticity of the point operator $\hat{\Delta}(n, m, \overline{x}, \overline{p})$ the Modular Wigner distribution is real. After taking the trace operation, the distribution takes the familiar form in the modular representation,

$$W_{\hat{\rho}}(n, m, \overline{x}, \overline{p}) = \int_{-\frac{\pi}{l}}^{\frac{\pi}{l}} \int_{-l/2}^{l/2} e^{2i\frac{2\pi}{l}n\overline{x'}} e^{-2i\overline{p'}ml} d\overline{x'} d\overline{p'} \langle \overline{\overline{x} - \overline{x'}}, \overline{\overline{p} - \overline{p'}} | \hat{\rho} | \overline{\overline{x} + \overline{x'}}, \overline{\overline{p} + \overline{p'}} \rangle. \tag{VII.75}$$

In the integer representation, the Wigner distribution has the form:

$$W_{\hat{\rho}}(n, m, \overline{x}, \overline{p}) = w_{\hat{\rho}}(2n, 2m, \overline{x}, \overline{p}) + \frac{2}{\pi} \sum_{n', m' \in \mathbb{Z}} \frac{(-1)^{n-n'}}{2n' + 1 - 2n} \frac{(-1)^{m-m'}}{2m' + 1 - 2m} w_{\hat{\rho}}(2n' + 1, 2m' + 1, \overline{x}, \overline{p}) \tag{VII.76}$$

where,

$$w_{\hat{\rho}}(2n+\alpha, 2m+\beta, \overline{x}, \overline{p}) = \sum_{n', m' \in \mathbb{Z}^2} e^{-i(2n'+\alpha)\frac{2\pi}{l}\overline{x}} e^{i(2m'+\beta)\overline{p}l} \left\langle 2n - n', 2m - m' \right| \hat{\rho} \left| 2n + n' + \alpha, 2m + m' + \beta \right\rangle, \tag{VII.77}$$

with $\alpha, \beta = 0, 1$. We also note that another definition of Wigner distribution was proposed in [Hush et al., 2010] for the number-phase Wigner distribution. It consists of a phase space

with half integer values. The two cylinder phase space $(\overline{x}, n)$ and $(\overline{p}, m)$ are not coupled if the modular wave function in Eq. (VII.10) or the integer one in Eq. (VII.19) is separable.

Summing over all variables of the distribution, we find the correct normalization of the modular Wigner distribution:

$$\int_{-\frac{\pi}{l}}^{\frac{\pi}{l}} \int_{-l/2}^{l/2} d\overline{x} d\overline{p} \sum_{n,m\in\mathbb{Z}^2} W_{\hat{\rho}}(n, m, \overline{x}, \overline{p}) = 1, \tag{VII.78}$$

since the density matrix $\hat{\rho}$ is normalized.

The marginals can be found by summing over different variables. By summing over n and m, we obtain the following marginal,

$$\sum_{n,m\in\mathbb{Z}^2} W_{\hat{\rho}}(n, m, \overline{x}, \overline{p}) = \langle \overline{x}, \overline{p}| \, \hat{\rho} \, |\overline{x}, \overline{p}\rangle \,, \tag{VII.79}$$

where we have used the series representation of the Dirac distribution: $\delta(\overline{x}) = \sum_{k\in\mathbb{Z}} e^{ik\overline{x}}$. It corresponds to what we expect for such probability distribution as it is the diagonal matrix element of the density matrix in the modular basis. The marginal obtained by integrating over the modular variables is :

$$\int_{-\frac{\pi}{l}}^{\frac{\pi}{l}} \int_{-l/2}^{l/2} d\overline{x} d\overline{p} W_{\hat{\rho}}(n, m, \overline{x}, \overline{p}) = \langle n, m| \, \hat{\rho} \, |n, m\rangle \,, \tag{VII.80}$$

and gives also the correct marginal. The integers variables of the integer wave function $\psi_{n,m}$ cannot be interpreted as the integers which label the lattices along the x and p-axis. Thus, the integer variables of the Wigner distribution do not have a simple physical meaning, which is a consequence of an additional phase. Nevertheless, the modular variables on phase space can be related to the coordinates of the two position and momentum lattices.

We can define two partial traces of the density matrix. One of them is obtained by summing over the integer n and by integrating over the position modular variable $\overline{x}$:

$$F_{\hat{\rho}}(m, \overline{p}) = \sum_{n\in\mathbb{Z}} \int_{-\frac{l}{2}}^{\frac{l}{2}} d\overline{x} W_{\hat{\rho}}(n, m, \overline{x}, \overline{p}) = \int_{-\frac{\pi}{l}}^{\frac{\pi}{l}} \int_{\frac{-l}{2}}^{\frac{l}{2}} d\overline{x} d\overline{p'} \left\langle \overline{x}, \overline{\overline{p} - \overline{p'}} \right| \hat{\rho} \left| \overline{x}, \overline{\overline{p} + \overline{p'}} \right\rangle e^{-2i\overline{p'}ml}. \tag{VII.81}$$

The other partial trace is obtained simply by exchanging the pairs of variables m, $\overline{p}$ and n, $\overline{x}$. In addition, two crossed marginals can be determined by summing over m (resp. n) and integrating over $\overline{p}$ (resp. $\overline{x}$):

$$M_1(m, \overline{x}) = \langle \overline{x}, m| \, \hat{\rho} \, |\overline{x}, m\rangle \,, \tag{VII.82}$$

$$M_2(n, \overline{p}) = \langle \overline{p}, n| \, \hat{\rho} \, |\overline{p}, n\rangle \,, \tag{VII.83}$$

and they correspond to the correct marginals (see Eq. (VII.25)). The density matrix can be obtained from the Modular Wigner distribution as:

$$\hat{\rho} = \sum_{n,m\in\mathbb{Z}^2} \int_{-\frac{\pi}{l}}^{\frac{\pi}{l}} \int_{-l/2}^{l/2} d\overline{x} d\overline{p} \hat{\Delta}(n, m, \overline{x}, \overline{p}) W_{\hat{\rho}}(n, m, \overline{x}.\overline{p}). \tag{VII.84}$$

With this last reconstruction property, the introduced distribution satisfies all the Stratanovich-Weyl postulates [Khvedelidze and Abgaryan, 2017].

We now explicitly study the case of two independent cylinder phase space, which corresponds to a separable bipartite system. For a pure state $\hat{\rho} = |\psi\rangle\langle\psi|$, and a separable wave function $\psi(\overline{x},\overline{p}) = f(\overline{x})g(\overline{p})$, we can write formally $|\psi\rangle = (\int d\overline{x} f(\overline{x})|\overline{x}\rangle)(\int d\overline{p} g(\overline{p}))|\overline{p}\rangle = |f\rangle|g\rangle$. Therefore, the modular Wigner distribution is also separable, and we can write:

$$W_{\hat{\rho}}(n,m,\overline{x},\overline{p}) = W_{|f\rangle}(n,\overline{x})W_{|g\rangle}(m,\overline{p}). \tag{VII.85}$$

Each distribution is an angle-momentum Wigner distribution and the two cylinders phase space are hence decoupled. In that case, the modular Wigner distribution in the integer representation takes the form:

$$W_{|f\rangle}(n,\overline{x}) = \int_{-l/2}^{l/2} e^{2i\frac{2\pi}{l}n\overline{x'}}\langle\overline{\overline{x}-\overline{x'}}|\,|f\rangle\langle f|\,|\overline{\overline{x}+\overline{x'}}\rangle d\overline{x'}, \tag{VII.86}$$

$$W_{|g\rangle}(m,\overline{p}) = \int_{-\frac{\pi}{l}}^{\frac{\pi}{l}} e^{-2im\overline{p'}l}\langle\overline{\overline{p}-\overline{p'}}|\,|g\rangle\langle g|\,|\overline{\overline{p}+\overline{p'}}\rangle d\overline{p'}. \tag{VII.87}$$

We note that the modular Wigner distribution $W_{|g\rangle}(m,\overline{p})$ has similar properties to the one introduced in Ref. [Rigas et al., 2008]. We also point out that $F(m,\overline{p})$, whose expression is given by Eq. (VII.81), when the state is pure and $|\psi\rangle = |f\rangle|g\rangle$, is related to $W_{|g\rangle}(m,\overline{p})$ up to a multiplicative factor.

VII.4.4 Application on the use of modular displacement operators: construction of physical GKP state

In this section, we describe a physical GKP state using the formalism developed in [Glancy and Knill, 2006, Motes et al., 2017]. For such, we will consider a noise model expressed in the integer and modular variables rather than in the position and momentum quadrature variables, which are equivalent in the limit described below.

We start by considering small shifts in position $\hat{\mathcal{D}}(u,0) = e^{iu\hat{p}}$ and momentum $\hat{\mathcal{D}}(0,v) = e^{-iv\hat{q}}$ quadrature where $u \in [-\sqrt{\pi}/2, \sqrt{\pi}/2[$ and $v \in [-\sqrt{\pi}, \sqrt{\pi}[$ applied to an ideal GKP state. The application of such small displacements to the state $\left|\overline{0}\right\rangle_x$ can be written in the modular basis:

$$e^{-iv\hat{q}}e^{iu\hat{p}}\left|\overline{0}\right\rangle_x = |\overline{x}=u,\overline{p}=v\rangle\,. \tag{VII.88}$$

If the displacement goes beyond the modular plane $u,v > \sqrt{\pi}$, additional phase factors appear. In addition, for small displacements, the displacement operator $\hat{\mathcal{D}}(u,0)$ and $\hat{\mathcal{D}}(0,v)$ coincide with the modular displacement operator $\hat{D}(0,\overline{x}=u)$ and $\hat{D}(0,\overline{p}=v)$. Hence, the noise models, using position-momentum variables or the bounded/integer position and momentum one, are equivalent in the limit of small shifts *i.e* $|u|,|v| < \sqrt{\pi}/6$ [Glancy and Knill, 2006]. It will be useful for finding a criteria of the correctability of GKP state as developed in [Glancy and Knill, 2006] and in Sec. VII.6.2.

Physical GKP states are constructed by applying the operator $\hat{U}$, expanded in the modular displacement basis, to the ideal GKP state $\left|\tilde{0}\right\rangle_x = \hat{U}\left|\overline{0}\right\rangle_x$ defined by:

$$\left|\tilde{0}\right\rangle_x = \int_{-\frac{\pi}{l}}^{\frac{\pi}{l}} \int_{\frac{-l}{2}}^{\frac{l}{2}} \sum_{n,m\in\mathbb{Z}^2} E(\overline{x},n,\overline{p},m)\hat{D}(\overline{x},n)\hat{D}(\overline{p},m)d\overline{x}d\overline{p}\left|\overline{0}\right\rangle_x, \tag{VII.89}$$

where $E(\overline{x},n,\overline{p},m)$ is the noise distribution or the Weyl-operator expansion of $\hat{U}$. This procedure for building physical GKP states is analog to the one described in [Motes et al., 2017].
After applying the displacement operators to the ideal GKP state, we get:

$$\hat{D}(\overline{x},n)\hat{D}(\overline{p},m)\left|\overline{0}\right\rangle_x = e^{-2i\pi\overline{x}n/l}e^{-i\pi n/2}e^{-i\overline{p}ml}\left|\overline{x}-l/4,\overline{p}\right\rangle. \tag{VII.90}$$

Using the previous equation, the state described by Eq. (VII.89) can be written as:

$$\left|\tilde{0}\right\rangle_x = \int_{-\frac{\pi}{l}}^{\frac{\pi}{l}} \int_{\frac{-l}{2}}^{\frac{l}{2}} \sum_{n,m\in\mathbb{Z}^2} E(\overline{x},n,\overline{p},m)e^{-2i\pi\overline{x}n/l}e^{-i\pi n/2}e^{-i\overline{p}ml}\left|\overline{x}-l/4,\overline{p}\right\rangle d\overline{x}d\overline{p}. \tag{VII.91}$$

After performing a change of variable on $\overline{x}$, the real GKP state reads:

$$\left|\tilde{0}\right\rangle_x = \int_{-\frac{\pi}{l}}^{\frac{\pi}{l}} d\overline{p}\int_{\frac{-l}{2}}^{\frac{l}{2}} d\overline{x}\psi(\overline{x},\overline{p})\left|\overline{x},\overline{p}\right\rangle, \tag{VII.92}$$

where the modular wavefunction is $\psi(\overline{x},\overline{p}) = \sum_{n,m} E(\overline{x},n,\overline{p},m)e^{-2i\pi\overline{x}n/l}e^{-i\pi n/2}e^{-i\overline{p}ml}$.

Square GKP states, whose envelope and peaks of the comb are Gaussian functions [Albert et al., 2018, Glancy and Knill, 2006, Gottesman et al., 2001], can be obtained assuming that the noise distribution E is separable in the pairs of variables: $E(\overline{x},n,\overline{p},m) = f(\overline{x},n)h(\overline{p},m)$. Then, to obtain such square GKP states, the sums over n and m must be equal to two Gaussian combs on each variable, namely $\sum_n e^{-2i\pi\overline{x}n/l}e^{-i\pi n/2}f(\overline{x},n) \times \sum_m e^{-i\overline{p}ml}h(\overline{p},m) = \sum_n G_\Delta(\overline{x}-nl)\sum_m G_\kappa(\overline{p}-ml)$, where G denotes the Gaussian function: $G_\Delta(\overline{x}) = \exp(-\overline{x}^2/(2\Delta^2))$. For such, we can use the Poisson summation formula to specify f and g : $\sum_{n\in\mathbb{Z}} s(t+nl) = \sum_{k\in\mathbb{Z}} \tilde{s}(k/l)e^{2i\pi kt/l}$, where $\tilde{s}$ is the Fourier transform of s. We obtain:

$$f(\overline{x},n) = e^{-(n\Delta/l)^2/2}, \tag{VII.93}$$

$$h(\overline{p},m) = e^{-(ml\kappa/2\pi)^2/2}, \tag{VII.94}$$

which do not depend explicitly on the modular variables.

Finally, the modular wave function $\psi(\overline{x},\overline{p})$ of square GKP states can be written as:

$$\psi(\overline{x},\overline{p}) = N(l,\kappa,\Delta)\cdot G_\Delta(\overline{x}-l/4)G_\kappa(\overline{p}), \tag{VII.95}$$

where $N(l,\kappa,\Delta) = 1/(2.\mathrm{erf}(\frac{\kappa\pi}{l}).(\mathrm{erf}(\frac{l}{4\Delta}) + \mathrm{erf}(\frac{3l}{4\Delta}))^{1/2}$ is a normalization constant and depends on the lattice lenght l. The function erf is the error function defined by $\mathrm{erf}(l/2\Delta) = \int_{-l/2}^{l/2} e^{-\overline{x}^2/2\Delta^2}d\overline{x}$. The modular wave function of the $\left|\tilde{1}\right\rangle_x$ state can be written as $\psi(\overline{x},\overline{p}) = N(l/\sigma).G_\Delta(\overline{x}+l/4)G_\kappa(\overline{p})$, with the same normalisation factor.

This formalism could be used for building hexagonal GKP state [Albert et al., 2018], and the corresponding functions f and h could be determined with a numerical approach.

VII.5 Examples of Modular Wigner distribution

In this section, we discuss the double cylinder phase space representation of GKP states and Gaussian states.

VII.5.1 Modular Wigner distribution of GKP state

VII.5.1.1 Ideal GKP state

The modular wave function of the GKP states described by Eq. (VII.41) is $\psi(\overline{x},\overline{p}) = \delta(\overline{x} \pm l/4)\delta(\overline{p}) = f(\overline{x})g(\overline{p})$ with $l = \sqrt{\pi}$ and has a corresponding modular Wigner distribution $W_{\left|\overline{0},\overline{1}\right\rangle_x}(n,m,\overline{x},\overline{p}) = W_{|f\rangle}(n,\overline{x})W_{|g\rangle}(m,\overline{p})$:

$$W_{|f\rangle}(n,\overline{x}) = \delta(\overline{x} \pm l/4), \tag{VII.96}$$

$$W_{|g\rangle}(m,\overline{p}) = \delta(\overline{p}), \tag{VII.97}$$

and do not depend on n and m owing to the non-normalizability of the ideal GKP states as mentioned in [Rigas et al., 2008]. Indeed, a localized state with an associated modular variable Dirac distribution is constant in the integer (canonical conjugate) basis. For a coherent superposition of the qubit state $\left|\overline{\pm}\right\rangle_x = \frac{1}{\sqrt{2}}(\left|\overline{0}\right\rangle_x \pm \left|\overline{1}\right\rangle_x)$ with associated modular wave function $\psi(\overline{x},\overline{p}) = \frac{1}{\sqrt{2}}(\delta(\overline{x} - l/4) + \delta(\overline{x} + l/4))\delta(\overline{p})$, the modular Wigner distribution $W_{\left|\overline{\pm}\right\rangle_x}(n,m,\overline{x},\overline{p})$ is given by:

$$W_{|f\rangle}(n,\overline{x}) = \delta(\overline{x} - l/4) + \delta(\overline{x} + l/4) \pm 2\delta(\overline{x})\cos(n\pi) \tag{VII.98}$$

$$W_{|g\rangle}(m,\overline{p}) = \delta(\overline{p}). \tag{VII.99}$$

The argument of the cosinus function does not depend on l since the state is localized in $\pm l/4$ and n is a multiple of $2\pi/l$. The modular Wigner distributions of the coherent superposition of GKP states $|\overline{\pm}\rangle$ has the shape of ideal even/odd Schrödinger cat states (with an infinite squeezing along one quadrature), and a periodicity of the fringes equals to the distance of the two localized states. The shape of such state in cylinder phase space can be easily understood since the GKP state $\left|\overline{\pm}\right\rangle_x$ are a superposition of localized states in the torus.

The presence of oscillations in the cylinder phase space $(n,\overline{x})$ (see Eq. (VII.98)) and not in the one $(m,\overline{p})$ one is not a special feature of this phase space but rather a matter of definition of the GKP states. Indeed, exchanging the definition of $\left|\overline{0}\right\rangle_p$ and $|\overline{+}\rangle_p$ (the two states being identical), the oscillations from the coherent superposition would appear on the other cylinder $(m,\overline{p})$.

We now study the effect of small shifts on the previous states $|u,v\rangle = \hat{D}(u,0))\hat{D}(v,0)\left|\overline{\pm}\right\rangle_x$ where $l = \sqrt{\pi} \gg u,v$ corresponds to a displaced ideal cat states in the modular plane and are not localized at the center of the left and right modular plane. The associated modular Wigner distribution $W_{|f,g\rangle}(n,m,\overline{x},\overline{p})$ is:

$$W_{|f\rangle}(n,\overline{x}) = \delta(\overline{x} - \overline{\frac{l}{4} - u}) + \delta(\overline{x} + \overline{\frac{l}{4} - u}) \pm 2\delta(\overline{x})\cos(n\pi) \tag{VII.100}$$

$$W_{|g\rangle}(m,\overline{p}) = \delta(\overline{p} + v). \tag{VII.101}$$

These displacements can be induced by noise. They shift the full Modular Wigner distribution in the two uncoupled cylinders phase space.

VII.5.1.2 Physical GKP states

We now consider physical GKP states which are not translationally invariant due to the finite envelope in both modular variables (see Eq. (VII.95) and Fig. VII.5). Using the condition $l \gg \Delta$, it is possible to compute the analytical expression of the modular Wigner distribution of the physical GKP state corresponding to the Gaussian modular wave function Eq. (VII.48). The wave function being separable in $(\overline{x}, \overline{p})$, the modular Wigner distribution $W_{|\tilde{\pm}\rangle}(n, m, \overline{x}, \overline{p})$ is also separable into two parts, the interference part:

$$W_{|f\rangle}(n, \overline{x}) \simeq e^{-\frac{(\overline{x}+l/4)^2}{2\Delta^2}} e^{-n^2(2\pi\Delta/l)^2} + e^{-\frac{(\overline{x}-l/4)^2}{2\Delta^2}} e^{-n^2(2\pi\Delta/l)^2} + 2.e^{-n^2(2\pi\Delta/l)^2} e^{-\frac{\overline{x}^2}{\Delta^2}} \cos(n\pi), \tag{VII.102}$$

and the envelope part:

$$W_{|g\rangle}(m, \overline{p}) = \exp(-\overline{p}^2\kappa^2)\exp(-m^2l^2/\kappa^2). \tag{VII.103}$$

The modular Wigner distribution in the two-cylinder phase space is shown in Fig. VII.6(a). The visibility of the oscillation is one since the state is a pure state but the purity $P = \mathrm{Tr}(\hat{\rho}^2)$ of the GKP states could be reduced if the state crosses a Gaussian channel [Albert et al., 2018, Glancy and Knill, 2006].

The number of oscillations on the cylinder phase space can be related to the probability of having an error in the encoding and will be studied in Sec. VII.6.

VII.5.2 Modular Wigner distribution of a coherent and cat state

A pure Gaussian state has always a positive Wigner distribution according to Hudson's theorem [Hudson, 1974], and the negativity of the Wigner distribution in the rectangular phase plane is frequently associated to the quantumness of a state. In the cylinder phase plane, a Gaussian state can have a negative Wigner distribution. As a matter of fact, in such phase space, the only state which has a positive Wigner distribution is the eigenvector of both $\hat{N}$ and $\hat{M}$, *i.e* the state $|n, m\rangle$, which can be seen as a direct generalization of the results on the single cylinder phase space [Rigas et al., 2010].

In this paragraph, we calculate analytically the modular Wigner distribution of a coherent state and of a cat state (a non-Gaussian one) .

The associated modular Wigner distribution of the state Eq. (VII.39), the coherent state, is separable $W_{|\psi\rangle}(n, m, \overline{x}, \overline{p}) = W_{|f\rangle}(n, \overline{x})W_{|g\rangle}(m, \overline{p})$ and can be written as:

$$W_{|f\rangle}(n, \overline{x}) \simeq e^{-\frac{\overline{x}^2}{2\sigma^2}} e^{-n^2(2\pi\sigma/l)^2} \tag{VII.104}$$

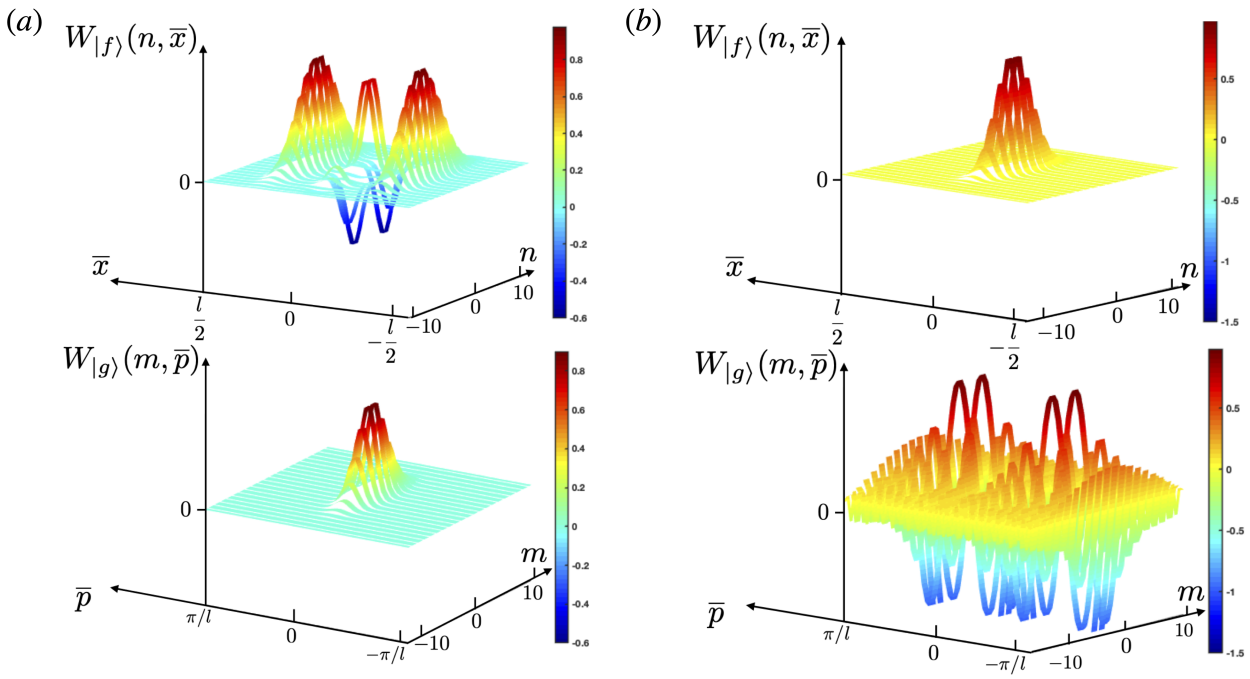

Figure VII.6: (a) Modular Wigner distribution of the physical GKP state for state with $l \gg \Delta$ which has the aspect of a Schrödinger cat state in the $(\overline{x}, n)$ cylinder phase space. The two parameters are here set to $\Delta = 0.1$ and $l = 1$. (b) Modular Wigner distribution of a coherent state in the two cylinders phase space. The figure is extracted from [Fabre et al., 2020b].

$$W_{|g\rangle}(m,\overline{p}) = \frac{\sin(2m(-|\overline{p}| + \pi/l))}{2m}. \tag{VII.105}$$

These functions are represented in Fig. VII.6(b).

We now study the modular Wigner distribution of the sum of two Gaussian state centered at $x_0 = \pm l/4$ and $p_0 = 0$ which corresponds to a Schrödinger cat in rectangular phase space. It exhibits an oscillatory pattern in one cylinder phase space, as the GKP state $\left|\tilde{\pm}\right\rangle_x$ (see Eq. (VII.98)):

$$W_{|f\rangle}(n,\overline{x}) \simeq e^{-\frac{(\overline{x}+l/4)^2}{2\sigma^2}} e^{-n^2(2\pi\sigma/l)^2} + e^{-\frac{(\overline{x}-l/4)^2}{2\sigma^2}} e^{-n^2(2\pi\sigma/l)^2} \pm e^{-n^2(2\pi\sigma/l)^2} e^{-\frac{\overline{x}^2}{\sigma^2}} \cos(n\pi) \tag{VII.106}$$

The other cylinder distribution $W_{|g\rangle}(m,\overline{p})$ is given by Eq. (VII.105) and is different from the one associated to $\left|\tilde{\pm}\right\rangle_x$ (see Eq. (VII.103)).

This example illustrates the relevance of representing the distribution of a quantum state in the two cylinder phase space.

VII.5.3 $\pi/2$ rotation in the cylinder phase space of the GKP states

In this section, we study the Modular Wigner function of the state $\psi_{\pi/2}$ obtained after a $\pi/2$ rotation in the two-cylinder phase plane of the ideal GKP state $\left|\tilde{\mp}\right\rangle_x$. In the $(n,\overline{x})$ cylinder phase space, the modular Wigner distribution of this $\pi/2$ rotated GKP state corresponds to two

peaks along the integer n-axis, and presents an oscillation pattern along the modular variable direction $\overline{x}$. In the other decoupled cylinder phase space $(m, \overline{p})$, the Dirac point along the $\overline{p}$ axis is after the $\pi/2$ rotation along the m axis. This ideal state, noted $\left|\psi_{\pi/2}\right\rangle$, constitutes a generalization of the OAM (orbital angular momentum) state described in [Rigas et al., 2008]. This is a consequence of the double cylinder aspect considered in this chapter. The state is a coherent superposition in the integers basis and can be written under the form:

$$\left|\psi_{\pi/2}\right\rangle = \frac{1}{\sqrt{2}}(|n_0, m_0\rangle \pm |-n_0, m_0\rangle), \tag{VII.107}$$

where n_0 is an even integer, and m_0 can be any integer. Using Eq. (VII.77), the corresponding modular Wigner distribution $W_{\left|\psi_{\pi/2}\right\rangle}(n, m, \overline{x}, \overline{p}) = W_{|f\rangle}(n, \overline{x}) W_{|g\rangle}(m, \overline{p})$ is

$$W_{|f\rangle}(n, \overline{x}) = \delta_{n,n_0} + \delta_{n,-n_0} \pm \delta_n \cdot \cos(\frac{8\pi\overline{x}}{l}), \tag{VII.108}$$

$$W_{|g\rangle}(m, \overline{p}) = \delta_{m,m_0}. \tag{VII.109}$$

As in Eq. (VII.98), the Modular Wigner distribution is flat in the modular variables $\overline{x}$ and $\overline{p}$ due to the non-normalizability of the state described by Eq. (VII.107). The calculation of the modular Wigner distribution of the corresponding physical state of $\left|\psi_{\pi/2}\right\rangle$; noted $\left|\tilde{\psi}_{\pi/2}\right\rangle$, using a Gaussian wave function instead of Dirac one could be handled using results in [Hinarejos et al., 2012]. We can now ask the question of how to perform such a $\pi/2$ rotation in the two uncoupled cylinders phase plane of a GKP states. A way to do so is to apply the sum of two projectors on the state defined by Eq. (VII.43): $\frac{1}{\sqrt{2}}(\hat{\Pi}(n_0, m_0) \pm \hat{\Pi}(-n_0, m_0)) \left|\overline{+}\right\rangle_x \left|\overline{+}\right\rangle_x$, where $\hat{\Pi}(\pm n_0, m_0) = |\pm n_0, m_0\rangle \langle n_0, m_0|$. The state $\hat{\Pi}(n_0, m_0)$ has a similar structure of a quantum state of a particle that passed through a diffraction slit (see (Eq. (VII.21)). Hence, using the transversal degree of freedom of single photon, this operation could be physically implemented with a spatial light modulator (SLM) [Tasca et al., 2011]. An alternative way would be to use the Fourier series relation between the modular basis and the integer one as in Eq. (VII.14) and Eq. (VII.15) and could be also implemented thanks to a SLM.

As a perspective, we could consider the analog of compass state in this phase space geometry as the coherent superposition of the logical GKP state $\left|\tilde{+}\right\rangle_x$ and $\left|\tilde{\psi}_{\pi/2}\right\rangle$ and find to what shape it corresponds in the rectangular phase space.

VII.6 Study of Quantum error correction in the double cylinder phase space

In this section, we investigate the quantum error correction of periodic and non-periodic states using ancilla GKP states. Our study is based on the scheme presented by Glancy and Knill in Ref. [Glancy and Knill, 2006] and is illustrated by the representation of modular Wigner distribution before and after the correction on the double cylinder phase space.

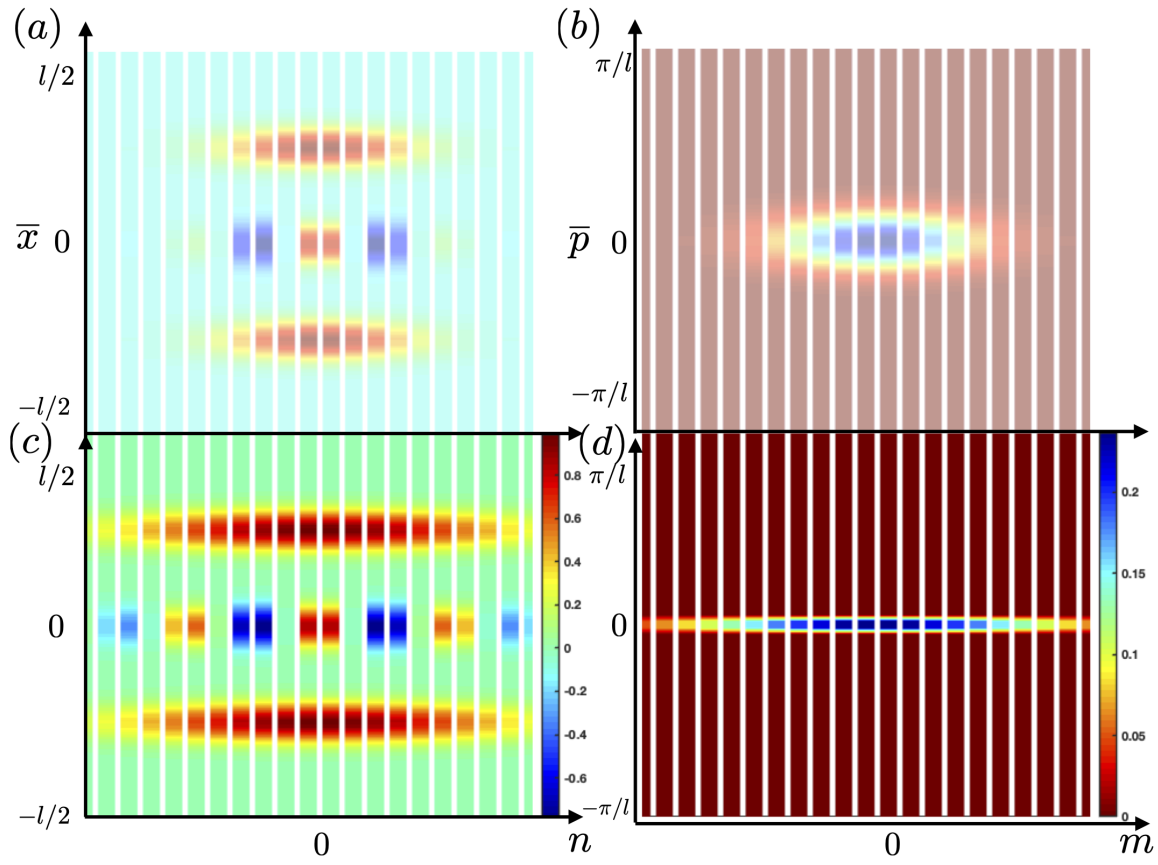

Figure VII.7: Illustration of the correction of a noisy data GKP state (a) and (b) representing the modular Wigner distribution. Projection of a GKP state on a slightly less noisy subspace (c) and (d) after the correction procedure. After the second homodyne detection, the probability of having an error less than than $\sqrt{\pi}/6$ goes from 0.9 to 0.99 as the number of oscillations goes from 3 to 5, see Fig. VII.8. The figure is extracted from [Fabre et al., 2020b].

VII.6.1 General formulation of the protocol

The quantum error correction of a density matrix $\hat{\rho}$ has been explained in Sec. II.5.2. In the following, we suppose for simplicity that the momentum p measured by the homodyne detection is equal to zero and the initial amplitude probability $\psi(x)$ becomes after the homodyne detection $\psi_0(x) = \psi(x+0)\tilde{\psi}_{\tilde{+}}(x)$. Our results can be generalized for different values of p by knowing the probability distribution of p.

VII.6.2 Quantum Error correction of a GKP state using a GKP state as ancilla

In Fig. VII.7, we present the modular Wigner distribution of the state before the error correction (a), (b) (see also Eq. (VII.102), Eq. (VII.103)) and after error correction Fig. VII.7(c), (d).

The two-phase spaces of the two separable GKP states are initially decoupled, and each GKP states have independent noises in each variable and consequently each phase space. The gate $\hat{C}_z$ entangles both qubits and hence couples the two-cylinder phase space of qubits and transfers shift errors from the ancilla qubit to the data one. Successive homodyne detection will lead to

the squeezing of the $\overline{x}$ and $\overline{p}$ and a broadening along the integer direction n and m.

An important figure of merit is the number of oscillations with respect to the ratio Δ/l. As the ratio $l/\Delta \to 0$ the two GKP logical states overlap and the oscillations disappear. On the contrary, the number of oscillations goes to infinity when $\Delta/l \to 0$, *i.e* when we consider ideal GKP states which are translationally invariant (see the previous section and Eq. (VII.98)). The number of oscillations is evaluated numerically as a function of the ratio Δ/l and is represented on Fig. VII.8.

In [Glancy and Knill, 2006], the authors have developed a figure of merit which indicates the error tolerance of GKP states which have undergone a distribution of shift errors of amplitude $|u| = |\overline{x}|, |v| = |\overline{p}| < \sqrt{\pi}/6$. Assuming an initial separable modular wave function, with $\Delta < 0.4$, the probability to have an error less than $\sqrt{\pi}/6$ is given by:

$$P_{\text{no err}}^{\sqrt{\pi/6}}(\Delta) = \int_{-\sqrt{\pi}/6}^{\sqrt{\pi/6}} d\overline{p} \int_{-\sqrt{\pi}/6}^{\sqrt{\pi/6}} d\overline{x} |\psi(\overline{x}, \overline{p})|^2, \tag{VII.110}$$

with $|\psi(\overline{x}, \overline{p})|^2 = G_\Delta(\overline{x}) G_\kappa(\overline{p})$. Numerically, for a mean number of photon $\overline{n} = 22.1$, and $\overline{n} = 10.4$ it corresponds to $P_{\text{no err}}^{\sqrt{\pi/6}}(\Delta = 0.15) = 0.99$ and $P_{\text{no err}}^{\sqrt{\pi/6}}(\Delta = 0.21) = 0.9$ respectively.

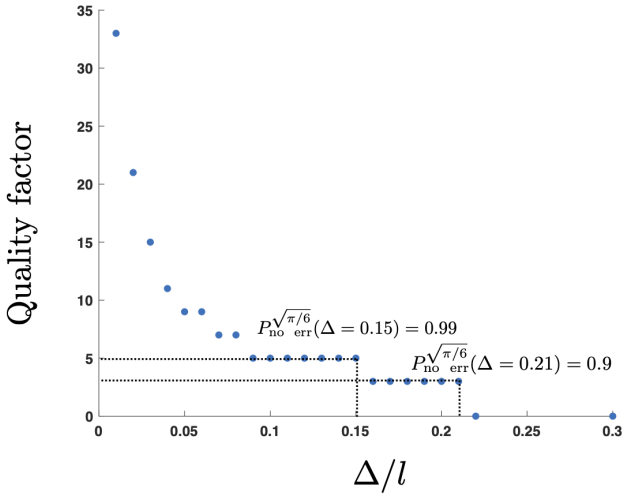

Figure VII.8: Quality factor (number of oscillations in the cylinder phase space) with respect to the ratio Δ/l for $l = \sqrt{\pi}$. After one homodyne detection along the p-quadrature for a GKP state, the number of oscillations of the GKP states increase (and so as the quality factor). If the GKP ancilla state is an ideal one, the number of oscillations becomes infinite. The figure is extracted from [Fabre et al., 2020b].

We report these values in Fig. VII.8. The correction of physical GKP states permits to approach the ideal GKP states which have an infinite number of oscillations in one cylinder phase space $(\overline{x}, n)$.

VII.6.3 Correction of non-periodic state using GKP state as ancilla

We now briefly discuss the case of a coherent state described by Eq. (VII.104) and represented in Fig. VII.9. (a),(b). The Steane error correction using as an ancilla the state $\left|\tilde{+}\right\rangle_x$

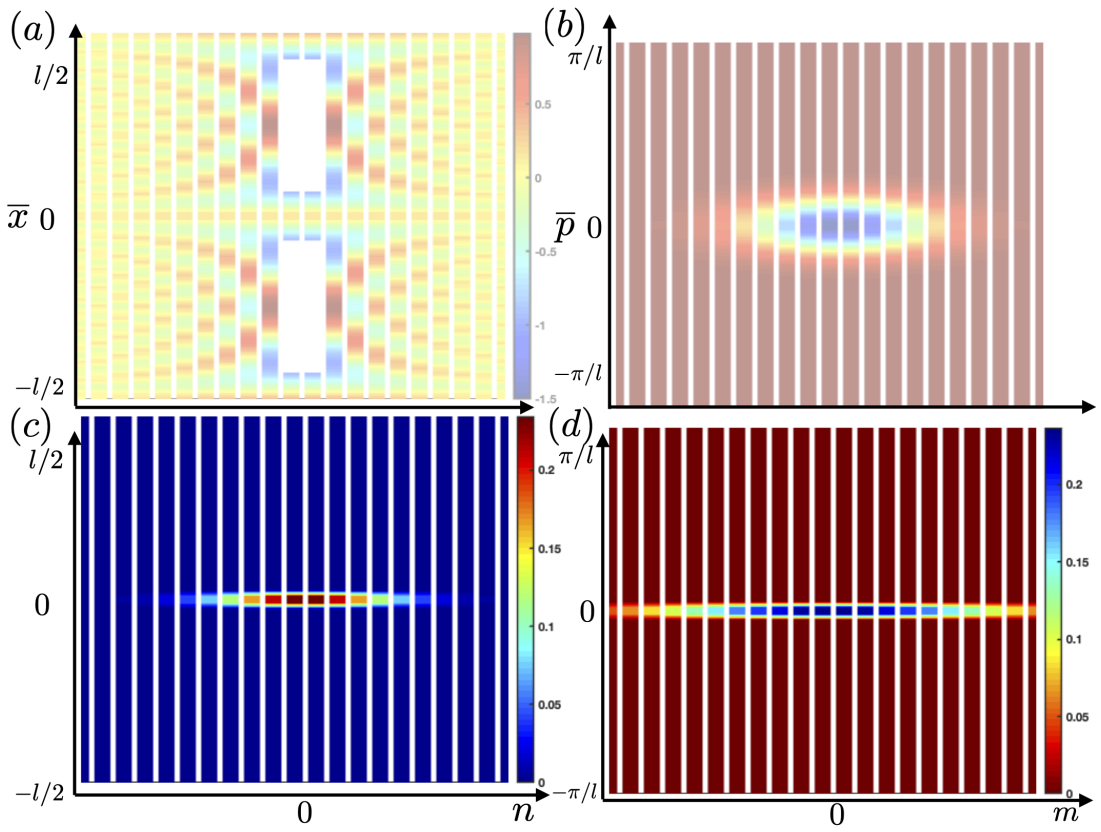

Figure VII.9: Illustration of the projection of a coherent state (a), (b) on a corrected GKP subspace (c), (d) in the double cylinder phase space. The figure is extracted from [Fabre et al., 2020b].

results in the projection of the coherent state $\hat{\rho}$ on the GKP subspace. After the protocol (see Fig. VII.9.(c),(d)), the initial coherent state becomes a random state on this subspace and can be used as a magic state to elevate GKP Clifford QC to fault-tolerant universal QC [Baragiola et al., 2019]. The protocol is a magic state distillation [Bravyi and Kitaev, 2005, Zhou et al., 2000]: the gate implemented corresponds to a quantum operation outside the set of Gaussian operations. The state produced is a non-Gaussian one and by consequence is hard to simulate by classical means. The non-Gaussian resource comes from the ancilla GKP state itself and acts as a position-momentum filter.

VII.7 Proposal of tomographic reconstruction of the Modular Wigner distribution

In this section, we propose a theoretical scheme to measure the modular Wigner distribution using results developed in [Mirhosseini et al., 2016] for measuring Wigner distribution for the azimuthal structure of light. The protocol starts with a separable density matrix $\hat{\mu} = \hat{\rho} \otimes |\overline{+}\rangle \langle\overline{+}|$ where $\hat{\rho}$ is the state to measure and $|\overline{+}\rangle \langle\overline{+}|$ is an ancilla ideal GKP state that here will be used as a pointer. The two states are then entangled by the gate $\hat{C}(\alpha, \beta)$, defined as:

$$\hat{C}(\alpha, \beta) = e^{i(\alpha \hat{N} + \beta \hat{M}) \otimes \hat{\Gamma}_z}, \tag{VII.111}$$

where $\alpha \in \mathbb{S}^1$ and $\beta \in \mathbb{S}^{1*}$. The operators $\hat{N}$ and $\hat{M}$ are defined by Eq. (VII.17) and are applied on the spatial port 1 (see Fig. VII.10). $\hat{\Gamma}_z$ is the modular readout observable defined by Eq. (VII.54) and Eq. (VII.55) applied on the spatial port 2. After the entangling gate, if we take as an example a pure state $\hat{\rho} = |\psi\rangle\langle\psi|$, the quantum state $\hat{\mu}_{\alpha,\beta} = \hat{C}(\alpha,\beta)\hat{\mu}\hat{C}^{-1}(\alpha,\beta) = |\mu\rangle_{\alpha,\beta}\langle\mu|_{\alpha,\beta}$ becomes a linear superposition,

$$|\mu\rangle_{\alpha,\beta} = \frac{1}{\sqrt{2}}(e^{i(\alpha\hat{N}+\beta\hat{M})}|\psi\rangle \otimes |\overline{0}\rangle + e^{-i(\alpha\hat{N}+\beta\hat{M})}|\psi\rangle \otimes |\overline{1}\rangle). \tag{VII.112}$$

A post-selection measurement on the modular state $\langle\overline{x},\overline{p}|$ gives the following reduced density matrix:

$$\hat{\mu}'_{\alpha,\beta} = \frac{\langle\overline{x},\overline{p}|\,\hat{\mu}_{\alpha,\beta}\,|\overline{x},\overline{p}\rangle}{\mathrm{Tr}(\langle\overline{x},\overline{p}|\,\hat{\mu}_{\alpha,\beta}\,|\overline{x},\overline{p}\rangle}. \tag{VII.113}$$

In the case of the pure case considered here, the numerator of the previous equation can be written as: $\frac{1}{\sqrt{2}}(\langle\overline{x}+\alpha,\beta+\overline{p}|\psi\rangle \otimes |\overline{0}\rangle + \langle\overline{x}-\alpha,\overline{p}-\beta|\psi\rangle \otimes |\overline{1}\rangle)$. We point out that the real and imaginary part of the correlation function

$$C(\overline{x},\overline{p},\alpha,\beta) = \langle\overline{x}+\alpha,\overline{p}+\beta|\,\hat{\rho}\,|\overline{x}-\alpha,\overline{p}-\beta\rangle\,, \tag{VII.114}$$

can be obtained by measuring the readout modular observables ($\hat{\Gamma}_x$ and $\hat{\Gamma}_y$ defined in Eq. (VII.55)) of the ancilla qubit. Indeed, thanks to Eq. (VII.113), the expectation value of the modular readout observables are

$$\langle\hat{\Gamma}_x\rangle = \mathrm{Re}(\langle\overline{x}+\alpha,\overline{p}+\beta|\,\hat{\rho}\,|\overline{x}-\alpha,\overline{p}-\beta\rangle), \tag{VII.115}$$

$$\langle\hat{\Gamma}_y\rangle = \mathrm{Im}(\langle\overline{x}+\alpha,\overline{p}+\beta|\,\hat{\rho}\,|\overline{x}-\alpha,\overline{p}-\beta\rangle). \tag{VII.116}$$

Once $\hat{\Gamma}_x, \hat{\Gamma}_y$ have been measured for the ancilla qubit we can reconstruct the correlation function of the quantum state of interest. A final Fourier transform of the expectation value of the modular readout observables permits to obtain the Modular Wigner distribution. The measurement of the $\hat{\Gamma}_{\hat{U}}$ matrices is fully detailed in [A.Ketterrer, 2016]. In Fig. VII.10, we present the full quantum circuit that allows to measure the modular Wigner distribution. The measurement of

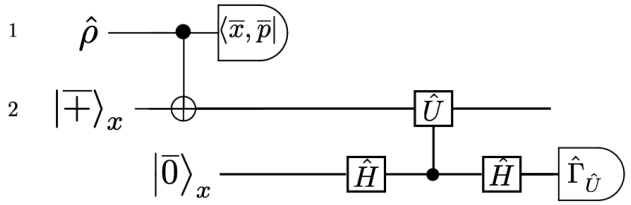

Figure VII.10: Tomography reconstruction of the modular Wigner distribution. The first step is to entangle the state with a GKP ancilla and perform a post-selection on the modular state $\langle\overline{x},\overline{p}|$. An indirect measurement is performed using an ancilla GKP qubit $|\overline{0}\rangle_x$ to measure the readout modular observable $\hat{\Gamma}_{\hat{U}}$ where $\hat{U} = \hat{X}, \hat{Y}$. The figure is extracted from [Fabre et al., 2020b].

the expectation value of the readout modular observables using an indirect measurement strategy is inspired from [Asadian et al., 2014, 2015] and could be performed in various experimental

platform, such as spatial degrees of freedom of single photons [Tasca et al., 2011], mechanical oscillators and vibrational modes of ions.

We detail now how to perform the post-selection measurement on the modular basis $\langle \overline{x}, \overline{p}|$, taking as an example a general pure state $|\psi\rangle = \int dq \psi(q) |q\rangle$. We start by applying two small displacements shifts $\hat{D}(\overline{x})\hat{D}(\overline{p})$ which transform the state as: $|\psi\rangle \rightarrow \int \psi(q+\overline{x}) |q\rangle e^{-i\overline{p}q} dq$. A projective measurement which selects the position $q = kl (k \in \mathbb{Z})$, that is equivalent to a projection onto state $\sum_k \langle q = kl|$, gives the probability: $\left|\sum_k \psi(kl+\overline{x}) e^{-i\overline{p}kl}\right|^2 = P(\overline{x}, \overline{p})$, which is the absolute value of the modular wave function $\psi(\overline{x}, \overline{p})$ (see Eq. (VII.10)). It could be experimentally implemented in the context of the transversal degrees of freedom of single photons [Tasca et al., 2011]. An experimental proposal to implement the entangling gate Eq. (VII.111) will be the subject of future work.

The mentioned protocol could be alternatively performed using the controlled displaced operator $\hat{E}'(a,b) = \exp(i(a\hat{\overline{x}} + b\hat{\overline{p}}) \otimes \hat{\Gamma}_Z)$, followed by a post-selection on the basis $\langle l, m|$ and then a measurement of the read-out modular variable. The choice of the most suitable protocols depends on the type of experimental devices available.

Tomographical reconstruction by direct measurement The tomographical reconstruction of the modular Wigner distribution can also be done by a straightforward generalization of the results in [Rigas et al., 2008]. It consists of applying the shear operator $\hat{S}(\alpha, \beta) = e^{-i\alpha\hat{N}^2/2} e^{-i\beta\hat{M}^2/2}$ (see Ref. [Potoček and Barnett, 2015])on the density matrix, followed by a measurement in the modular basis:

$$p(\overline{x}, \overline{p}, \alpha, \beta) = \langle \overline{x}, \overline{p}| e^{i\alpha\hat{N}^2/2} e^{i\beta\hat{M}^2/2} \hat{\rho} e^{-i\alpha\hat{N}^2/2} e^{-i\beta\hat{M}^2/2} |\overline{x}.\overline{p}\rangle . \tag{VII.117}$$

This procedure is in the spirit of the homodyne detection, where "all" the marginals of the Wigner distribution are measured, by performing a rotation (not shear) of angle θ in phase space given by the rotation operator $\exp(i\theta(\hat{X}^2 + \hat{P}^2))$. Then, the modular characteristic distribution can be evaluated by [Rigas et al., 2008]:

$$\chi_{\hat{\rho}}(\overline{x}, \overline{p}, n, m) = \iint d\overline{x} d\overline{p} e^{-in\overline{x'}} e^{-im\overline{p'}} p(\overline{x'}, \overline{p'}, \overline{x}/n, \overline{p}/m). \tag{VII.118}$$

Finally, the modular Wigner distribution can be reconstructed by a double Fourier transform of Eq. (VII.118). The shear operator could be realized using a SLM [Tasca et al., 2011], again in the context of the transversal degrees of freedom of single photons.

VII.8 Conclusion

In this chapter, a new Wigner distribution has been introduced which is well adapted for describing translational invariant states, based on the tools developed in [A.Ketterrer, 2016, Englert et al., 2006]. This modular Wigner distribution has its support on a double cylinder. Each

cylinder could be coupled or not depending on the considered quantum state and its associated noise model. The superposition of localized states in the modular plane has a Schrödinger cat shape in one cylinder phase space. We have seen that one figure of merit which quantifies the possibility to correct the GKP states is related to the number of oscillations in one cylinder phase space. We hope that this work gives a new framework to implement other quantum information protocols involving discrete symmetry, as the period finding problem [Lomonaco and Kauffman, 2002]. In addition, the equation of motion of the Wigner distribution on a cylinder phase space [Bizarro, 1994] could be considered for developing the time evolution of the noise model. Hexagonal GKP states could also be represented in that phase space along with the presented error correction protocol applied to that state.

Chapter VIII

Summary and conclusion

This thesis explores a new way of doing quantum computation using the time-frequency variables of single-photons. The deterministic interaction between different single-photons stays the major obstacle for experimental implementations of this encoding, which is the same problem when one uses the finite dimensional degrees of freedom of single-photons, as the polarization. As mentioned in Chap. V, one perspective would be to consider a new hybrid quantum computing approach which combines continuous variables degree of freedom of single-photons and the CV particle-sensitive one. Then, the Gaussian entanglement of such hybrid state could be assessed with a generalization of Simon's criterion as mentioned in Chap. VI. The experimental generation of time-frequency cluster states is also a promising, but challenging approach.

Three types of continuous variables have been studied: the quadrature position and momentum variables of an electromagnetic field, the time-frequency continuous variables of single photons, and the amplitude spectrum function which combines the quadrature position and momentum and the spectral variables.

The continuous variables of single-photons in quantum optics formalism could bring a new light for understanding the transversal quark Wigner distribution used in particle physics [Belitsky et al., 2004]. Indeed, the considered distribution is similar to the chronocyclic Wigner distribution, since for both of these distributions, we are restricted to the single-particle subspace, and depend on continuous variables degree of freedom. The main ingredients of the phase space construction, the symplectic aspect along with the deformation quantization are present in both cases. But there are also major differences. First, the nature of the particle is different, fermionic and bosonic, and leads to different algebras and expressions of correlation functions. The relativistic (resp. ultrarelativistic) aspect of the particle is also one difference. In the quark position-momentum transversal distribution, additional physical constraints are added, the covariance and the color invariance is introduced by adding Gamma matrices and integrating over a Wilson's line but this last can be simplified by a certain choice of gauge. The analogies between the two formalisms from different physics communities could bring a new light on particle physics.

In Chap. VII, we explore one example of the underlying connection between the symmetry of phase space and bosonic codes. This aspect could be used as a systematic way to define any bosonic code. The phase space adapted to the binomial code, according to its symmetry would be a generalized Bloch sphere. Another instance is the affine phase space, which is a half-plane built by using displacement operation into one direction and squeezed operation in the other. Given this special geometry, a new code can arise which is the common eigenvalue of the squeezing operator in one direction and the displacement in the orthogonal direction. The affine Wigner distribution is in particular well-adapted for quantum systems with time-frequency variables, as the frequency can not be negative.

We now consider different perspectives of chapter five.

A new hybrid quantum computing approach The experimental difficulty in such encoding is the realization of two-photons gate, since it relies on the need of an optical medium which exhibits high non-linearity, while the time-frequency cubic phase gate is easy to implement. As mentioned in [Tasca et al., 2011], single-photon interaction could be replaced by using only linear optical devices and post-selection as it was done with DVs system, which corresponds to the so-called probabilistic KLM scheme [Knill et al., 2001]. In such a scheme, the measurement can induce non-linearities. It could help for building large initial entangled states by using probabilistic entangling gates, and then by performing time-frequency Gaussian measurement. The obtained result is then used to feed-forward the remaining nodes as in the MBQC approach.

In CV quantum optics, the entanglement between two spatial modes is easy to implement since it requires only a beam-splitter, but the non-Gaussian gate is hard to implement experimentally in a deterministic way (see details in Chap. II). A perspective would be to build a universal set of gates set composed of CV (degree of freedom of single photon)-CV (quadrature position-momentum), such as the non-Gaussian element of the universal set is performed with the CV degree of freedom of single photons (transversal position-momentum or time-frequency), and the entanglement "part" is handled with the CV degree of freedom. This idea consists of a generalization of the hybrid quantum computing with DV-CV [Lloyd, 2003] where the two-dimensional DVs degree of freedom of the single photon can be its polarization [Masse et al., 2020] or time-bins [Gouzien et al., 2020] for instance.

Concatenation of time-frequency GKP qubit state The time-frequency GKP state is one possible way to build a robust qubit using continuous variables of single photons. They could be concatenated into a 2D surface code and it would be interesting to evaluate the threshold value for fault-tolerant quantum computing. If one wants to build a quantum computer with time-frequency GKP states, it is imperative to have multiple single-photon sources which produce such a grid state.

Multiparameter estimation The translational symmetry of the time-frequency GKP state allows using it for multiparameter estimation, for simultaneous measurement of time and frequency parameters (modulo 2π). Also, we could consider the transversal position-momentum GKP states, and would consist of a robust qubit against noises coming from turbulence effects.

Tomography of the POVM of single photon detector A single-photon detector has a frequency-dependent response. It can be characterized by a POVM which could be measured with a technique similar to the one used for the tomographical reconstruction of a particle-sensitive detector [Humphreys et al., 2015, Lundeen et al., 2009] where a coherent state is used as a probe.

In order to perform the time-frequency characteristic of a detector, the idea is the same. A tomographical complete set of states is needed, which is provided in our context by time-frequency single-photons with a Gaussian spectrum. Again, they are mathematically analog to the coherent states. The central frequency of the single-photon wavepacket can be shifted with an EOM and the time shift is simply a time delay. Experimentally, we access the fidelity, the overlap between the spectrum of the single photon state and the one of the detector, by assuming that both quantum states are pure. In order to reconstruct the characteristic of the detector, we will use semi-definite programming (SDP) as it was first developed in [Lundeen et al., 2009], since the tomographical reconstruction of the POVM of the detector is a convex problem.

The full knowledge of single-photon detectors allows the reduction of errors during a quantum computation using the time-frequency continuous variables of single-photon. In addition, any imperfections on the measurement device potentially impact CV-QKD performance against attacks and such a fact still holds in this encoding.

Appendix A

Appendices

A.1 Cavity functions

In this appendix, we detail how to model the cavity function by a sum of Gaussians. We remind that the cavity function is the Airy one:

$$|f(\omega)|^2 = \frac{1-R}{(1-R^2)^2 + 4R\sin^2(\omega\tau/2)} \tag{A.1}$$

and is represented in Fig. A.1. R is the reflectivity of the cavity. The periodicity of the Airy function is given by $\Delta\omega = 2\pi/\tau$, called the free spectral range, and the half-width of each peak is $\delta\omega = \frac{4}{\tau}\text{asin}((1-R^2)/4\sqrt{R})$. When $R \to 1$, the Airy function becomes a sum of Dirac distributions and it is only in that case that the minimum of the each peak reached the zero value.

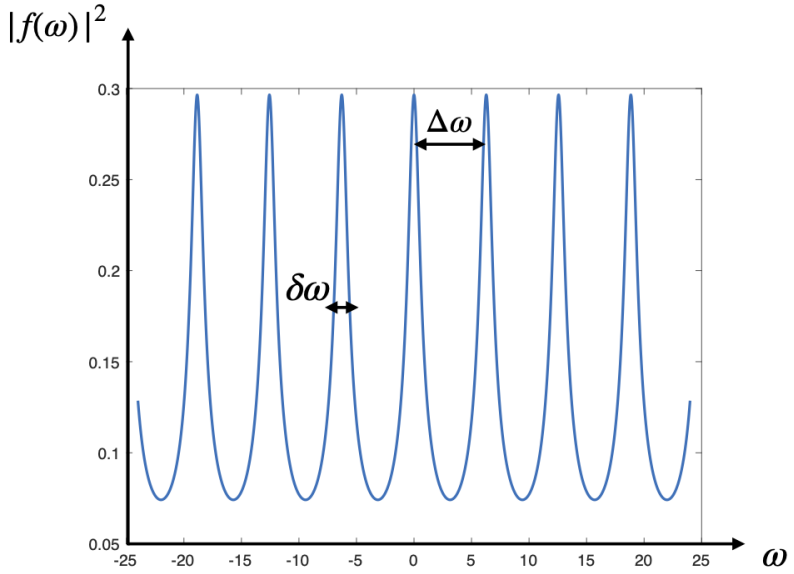

Figure A.1: Airy function for a reflectivity of $R = 0.6$ and with a free spectral range of $\Delta\omega = 2\pi$.

We now want to model the cavity function by a sum of Gaussian:

$$g(\omega) = \sum_{n\in\mathbb{Z}} \exp(-\frac{(\omega - n\overline{\omega})^2}{2\sigma^2}), \tag{A.2}$$

where σ is the width of each Gaussian peak and Δ is the periodicity of g, by minimizing the distance between the f and g functions, defined as the 1-norm:

$$D = \int |f(\omega) - g(\omega)| d\omega. \tag{A.3}$$

When $D = 0$ the functions f and g perfectly match. We will fix the parameters of the Airy function $(\Delta\omega, \delta\omega)$ and the distance between f and g is chosen to be the closer as possible to zero by finding the right width of the Gaussian σ. Since g must be normalized to one, it is a convex problem and can be solved efficiently. The periodicity of the Gaussian peaks has to be necessarily the free spectral range, so that $\overline{\omega} = \Delta\omega$.

For $R = 0.3$, the distance is minimized to 0.0061 by choosing $\sigma = 1.972$, and the two functions f and g are represented in Fig. A.2(a). For such σ, the Gaussian peaks do not reach the zero values and this value allows to correctly match the Airy functions. For $R = 0.9$, the distance is minimized to 0.0493 by choosing $\sigma = 0.36$, and again the two functions f and g are represented in Fig. A.2(b). The fidelity is larger than in the first case and can be understood since for such Gaussian width, the amplitudes of the peaks always reach the zero value. Then, the approximation of the Airy functions by a sum of Gaussian is better accurate for lower reflectivity of the cavity. However, in the extreme case of an ideal cavity function $R \to 1$, the Airy function approached the sum. of Dirac distributions, in that case it is possible to reach a distance $D \to 0$ with the Gaussian functions by choosing $\sigma \to 0$.

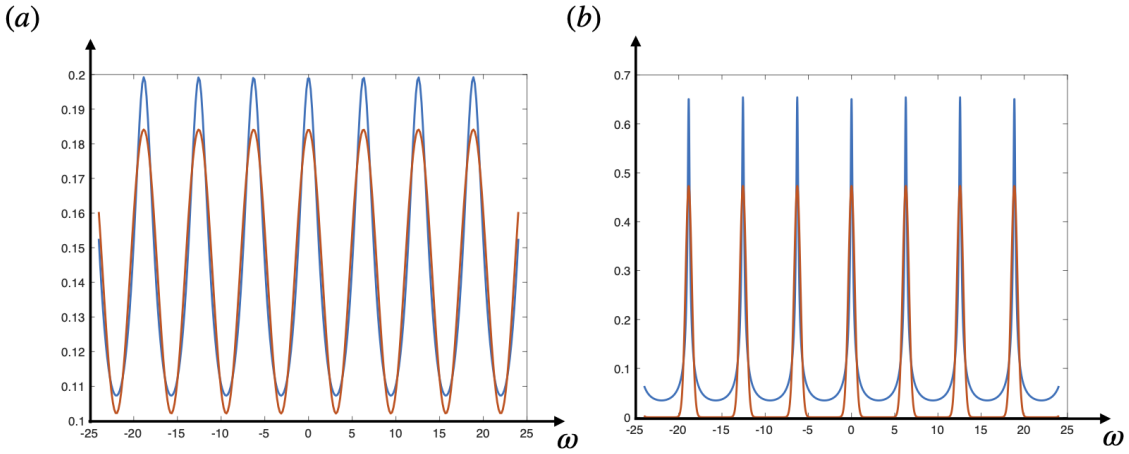

Figure A.2: Overlay of the Airy function (in blue) and the sum of Gaussian function (in red) for different values of reflectivity. (a) $R = 0.3$ (b) $R = 0.9$.

A.2 Details of calculations of Chapter six

A.2.1 Commutator of bosonic operator at spectrum S

In this appendix, we give an effective method to calculate the commutator of polynomial of bosonic ladders operators [Pain, 2013]. For general functions f and g of bosonic operators $\hat{a}$ and

$\hat{a}^\dagger$, we can develop their commutator into Taylor's series. Since $[\hat{a}, \hat{a}^\dagger] = 1$, we obtain:

$$[f(\hat{a}), g(\hat{a}^\dagger)] = -\sum_{k=1}^{\infty} \frac{1}{k!} f^{(k)}(\hat{a}) g^{(k)}(\hat{a}^\dagger). \tag{A.4}$$

For specific functions $f(x) = x^n$ and $g(x) = x^m$ we get:

$$[\hat{a}^n, (\hat{a}^\dagger)^m] = \sum_{k=1}^{\min(n,m)} k! \binom{n}{k} \binom{m}{k} (\hat{a}^\dagger)^{m-k} \hat{a}^{n-k}. \tag{A.5}$$

With this result in hand, we can easily prove the orthogonality of the Fock basis: $\langle n|m\rangle = \delta_{n,m}$. The result can be generalized for bosonic creation and annihilation operator at spectrum S, which obeys to $[\hat{a}[S], \hat{a}^\dagger[S']] = \langle S|S'\rangle \mathbb{I}$:

$$[\hat{a}^n[S], (\hat{a}^\dagger[S'])^m] = \sum_{k=1}^{\min(n,m)} (\langle S|S'\rangle)^k k! \binom{n}{k} \binom{m}{k} (\hat{a}^\dagger[S])^{m-k} \hat{a}[S']^{n-k} \tag{A.6}$$

and thanks to this last relation, we can then prove the non-orthogonality of the fixed-spectrum Fock state.

A.2.2 Action of the bosonic ladders operator on fixed-spectrum Fock state

The action of the bosonic annihilation operator on a fixed-spectrum Fock state reads as:

$$\hat{a}[S] \,|n, \mathbf{S}\rangle = \left(\frac{1}{\sqrt{n}} \iint d\omega d\omega' S(\omega) S^*(\omega') \hat{a}(\omega) \hat{a}^\dagger(\omega')\right) \frac{(\hat{a}^\dagger)^{n-1}}{\sqrt{(n-1)!}} \,|0\rangle \tag{A.7}$$

We then use the commutator $[\hat{a}(\omega), \hat{a}^\dagger(\omega')] = \delta(\omega - \omega')$ n times to shift the operator $\hat{a}(\omega)$ on the right. The only terms which remain are $n\delta(\omega - \omega') \cdot \frac{(\hat{a}^\dagger)^{n-1}}{\sqrt{(n-1)!}}$. We finally obtain:

$$\hat{a}[S] \,|n, \mathbf{S}\rangle = \sqrt{n} \left(\int |S(\omega)|^2 \mathrm{d}\omega\right) |n-1, \mathbf{S}\rangle = \sqrt{n} \,|n-1, \mathbf{S}\rangle \tag{A.8}$$

The number operator at spectrum S applied on a fixed-spectrum Fock state is:

$$\begin{aligned} \hat{a}^\dagger[S]\hat{a}[S] \,|n, \mathbf{S}\rangle &= \sqrt{n} \left(\int |S(\omega)|^2 \mathrm{d}\omega\right) \times \sqrt{n} \int S(\omega) \mathrm{d}\omega \,|n-1, S; 1, \omega\rangle \\ &= n \int |S(\omega)|^2 \mathrm{d}\omega \,|n, \mathbf{S}\rangle \end{aligned} \tag{A.9}$$

In a more general case where we consider the annihilation operator of a photon of spectrum ψ on a fixed-spectrum Fock state of spectrum S:

$$\hat{a}[\psi] \,|n, \mathbf{S}\rangle = \sqrt{n} \,\langle S|\psi\rangle \,|n-1, \mathbf{S}\rangle \,. \tag{A.10}$$

A.2.3 Multimode Squeezed state

In this section, we provide the mathematical demonstration of Eq. (VI.74). The development into a power series of the exponential of the squeezed operator gives the commutator:

$$\hat{S}^\dagger[\beta]\hat{a}[\psi]\hat{S}[\beta] = \sum_k \frac{1}{k!} [\hat{A}, [\hat{A}, ...[\hat{A}, \hat{a}[\psi]]]]_k, \tag{A.11}$$

where $\hat{A} = \int \mathrm{d}x(\beta(x)\hat{a}^\dagger(x)\hat{a}^\dagger(-x) - \beta^*(x)\hat{a}(x)\hat{a}(-x))$. The index on the commutator $[]_k$ indicated the number of times the commutation with the operator $\hat{A}$ is involved. We then calculate the commutator appearing in Eq. (A.11):

$$[\hat{A}, \hat{a}[\psi]] = -\int (\beta(x) + \beta(-x))\psi^*(-x)\mathrm{d}x\hat{a}^\dagger(x) = -\hat{a}^\dagger(\tilde{\psi}), \tag{A.12}$$

$$[\hat{A}, \hat{a}^\dagger_\psi] = -\int (\beta^*(x) + \beta^*(-x))\psi(-x)\mathrm{d}x\hat{a}(x) = -\hat{a}(\tilde{\psi^*}), \tag{A.13}$$

where we have defined the field $\tilde{\psi} = (\beta + \Pi\beta)\Pi\psi^*$. Hence, the commutator is:

$$[\hat{A}, [\hat{A}, ...[\hat{A}, \hat{a}[\psi]]]]_k = \begin{cases} -\int \mathrm{d}x z(x)|z(x)|^{n-1}\psi^*(-x)\hat{a}^\dagger(x) \text{ if } k \text{ even} \\ \int \mathrm{d}x|z(x)|^{2n}\psi(x)\hat{a}(x) \text{ if } k \text{ odd,} \end{cases} \tag{A.14}$$

with $z(x) = (\beta(x) + \Pi\beta(x))$ where the parity operator $\hat{\Pi}$ applied on the field ψ only if k is even. Finally after calculation,

$$\hat{S}^\dagger[\beta]\hat{a}[\psi]\hat{S}[\beta] = \int \mathrm{d}x[\psi(x)\hat{a}(x)\mathrm{ch}(|z(x)|) - \psi^*(-x)\hat{a}^\dagger(x)e^{i\theta(x)}\mathrm{sh}(|z(x)|)], \tag{A.15}$$

which is indeed Eq. (VI.74).

A.3 Gaussian functional state

The Functional Gaussian integration which is extensively used take the form:

$$\iint D^\circ[\psi]D^\circ[\psi^*]\exp(-\iint \mathrm{d}x\mathrm{d}y\psi^*(x)A(x,y)\psi(y))\exp(\int \psi^*(x)\phi(x)\mathrm{d}x + h.c)$$
$$= \exp(-\iint \mathrm{d}x\mathrm{d}y\phi^*(x)A^{-1}(x,y)\phi(y)). \tag{A.16}$$

We precise now the calculation of the inverse of the correlation function matrix for the bosonic coherent state.

Bosonic coherent state From the Eq. (VI.93), the covariance matrix $\Sigma(x,y) = \delta(x-y)$ and the first moment $\psi(x) = \psi(x) - \beta(x)$. The inverse of the covariance matrix is also a Dirac distribution $A^{-1}(x,y) = \delta(x-y)$. We hence find the Wigner functional of the bosonic coherent state Eq. (VI.95). The calculation of the Wigner functional of the bosonic squeezed state is similar.

A.4 Figure of merit for error correction of GKP states

Here we recall the calculation of the probability that physical GKP state has shifts smaller than $\sqrt{\pi/6}$ in both quadrature [Glancy and Knill, 2006]. If the ideal $\left|\overline{0}\right\rangle$ logical state has errors shifts u, v in position and momentum quadrature, it can be written as:

$$|u,v\rangle = e^{-iv\hat{q}}e^{iu\hat{p}}\left|\tilde{0}\right\rangle. \tag{A.17}$$

This basis actually corresponds to the modular basis described by Eq. (VII.7), only when $|u| < \sqrt{\pi}$ and $|v| < \sqrt{\pi}$. From this consideration, we can develop any wave function into that basis:

$$|\psi\rangle = \int_{-\sqrt{\pi}}^{\sqrt{\pi}}\int_{-\sqrt{\pi}/2}^{\sqrt{\pi}/2} \mathrm{d}v\mathrm{d}u\psi(u,v)\left|u,v\right\rangle, \tag{A.18}$$

where $\psi(u,v)$ corresponds to the modular wave function Eq. (VII.10). The probability of having an error u,v is $P(u,v) = |\langle\psi|u,v\rangle|^2$ and the probability of having an error less than $\sqrt{\pi/6}$ is given by:

$$P_{\text{no err}}^{\sqrt{\pi/6}}(\Delta) = \int_{-\sqrt{\pi}/6}^{\sqrt{\pi/6}} \mathrm{d}\overline{p} \int_{-\sqrt{\pi}/6}^{\sqrt{\pi/6}} \mathrm{d}\overline{x} |\psi(\overline{x},\overline{p})|^2, \tag{A.19}$$

and is evaluated numerically for different average value of the photon number $\overline{n} \sim \frac{1}{2\Delta^2}$ in Sec. VII.6.2, Δ being the variance of the Gaussian distribution of both variables u and v.

A.5 Physical GKP states in the Zak's integer basis

In this section, we calculate the physical GKP state $\left|\tilde{0}\right\rangle$ in the Zak's integer basis $\left\langle n,m\middle|\tilde{0}\right\rangle = f_n g_m$, where

$$f_n = \int_{-l/2}^{l/2} \mathrm{d}\overline{x} e^{-\frac{2i\pi}{l} n\overline{x}} e^{-(\overline{x}-l/4)^2/2\Delta^2} \tag{A.20}$$

and

$$g_m = \int_{-\pi/l}^{\pi/l} \mathrm{d}\overline{p} e^{-iml\overline{p}} e^{-\overline{p}^2/2\kappa^2}. \tag{A.21}$$

We first calculate Eq. (A.20). After performing a change of variable, we obtain:

$$f_n = e^{i\pi n/2} \int_{-l/4}^{3l/4} \mathrm{d}\overline{x} e^{-\frac{2i\pi}{l} n\overline{x}} e^{-\overline{x}^2/2\Delta^2} \tag{A.22}$$

$$= e^{i\pi n/2} e^{-2(\frac{\pi n\Delta}{l})^2} \int_{-l/4}^{3l/4} \mathrm{d}\overline{x} e^{-(\overline{x}+2i\pi n\Delta^2/l)/2\Delta^2} \tag{A.23}$$

We hence recognize the error function $\mathrm{erf}(l/2\Delta) = \int_{-l/2}^{l/2} e^{-\overline{x}^2/2\Delta^2} \mathrm{d}\overline{x}$, with a complex argument. The integer coefficient of the physical GKP state is

$$f_n = \sqrt{\frac{\pi}{2}} e^{i\pi n/2} e^{-2(\frac{\pi n\Delta}{l})^2} [\mathrm{erf}(\frac{l}{4\sqrt{2}\Delta} - \frac{\sqrt{2}in\pi\Delta}{l}) + \mathrm{erf}(\frac{3l}{4\sqrt{2}\Delta} + \frac{\sqrt{2}in\pi\Delta}{l})]. \tag{A.24}$$

A similar calculation leads to the other coefficient Eq. (A.21):

$$g_m = e^{-(ml\kappa)^2/2} [\mathrm{erf}(\frac{\pi}{\sqrt{2}\kappa l} - i\frac{m\kappa}{l\sqrt{2}}) + \mathrm{erf}(\frac{\pi}{\sqrt{2}\kappa l} + \frac{im\kappa l}{\sqrt{2}})]. \tag{A.25}$$

The $\left|\tilde{1}\right\rangle$ physical GKP state can be expressed in the integer basis using similar calculation.

Bibliography

Achilles, R. and Bonfiglioli, A. (2012). The early proofs of the theorem of campbell, baker, hausdorff, and dynkin. *Archive for History of Exact Sciences*, 66(3):295–358. 61

Aharonov, D. and Ben-Or, M. (1999). Fault-tolerant quantum computation with constant error rate. *arXiv:quant-ph/9906129*. 21

Aharonov, Y. and Bohm, D. (1959). Significance of electromagnetic potentials in the quantum theory. *Phys. Rev.*, 115:485–491. 169

Aharonov, Y., Pendleton, H., and Petersen, A. (1969). Modular variables in quantum theory. *International Journal of Theoretical Physics*, 2(3):213–230. 166, 167

Aiello, A., Töppel, F., Marquardt, C., Giacobino, E., and Leuchs, G. (2015). Quantum-like nonseparable structures in optical beams. *New Journal of Physics*, 17(4):043024. 73

A.Ketterrer (2016). Modular variables in quantum information. *Quantum Physics [quant-ph], Universite Paris 7, Sorbonne Paris Cite*. 172, 190, 191

Albert, V. V., Covey, J. P., and Preskill, J. (2020). Robust encoding of a qubit in a molecule. *Phys. Rev. X*, 10:031050. 45

Albert, V. V., Noh, K., Duivenvoorden, K., Young, D. J., Brierley, R. T., Reinhold, P., Vuillot, C., Li, L., Shen, C., Girvin, S. M., Terhal, B. M., and Jiang, L. (2018). Performance and structure of single-mode bosonic codes. *Phys. Rev. A*, 97:032346. 45, 48, 110, 173, 182, 184

Alexander, R. N., Wang, P., Sridhar, N., Chen, M., Pfister, O., and Menicucci, N. C. (2016). One-way quantum computing with arbitrarily large time-frequency continuous-variable cluster states from a single optical parametric oscillator. *Phys. Rev. A*, 94:032327. 123

Anastopoulos, C. and Savvidou, N. (2017). Time-of-arrival correlations. *Phys. Rev. A*, 95:032105. 56

Ansari, V., Harder, G., Allgaier, M., Brecht, B., and Silberhorn, C. (2017). Temporal-mode measurement tomography of a quantum pulse gate. *Phys. Rev. A*, 96:063817. 98

Arvind, Dutta, B., Mukunda, N., and Simon, R. (1995). The real symplectic groups in quantum mechanics and optics. *Pramana*, 45(6):471–497. 67

Asadian, A., Brukner, C., and Rabl, P. (2014). Probing macroscopic realism via ramsey correlation measurements. *Phys. Rev. Lett.*, 112:190402. 190

Asadian, A., Budroni, C., Steinhoff, F. E. S., Rabl, P., and Gühne, O. (2015). Contextuality in phase space. *Phys. Rev. Lett.*, 114:250403. 190

Asadian, A., Erker, P., Huber, M., and Klockl, C. (2016). Heisenberg-weyl observables: Bloch vectors in phase space. *Physical Review A*, 94(1):010301. 23

Asavanant, W., Shiozawa, Y., Yokoyama, S., Charoensombutamon, B., Emura, H., Alexander, R. N., Takeda, S., Yoshikawa, J.-i., Menicucci, N. C., Yonezawa, H., and Furusawa, A. (2019). Generation of time-domain-multiplexed two-dimensional cluster state. *Science*, 366(6463):373–376. 42, 80

Austin, D. R., Witting, T., Wyatt, A. S., and Walmsley, I. A. (2010). Measuring sub-planck structural analogues in chronocyclic phase space. *Optics Communications*, 283(5):855 – 859. 109

Autebert, C., Boucher, G., Boitier, F., Eckstein, A., Favero, I., Leo, G., and Ducci, S. (2015). Photon pair sources in algaas: from electrical injection to quantum state engineering. *Journal of Modern Optics*, 62(20):1739–1745. 100, 104

Bacon, D. (2006). Cse 599d, quantum computing. *https://courses.cs.washington.edu/courses/cse599d/06wi/*. 20

Bacon, D. and Flammia, S. T. (2009). Adiabatic gate teleportation. *Phys. Rev. Lett.*, 103:120504. 43

Baragiola, B. Q., Pantaleoni, G., Alexander, R. N., Karanjai, A., and Menicucci, N. C. (2019). All-gaussian universality and fault tolerance with the gottesman-kitaev-preskill code. *Physical Review Letters*, 123(20):200502. 48, 49, 50, 116, 120, 189

Bardeen, J., Cooper, L. N., and Schrieffer, J. R. (1957). Microscopic theory of superconductivity. *Phys. Rev.*, 106:162–164. 162

Barnett, S. and Radmore, P. (2002). *Methods in Theoretical Quantum Optics*. Oxford Series in Optical and Imaging Sciences. Clarendon Press. 151, 158, 159

Barros, M. R., Ketterer, A., Farías, O. J., and Walborn, S. P. (2017). Free-space entangled quantum carpets. *Phys. Rev. A*, 95:042311. 125

Bartlett, S. D., de Guise, H., and Sanders, B. C. (2002a). Quantum encodings in spin systems and harmonic oscillators. *Phys. Rev. A*, 65:052316. 23

Bartlett, S. D., Sanders, B. C., Braunstein, S. L., and Nemoto, K. (2002b). Efficient classical simulation of continuous variable quantum information processes. *Phys. Rev. Lett.*, 88:097904. 38

Beduini, F. A., Zielińska, J. A., Lucivero, V. G., de Icaza Astiz, Y. A., and Mitchell, M. W. (2014). Interferometric measurement of the biphoton wave function. *Phys. Rev. Lett*, 113(18):120402. 102

Belhassen, J., Baboux, F., Yao, Q., Amanti, M., Favero, I., Lemaître, A., Kolthammer, W. S., Walmsley, I. A., and Ducci, S. (2018). On-chip iii-v monolithic integration of heralded single photon sources and beamsplitters. *Applied Physics Letters*, 112(7):071105. 87

Belitsky, A. V., Ji, X., and Yuan, F. (2004). Quark imaging in the proton via quantum phase-space distributions. *Physical Review D*, 69(7):074014. 193

Berge, E., Berge, S. M., and Luef, F. (2019). The affine wigner distribution. *arXiv:1912.03112 [math-ph]*. 64

Bergmann, M. and Van Loock, P. (2016). Quantum error correction against photon loss using multicomponent cat states. *Phys. Rev. A*, 94:042332. 20

Berra-Montiel, J. and Molgado, A. (2020). Coherent representation of fields and deformation quantization. *arXiv:2005.14333 [gr-qc, physics:math-ph, physics:quant-ph]*. 163

Berry, M. (1987). The adiabatic phase and pancharatnam's phase for polarized light. *Journal of Modern Optics*, 34(11):1401–1407. 63

Bertrand, J. and Bertrand, P. (1992). A class of affine wigner functions with extended covariance properties. *Journal of Mathematical Physics*, 33(7):2515–2527. 64

Bialynicki-Birula, I. (2000). The wigner functional of the electromagnetic field. *Optics Communications*, 179(1):237–246. 141

Bizarro, J. a. P. (1994). Weyl-wigner formalism for rotation-angle and angular-momentum variables in quantum mechanics. *Phys. Rev. A*, 49:3255–3276. 166, 169, 178, 179, 192

Björklund, A., Gupt, B., and Quesada, N. (2019). A faster hafnian formula for complex matrices and its benchmarking on a supercomputer. *Association for Computing Machinery (ACM)*, 24(1). 38

Bogdanov, A. Y., Bogdanov, Y. I., and Valiev, K. A. (2006). Schmidt modes and entanglement in continuous-variable quantum systems. *Russian Microelectronics*, 35(1):7–20. 93

Borges, C. V. S., Hor-Meyll, M., Huguenin, J. A. O., and Khoury, A. Z. (2010). Bell-like inequality for the spin-orbit separability of a laser beam. *Phys. Rev. A*, 82:033833. 73

Boucher, G. (2016). Biphoton Frequency-Correlations Engineering and Measurement with a Semiconductor Microcavity. *Hal tel-01467419Sorbonne Paris Cité ; Université paris diderot.* 78

Boucher, G., Douce, T., Bresteau, D., Walborn, S. P., Keller, A., Coudreau, T., Ducci, S., and Milman, P. (2015). Toolbox for continuous-variable entanglement production and measurement using spontaneous parametric down-conversion. *Phys. Rev. A*, 92:023804. 104, 109

Braunstein, S. L. and Van Loock, P. (2005). Quantum information with continuous variables. *Rev. Mod. Phys.*, 77:513–577. 25, 31

Bravyi, S. and Kitaev, A. (2005). Universal quantum computation with ideal clifford gates and noisy ancillas. *Phys. Rev. A*, 71:022316. 15, 50, 189

Brecht, B. and Silberhorn, C. (2013). Characterizing entanglement in pulsed parametric down-conversion using chronocyclic wigner functions. *Phys. Rev. A*, 87:053810. 95

Brif, C. and Mann, A. (1998). A general theory of phase-space quasiprobability distributions. *Journal of Physics A: Mathematical and General*, 31(1):L9–L17. 165

Brif, C. and Mann, A. (1999). Phase-space formulation of quantum mechanics and quantum-state reconstruction for physical systems with lie-group symmetries. *Phys. Rev. A*, 59:971–987. 61, 64

Brod, D. J., Galvão, E. F., Crespi, A., Osellame, R., Spagnolo, N., and Sciarrino, F. (2019). Photonic implementation of boson sampling: a review. *Advanced Photonics*, 1(3):1 – 14. 84

Brown, R. H. and Twiss, R. Q. (1956). Correlation between photons in two coherent beams of light. *Nature*, 177(4497):27–29. 87

Busch, P. and Lahti, P. J. (1986). To what extent do position and momentum commute? *Physics Letters A*, 115(6):259 – 264. 167

Cahill, K. E. and Glauber, R. J. (1969). Density operators and quasiprobability distributions. *Phys. Rev.*, 177:1882–1902. 29, 153

Cai, Y., Roslund, J., Ferrini, G., Arzani, F., Xu, X., Fabre, C., and Treps, N. (2017). Multimode entanglement in reconfigurable graph states using optical frequency combs. *Nature Communications*, 8(1):15645. 80

Caillet, X., Berger, V., Leo, G., and Ducci, S. (2009). A semiconductor source of counterpropagating twin photons: a versatile device allowing the control of the two-photon state. *Journal of Modern Optics*, 56(2-3):232–239. 128

Campagne-Ibarcq, P., Eickbusch, A., Touzard, S., Zalys-Geller, E., Frattini, N. E., Sivak, V. V., Reinhold, P., Puri, S., Shankar, S., Schoelkopf, R. J., Frunzio, L., Mirrahimi, M., and Devoret, M. H. (2020). Quantum error correction of a qubit encoded in grid states of an oscillator. *Nature*, 584(7821):368–372. 45, 47

Campbell, E. T. and Howard, M. (2017). Unified framework for magic state distillation and multiqubit gate synthesis with reduced resource cost. *Phys. Rev. A*, 95:022316. 48

Campbell, E. T., Terhal, B. M., and Vuillot, C. (2017). Roads towards fault-tolerant universal quantum computation. *Nature*, 549(7671):172–179. 21

Carvalho, M. A. D., Ferraz, J., Borges, G. F., de Assis, P. L., Pádua, S., and Walborn, S. P. (2012). Experimental observation of quantum correlations in modular variables. *Phys. Rev. A*, 86(3):032332. 166

Cerf, N. J., Bourennane, M., Karlsson, A., and Gisin, N. (2002). Security of quantum key distribution using d-level systems. *Phys. Rev. Lett.*, 88:127902. 22

Chabaud, U., Markham, D., and Grosshans, F. (2020). Stellar representation of non-gaussian quantum states. *Phys. Rev. Lett.*, 124:063605. 151

Chen, M., Menicucci, N. C., and Pfister, O. (2014). Experimental realization of multipartite entanglement of 60 modes of a quantum optical frequency comb. *Phys. Rev. Lett.*, 112:120505. 80

Chen, Y., Fink, M., Steinlechner, F., Torres, J. P., and Ursin, R. (2019). Hong-ou-mandel interferometry on a biphoton beat note. *npj Quantum Information*, 5(1). 109

Cochrane, P. T., Milburn, G. J., and Munro, W. J. (1999). Macroscopically distinct quantum-superposition states as a bosonic code for amplitude damping. *Phys. Rev. A*, 59:2631–2634. 45

Combescure, M. and Robert, D. (2012). *Coherent States and Applications in Mathematical Physics*. Texts and Monographs in Physics. Springer. 146, 149, 150, 152, 163

Curtright, T. L. and Zachos, C. K. (2012). Quantum mechanics in phase space. *Asia Pacific Physics Newsletter*, 01(01):37–46. 32, 35

Dawson, C. M. and Nielsen, M. A. (2005). The solovay-kitaev algorithm. *arXiv:quant-ph/0505030*. 15

Dias, E. O. and Parisio, F. (2017). Space-time-symmetric extension of nonrelativistic quantum mechanics. *Phys. Rev. A*, 95:032133. 56

Douce, T., Eckstein, A., Walborn, S. P., Khoury, A. Z., Ducci, S., Keller, A., Coudreau, T., and Milman, P. (2013). Direct measurement of the biphoton wigner function through two-photon interference. *Scientific Reports*, 3:3530. 99, 100, 111, 122, 128, 130

Duivenvoorden, K., Terhal, B. M., and Weigand, D. (2017). Single-mode displacement sensor. *Phys. Rev. A*, 95:012305. 110, 120

Eastin, B. and Knill, E. (2009). Restrictions on transversal encoded quantum gate sets. *Phys. Rev. Lett.*, 102:110502. 21

Eckstein, A., Boucher, G., Lemaître, A., Filloux, P., Favero, I., Leo, G., Sipe, J. E., Liscidini, M., and Ducci, S. (2014). High-resolution spectral characterization of two photon states via classical measurements. *Laser & Photonics Reviews*, 8(5):L76–L80. 85, 96

Eckstein, A. and Silberhorn, C. (2008). Broadband frequency mode entanglement in waveguided parametric downconversion. *Opt. Lett.*, 33(16):1825–1827. 100, 128

Ellens, W. and Kooij, R. E. (2013). Graph measures and network robustness. *arXiv:1311.5064 [physics]*. 43

Englert, B.-G., Lee, K. L., Mann, A., and Revzen, M. (2006). Periodic and discrete zak bases. *Journal of Physics A: Mathematical and General*, 39(7):1669–1682. 169, 177, 191

Ercolessi, E., Marmo, G., Morandi, G., and Mukunda, N. (2007). Wigner distributions in quantum mechanics. *Journal of Physics: Conference Series*, 87:012010. 179

Esmaeil Zadeh, I., Los, J. W. N., Gourgues, R. B. M., Chang, J., Elshaari, A. W., Zichi, J. R., van Staaden, Y. J., Swens, J. P. E., Kalhor, N., Guardiani, A., Meng, Y., Zou, K., Dobrovolskiy, S., Fognini, A. W., Schaart, D. R., Dalacu, D., Poole, P. J., Reimer, M. E., Hu, X., Pereira, S. F., Zwiller, V., and Dorenbos, S. N. (2020). Efficient single-photon detection with 7.7 ps time resolution for photon-correlation measurements. *ACS Photonics*. Publisher: American Chemical Society. 119

Fabre, N., Belhassen, J., Minneci, A., Felicetti, S., Keller, A., Amanti, M. I., Baboux, F., Coudreau, T., Ducci, S., and Milman, P. (2020a). Producing a delocalized frequency-time schrödinger-cat-like state with hong-ou-mandel interferometry. *Phys. Rev. A*, 102:023710. 46, 97, 98, 104, 108, 125, 126, 129, 130, 131, 133, 134

Fabre, N., Keller, A., and Milman, P. (2020b). Wigner distribution on a double-cylinder phase space for studying quantum error-correction protocols. *Phys. Rev. A*, 102:022411. 49, 50, 165, 168, 171, 174, 185, 187, 188, 189, 190

Fabre, N., Maltese, G., Appas, F., Felicetti, S., Ketterer, A., Keller, A., Coudreau, T., Baboux, F., Amanti, M. I., Ducci, S., and Milman, P. (2020c). Generation of a time-frequency grid state with integrated biphoton frequency combs. *Phys. Rev. A*, 102:012607. 47, 53, 62, 86, 110, 111, 113, 116, 117, 119, 121, 123

Farías, O. J., de Melo, F., Milman, P., and Walborn, S. P. (2015). Quantum information processing by weaving quantum talbot carpets. *Phys. Rev. A*, 91:062328. 124, 125

Fedorov, M. V., Efremov, M. A., Kazakov, A. E., Chan, K. W., Law, C. K., and Eberly, J. H. (2005). Spontaneous emission of a photon: Wave-packet structures and atom-photon entanglement. *Phys. Rev. A*, 72:032110. 56

Fedrizzi, A., Herbst, T., Aspelmeyer, M., Barbieri, M., Jennewein, T., and Zeilinger, A. (2009). Anti-symmetrization reveals hidden entanglement. *New Journal of Physics*, 11(10):103052. 100

Flühmann, C. and Home, J. P. (2020). Direct characteristic-function tomography of quantum states of the trapped-ion motional oscillator. *Phys. Rev. Lett.*, 125:043602. 30

Fluhmann, C., Negnevitsky, V., Marinelli, M., and Home, J. (2018). Sequential modular position and momentum measurements of a trapped ion mechanical oscillator. *Phys. Rev. X*, 8(2). 46, 47

Francesconi, S., Baboux, F., Raymond, A., Fabre, N., Boucher, G., Lemaître, A., Milman, P., Amanti, M. I., and Ducci, S. (2020). Engineering two-photon wavefunction and exchange statistics in a semiconductor chip. *Optica*, 7(4):316. 85, 87, 100, 115, 128, 137

Freidel, L., Leigh, R. G., and Minic, D. (2017). Modular spacetime and metastring theory. *Journal of Physics: Conference Series*, 804:012032. 166, 167

Gagatsos, C. N. and Guha, S. (2019). Efficient representation of gaussian states for multimode non-gaussian quantum state engineering via subtraction of arbitrary number of photons. *Phys. Rev. A*, 99:053816. 151

Gersten, A. (1999). Maxwell?s equations as the one-photon quantum equation. *Foundations of Physics Letters*, 12(3):291–298. 55

Giedke, G., Wolf, M. M., Krüger, O., Werner, R. F., and Cirac, J. I. (2003). Entanglement of formation for symmetric gaussian states. *Phys. Rev. Lett.*, 91:107901. 90

Giorda, P. and Paris, M. G. A. (2010). Gaussian quantum discord. *Physical Review Letters*, 105(2):020503. 10

Giovannetti, V., Lloyd, S., and Maccone, L. (2011). Advances in quantum metrology. *Nature Photonics*, 5(4):222–229. 31

Glancy, S. and Knill, E. (2006). Error analysis for encoding a qubit in an oscillator. *Phys. Rev. A*, 73:012325. 112, 117, 119, 175, 181, 182, 184, 186, 188, 200

Gneiting, C. and Hornberger, K. (2011). Detecting entanglement in spatial interference. *Phys. Rev. Lett.*, 106:210501. 167, 168

Gonzalez, J. A., del Olmo, M. A., and Tosiek, J. (2003). Quantum mechanics on the cylinder. *Journal of Optics B: Quantum and Semiclassical Optics*, 5(3):S306–S315. 166, 168

Gottesman, D. (1998). The heisenberg representation of quantum computers. *Group theoretical methods in physics. Proceedings, 22nd International Colloquium, Group22, ICGTMP'98, Hobart, Australia, July 13-17*. 15, 17

Gottesman, D. and Chuang, I. L. (1999). Demonstrating the viability of universal quantum computation using teleportation and single-qubit operations. *Nature*, 402(6760):390–393. 41

Gottesman, D., Kitaev, A., and Preskill, J. (2001). Encoding a qubit in an oscillator. *Phys. Rev. A*, 64(1):012310. 38, 47, 48, 110, 111, 173, 182

Gouzien, E., Brunel, F., Tanzilli, S., and D'Auria, V. (2020). Scheme for the generation of hybrid entanglement between time-bin and wavelike encodings. *Phys. Rev. A*, 102:012603. 194

Grassani, D., Azzini, S., Liscidini, M., Galli, M., Strain, M. J., Sorel, M., Sipe, J. E., and Bajoni, D. (2015). Micrometer-scale integrated silicon source of time-energy entangled photons. *Optica*, 2(2):88. 51

Greenberger, D. M., Horne, M. A., and Zeilinger, A. (1989). Going beyond bell's theorem. In Kafatos, M., editor, *Bell's Theorem, Quantum Theory and Conceptions of the Universe*, pages 69–72. Springer Netherlands. 43

Grimsmo, A. L., Combes, J., and Baragiola, B. Q. (2020). Quantum computing with rotation-symmetric bosonic codes. *Phys. Rev. X*, 10:011058. 45

Gu, M., Weedbrook, C., Menicucci, N. C., Ralph, T. C., and van Loock, P. (2009). Quantum computing with continuous-variable clusters. *Phys. Rev. A*, 79:062318. 43

Guerreiro, T., Martin, A., Sanguinetti, B., Pelc, J. S., Langrock, C., Fejer, M. M., Gisin, N., Zbinden, H., Sangouard, N., and Thew, R. T. (2014). Nonlinear interaction between single photons. *Phys. Rev. Lett.*, 113:173601. 140

Guillaud, J. and Mirrahimi, M. (2019). Repetition cat qubits for fault-tolerant quantum computation. *Phys. Rev. X*, 9(4):041053. 46

Halliwell, J. J., Evaeus, J., London, J., and Malik, Y. (2015). A self-adjoint arrival time operator inspired by measurement models. *Physics Letters A*, 379(39):2445 – 2451. 56

Hamadou Ibrahim, A., Roux, F. S., McLaren, M., Konrad, T., and Forbes, A. (2013). Orbital-angular-momentum entanglement in turbulence. *Phys. Rev. A*, 88:012312. 52

Hamilton, C. S., Kruse, R., Sansoni, L., Barkhofen, S., Silberhorn, C., and Jex, I. (2017). Gaussian boson sampling. *Phys. Rev. Lett.*, 119(17):170501. 38, 45

Haroche, S., Raimond, J., and Press, O. U. (2006). *Exploring the Quantum: Atoms, Cavities, and Photons*. Oxford Graduate Texts. OUP Oxford. 26

Hastrup, J., Larsen, M. V., Neergaard-Nielsen, J. S., Menicucci, N. C., and Andersen, U. L. (2020). Cubic phase gates are not suitable for non-clifford operations on GKP states. *arXiv:2009.05309 [quant-ph]*. 48

Hepp, K. (1974). The classical limit for quantum mechanical correlation functions. *Communications in Mathematical Physics*, 35(4):265–277. 163

Hepp, K. and Lieb, E. H. (1973). Equilibrium statistical mechanics of matter interacting with the quantized radiation field. *Physical Review A*, 8(5):2517–2525. 163

Heshami, K., England, D. G., Humphreys, P. C., Bustard, P. J., Acosta, V. M., Nunn, J., and Sussman, B. J. (2016). Quantum memories: emerging applications and recent advances. *Journal of Modern Optics*, 63(20):2005–2028. PMID: 27695198. 16

Hillery, M., Bužek, V., and Berthiaume, A. (1999). Quantum secret sharing. *Phys. Rev. A*, 59:1829–1834. 43

Hinarejos, M., Pérez, A., and Bañuls, M. C. (2012). Wigner function for a particle in an infinite lattice. *New Journal of Physics*, 14(10):103009. 186

Hong, C. K. and Mandel, L. (1985). Theory of parametric frequency down conversion of light. *Phys. Rev. A*, 31:2409–2418. 78

Hong, C. K., Ou, Z. Y., and Mandel, L. (1987). Measurement of subpicosecond time intervals between two photons by interference. *Phys. Rev. Lett.*, 59:2044–2046. 121, 130

Hosseini, S., Rahimi-Keshari, S., Haw, J. Y., Assad, S. M., Chrzanowski, H. M., Janousek, J., Symul, T., Ralph, T. C., and Lam, P. K. (2014). Experimental verification of quantum discord in continuous-variable states. *Journal of Physics B: Atomic, Molecular and Optical Physics*, 47(2):025503. 75, 76

Hudson, R. L. (1974). When is the wigner quasi-probability density non-negative? *Reports on Mathematical Physics*, 6(2):249 – 252. 31, 184

Humphreys, P. C., Metcalf, B. J., Gerrits, T., Hiemstra, T., Lita, A. E., Nunn, J., Nam, S. W., Datta, A., Kolthammer, W. S., and Walmsley, I. A. (2015). Tomography of photon-number resolving continuous-output detectors. *New Journal of Physics*, 17(10):103044. 195

Hush, M. R., Carvalho, A. R. R., and Hope, J. J. (2010). Number-phase wigner representation for efficient stochastic simulations. *Phys. Rev. A*, 81:033852. 179

Husimi, K. (1940). Husimi distribution. *Proc. Phys. Math. Soc. Jpn*, 22. 69

IBM (2019). *The IBM Quantum Experience, http://www.research.ibm.com/quantum.* 16

Imany, P., Jaramillo-Villegas, J. A., Alshaykh, M. S., Lukens, J. M., Odele, O. D., Moore, A. J., Leaird, D. E., Qi, M., and Weiner, A. M. (2019). High-dimensional optical quantum logic in large operational spaces. *npj Quantum Information*, 5(1):59. 22

Imany, P., Odele, O. D., Alshaykh, M. S., Lu, H.-H., Leaird, D. E., and Weiner, A. M. (2018). Frequency-domain hong-ou-mandel interference with linear optics. *Opt. Lett.*, 43(12):2760–2763. 120, 123

Jin, R.-B., Shiina, R., and Shimizu, R. (2018). Quantum manipulation of biphoton spectral distributions in a 2d frequency space toward arbitrary shaping of a biphoton wave packet. *Opt. Express*, 26(16):21153–21158. 136

Joo, J., Lee, C.-W., Kono, S., and Kim, J. (2019). Logical measurement-based quantum computation in circuit-QED. *Scientific Reports*, 9(1):16592. 47

J.Tosiek and Przanowski, M. (1995). Weyl-wigner-moyal formalism. i. operator ordering. *Acta Phys. Polon. B 26, 1703.* 170, 178

Ketterer, A., Keller, A., Walborn, S. P., Coudreau, T., and Milman, P. (2016). Quantum information processing in phase space: A modular variables approach. *Phys. Rev. A*, 94:022325. 166, 167, 168, 175, 176

Khrennikov, A. (2020). Quantum versus classical entanglement: Eliminating the issue of quantum nonlocality. *Foundations of Physics.* 73

Khvedelidze, A. and Abgaryan, V. (2017). On the family of wigner functions for n-level quantum system. *arXiv:1708.05981 [math-ph, physics:quant-ph].* 155, 166, 181

Klimov, A. B., Romero, J. L., and de Guise, H. (2017). Generalized SU(2) covariant wigner functions and some of their applications. *Journal of Physics A: Mathematical and Theoretical*, 50(32):323001. 166

Knill, E. (2005). Quantum computing with realistically noisy devices. *Nature*, 434(7029):39–44. 15

Knill, E. and Laflamme, R. (1997). Theory of quantum error-correcting codes. *Phys. Rev. A*, 55:900–911. 20

Knill, E., Laflamme, R., and Milburn, G. J. (2001). A scheme for efficient quantum computation with linear optics. *Nature*, 409(6816):46–52. 42, 194

Kobayashi, T., Yamazaki, D., Matsuki, K., Ikuta, R., Miki, S., Yamashita, T., Terai, H., Yamamoto, T., Koashi, M., and Imoto, N. (2017). Mach-zehnder interferometer using frequency-domain beamsplitter. *Opt. Express*, 25(10):12052–12060. 140

Koczor, B., Zeier, R., and Glaser, S. J. (2020). Continuous phase-space representations for finite-dimensional quantum states and their tomography. *Phys. Rev. A*, 101:022318. 156

Kribs, D. W., Laflamme, R., Poulin, D., and Lesosky, M. (2006). Operator quantum error correction. *Quantum Info. Comput.*, 6(4):382–399. 20

Kues, M., Reimer, C., Lukens, J. M., Munro, W. J., Weiner, A. M., Moss, D. J., and Morandotti, R. (2019). Quantum optical microcombs. *Nature Photonics*, 13(3):170–179. 83, 84

Kues, M., Reimer, C., Roztocki, P., Cortés, L. R., Sciara, S., Wetzel, B., Zhang, Y., Cino, A., Chu, S. T., Little, B. E., Moss, D. J., Caspani, L., Azaña, J., and Morandotti, R. (2017). On-chip generation of high-dimensional entangled quantum states and their coherent control. *Nature*, 546(7660):622–626. 51

Kwiat, P. G., Steinberg, A. M., and Chiao, R. Y. (1992). Observation of a quantum eraser: A revival of coherence in a two-photon interference experiment. *Physical Review A*, 45(11):7729–7739. 130

Lamata, L. and Leon, J. (2005). Dealing with entanglement of continuous variables: Schmidt decomposition with discrete sets of orthogonal functions. *J. Opt. B: Quantum Semiclass. Opt.*, 7(8):224–229. 91

Larsen, M. V., Guo, X., Breum, C. R., Neergaard-Nielsen, J. S., and Andersen, U. L. (2019). Deterministic generation of a two-dimensional cluster state. *Science*, 366(6463):369–372. 42, 80, 116

Le Bellac, M. (2013). *Physique quantique - Fondements Tome 1: Fondements*. Savoirs Actuels. EDP Sciences. 5, 61

Legero, T., Wilk, T., Hennrich, M., Rempe, G., and Kuhn, A. (2004). Quantum beat of two single photons. *Phys. Rev. Lett.*, 93:070503. 130, 132

Legero, T., Wilk, T., Kuhn, A., and Rempe, G. (2006). Characterization of single photons using two-photon interference. *Academic Press*, 53:253 – 289. 98, 132

Leibfried, D., DeMarco, B., Meyer, V., Lucas, D., Barrett, M., Britton, J., Itano, W. M., Jelenković, B., Langer, C., Rosenband, T., and Wineland, D. J. (2003). Experimental demonstration of a robust, high-fidelity geometric two ion-qubit phase gate. *Nature*, 422(6930):412–415. 63

Leibfried, D., Pfau, T., and Monroe, C. (1998). Shadows and mirrors: Reconstructing quantum states of atom motion. *Physics Today*, 51:22–28. 133

Liscidini, M. and Sipe, J. E. (2013). Stimulated emission tomography. *Phys. Rev. Lett.*, 111:193602. 85

Lloyd, S. (2003). *Hybrid Quantum Computing*. Springer Netherlands, Dordrecht. 194

Lloyd, S. and Braunstein, S. L. (1999). Quantum computation over continuous variables. *Phys. Rev. Lett.*, 82:1784–1787. 38

Lomonaco, J. and Kauffman, L. H. (2002). A continuous variable shor algorithm. *arXiv:quant-ph/0210141*. 192

Looi, S. Y., Yu, L., Gheorghiu, V., and Griffiths, R. B. (2008). Quantum-error-correcting codes using qudit graph states. *Phys. Rev. A*, 78:042303. 23

Lu, H.-H., Lukens, J. M., Williams, B. P., Imany, P., Peters, N. A., Weiner, A. M., and Lougovski, P. (2019). Quantum interference and correlation control of frequency-bin qubits. *NPJ Quantum Information*. 51, 123

Lu, Y. J., Campbell, R. L., and Ou, Z. Y. (2003). Mode-locked two-photon states. *Phys. Rev. Lett.*, 91:163602. 121

Lukens, J. M. and Lougovski, P. (2017). Frequency-encoded photonic qubits for scalable quantum information processing. *Optica*, 4(1):8. 51, 120, 121, 140

Lundeen, J. S., Feito, A., Coldenstrodt-Ronge, H., Pregnell, K. L., Silberhorn, C., Ralph, T. C., Eisert, J., Plenio, M. B., and Walmsley, I. A. (2009). Tomography of quantum detectors. *Nature Phys*, 5(1):27–30. 195

Luo, M. and Wang, X. (2014). Universal quantum computation with qudits. *Science China Physics, Mechanics & Astronomy*, 57(9):1712–1717. 23

Lvovsky, A. I. (2015). Squeezed light. *Photonics*, pages 121–163. 79

Maccone, L. and Sacha, K. (2020). Quantum measurements of time. *Phys. Rev. Lett.*, 124(11):110402. 56, 57, 58, 59

MacLean, J.-P. W., Schwarz, S., and Resch, K. J. (2019). Reconstructing ultrafast energy-time-entangled two-photon pulses. *Phys. Rev. A*, 100:033834. 66, 70, 76, 102

Madsen, L. S., Berni, A., Lassen, M., and Andersen, U. L. (2012). Experimental investigation of the evolution of gaussian quantum discord in an open system. *Phys. Rev. Lett.*, 109:030402. 74

Maltese, G. (2019). Generation and manipulation of high-dimensional photonics states with AlGaAs chips. *Hal tel-02494453*, "(2019USPCC009). 85

Maltese, G., Amanti, M. I., Appas, F., Sinnl, G., Lemaître, A., Milman, P., Baboux, F., and Ducci, S. (2020). Generation and symmetry control of quantum frequency combs. *npj Quantum Information*, 6(1):13. 84, 85, 123

Marcikic, I., de Riedmatten, H., Tittel, W., Scarani, V., Zbinden, H., and Gisin, N. (2002). Time-bin entangled qubits for quantum communication created by femtosecond pulses. *Phys. Rev. A*, 66:062308. 51

Marcikic, I., de Riedmatten, H., Tittel, W., Zbinden, H., Legré, M., and Gisin, N. (2004). Distribution of time-bin entangled qubits over 50 km of optical fiber. *Phys. Rev. Lett.*, 93:180502. 51

Marshall, K., Pooser, R., Siopsis, G., and Weedbrook, C. (2015). Repeat-until-success cubic phase gate for universal continuous-variable quantum computation. *Phys. Rev. A*, 91:032321. 38, 80

Masse, G., Coudreau, T., Keller, A., and Milman, P. (2020). Implementable hybrid entanglement witness. *arXiv:2004.00492 [quant-ph]*. 194

Matthews, J. C. F., Poulios, K., Meinecke, J. D. A., Politi, A., Peruzzo, A., Ismail, N., Wörhoff, K., Thompson, M. G., and O'Brien, J. L. (2013). Observing fermionic statistics with photons in arbitrary processes. *Scientific Reports*, 3(1):1539. 136

Mazzotta, Z., Cialdi, S., Cipriani, D., Olivares, S., and Paris, M. G. A. (2016). High-order dispersion effects in two-photon interference. *Phys. Rev. A*, 94:063842. 105, 139

McGuinness, H. J., Raymer, M. G., and McKinstrie, C. J. (2011). Theory of quantum frequency translation of light in optical fiber: application to interference of two photons of different color. *Opt. Express*, 19(19):17876–17907. 138

Menicucci, N. C. (2014). Fault-tolerant measurement-based quantum computing with continuous-variable cluster states. *Phys. Rev. Lett.*, 112. 45, 113, 116, 117

Menicucci, N. C., Flammia, S. T., and Van Loock, P. (2011). Graphical calculus for gaussian pure states. *Phys. Rev. A*, 83:042335. 68

Menzel, R., Heuer, A., Puhlmann, D., Dechoum, K., Hillery, M., Spahn, M., and Schleich, W. (2013). A two-photon double-slit experiment. *Journal of Modern Optics*, 60(1):86–94. 133

Merkouche, S., Thiel, V., Davis, A. O., and Smith, B. J. (2018). Frequency entanglement swapping. *Conference on Lasers and Electro-Optics*, page FM4G.1. 140

Miquel, C., Paz, J. P., and Saraceno, M. (2002). Quantum computers in phase space. *Physical Review A*, 65(6). 23, 24, 176, 179

Mirhosseini, M., Magaña-Loaiza, O. S., Chen, C., Hashemi Rafsanjani, S. M., and Boyd, R. W. (2016). Wigner distribution of twisted photons. *Physical Review Letters*, 116(13). 189

Moller, K. B., Jorgensen, T. G., and Dahl, J. P. (1996). Displaced squeezed number states: Position space representation, inner product, and some applications. *Phys. Rev. A*, 54:5378–5385. 71

Motes, K. R., Baragiola, B. Q., Gilchrist, A., and Menicucci, N. C. (2017). Encoding qubits into oscillators with atomic ensembles and squeezed light. *Phys. Rev. A*, 95:053819. 48, 112, 181, 182

Moya-Cessa, H. (2003). A number-phase wigner function. *Journal of Optics B*, 5(3). 166

Mrowczynski, S. (2013). Wigner functional of fermionic fields. *Physical Review D*, 87(6):065026. 141, 163

Mrowczynski, S. and Mueller, B. (1994). Wigner functional approach to quantum field dynamics. *Physical Review D*, 50(12):7542–7552. 141, 155, 161

Muga, G., Ruschhaupt, A., and Campo, A. (2012). *Time in Quantum Mechanics* -. Number vol. 2 in Lecture Notes in Physics. Springer Berlin Heidelberg. 56

Mukunda, N. (1979). Wigner distribution for angle coordinates in quantum mechanics. *American Journal of Physics*, 47(2):182–187. 177

Nehra, R., Eaton, M., Gonzalez-Arciniegas, C., Kim, M. S., and Pfister, O. (2019a). Loss tolerant quantum state tomography by number-resolving measurements without approximate displacements. *arXiv:1911.00173 [quant-ph]*. 41

Nehra, R., Win, A., Eaton, M., Shahrokhshahi, R., Sridhar, N., Gerrits, T., Lita, A., Nam, S. W., and Pfister, O. (2019b). State-independent quantum state tomography by photon-number-resolving measurements. *Optica*, 6(10):1356–1360. 41

Newton, T. D. and Wigner, E. P. (1949). Localized states for elementary systems. *Rev. Mod. Phys.*, 21:400–406. 56

Nielsen, M. A. and Chuang, I. L. (2011). *Quantum Computation and Quantum Information: 10th Anniversary Edition*. Cambridge University Press, New York, NY, USA, 10th edition. 170

Noh, K., Albert, V. V., and Jiang, L. (2019). Quantum capacity bounds of gaussian thermal loss channels and achievable rates with gottesman-kitaev-preskill codes. *IEEE Transactions on Information Theory*, 65(4):2563–2582. 48

Nonnenmacher, S. and Voros, A. (1997). Eigenstate structures around a hyperbolic point. *Journal of Physics A: Mathematical and General*, 30(1):295–315. 151

Ofek, N., Petrenko, A., Heeres, R., Reinhold, P., Leghtas, Z., Vlastakis, B., Liu, Y., Frunzio, L., Girvin, S. M., Jiang, L., Mirrahimi, M., Devoret, M. H., and Schoelkopf, R. J. (2016). Extending the lifetime of a quantum bit with error correction in superconducting circuits. *Nature*, 536(7617):441–445. 46

Orieux, A. (2012). Source semiconductrices d'etats a deux photons a temperature ambiante. *HAL-tel-00769573 PhD thesis*. 93

Orieux, A., Caillet, X., Lemaître, A., Filloux, P., Favero, I., Leo, G., and Ducci, S. (2011). Efficient parametric generation of counterpropagating two-photon states. *J. Opt. Soc. Am. B*, 28(1):45–51. 128

Orieux, A., Eckstein, A., Lemaitre, A., Filloux, P., Favero, I., Leo, G., Coudreau, T., Keller, A., Milman, P., and Ducci, S. (2013). Direct bell states generation on a iii-v semiconductor chip at room temperature. *Phys. Rev. Lett.*, 110:160502. 104, 128

Orieux, A., Versteegh, M. A. M., Jöns, K. D., and Ducci, S. (2017). Semiconductor devices for entangled photon pair generation: a review. *Reports on Progress in Physics*, 80(7):076001. 82

Ou, Z. Y. and Mandel, L. (1988). Observation of spatial quantum beating with separated photodetectors. *Phys. Rev. Lett.*, 61:54–57. 125, 128

Ou, Z. Y., Zou, X. Y., Wang, L. J., and Mandel, L. (1990). Experiment on nonclassical fourth-order interference. *Phys. Rev. A*, 42:2957–2965. 100

Pain, J.-C. (2013). Commutation relations of operator monomials. *J. Phys. A: Math. Theor.*, 46(3):035304. 198

Paler, A. and Devitt, S. J. (2015). An introduction to fault-tolerant quantum computing. *arXiv:1508.03695 [quant-ph].* 21

Paris, M. G. (1996). Displacement operator by beam splitter. *Physics Letters A*, 217(2):78 – 80. 40

Park, J. L. (1970). The concept of transition in quantum mechanics. *Foundations of Physics*, 1(1):23–33. 16

Park, K., Marek, P., and Filip, R. (2018). Deterministic nonlinear phase gates induced by a single qubit. *New J. Phys.*, 20(5):053022. 38

Parker, S., Bose, S., and Plenio, M. B. (2000). Entanglement quantification and purification in continuous-variable systems. *Phys. Rev. A*, 61:032305. 114

Patera, G., Horoshko, D. B., and Kolobov, M. I. (2018). Space-time duality and quantum temporal imaging. *Phys. Rev. A*, 98:053815. 105

Peres, A. (1996). Separability criterion for density matrices. *Phys. Rev. Lett.*, 77:1413–1415. 88

Potoček, V. and Barnett, S. M. (2015). On the exponential form of the displacement operator for different systems. *Physica Scripta*, 90(6):065208. 166, 191

Poulin, D. (2005). Stabilizer formalism for operator quantum error correction. *Phys. Rev. Lett.*, 95:230504. 20

Preskill, J. (2018). Simulating quantum field theory with a quantum computer. *arXiv:1811.10085 [hep-lat, physics:hep-th, physics:quant-ph].* 45

Proctor, T. J., Dooley, S., and Kendon, V. (2015). Quantum computation mediated by ancillary qudits and spin coherent states. *Physical Review A*, 91(1):012308. 23

Puri, S., St-Jean, L., Gross, J. A., Grimm, A., Frattini, N. E., Iyer, P. S., Krishna, A., Touzard, S., Jiang, L., Blais, A., Flammia, S. T., and Girvin, S. M. (2020). Bias-preserving gates with stabilized cat qubits. *Science Advances*, 6(34). 46

Qian, X.-F. and Eberly, J. H. (2011). Entanglement and classical polarization states. *Opt. Lett.*, 36(20):4110–4112. 73

Qiang, X., Zhou, X., Wang, J., Wilkes, C. M., Loke, T., O'Gara, S., Kling, L., Marshall, G. D., Santagati, R., Ralph, T. C., Wang, J. B., O'Brien, J. L., Thompson, M. G., and Matthews, J. C. F. (2018). Large-scale silicon quantum photonics implementing arbitrary two-qubit processing. *Nature Photonics*, 12(9):534–539. 84

R, K. and Bosture, S. (1985). *Coherent States: Applications In Physics And Mathematical Physics*. World Scientific Publishing Company. 34

Rahimi-Keshari, S., Caves, C. M., and Ralph, T. C. (2013). Measurement-based method for verifying quantum discord. *Phys. Rev. A*, 87:012119. 75

Raussendorf, R., Browne, D. E., and Briegel, H. J. (2003). Measurement-based quantum computation on cluster states. *Phys. Rev. A*, 68:022312. 41

Raymer, M., van Enk, S., McKinstrie, C., and McGuinness, H. (2010). Interference of two photons of different color. *Optics Communications*, 283(5):747 – 752. Quo vadis Quantum Optics? 139

Rigas, I., Sánchez-Soto, L. L., Klimov, A. B., Řeháček, J., and Hradil, Z. (2008). Full quantum reconstruction of vortex states. *Phys. Rev. A*, 78:060101. 166, 178, 179, 181, 183, 186, 191

Rigas, I., Sánchez-Soto, L. L., Klimov, A. B., Řeháček, J., and Hradil, Z. (2010). Non-negative wigner functions for orbital angular momentum states. *Phys. Rev. A*, 81:012101. 178, 184

Robertson, H. P. (1929). The uncertainty principle. *Phys. Rev.*, 34:163–164. 59

Rodiek, B., Lopez, M., Hofer, H., Porrovecchio, G., Smid, M., Chu, X.-L., Gotzinger, S., Sandoghdar, V., Lindner, S., Becher, C., and Kuck, S. (2017). Experimental realization of an absolute single-photon source based on a single nitrogen vacancy center in a nanodiamond. *Optica*, 4(1):71. 88

Roslund, J., de Araújo, R., Jiang, S., Fabre, C., and Treps, N. (2014). Wavelength-multiplexed quantum networks with ultrafast frequency combs. *Nature Photonics*, 8(2):109–112. 31, 80

Roux, F. S. (2017). Quantum state of a frequency comb. *arXiv:1702.04514 [physics, physics:quant-ph]*. 142

Roux, F. S. (2018). Combining spatiotemporal and particle-number degrees of freedom. *Phys. Rev. A*, 98:043841. 141, 142, 143, 144, 147

Roux, F. S. (2020a). Erratum: Combining spatiotemporal and particle-number degrees of freedom [phys. rev. a 98, 043841 (2018)]. *Phys. Rev. A*, 101:019903. 143, 144, 147, 148, 150

Roux, F. S. (2020b). Quantifying entanglement of parametric down-converted states in all degrees of freedom. *arXiv:2004.06412 [physics, physics:quant-ph]*. 141, 154, 155, 158, 162

Roux, F. S. and Fabre, N. (2020). Wigner functional theory for quantum optics. *arXiv:1901.07782 [physics, physics:quant-ph]*. 54, 141, 142, 147, 160, 163

Royer, A. (1977). Wigner function as the expectation value of a parity operator. *Phys. Rev. A*, 15:449–450. 30, 64

Ruetsche, L. (2011). *Interpreting Quantum Theories*. OUP Oxford. 167, 179

Ryl, S., Sperling, J., and Vogel, W. (2017). Quantifying nonclassicality by characteristic functions. *Phys. Rev. A*, 95:053825. 29

Santos, E. A., Castro, F., and Torres, R. (2018). Huygens-fresnel principle: Analyzing consistency at the photon level. *Physical Review A*, 97(4). 133

Sawicki, A. and Karnas, K. (2017). Universality of single qudit gates. *Annales Henri Poincaré*, 18(11):3515–3552. 23

Schroeck, F. E. (1989). On the entropic formulation of uncertainty for quantum measurements. *Journal of Mathematical Physics*, 30(9):2078–2082. 167

Schwartz, I., Cogan, D., Schmidgall, E. R., Don, Y., Gantz, L., Kenneth, O., Lindner, N. H., and Gershoni, D. (2016). Deterministic generation of a cluster state of entangled photons. *Science*, 354(6311):434–437. 42

Senellart, P., Solomon, G., and White, A. (2017). High-performance semiconductor quantum-dot single-photon sources. *Nature Nanotechnology*, 12:1026 EP –. 42, 88, 100, 120

Sharapova, P., Pérez, A. M., Tikhonova, O. V., and Chekhova, M. V. (2015). Schmidt modes in the angular spectrum of bright squeezed vacuum. *Phys. Rev. A*, 91:043816. 98

Sheridan, L. and Scarani, V. (2010). Security proof for quantum key distribution using qudit systems. *Phys. Rev. A*, 82:030301. 22

Shi, Y., Chamberland, C., and Cross, A. (2019). Fault-tolerant preparation of approximate GKP states. *New Journal of Physics*, 21(9):093007. 117

Shor, P. W. (1995). Scheme for reducing decoherence in quantum computer memory. *Phys. Rev. A*, 52:R2493–R2496. 18

Simon, R. (2000). Peres-horodecki separability criterion for continuous variable systems. *Phys. Rev. Lett.*, 84:2726–2729. 88, 89

Sjöqvist, E. (2015). Geometric phases in quantum information. *International Journal of Quantum Chemistry*, 115(19):1311–1326. 63

Smith, B. J. and Raymer, M. G. (2007). Photon wave functions, wave-packet quantization of light, and coherence theory. *New Journal of Physics*, 9(11):414–414. 53, 56

Spring, J. B., Mennea, P. L., Metcalf, B. J., Humphreys, P. C., Gates, J. C., Rogers, H. L., Söller, C., Smith, B. J., Kolthammer, W. S., Smith, P. G. R., and Walmsley, I. A. (2017). Chip-based array of near-identical, pure, heralded single-photon sources. *Optica*, 4(1):90–96. 88

Steane, A. M. (1996). Error correcting codes in quantum theory. *Phys. Rev. Lett.*, 77:793–797. 116

Stratonovich, R. L. (1956). Stratonovich rules. *Zh. Eksp. Teor. Fiz.* **31**, *1012.* 155, 165

Su, D., Sabapathy, K. K., Myers, C. R., Qi, H., Weedbrook, C., and Brádler, K. (2018). Implementing quantum algorithms on temporal photonic cluster states. *Phys. Rev. A*, 98:032316. 45

Sudarshan, E. C. G. (1963). Equivalence of semiclassical and quantum mechanical descriptions of statistical light beams. *Phys. Rev. Lett.*, 10:277–279. 69

Sychev, D. V., Ulanov, A. E., Tiunov, E. S., Pushkina, A. A., Kuzhamuratov, A., Novikov, V., and Lvovsky, A. I. (2018). Entanglement and teleportation between polarization and wave-like encodings of an optical qubit. *Nature Communications*, 9(1):3672. 34

Tasca, D. S., Gomes, R. M., Toscano, F., Ribeiro, P. H. S., and Walborn, S. P. (2011). Continuous variable quantum computation with spatial degrees of freedom of photons. *Phys. Rev. A*, 83(5):052325. 53, 62, 68, 70, 138, 186, 191, 194

Tasca, D. S., Walborn, S. P., Souto Ribeiro, P. H., Toscano, F., and Pellat-Finet, P. (2009). Propagation of transverse intensity correlations of a two-photon state. *Phys. Rev. A*, 79:033801. 138

Tilma, T., Everitt, M. J., Samson, J. H., Munro, W. J., and Nemoto, K. (2016). Wigner functions for arbitrary quantum systems. *Phys. Rev. Lett.*, 117(18):180401. 64, 165, 166

Tollaksen, J., Aharonov, Y., Casher, A., Kaufherr, T., and Nussinov, S. (2010). Quantum interference experiments, modular variables and weak measurements. *New Journal of Physics*, 12(1):013023. 166

Tong, D. (2012). Lectures on string theory. *arXiv:0908.0333 [hep-th].* 60

Toscano, F., Dalvit, D. A. R., Davidovich, L., and Zurek, W. H. (2006). Sub-planck phase-space structures and heisenberg-limited measurements. *Physical Review A*, 73(2):023803. 36, 109

Töppel, F., Aiello, A., Marquardt, C., Giacobino, E., and Leuchs, G. (2014). Classical entanglement in polarization metrology. *New Journal of Physics*, 16(7):073019. 73

Ukai, R., Iwata, N., Shimokawa, Y., Armstrong, S. C., Politi, A., Yoshikawa, J.-i., Van Loock, P., and Furusawa, A. (2011). Demonstration of unconditional one-way quantum computations for continuous variables. *Phys. Rev. Lett.*, 106:240504. 41

Vaccaro, J. A. and Pegg, D. T. (1990). Wigner function for number and phase. *Phys. Rev. A*, 41:5156–5163. 166

Van Enk, S. J. and Fuchs, C. A. (2001). Quantum state of an ideal propagating laser field. *Phys. Rev. Lett.*, 88:027902. 150

Van Loock, P. (2007). Optical quantum computation with continuous-variable cluster states. In *2007 Conference on Lasers and Electro-Optics - Pacific Rim*, pages 1–2. 42

Van Loock, P., Munro, W. J., Nemoto, K., Spiller, T. P., Ladd, T. D., Braunstein, S. L., and Milburn, G. J. (2008). Hybrid quantum computation in quantum optics. *Phys. Rev. A*, 78:022303. 34, 45

Vuillot, C., Asasi, H., Wang, Y., Pryadko, L. P., and Terhal, B. M. (2019). Quantum error correction with the toric gottesman-kitaev-preskill code. *Phys. Rev. A*, 99:032344. 50

Walborn, S., Monken, C., Pádua, S., and Souto Ribeiro, P. (2010). Spatial correlations in parametric down-conversion. *Physics Reports*, 495(4):87 – 139. 78

Walborn, S. P., de Oliveira, A. N., Pádua, S., and Monken, C. H. (2003). Multimode hong-ou-mandel interference. *Phys. Rev. Lett.*, 90:143601. 100, 136

Wan, K. H., Neville, A., and Kolthammer, W. S. (2019). A memory-assisted decoder for approximate gottesman-kitaev-preskill codes. *arXiv:1912.00829 [quant-ph]*. 50

Wang, Y. (2019). Quantum error correction with the GKP code and concatenation with stabilizer codes. *arXiv:1908.00147 [quant-ph]*. 50

Wenger, J., Hafezi, M., Grosshans, F., Tualle-Brouri, R., and Grangier, P. (2003). Maximal violation of bell inequalities using continuous-variable measurements. *Phys. Rev. A*, 67:012105. 31

Wootters, W. K. (2004). Picturing qubits in phase space. *IBM Journal of Research and Development*, 48(1):99–110. 23, 176, 179

Wootters, W. K. and Zurek, W. H. (1982). A single quantum cannot be cloned. *Nature*, 299(5886):802–803. 16

W.Paul (1933). Die allgemeinen prinzipien der wellenmechanik inhandbuch der physik eds. *Geiger H and Scheel K Vol. 24 part 1 (Berlin: Springer Verlag)*. 56

Yanagimoto, R., Onodera, T., Ng, E., Wright, L. G., McMahon, P. L., and Mabuchi, H. (2020). Engineering a kerr-based deterministic cubic phase gate via gaussian operations. *Phys. Rev. Lett.*, 124:240503. 38

Yargic, Y. (2020). Path integral in modular space. *arXiv:2002.01604*. 166

Yargic, Y. and Geiller, M. (2020). Modular polymer representations of the weyl algebra. *arXiv:2002.04541 [gr-qc, physics:math-ph, physics:quant-ph]*. 166

Zhou, X., Leung, D. W., and Chuang, I. L. (2000). Methodology for quantum logic gate construction. *Phys. Rev. A*, 62:052316. 15, 50, 189

Zhu, X., Chang, C.-H., González-Arciniegas, C., Higgins, J., Pe'er, A., and Pfister, O. (2019). Graph state engineering by phase modulation of the quantum optical frequency comb. *arXiv:1912.11215 [quant-ph]*. 80

Zhuang, Q., Preskill, J., and Jiang, L. (2020). Distributed quantum sensing enhanced by continuous-variable error correction. *New J. Phys.*, 22(2):022001. 52

Zielnicki, K., Garay-Palmett, K., Cruz-Delgado, D., Cruz-Ramirez, H., O'Boyle, M. F., Fang, B., Lorenz, V. O., U'Ren, A. B., and Kwiat, P. G. (2018). Joint spectral characterization of photon-pair sources. *Journal of Modern Optics*, 65(10):1141–1160. 92

Zurek, W. H. (2001). Sub-planck structure in phase space and its relevance for quantum decoherence. *Nature*, 412(6848):712–717. 65